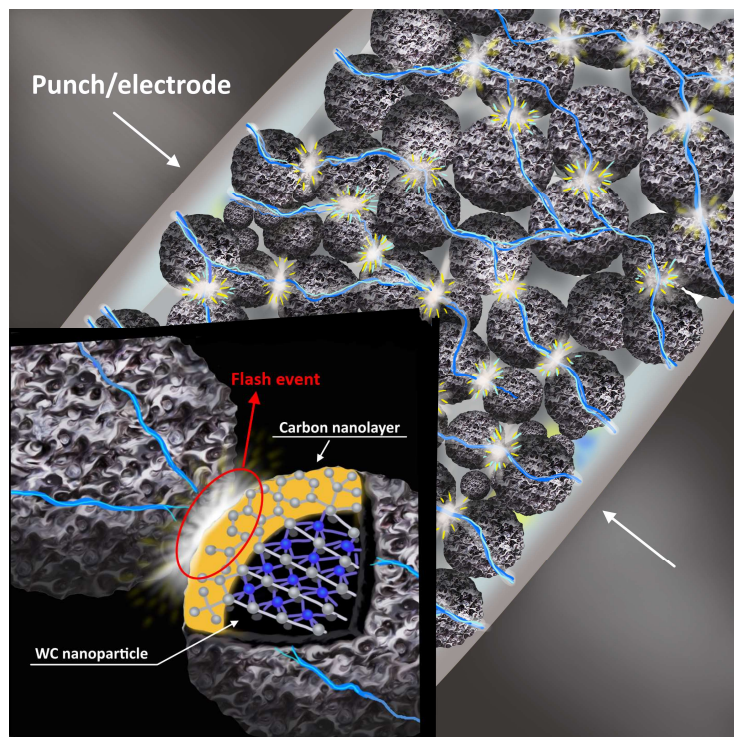UNIVERSITÀ DI TRENTO | **Department of Industrial Engineering**

Doctoral School in Materials, Mechatronics and Systems Engineering

Flash sintering of tungsten carbide

Punch/electrode

Flash event

Carbon nanolayer

WC nanoparticle

Isacco Mazo

14/07/2023

Flash sintering of tungsten carbide

Isacco Mazo

Email: isacco.mazo@unitn.it

Approved by:

PhD commission:

Prof. Vincenzo Maria Sglavo, Advisor

Prof. Claude Estournes

Prof. Alberto Molinari, Advisor

CNRS, France

DII, Dept. of Industrial Engineering

Emilio Rustighi

University of Trento, Italy

University of Trento, Italy

Tiziano Bellezze

Prof. Claire Dancer

SIMAU, Marche

Polytechnic

University of Warwick, GB

University, Italy

Prof. Claude Estournes

CNRS, Centre national de la recherche *scientifique France*

Abstract

Binderless tungsten carbide (BTC) ceramics are inherently difficult to process and very brittle. Most consolidation techniques for processing pure WC powder require long sintering times and intense energy consumption. High-T pressureless and pressure-assisted sintering processes often lead to low-quality and coarsened microstructures, thus limiting the use of WC ceramics to few niche applications. Field-assisted sintering techniques (FAST), like spark plasma sintering (SPS), significantly improve the densification of fine and ultrafine WC powders. However, SPS requires high current outputs and expensive apparatus. SPS ceramics still lack adequate toughness to extend the use of BTC components in heavy-duty applications requiring reliable load-bearing capability and/or resistance against rapid and unexpected impacts or temperature drops. This research work explored a new consolidation route capable of boosting the mass transport phenomena (accelerated sintering) and, simultaneously, introducing new microstructural features. The process called flash sintering (FS) offers great potential in accelerating diffusion phenomena and altering the crystallographic and/or the defect chemistry of the sintered ceramics. Many scientific studies reported structural alterations, enhanced plastic flow and material softening by introducing "out-of-equilibrium" characteristics. Currently, FS technology requires, for its activation, a negative dependence of the electrical resistivity with temperature (NTC) of the material to be sintered. This is a universal requirement for the flash event to occur thus theoretically inhibiting the flash sintering of conductive materials with a positive temperature coefficient for resistivity (PTC), like metals or WC.

In the present work, we reported how during electrical resistance sintering (ERS) experiments conducted on pure WC nanopowders, a flash event was triggered during the first seconds of the process. This was demonstrated to occur thanks to the different evolution of the electrical properties of a granular compact with temperature. WC powders possess an initial NTC behaviour which can activate a transitory thermal runaway phenomenon which makes the activation of a flash event in

these materials possible, intense enough to allow ultrafast densification in less than 10 s. This breakthrough allows to verify whether and how the flash event modifies the final sintered material. FS and SPS sintered ceramics were compared in their microstructural, physical and mechanical properties, thus pointing out how some peculiar modifications are exclusively present in the flash-sintered material. FS can stabilize the WC_{1-x} metastable phase after cooling to room temperature, and this was demonstrated to alter the high-temperature deformation of WC micropillars during compression. In addition, FS BTC are inherently softer with respect to SPS ones, resulting in higher fracture toughness and slightly lower hardness.

Even if not final, the results indicate how the flash sintering of WC can be explored further to process engineered BTC ceramics with an optimized hardness/toughness ratio and an enhanced deformability.

List of Figures

List of Tables

List of Abbreviations

- Tungsten carbide (WC)
- Binderless tungsten carbide (BTC)
- Fast breeder test reactor (FBTR)
- Flash sintering (FS)
- Hot pressing (HP)
- Hot isostatic pressing (HIP)
- High-pressure high-temperature (HPHT)
- Field assisted sintering (FAST)
- Negative temperature coefficient of resistivity (NTC)
- Positive temperature coefficient of resistivity (PTC)
- Electric-current assisted sintering (ECAS)
- Spark Plasma sintering (SPS)
- Electrical resistance sintering (ERS)
- Electrical resistance flash sintering (ERFS)
- Mechanical testing system (MTS)
- Data acquisition system (DAQ)
- Digital multimeter (DMM)
- Thermocouple (TC)
- Scanning electron microscopy (SEM)
- Field emission scanning electron microscopy (FESEM)
- Field emission gun scanning electron microscopy (FEG-SEM)
- Energy dispersive X-Ray spectroscopy (EDXS)
- X-Ray diffraction (XRD)
- International Center for Diffraction Data (ICDD)
- Electrical contact resistance (ECR)
- Backscattered electron (BSE)
- Electron backscattered diffraction (EBSD)
- Transmission electron backscattered diffraction (t-EBSD)
- Transmission Kikuchi diffraction (TKD)
- High resolution transmission electron microscopy (HRTEM)
- Scanning transmission electron microscopy (STEM)
- High-angle annular dark filed (HAADF)
- Focused ion beam (FIB)
- Differential scanning calorimetry (DSC)
- Thermogravimetric analysis (TGA)
- X-ray photoelectron spectroscopy (XPS)
- Finite element methods (FEM)
- Atomic Force Microscopy (AFM)

Contents

Preface

This thesis reports the research activities conducted during my PhD program, at the Industrial Engineering Department of University of Trento, under supervision of Professor Vincenzo M. Sglavo and Professor Alberto Molinari. Part of the research was performed in collaboration with IMdea Materials Institute (Madrid, Spain) under the supervision of Professor Jon M. Molina-Aldareguia.

This thesis aims to disclose a new energy-efficient consolidation route for WC ceramics, exploring the rapid heating generated by an electric current interacting with the powdered material. Specifically, this work wants to elucidate the electro-thermal-mechanical phenomena occurring when a high AC current output interacts exclusively with pure WC powders without a binder phase.

The thesis illustrates the materials and adopted methods, performed experiments and the results. Chapter 1 briefly introduces the technological importance of cemented carbide materials and summarises the current state-of-the-art of the consolidation processes for binderless tungsten carbide (BTC) ceramics; an overview of the main advantages and limitations of processes like Hot Isostatic Pressing (HIP), high temperature solid-state sintering and advanced field assisted-techniques like Spark Plasma Sintering (SPS) and Electrical Resistance Sintering (ERS) is reported. Chapter 2 describes the conditions and the phenomenology of the newly discovered Electrical Resistance Flash Sintering (ERFS) for WC. The remarkable acceleration in the sintering kinetic when a high-output alternate current (AC) interacts with the sample is studied in connection with the evolution of the material electrical properties during sintering. Chapter 3 reports the research carried out for the optimisation of the process, especially on the relation between final microstructure and sintering parameters. Different peculiar microstructures can be obtained during the flash sintering process, characterised by a high density of crystalline defects and different WC/W$_2$C ratio. The same Chapter also presents a comparison of the microstructures achieved when the same powders are consolidated by SPS. The last Chapter 4 reports the mechanical properties, at the macro and micro scale, of the

flash sintered materials in relation to those microstructures obtained. A study of the small-scale plasticity of BTC products at room and high temperature by in-situ compression tests of micrometric pillars is reported. The high temperature deformability of BTC products differs according to the consolidation technique, FS or SPS, this pointing out how the flash sintering process can alter the high temperature deformability in BTC products.

At the end, future perspectives are presented on new strategies for the fast and energy efficient consolidation of electronic conductive ultra-high temperature ceramics (UHTC) by the Electrical Resistance Flash Sintering (ERFS) process.

Chapter 1

Introduction

1.1 Tungsten carbide: properties & technological importance

Tungsten carbide (WC) ceramic, usually referred as WIDIA, in German "wie diamant", i.e. "hard as diamond", is a transition metal carbide very famous for its widespread use as tool for mechanical machining. Despite being known as Widia, its notoriety is primarily related to a very peculiar combination of mechanical, physical and chemical properties rather than an exceptionally high hardness. WC is not the hardest material among the other Group IV-VI transition metal carbides, nor it is the most refractory compound (melting point 2870ºC). However, it combines some of the most important properties to be used for many heavy-duty industrial applications. It possesses one of the highest Young's modulus after diamond (E≈700GPa), its high hardness (26-30 GPa) remains more stable than in nonstoichiometric carbides (such as TiC, ZrC, HfC, VC, NbC, TaC) in the temperature range of 25-1000ºC and its stoichiometry gives origin to unconventional low concentration of defects (carbon vacancies) which in turn boost the thermal, oxidation and chemical stability of such ceramic. WC also has a thermal expansion coefficient ($\sim 5.5 \times 10^{-6}$ K^{-1}) which is half of the other transition carbides; a property which coupled well with its low friction coefficient and high thermal conductivity (100-150 W / m K) making WC an ideal material for mechanically strong and wear resistant inserts and coatings. However, the high hardness and brittleness of pure WC make it difficult to exploit all these appealing properties on bulk components. Polycrystalline WC components have low fracture toughness, around 4-5 MPam$^{-0.5}$, making their use impracticable for any applications requiring reliable load-bearing capability and/or resistance against rapid and unexpected impacts or temperature drops.

In addition to said problematics, tungsten carbide ceramics are extremely difficult to consolidate by solid-state sintering in the absence of sintering aids. The high melting point and the highly covalent character of W-C and W-W bonds results in sluggish diffusivities of C and W atoms under pure solid-state diffusion [1]. Sintering of pure WC powders requires unnaturally long duration and/or very high temperatures in excess of 2000ºC, which can only be reached in specialised graphitic furnaces working in a controlled atmosphere [2]. Pressureless sintering of pure WC powders in such conditions results in bulk components of low microstructural quality, characterised by high residual porosity and coarsened microstructures. An example of such a low-quality microstructure is shown in Figure 1.
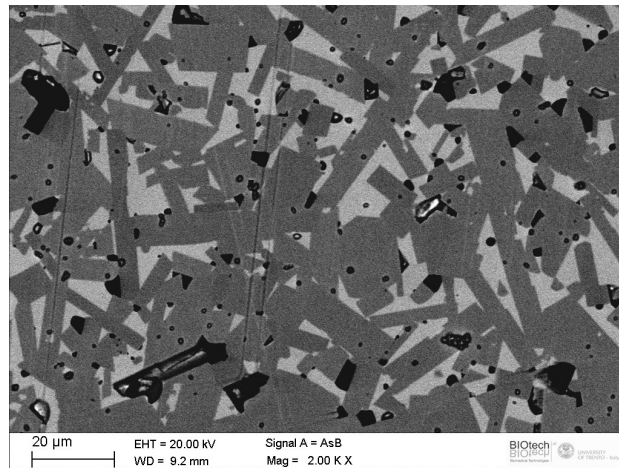
Figure 1. Example of the microstructure of polycrystalline WC, in the absence of sintering aids, after pressureless sintering at 2100ºC with 2 h of holding time. Particle size of the starting powder was about 240 nm (Original figure by Mazo).

To face these problems the development of new WC-based cemented carbides started since the 1930s [3,4]. The solution for both limited sinterability and toughness of pure WC was found in the incorporation of carbide grains into metallic matrix composed of element with high chemical affinity to WC, like Fe, Ni or Co. The obtained composites retained a large portion of the WC hardness while at the same time boost the material toughness by the presence of ductile metal bonding together the ceramic grains. The

incorporation of Ni or Co during sintering is also fundamental for activating the liquid phase sintering which allows (i) fast sintering under the capillary force of liquid between the WC grains, (ii) grains rotation and particle re-arrangement and (iii) higher diffusion kinetics of C and W atoms. A suitable metallic binder needs to form an eutectic with WC and the produced liquid phase must have a good wettability and solubility concerning the WC grains. Under these conditions the temperature required for consolidating the starting powders sharply decreases from 2000ºC (solid-state sintering) to about 1280-1450ºC (liquid-phase sintering) [5].

In the beginning, cemented carbides, also referred as "hardmetals", were developed as substitute for the very costly diamond dies used for drawing W wires [6]. Their development and commercialisation skyrocketed when tools with WIDIA-hardmetal inserts started to be used for the turning and milling of cast iron and hardened steels. The materials science of cemented carbide progressed for more than a century and it remained a rich field of research since nowadays. Its development was initially focused on the effect of the composition on the mechanical properties; the main constituents of cemented carbides were Co, WC, TiC, TaC and NbC [5]. The most important constituent was the binder phase, Co, which tunes the material hardness/toughness ratio to the required values. For example, fracture toughness of about 14-15 MPam^{-1} and bending strength up to 3000 MPa can be reached by increasing Co content up to 20 ± 5 wt%. Successively, fine grained hardmetals become the new focus of the research and accordingly new materials composition and/or processing techniques were implemented in search of limiting the very rapid grain growth occurring in the presence of the liquid phase during sintering. Micrometric and sub-micrometric WC-Co grades strongly benefit from the increased hardness and flexural strength granted by the reduced WC grains size without the necessity in decreasing the binder content. Fine and ultrafine WC-Co grades possess the microstructural uniformity required for tools used in the micro-machining of delicate components, such as those for the electronic industry. The most

3

important WC-based cemented carbides developed since nowadays were summarised by Garcia et al. (Sandvik company) in their review [7] and reported in Figure 2.
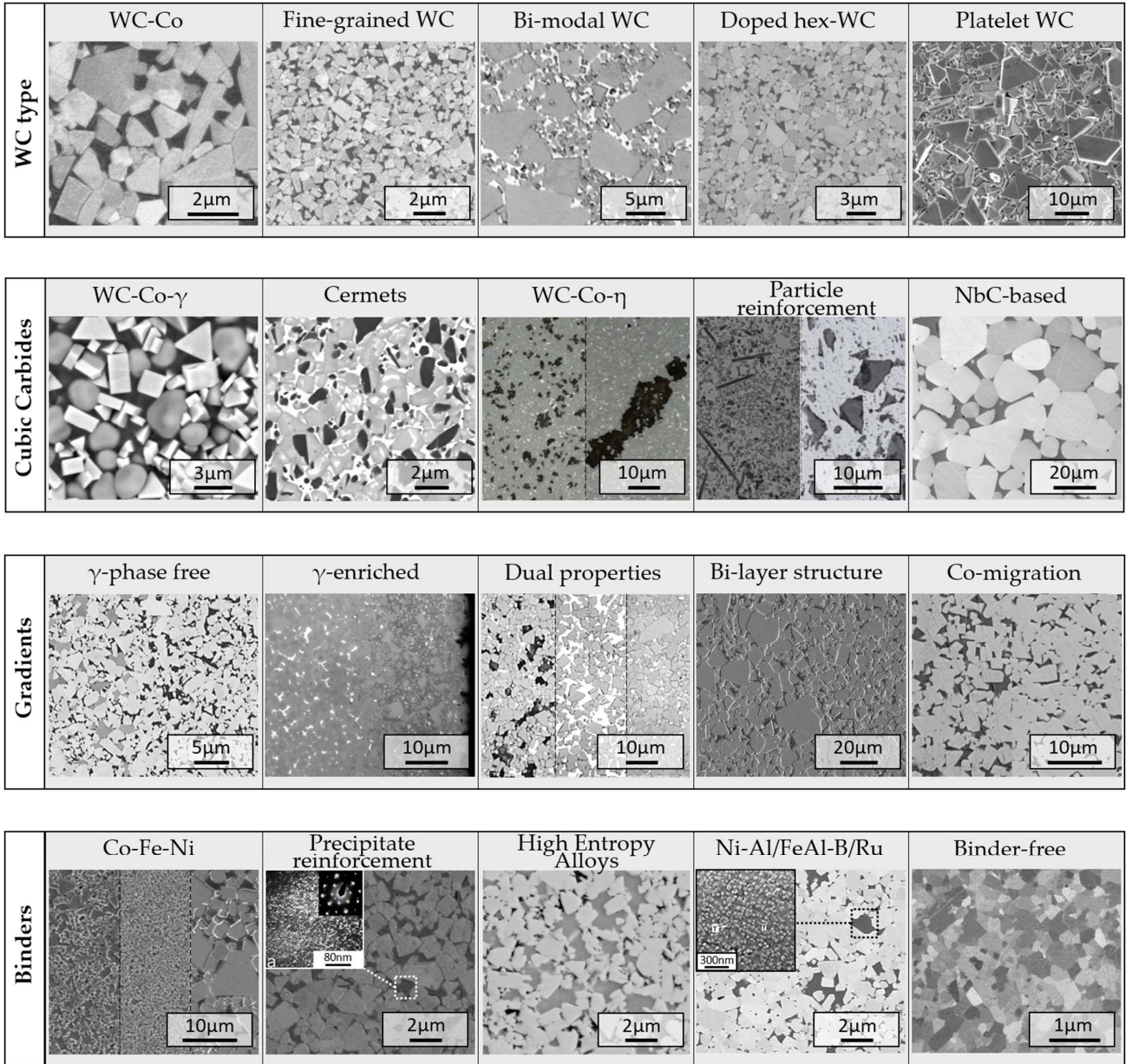
Figure 2. Microstructures of different types of WC-based materials represent the state-of-the-art development of cemented carbides and cermet materials. (Original figure by Garcia et al. [7], distributed under a creative commons CC BY NC ND license).

The reader can notice how binder-free WC, represented by the last image of Figure 2, is the most recent type of WC-based material being researched nowadays. This is a controversial fact since the simplicity of binderless WC, which consists of only the hard WC phase, suggests it should be the first researched and studied material from a chronological point of view. Nevertheless, the focus on this material started only recently because of two fundamental aspects: (i) the lack in the past of the need for pure WC bulk components and (ii) the absence of advanced sintering techniques for efficient and effective consolidation of pure WC materials.

1.2 Necessities for binderless WC products

The main reason at the base of binderless WC development is the creation of bulk components retaining all the native properties of tungsten carbide, i.e. refractory materials with exceptionally high hardness, elastic modulus and chemical stability, which at the same time are very good electronic and thermal conductors. These combinations of unique properties derives directly from the WC crystal structure, which is characterised by a mixture of covalent, ionic and metallic bonds [8]. WC is sometime referred as a "metallic ceramic" because it retains a portion of the metallic bonds from tungsten, a characteristic allowing the presence of free electrons in its lattice giving rise to an unusually high electrical and thermal conductivity for a ceramic material [9]. To have an idea, its electrical conductivity ($\sim 4.5 \times 10^6$ S/m) is only one order of magnitude far from metals used in the electronic industry such as copper, silver and gold ($\sim 6 \times 10^7$ S/m).

Now binderless tungsten carbide (BTC) components are used is some specific applications that require the absence of the metallic phase. An example is the production of moulds for aspherical glass lenses, used in miniaturised camera devices [10]. The high level of precision required for moulding these lenses

is not achievable in the presence of Co for two main reasons: (i) the difference in the thermal expansion coefficient between Co ($\sim 13 \times 10^{-6}$ K^{-1}) and WC ($\sim 5 \times 10^{-6}$ K^{-1}) and (ii) the higher wear rate of Co in contact with hot glass at 500-600 ºC degrade the moulding precision. BTC extreme resistance to abrasion and wear resistance is also a requisite for mechanical seals, sliding parts and high-T electrical contacts. Without Co it can be polished to very fine surface roughness, ideal in the use of miniaturised tools for electrical micro-devices. In general, the elimination of the metallic part dramatically boosts the oxidation and corrosion resistance especially at the high temperatures and/or in harsh environments where metals are susceptible to a chemical and mechanical degradation. As pointed out by Sun et al. in their comprehensive reviews [11,12], BTC composites have the potential to exhibit superior performance in extremely tough environmental conditions.

In these regards, BTC and WC-based materials are gaining a new interest from the scientific community in neutron shielding and extreme heat flux applications. Highly dense tungsten monocarbide (WC) is considered the most suitable option for extending the life of grid plate components for the Fast Breeder Test Reactor (FBTR), a high temperature fission reactor [13]. WC has been studied for its large thermal neutron absorption capabilities [14], the combination of high-Z and low-Z elements result in a low neutron and gamma attenuation lengths [15]. Dash et al. suggested WC as a possible candidate in lieu of W, due to the presence of C in the crystalline structure which is known to be a good moderator material for high-energy neutrons [14]. In these regards the strong atomic bonding, expressed by one of the highest Young's modulus of material in nature (700 GPa), can potentially hinder or retard the mechanical degradation driven by the atomic displacement caused by neutron radiation damage.

In 2022 Baker and Smith compared metallic W with monolithic tungsten carbide and its composites as an attractive class of neutron-attenuating materials in the development of compact spherical tokamak for nuclear fusion technology (Figure 3). In this perspective, the high linear neutron absorption coefficient

of WC and especially of WC+5 wt% B_4C [14] are beneficial to protect the high-temperature superconducting (HTS) tapes from the radiation damage.
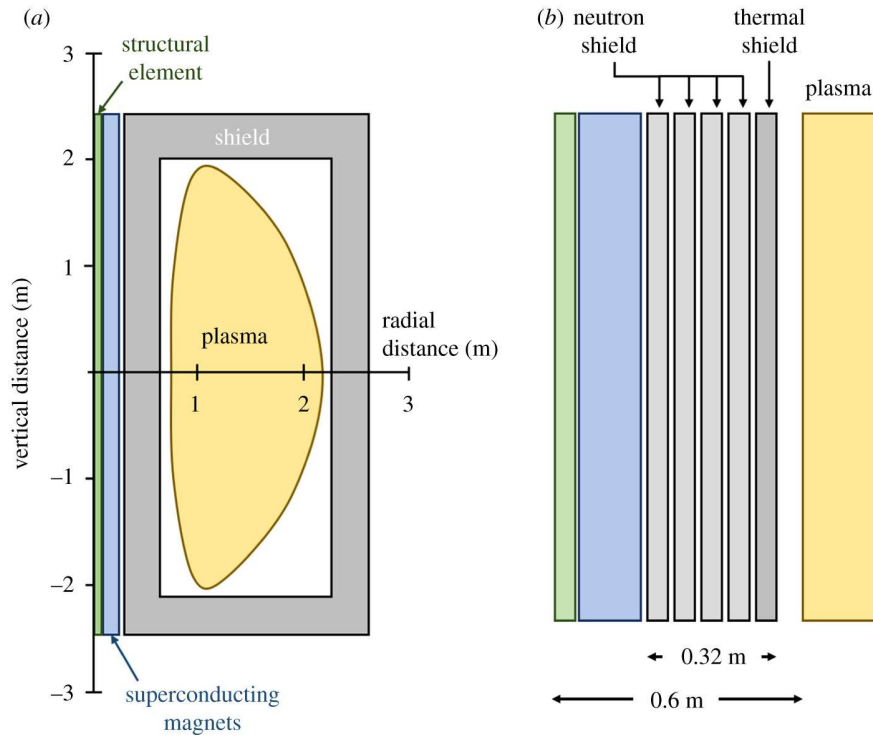
Figure 3. Example of a pilot plant design for a compact spherical tokamak (c-ST), with only 1.35m of major radius. The space available for the shield is only 0.32m, which contains five concentric layers of shield material with water cooling channels in between. (From Baker and Smith [16]*).*

In addition to neutron and gamma attenuation properties, plasma facing materials must address three fundamental challenges, regarding (i) heat flux, (ii) irradiation and (iii) plasma surface interactions [16]. Plasma facing materials, such as those used in the first wall and in the divertor will experience an enormous heat flux, in the order of 1-10 MW/m^2 (steady-state). Hence, the maximum wall loading scales inversely with the thermal conductivity (k) for a certain geometry design. In addition, plasma instabilities events such as edge-localised modes (ELMs) contribute for transitory heat fluxes of ~10 MW/m^2 for a fraction of a millisecond, leading to surface erosion, melting and cracking due to thermal shock.

As reported by Kundu et al., a highly dense monolithic WC is characterised by an "anomalously" large lattice thermal conductivity [17]. WC has a lattice thermal conductivity evaluated as high as 130-160 W/mK at RT [17], of which the phonon contribution (k_{ph}) is three times larger than the electronic one (k_e) (Figure 4). Usually, the electron-phonon interaction has a negligible effect on the lattice thermal conductivity in metals. In the case of WC, the large k_{ph} is due to a weak phonon-phonon and electron-phonon scatterings, consequence of a unique combination of very strong interatomic bonding and the large mass of W that creates a large acoustic-optical phonon gap. k_{ph} also possesses a weak temperature dependence which is desirable in such applications where high heat fluxes must be dissipated at an increasing material's temperature.
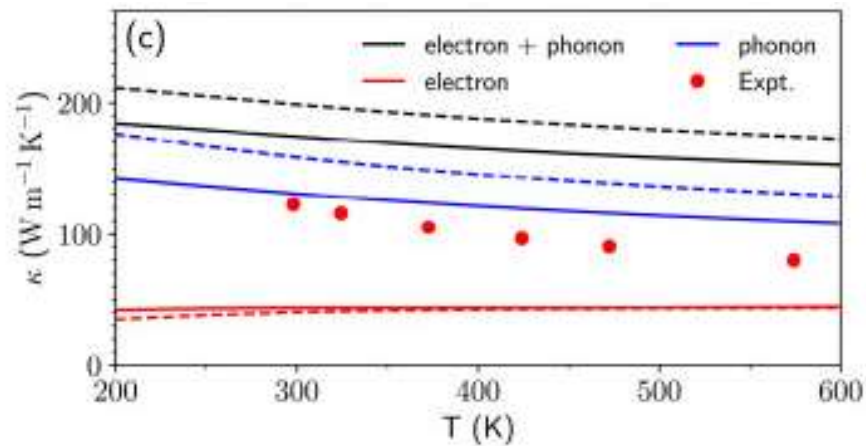
Figure 4. Total thermal conductivity (k = k_{ph} + k_e) as a function of temperature for WC. The solid and the dashed lines correspond to the lattice thermal conductivity along the a and c axes. (Original figure by Kundu et al. [17]).

During dynamic heating conditions, the thermal stress resistance parameter can be represented by:

$$R = \frac{(1-\nu)\sigma_f}{E\alpha}$$

(1)

Where σ_f is the fracture stress, E the Young's modulus, ν the Poisson's ratio and α the linear thermal expansion coefficient. According to the data presented in Table 1, the properties of WC granted a thermal shock resistance (R) three times higher than a powder metallurgy processed W [16].

Table 1. Room temperature properties of candidate plasma-facing materials.

	flexural strength, σ_f (GPa)	Young's modulus, E (GPa)	Poisson's ratio, ν	thermal expansion coefficient, α (x10^{-6})	thermal stress resistance, R (K^{-1})
W	0.4	380	0.28	4.4	**3**
WC	1.6	700	0.18	3.4	**10**
WC-10Co	3.9	580	0.21	6	**13**

Very recently, Baker et al. tested the resistance of rolled W, monolithic WC and a WC-FeCr cermet under plasma-induced thermal shock conditions [18]. Surprisingly, monolithic WC outperformed the metallic W and the engineered WC-FeCr cermet (Figure 5). The authors explained the results because of three important aspects: (i) the preferential melting of the metallic FeCr during the thermal cycles, (ii) the rapid loss of the flexural strength with temperature of the cermet (1.72 GPa at 400 ºC vs 0.61 GPa at 1000ºC) and (iii) the decrease in the thermal conductivity driven by the presence of a second phase between the WC grains (k = 70-50 W/mK). The thermal shock resistance of monolithic WC was higher than the other two candidates because of its higher fracture strength at elevated temperatures, 1.16 GPa at 400ºC and 1.84 GPa at 1000ºC.
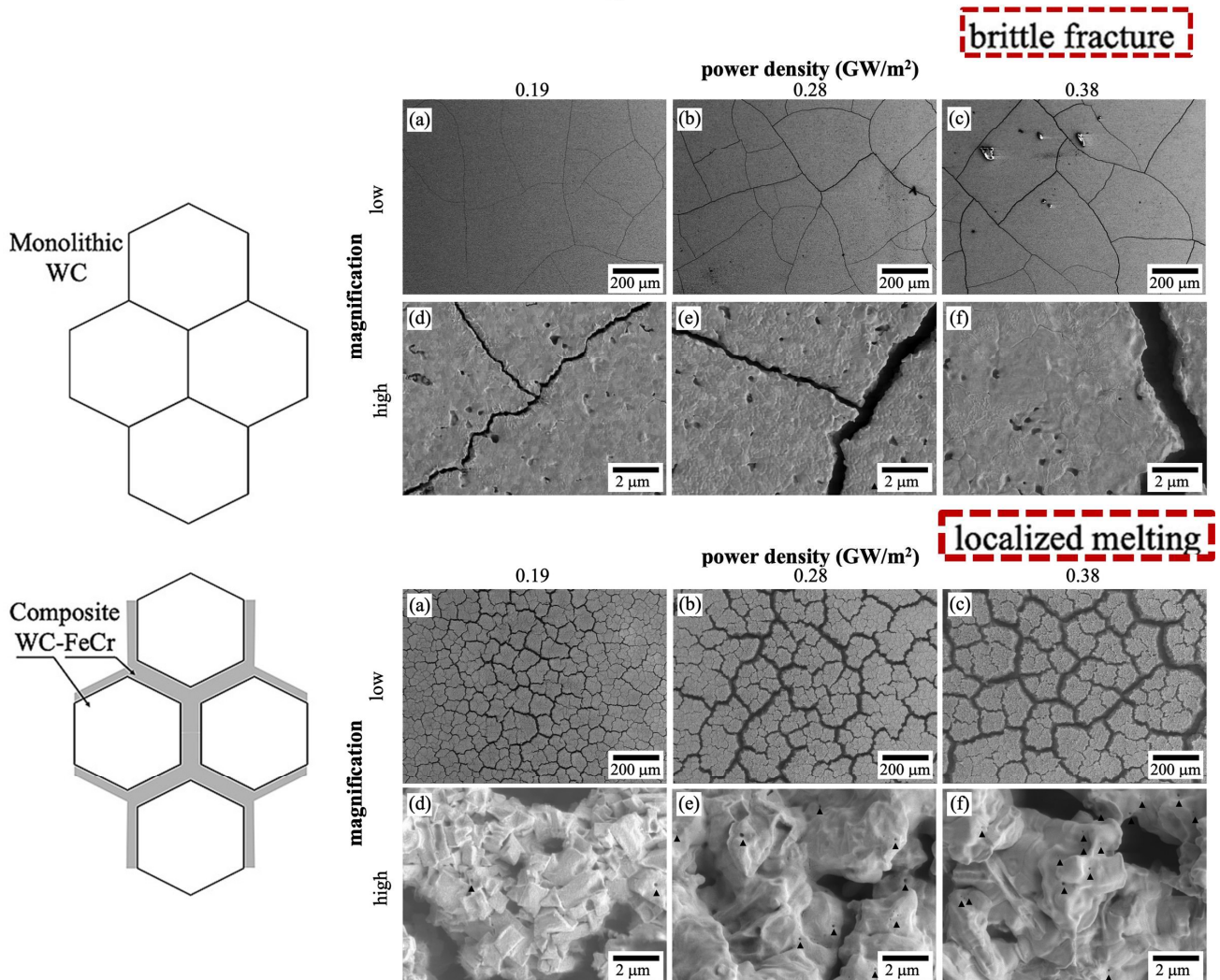
Figure 5. SEM images of monolithic WC (top) and WC-FeCr (bottom) after thermal shock at 1000℃ for 1000 cycles under increasingly higher power densities: from 0.19 to 0.38 GW/m². (Original figure by Baker et al. [18]).

The radiation-induced evolution of defects and their clustering has been recently studied by S. Oliver et al. [14], although, as the author pointed out, more studies are necessary to confirm or exclude this material as a possible shield material.

1.3 Sintering of binderless tungsten carbide

There are two main strategies for the successful densification of pure WC powders: (i) pressure-assisted sintering techniques: hot pressing (HP), hot isostatic pressing (HIP) / gas pressurised sintering (GPS) and high pressure - high temperatures (HPHT) and (ii) field assisted sintering technologies (FAST): like spark plasma sintering (SPS) and electrical resistance sintering (ERS).

1.3.1 Pressure-assisted sintering

Hot Pressing. Of the former category, hot pressing (HP) was the first technique used to consolidate fine WC powders without sintering aids. As described by Gubernat et al. [19] it is possible to produce dense and single-phased BTC products by the HP practice. To achieve densities in the 97-99 % range, the powder was hot pressed at 2150ºC, 30 min holding time, under 25 MPa (Figure 6, a). Poetschke et al. reported satisfactory densification at 1900ºC under 80 and 100 bar of Ar gas pressure using GPS/HIP furnaces [20,21]. The authors also reported that in the absence of a binder phase critical is the control of the carbon content during the sintering process; a sub-stoichiometric carbon content (C < 6.13 wt%) lead to the formation of the sub-carbide phase (W_2C) as well as a lower overall densification. The introduction of free carbon in the system, in the right amount to restore a stochiometric W-C composition, decrease the required temperature for sintering by 200ºC, from 2150ºC to 1950ºC (Figure 6, a and b, respectively). Since the stability range of W-C is virtually a vertical line in the phase diagram [22] is very difficult to tune the C addition perfectly, it often results in the presence of free carbon in the sintered materials.

Gubernat et al. reported the presence of C excess as graphite nanolayers on intergranular boundaries. This C nanolayer leads to adverse mechanical properties in grain boundary decohesion, although it is greatly beneficial in boosting the thermal conductivity of the bulk (Figure 6, c).
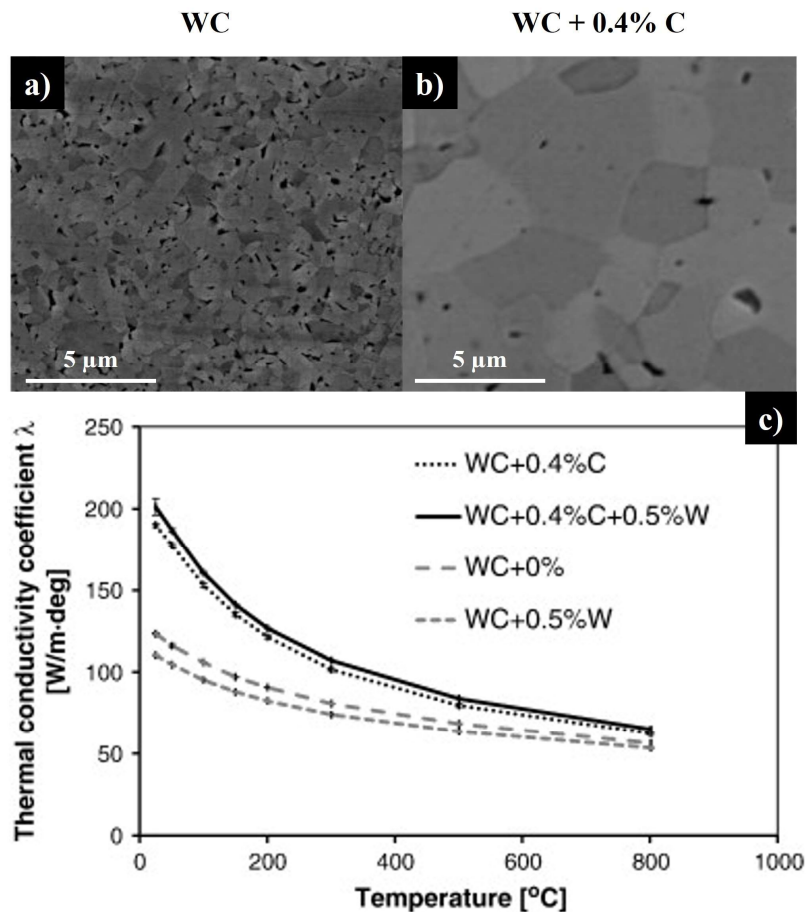
Figure 6. SEM micrographs of monolithic WC components sintered by HP: a) pure WC; b) WC + 0.5% C. WC bulk thermal conductivity as a function of temperature for different composition of the starting powder (c). (Original figures by Gubernat et al. [19]).

To understand the possible uses of monolithic WC obtained by HP, the authors tested the produced polycrystals as cutting tools in C45 carbon steel grade machining. The longest cutting tool life was only about 10 minutes, where the intense abrasive wear was caused by the cracking along intergranular

boundaries and the loss of grains cohesion. The lowest tool life was observed in WC samples with C additions, characterised by a coarsened microstructure and a weaker grain boundary (Figure 6 b). None of the tested samples was suitable for machining carbon steels, highlighting how the material prepared by hot pressing is not enough damage tolerant (low fracture toughness, K_{IC} = 5 - 6 MPa m$^{0.5}$) to replace commercial cemented carbide products.

High pressure-high temperature. The high pressure-high temperature (HPTP) differs from HP or hot isostatic pressing (HIP) in the maximum pressure attainable during the sintering procedure. HPHT exploits special cubic anvils (Figure 7) capable of applying a quasi-hydrostatic pressure, in the order of several GPa, to the green material by a medium deformable material, usually NaCl.
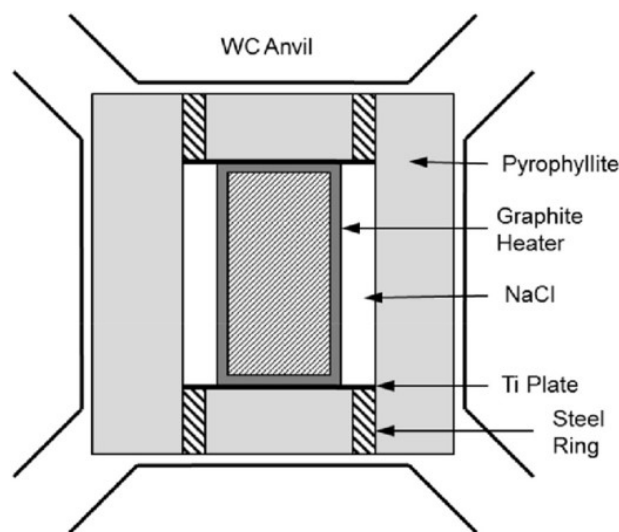
Figure 7 Schematic of high-pressure high-temperature (HPHT) sintering apparatus. (Original figure by Mukhopadhyay [23]*, licensed under a CC BY-NC-ND 4.0).*

Kou et al. reported full consolidation of nano-WC powders (200 nm) at considerably lower sintering temperatures: 1500ºC (30 min holding time) under 5 GPa of pressure [24] and as low as 1300 ºC under 10 GPa [25]. The author also reported a strengthening mechanism driven by the very high pressure

applied during sintering. Sintered grains in the presence of ultra-high pressures are full of planar defects, such as: dislocations, stacking faults (SF) and nano-twins (Figure 8). Vickers indentations performed at 98 N result in hardness as high as 29 GPa with fracture toughness (K_{IC}) of about 8-9 MPa m$^{0.5}$ (Anstis formalism [26]), a value two times higher than conventionally BTC sintered products. The author suggested a connection between the deformed twin structures and the increased mechanical properties of the materials, although no explanations were reported explaining how the material can be at the same time so hard and tough.

In the absence of extrinsic toughening mechanisms able to dissipate the energy for crack propagation, as in the case of monolithic WC components with equiaxed grains, the fracture toughness measured by the indention method is exclusively related to the material plasticity (intrinsic toughening mechanisms) a property which theoretically is mutually exclusive with the hardness [27].
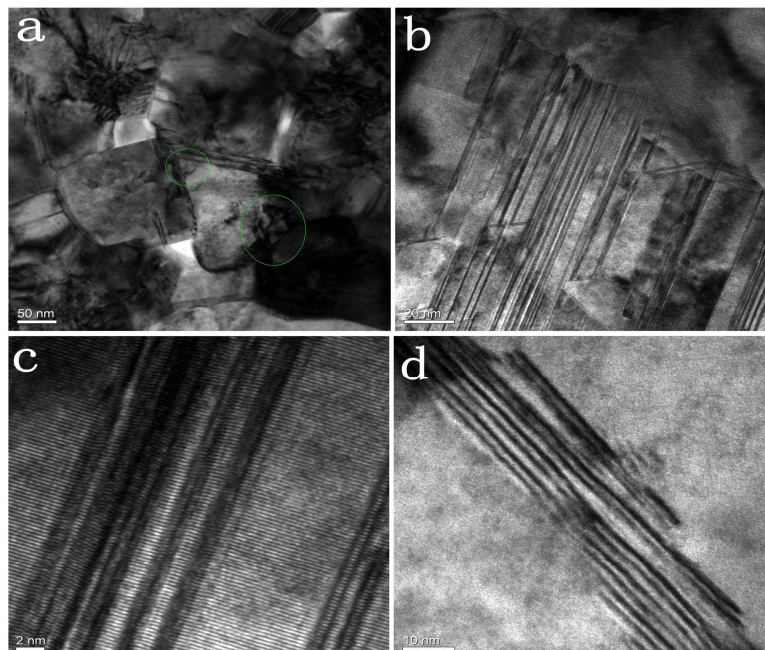
Figure 8 TEM images of WC grains sintered by HPHT technique under 5 GPa at 1500 °C (a).

Deformation twins (b)(c) and stacking fault microstructures (d). (Original figure from Kou et al. [24]).

1.3.2 Field-assisted sintering technologies (FAST)

FAST techniques exploit the interaction of an electric current with the powdered material to achieve full density at lower temperatures and/or in shorter times. There are mainly two reasons for their superior sintering efficiency: (i) a faster generation of heat by Joule heating, thus allowing heating rates as high as 200-1000 °C/min and (ii) the activation of the particle surfaces due to thermo-electric breakdown of the surface oxides.

Spark plasma sintering. The most successful FAST process to consolidate WC ceramics is spark plasma sintering (SPS). A conspicuous scientific outcome has proven its potential in the last two decades [28–38]. Despite the very high cost of the apparatus and the constraints imposed for simple geometries, which increase the post-sintering machining costs, SPS is also being used in some specific industrial applications. This processing route allows the consolidation of high-quality BTC ceramics, with exceptional control over the final microstructure in phase composition and grain size. It is the only technique capable of producing hard (26-30 GPa), single-phase (α-WC) BTC components with an average grain size < 0.5 μm without the necessity to use grain growth inhibitors (Cr_3C_2 or VC) [20,39] (Figure 9). SPS considerably shortens the sintering time to fully densify monolithic BTC materials, passing from the typical 2-3 hours required for the HP or HIP processes to just 20-30 min. For example, a full density (99%+) BTC component with the microstructure shown in Figure 9 can be produced in only 25 min, also considering the cooling steps, starting from an ultrafine pure WC powder (APS~240 nm).
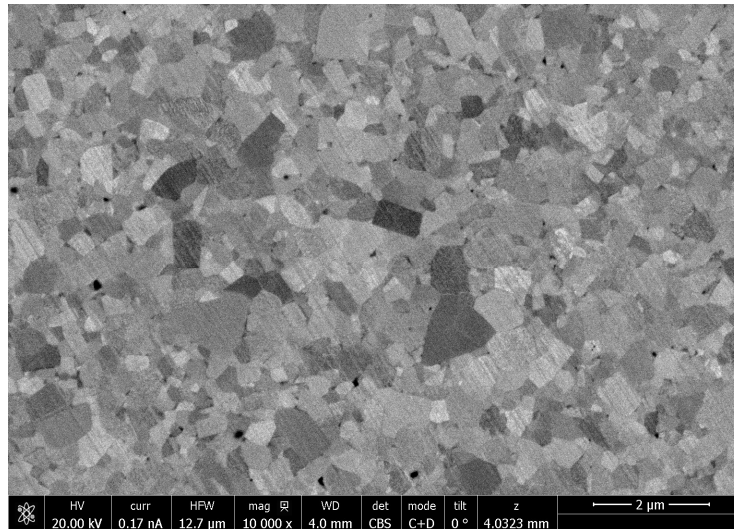
Figure 9 Example of the microstructure of monolithic α-WC with an average grain size <0.5 µm produced by SPS. Average particle size (APS) of the starting powder = 240 nm. (Original figure from Mazo)

Despite the name, during the spark plasma sintering practice, there are no real conditions for electrical arching and/or for the generation of interparticle plasma [40]. As schematised in Figure 10, a commercial SPS apparatus should be more properly classified as a pressure-assisted fast sintering process where the pressure is applied uniaxially by graphitic punches that serve at the same time as high current-density electrical contacts. The powdered material is stored inside a cylindrical graphite die where the two electrodes apply pressure and allow to close the circuit to an external power supply.
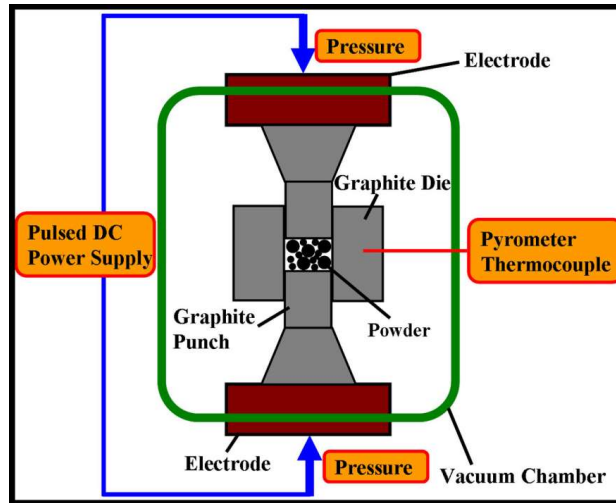
Figure 10 Schematic of an SPS apparatus. (Original figure from Chang et al. [32]*, distributed under the Creative Commons Attribution 3.0 Unported License (CC BY 3.0)).*

All the punch/die assembly is sealed in a vacuum chamber, usually filled with an inert Ar gas to prevent oxygen contaminations at high sintering temperatures. The natural electrical conductivity of graphite permits the current to circulate in the systems at very low voltages (2-12 V) but currents as high as 1-4 kA are required to generate enough heat for sintering. In this configuration, the powdered material is directly in contact with the heating elements and can be heated much faster than in hot pressing or HIP processes. The main advantage of SPS over other pressured-assisted sintering techniques is the rapidity with which the powder can be heated up to the maximum sintering temperature, decreasing the residence at lower temperatures during the heating cycle. A faster heating rate limits the activation of non-densifying sintering mechanisms (i.e. surface diffusion) in favour of the densifying ones (lattice and GB diffusion). Since the driving force for sintering scales inversely with the 4th power of the particle size (or

grain size), limiting surface diffusion and so particle coarsening is strongly beneficial to boost the sintering rate (Eq. 2) of fine and ultrafine powders [41].

SPS apparatus also takes advantage of pulsing the electric current in very short (ms) on/off cycles (pulsed DC current). This strategy promotes a localised electro-thermal breakdown of the oxide layers between particles (Figure 11). The removal of surface oxide enhances the densification kinetic, especially during the I-stage of sintering, and contributes to the formation of clean grain boundaries free from oxide second phases. This phenomenon is more pronounced for systems composed of conductive powders, susceptible to passivation in air, like metallic particles (i.e., Cu, Al, Fe, Ni…) or transition metal carbides like WC [42].
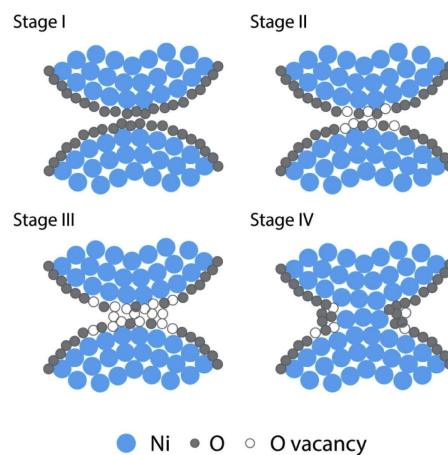
Figure 11 Example of different surface cleaning stages at nanometric particles' contact areas promoted by electric-field-induced dielectric breakdown. Stage I before current application; stage II-III formation and migration of oxygen vacancies and stage IV complete removal of the oxide layer with clean particle-particle contacts. (Original figure from Bonifacio et al. [42]).

Lastly, the electromigration effect is a possible athermal contribution of electric current to the densification of conductive materials [43–46]. Some researchers included the electromigration effect in the constitutive equations for the sintering kinetic, demonstrating how higher current densities affect the

sintering rate during isothermal SPS experiments [43,46]. Electromigration was included in the hot-pressing (creep) equations for the densification rate as an extra term for the activation energy; although the authors assumed it does not affect the sintering mechanism. The contribution of electromigration on the sintering kinetic is important only in the first stages of sintering when the current densities at particle contacts are maximum, while it plays a minor role if compared with pressure and temperature when the porosity of the green start to decrease [44].

Another class of FAST techniques is represented by applications where sintering occurs under exclusive interaction of the electric current with the powdered material. In other words, the heat is generated within the powdered materials to be sintered because of the Joule heating. These techniques can be divided into Flash Sintering (FS) and Electrical Resistance Sintering (ERS), depending on the electrical conductivity of the processed material. Flash sintering was discovered in 2010 by Raj and Cologna [47] in an attempt to study the effect of electric fields applied during the conventional sintering of oxide ceramics. Zirconia samples (ZrO_2), in the form of dog-bone green samples (Figure 12), were initially tested inside a tubular furnace while connected by two platinum wires with an external power source. Zirconia, but in general all oxide ceramics, possesses a strong dependence of resistivity with temperature: passing from an insulator to a semiconductor character at high temperatures (~10^{15} Ωm at 25ºC → ~10^2 Ωm at 1000ºC).
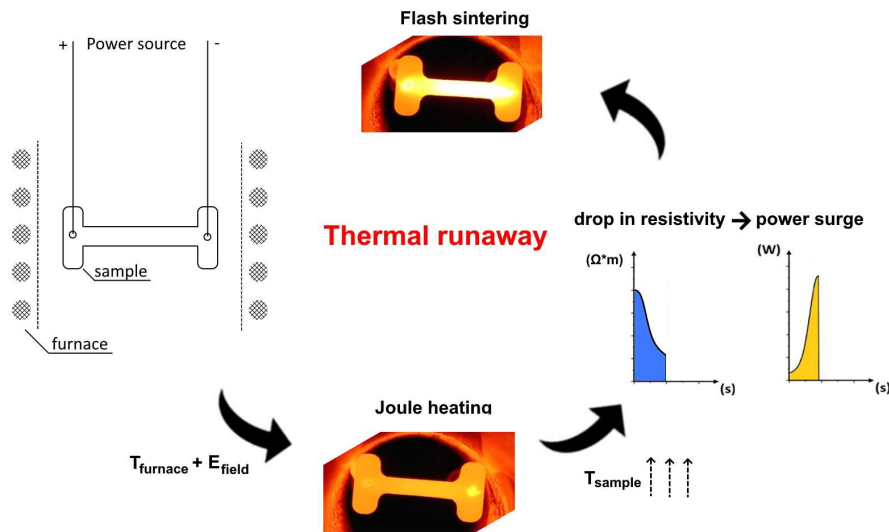
Figure 12 Schematic of the Flash Sintering (FS) process. (Original figure from Mazo)

This substantial variation in resistivity with temperature allows an increasingly higher current to circulate in the green body while heated within the furnace (Figure 12). The flash event occurs at the right furnace temperature and applied electric field conditions and corresponds to a burst in the dissipated electrical power in the ceramic green body. This phenomenon is conventionally referred to as a thermal runaway because the avalanche reduction in resistivity, which allows a higher current to circulate, is also responsible for increased heat generated by Joule heating in a positive feedback thermal reaction loop (Figure 12). During the power surge, the green body experiences an enormous temperature increase in few seconds, resulting in almost instantaneous densification of the ceramic. This electro-thermal reaction (thermal runaway) and the ultra-fast densification rate give rise to the term "flash" sintering (FS).

FS drastically reduces the sintering temperature and time for a large group of different oxide ceramics [48–50]. Since the heat is generated internally from the interaction of the current with the ceramic body, the actual sample temperature is much greater than the furnace temperature. The possibility of fully densifying a ceramic green body in few seconds, in the absence of a liquid phase, hence only by solid-

state diffusion mechanisms generated a long debate among the scientific community. The reasons behind this anomaly acceleration in the sintering rates, and so in the diffusion kinetics of the atoms involved in the process, are still not completely understood. From a general point of view, it has been demonstrated that the major contribution to the accelerated kinetic is the rapidity with which the heat is generated, hence the heating rate. As previously discussed for the SPS practice, also for FS the major contribution to the vast acceleration in the kinetic is connected to the heating rates [51–54]. At the current state, the constitutive equation for sintering does not directly relates the sintering rates with the thermal T(t) profile; Eq. 2 show an example of the sintering equation for grain boundary (GB) diffusion mechanism:

$$\frac{1}{\rho}\frac{d\rho}{dt} \cong \frac{4}{3}\left[\frac{D_{gb}\delta_{gb}\gamma_{gb}\Omega}{\rho(1-\rho)^{\frac{1}{2}}G^4 kT}\right] \tag{2}$$

where ρ is the relative density, D_{gb} the diffusion coefficient for grain boundary diffusion, δ_{gb} the thickness for grain boundary diffusion, γ_{gb} the specific surface energy, G the grain size, k Boltzmann constant and T the temperature. In Eq.2 it is possible to observe how the sintering rate $(1/\rho dp/dt)$, apart from some material-dependent constants, depends only on the grain size (in the form $1/G^4$) and the temperature $(D_{gb} = D_0 exp^{(\frac{-Q}{RT})})$.

However, Zhang et al. [53,54] and some other scientists [52], demonstrated how the ultrafast densification during FS is mainly driven by a term containing the heating rate, hence the evolution of temperature with time T(t). During the thermal runaway, heating rates are two to three orders of magnitude higher than in SPS (10^4-10^5 ºC/min). For this reason, FS can be classified as an ultrafast sintering process. Todd et al. [54] recently reported several fast-firing sintering results conducted on 3YSZ (3%mol Yttria-stabilized Zirconia), showing how the ultra-fast densification can be achieved with or without the presence of an electric field. The authors reported that by comparing ceramic sintered at

the same density, the higher the heating rate and the lower the pore structure and the grain coordination number. This result agrees well with the "fast-firing" concept concerning the competition between surface diffusion and densification mechanisms. In conclusion, the direct role of the electric field on densification seems to be marginal. However, it possesses other secondary microstructural effects, such as modification of GB structure and the grain growth kinetic [54–56], alteration on the defect chemistry [57] with a redistribution of oxygen vacancies between anode and cathode [55] and on the occurrence of transient phases during the flash event [58].

The conditions for activating flash sintering are restricted to all those ceramics that share a negative dependance of their resistivity with temperature, usually referred as NTC ceramics. A material that become more resistive while being heated can not experience a thermal runaway phenomenon and so cannot be flash sintered at any applied electric field and/or furnace temperature.

Electrical resistance sintering. Metals and also some non-oxide ceramics, like in our case WC, possess the opposite electrical characteristic referred as PTC behavior, i.e. positive dependance of resistivity with temperature. For this class of materials sintering experiments that involve the direct effect of an electric current with the powdered material are referred as Electrical Resistance Sintering (ERS). The ERS process shares some similarities with the SPS one, although the graphite die is substituted by an electrically insulating ceramic die which forces the current to pass only through the powdered material (Figure 13) [59–61].
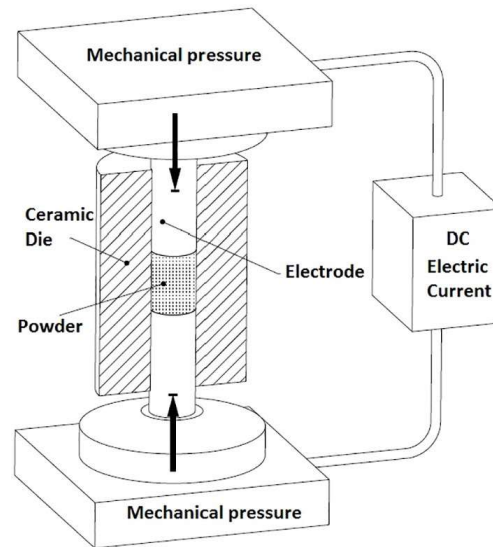
Figure 13 Schematic of the ERS apparatus. (Original figure from Lagos et al. [62]*)*

The lack of the graphite dies as an additional heating element strongly modifies the requirements of the power source for the ERS apparatus. Since all the heat must be generated inside a highly conductive material, it is necessary to apply current densities that are much higher with respect to SPS, usually in the order of 10-15 kA [60,61]. This requirement restricts the geometry of the green ceramic sample to cylinders or disks, that can be connected to the external power supply by flat punches thus allowing elevated contacts areas and so high current densities. Another issue of such process is that power supplies capable of supporting these high current densities, in a continuous operational mode, are not commercialised for a laboratory scale practice and are used only in particular industrial applications. For these reasons only a few research groups are currently studying the ERS process. For example, Lagos et al. exploited the modification of spot-welding machines for the rapid consolidation of (i) iron powders [61,63], WC-Co hardmetals [59,64] and Cr_3C_2-Ni based cermet [65]. The authors reported very fast densification usually achieved in the range of $1 - 2$ seconds, during which the conductive powders were subjected to very high currents ($8 - 12$ kA). Since all the tested materials contain a low melting point metallic component, Fe, Co or Ni, it is very probably that the sintering in these situations occurs under

the presence of a liquid phase. In such conditions is difficult to compare the very fast densification reached during the above reported ERS experiments with the increased in sintering kinetic occurring during the flash sintering of pure ceramic components.

The absence of any scientific reports on the application of the ERS process on pure ceramic systems, without any low melting point materials, highlights a gap in the scientific knowledge concerning the ultrafast sintering of conductive ceramic, i.e., of "metallic ceramics". For this reason, starting from Chapter 2 we will present and discuss the experimental procedure and the results of the application of the ERS process on pure WC powders.

Chapter 2

Nature and phenomenology of flash sintering in WC

Paragraph 2.1 reports the Electrical Resistance Sintering (ERS) experiments conducted on tungsten carbide (WC) nanopowders in the absence of a metallic components, hence without any presence of a liquid phase during sintering. (Published in Materials & Design, 2022, 213, 110330). In the following paragraph 2.2, the origin of the initial NTC characteristic of WC green compacts will be studied in connection with surface chemistry and with the nature of the electrical contacts generated between two WC nanoparticles. (Published in International Journal of Refractory Metals and Hard Materials, 2022, 111, 106090). In the last paragraph 2.3, the flash sintering phenomena will be reproduced and modelled by finite element method (FEM) to study the physics behind the ultrafast heating and the high temperature generated during the sintering experiments. (Published in the Journal of Materials Research and Technology, https://doi.org/10.1016/j.jmrt.2023.02.213, 2023, 23)

2.1 Electrical resistance flash sintering of tungsten carbide

Isacco Mazo[#], Alberto Molinari [#], Vincenzo M. Sglavo[#‡]

Department of Industrial Engineering, University of Trento, via Sommarive 9, Trento, Italy

‡ INSTM, National Interuniversity Consortium of Materials Science and Technology, Trento Research Unit, Via G. Giusti 9, 50123 Firenze, Italy

Graphical abstract
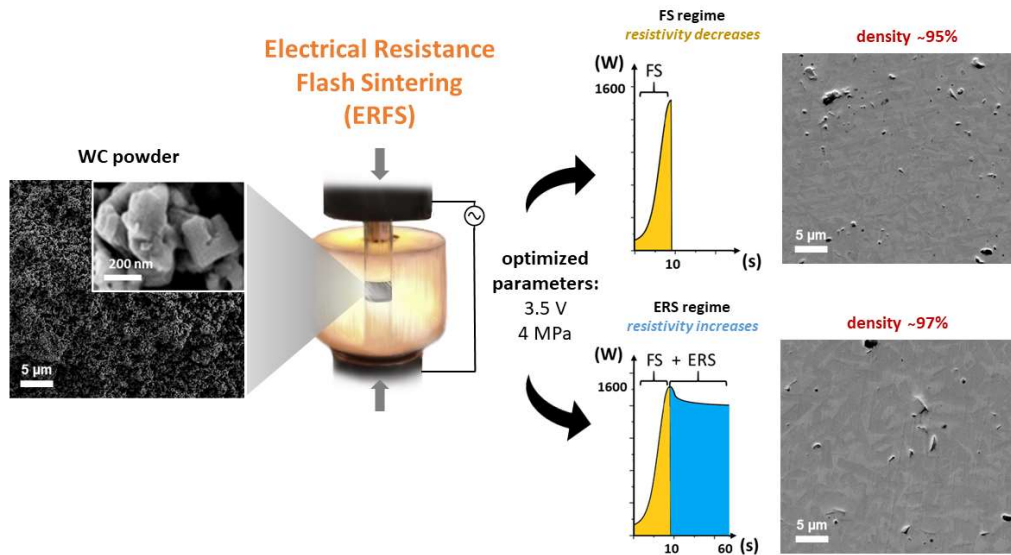
ABSTRACT

This work explores the possibilities for the ultrafast sintering of binderless tungsten carbide by electric/pressure assisted sintering. A limited voltage (3–4 V) in AC condition was applied to WC powder compact in combination with uniaxial pressure. The thermal insulating ceramic die allows the ultrafast heating (10^4 °C/min) of the powder compact which undergoes a rapid transition of its electrical properties, from negative to positive dependence of resistivity on temperature, i.e. from NTC to PTC behaviour. Such effect is fundamental for inducing a thermal runaway phenomenon associated with ultrarapid temperature increase and massive electric power dissipation, thus inducing very rapid sintering. The relationship between electrical properties of tungsten carbide and the possibility to achieve "flash sintering" conditions to complete densification in a couple of seconds was investigated. At the optimal conditions of 3.5 V and 4 MPa pressure, pure WC sinters up to 95% in less than 10 s. Longer sintering time after the flash improves only slightly the density, despite a significant energetic

consumption. It is also shown that if larger pressure is applied, the flash event duration and final density decrease.

2.1.1 Introduction

Tungsten carbide (WC) is a relevant material in the manufacturing of steels and metal alloys due to its outstanding hardness and stiffness. In the last 60 years, the research has been focused on the possibility to enhance WC intrinsic brittleness and poor sinterability by the activation of liquid phase sintering through the incorporation of limited amount of Co or Ni [7,66]. The poor oxidation resistance and the loss of hardness at high temperature of the metallic phase has lead the researchers to the development of metal-free or binderless tungsten carbide (BTC) [12,67]. The strong covalent chemical bonds and the low diffusion of carbon atoms represent fundamental issues in WC processing. Traditional pressureless sintering is unsuccessful, it requiring temperature above 2000 ºC and long times which account for coarse microstructures [2]. Even hot isostatic pressing (HIP) and hot pressing (HP) require grain growth inhibitors to control the sintering kinetic and limit coarsening [21,68,69]. Recently, binderless production has been enhanced by innovative techniques like spark plasma sintering (SPS) where the application of a high current density combined with uniaxial pressure allows the complete densification of the starting pure WC powder in 10-30 min. In this way, it is possible to obtain monophasic (hexagonal), dense ($\geq$ 98-99%), stiff ($\approx$700 GPa), and hard (26-30 GPa) materials without the use of any sintering aids [35,37,70]. In spite of said outstanding properties, the possible uses of binderless WC are restricted to applications not exposing the material to violent and unexpected loads, like wear components, drawing dies, corrosion resistant mechanical seals, friction parts, optical glass moulds and high temperature electrical contacts. In addition to said limitations, the use of the graphite die as heating element in SPS strongly limits productivity and freedom in component geometry. BTC intrinsic brittleness makes its use

in the manufacturing industry impossible as a possible substitute of the cemented carbide counterpart (WC-Co/Ni) [71]; as a matter of fact, the typical fracture toughness of BTC produced by SPS is in the range of 4-6 MPam$^{0.5}$ while cemented counterpart can achieve values three times larger, 10-16 MPam$^{0.5}$ [72]. As recently pointed out by Sun et al., [12] the rapid production of fully dense and high toughness sintered bodies is the biggest challenge for the development of BTC.

In this perspective, the consolidation of ceramics under "flash sintering" conditions has revealed an enormous potentiality since (i) it allows the complete densification of ceramics in few seconds with an enormous saving in the required energy [48,49] and (ii) it allows to process materials with new and/or improved functional and structural properties [73,74]. Several studies indicate how flash sintered ceramics possess peculiar microstructures, out of equilibrium phases and even enhanced plasticity accounted for by defects chemistry modification [75–78]. The flash sintering phenomenon occurs at an onset combination of electric field and furnace temperature, forcing an electrical current through the material, responsible for a thermal runaway of Joule heating. The thermal runaway is a non linear event characterized by extremely high heating rates [79,80] which has been successfully modelled by Zhang et al. [81] and Todd et al. [82] in electronic (ZnO) and ionic conductors (3YSZ), respectively. The enormous heating rates of about 104°C/min developed during such event was found to be responsible for a large boost in the sintering rate [52,83,84].

According to the existing theories, the flash event can not occur in materials characterized by a positive temperature coefficient (PTC) for resistivity like metals or, for example, tungsten carbide (WC). In spite of that, Grasso et al. [85] and McKinnon et al. [86] found evidence of ultrafast sintering of PTC ceramics, like ZrB2 and TiB$_2$/hBN. McWilliams et al. [87,88] recently discovered the activation of a flash event in a metallic Al powder due to the presence of a surface oxide layer and the rapid transition of the compact from insulator to conductor. Heating rates in the order of 10^3-10^4°C/min, as found during the flash event

in Al powder, was proposed to excite certain phonons more than others, thus allowing the generation of point defects far beyond the equilibrium concentration. Jongmanns and Raj [89] simulated how driving an Al single crystal lattice out of equilibrium by nonlinear lattice vibration can lead to this proliferation of interstitials and vacancies which promotes ultrafast sintering.

The possibility to activate a flash event in aluminium powder and the ultrafast sintering of PTC ceramics similar to WC, stimulated the following question: is it possible to trigger a flash like event also in pure tungsten carbide?

The present work aims to explore the interaction of an alternated current with WC green bodies and the conditions, if existing, to activate ultrafast sintering. More in detail, the conditions for (i) non linear variation of the electrical resistivity, (ii) abrupt increase of the electrical power dissipation, (iii) heating rate as high as 10^4°C/min and (iv) sintering rates which can allow densification in few seconds are investigated. In order to achieve these results, pure tungsten carbide was tested in a specifically designed pressure assisted-flash sintering apparatus [90,91]. To fully prove the occurrence of a flash event, sintering experiments were carried out taking care of (1) not changing the native electrical properties of the powder, (2) promoting exclusive interaction of the electrical current with the material to be tested, (3) accurate in situ monitoring of the phenomenon and (4) large current density capabilities of the contacts electrodes. Therefore,

1.   the starting WC powder was not treated, green samples for sintering tests were uniaxially pressed without additives and without a presintering;

2.   the graphite die used in SPS was substituted with an insulating ceramic die;

3.   a fast data acquisition system was developed for monitoring sintering shrinkage, temperature, resistivity and electrical power dissipation;

4.   flash sintering experiment was performed on pellets [49], where the flat punches for applying pressure serve also as electrodes.

In this way, differently with respect to SPS, possible superimposed electro-thermal effects between the material and the graphitic die are eliminated [92]. In addition, important information on flash sintering behaviour of conductive material like tungsten carbide can be obtained.

2.1.2 Materials and Methods

Powder properties. Commercially available nanocrystalline WC powder (Inframat Advanced Materials) with an average particle size of 150-240 nm (Figure 14(a)) was used in the present work. According to preliminary XRD analysis (Figure 14(b)), the powder is mainly composed of α-WC (crystallite size ~ 40-70 nm) with limited amount of tungsten oxides (WO_3 and WO_4H_2). The powder was uniaxially pressed (350 MPa) in a steel mould by a manual hydraulic press (Specac) to produce cylindrical pellets with 6 mm diameter and thickness between 3 and 8 mm. The different thickness was obtained just by using different amount of powder. The average relative density of the green specimens was 40%.
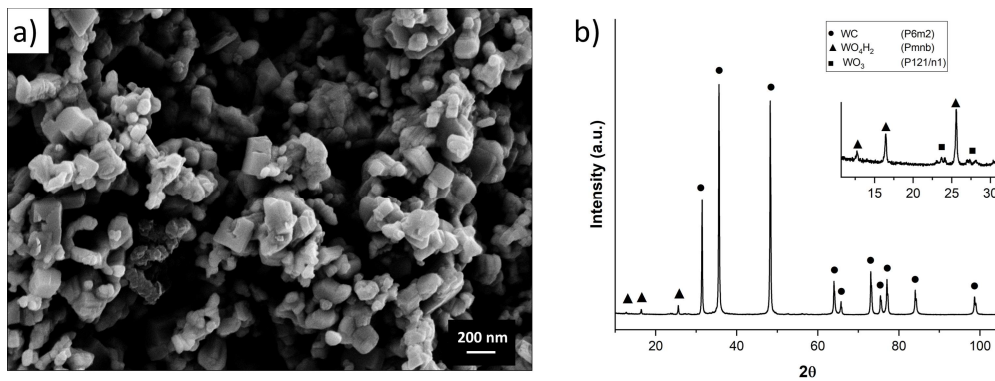
Figure 14. SEM micrograph (a) and XRD spectrum (b) of the tungsten carbide powder used in the present work.

Sintering apparatus. The apparatus used for the sintering experiments is shown in Figure 15. It consists of a modified mechanical testing machine (MTS System, model 810) whose load cell and lower piston are connected to two copper/molybdenum electrodes. The green sample (WC pellet) is inserted into an insulating die made of partially stabilized zirconia (3YSZ) and pressed by the electrodes; the ceramic die

forces the electrical current to flow only through the specimen and avoids rapid heat loss generated during the experiment [93].
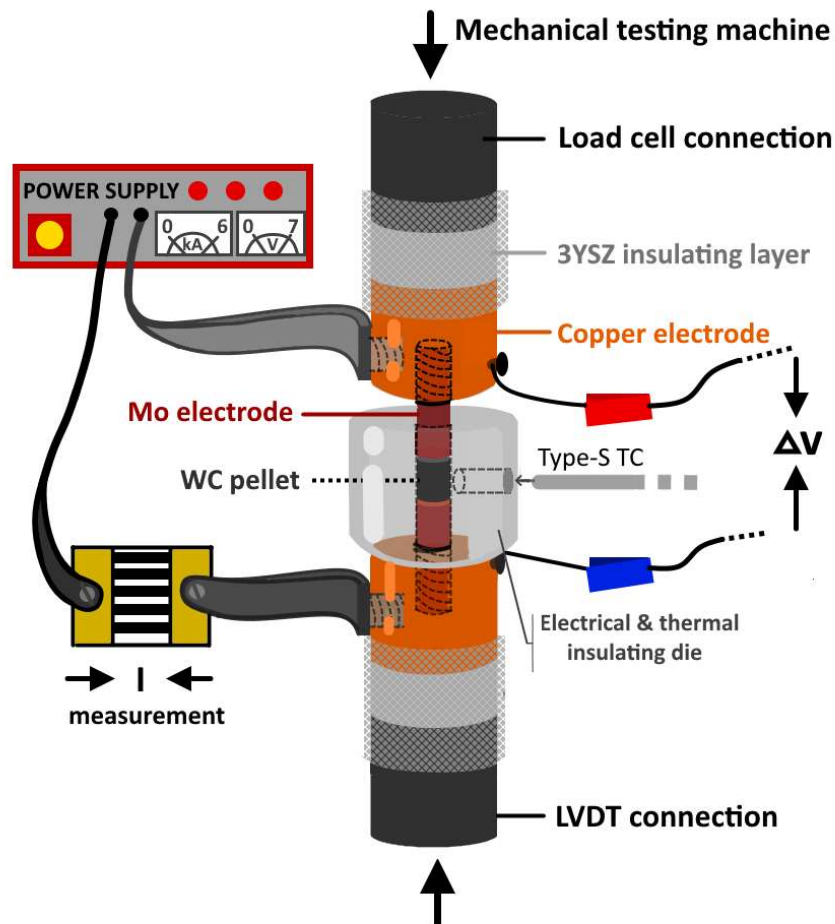
Figure 15. Apparatus used for the sintering experiments.

The mechanical testing machine is equipped with a load cell and a linear differential transducer (LVDT) to record the applied load and the vertical displacement, which enables to evaluate the pressure applied to the pellet and the shrinkage during sintering. An AC, 50 Hz, power supply (TECNA item 3870) is connected to the electrodes to provide the electrical power. Sintering experiments were performed under an electric field ranging between 3 and 9 V/cm for 10 and 60 s and a current density between 2.8 and 4.5

kA/cm^2. Two different contact pressures (4 and 60 MPa) and three different voltages (3, 3.5 and 4 V) were used. Each combination was run in triplicate to assess the repeatability of the experiment.

Microstructural investigation. After being extracted from the 3YSZ die, the sintered WC samples were sectioned axially by a diamond blade, mounted in resin and polished progressively with diamond abrasives down to 1 μm. The microstructure was analyzed by a digital optical microscope (Olympus OLS5000) and by SEM (JEOL IT300) on fresh fracture surface and polished cross sections. Density and apparent porosity were measured according to the Archimedes' method using a precision balance (Kern ALJ 310 4A).

Electrical investigation. The evolution of the electrical parameters during sintering was measured directly on the WC sample, according to the electrical configuration shown in Figure 16(a). A multichannel data acquisition system (DAQ NI USB 6211) scanned almost simultaneously voltage and current. The voltage difference was acquired between the two copper electrodes, as shown in Figure 15. The current was measured by placing a calibrated shunt resistance (2500 A, 60 mV) in series with the circuit. The acquisition was carried out by LabView software, sampling the two alternated signals at 100 ksample/s. Voltage and current root mean square (RMS) values were evaluated with an average integration cycle of 0.02 s. The temperature was measured by placing a type S thermocouple in contact with the pellet, laterally within the zirconia die through a 4 mm hole produced halfway up its height (Figure 15). A digital multimeter (Keithley DMM6500) equipped with an acquisition card for thermocouples (2001 TCSCAN CARD) performed the temperature recording at around 50 readings/s. The influence of pressure on the resistivity of green pellets was measured within the zirconia die by using the electrical configuration shown in Figure 16(b). The resistance was measured in a 4 point configuration while increasing the pressure from 0 to 100 MPa, with a high resolution (1 μΩ) multimeter (Keithley

DMM6500). The resistive contribution of the electrodes in contact with the specimen was subtracted from the resistivity data [94].
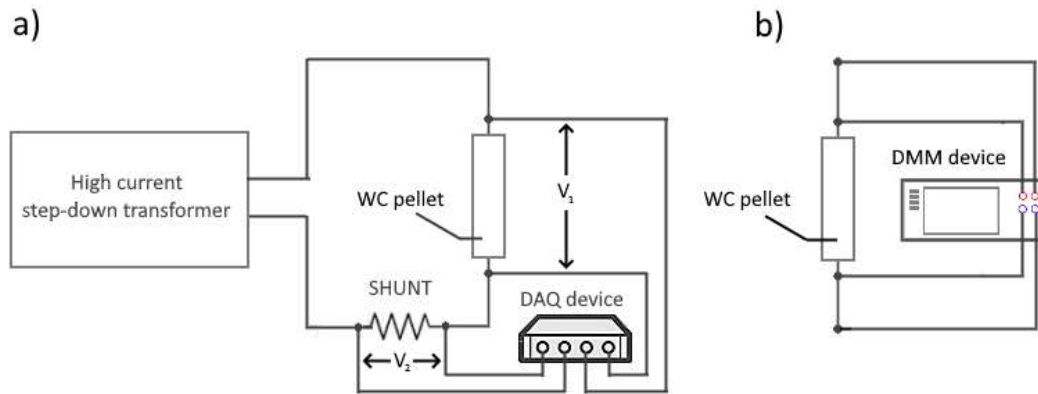
Figure 16. Configurations used for the acquisition of electrical data on pellet sample within the die: voltage and current measurement during sintering experiments (a); 4-point resistance measurements at different pressures (b). (TC = thermocouple).

The effect of temperature on the resistivity of both WC green pellets and bulk material was analysed within a dilatometer (Linseis DIL L75 PT), heating the material from 25 to 1550°C (10°C/min) under argon atmosphere. In this case, the green specimen was inserted in an alumina tube (Figure 17 (a)) and four shielded platinum wires were placed in contact with it to generate a 4 point configuration. The shrinkage of the pellet was also measured upon heating. The bulk resistivity was measured as a function of temperature using the configuration shown in Figure 17(b). Fully dense (99%+) 20 mm diameter disks were produced by SPS (Dr. Sinter 1050) at 2100°C with 5 min holding time and 200°C/min heating rate. Small bars (13x4x1 mm^3) were machined from such disks, placed in a small tubular furnace and connected by four shielded platinum wires to the multimeter.
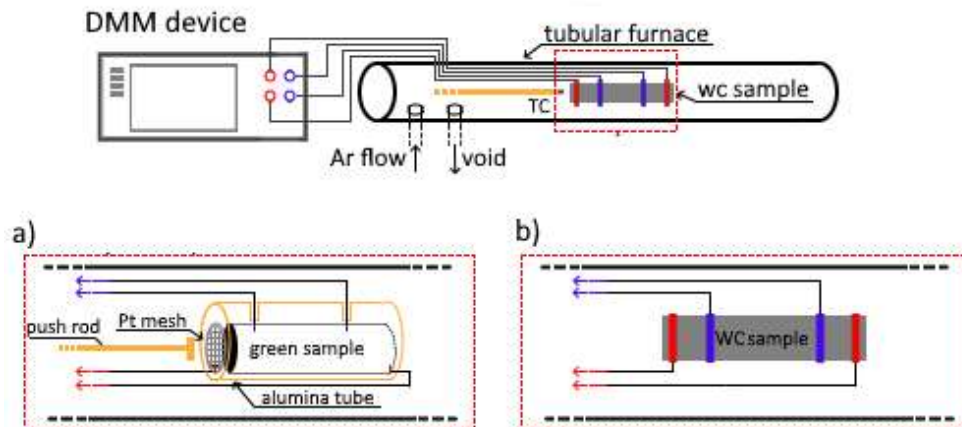
Figure 17. Apparatus used to measure the electrical resistivity as a function of temperature of the green sample (a) and the bulk specimen (b).

2.1.3 Results and Discussion

Flash event in pure tungsten carbide green compacts

The application of an alternated current to the tungsten carbide green sample induces a rapid evolution of the electrical and physical properties. As shown in Figure 18, the applied voltage decreases from about 3 V to 1 V while the current increases from 40 A up to 800 A in less than 10 s. This behaviour corresponds to a very rapid change in the material resistivity, which decreases by three orders of magnitude from 6.7×10^{-3} Ω m to 7.6×10^{-6} Ωm in the same time interval; then, it remains almost constant until the end of the sintering experiment. Correspondingly, the absorbed electrical power reaches a maximum of about 1000 W (9800 mW/mm^3) and it slightly decreases to 850 W afterwards. As clearly reported in Figure 18 (c), the observed sudden variation of the material resistivity is also associated with (i) a very rapid increase of its temperature, which reaches values in excess of 1720°C, as proven by the thermocouple tip melting, and, more importantly, (ii) an abrupt shrinkage of the sample (about 20%) in the first 10-12 s.

The estimated heating rate is exceptionally high with an average of 2×10^{4} °C/min in the first 9 s and a maximum value of about 5×10^{4} °C/min. Just as a reference, similar heating rates (in the order of 10^{4} °C/min) have been estimated during the thermal runaway of flash sintered ceramics [48,49,53,80,83,95,96]. Based on the features pointed out so far, the observed phenomenon can be defined as Electrical Resistance Flash Sintering (ERFS).
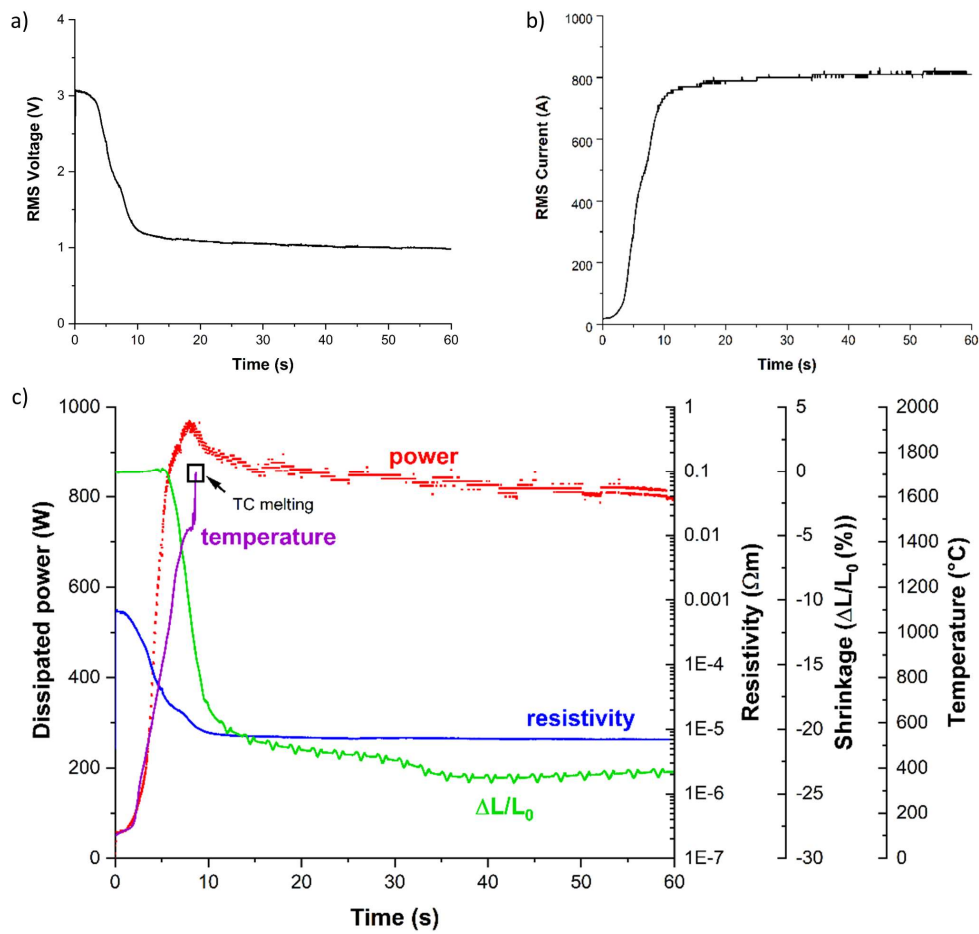
Figure 18. Data acquisition during the test of a WC pellet under 3 V and 4 MPa; a) voltage, b) current, c) dissipated power, resistivity, shrinkage and temperature.

Figure 19 (a) shows the evolution of the WC pellet during the electrical current assisted sintering test. After 60 s, the density evolves from 40% up to 75% under 1000 W maximum power peak and 4 MPa

pressure. Both thickness and diameter of the specimen sensibly decrease, the latter becoming smaller in the central region. Such anisotropic effect can be accounted for by the very different thermal conductivity of molybdenum (138 W/m K) with respect to zirconia (1-3 W/m K) which induces a larger dissipation of the internally generated heat through the electrodes, thus making sintering less efficient on the top and bottom portions of the pellet. Correspondingly, the sintered component appears denser in the mid height region, as revealed by the observation of pellet cross section (Figure 6(b)), which points out the presence of some residual porosity.
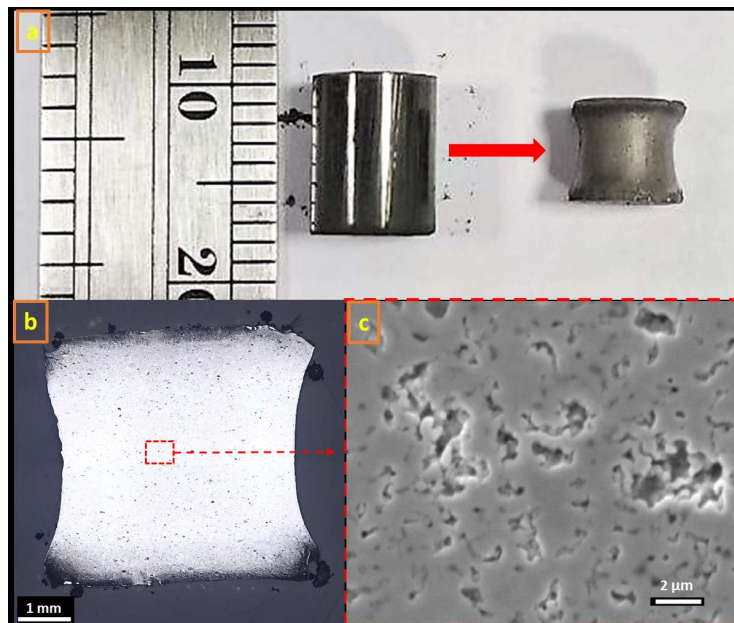
Figure 19. WC sample before and after the sintering experiment (3 V, 4 MPa, 60 s) (a); optical (b) and SEM (c) micrographs of polished cross section after sintering.

The sintering rate $\dot{\varepsilon}$ during the ERSF process can be determined as:

$$\dot{\varepsilon} = \frac{1}{\rho}\frac{d\rho}{dt} \tag{3}$$

where ρ is the density. Since the electrodes act as constraints for sintering on the top and bottom region of the pellet, the evaluation of the sintering rate has to take said non isotropic shrinkage into account. For

this reason, two limiting cases can be considered for the evaluation of density and sintering rate corresponding to (i) the pellet maintaining the original diameter (with axial shrinkage, only) and (ii) isotropic shrinkage.

In the former case, the density can be calculated as:

$$\rho = \frac{\rho_0}{\varepsilon + 1} \qquad (4)$$

where ε is the shrinkage and ρ_0 the green density. In the case of isotropic shrinkage, the density is instead:

$$\rho = \frac{\rho_0}{(\varepsilon + 1)^3} \qquad (5)$$

If the shrinkage is equal to the axial one ($\Delta L/L_0$) as reported in Figure 18, the sintering rate can be estimated by Eqs 4 and 5 and plotted as in Figure 20, together with the dissipated electrical power. It is possible to observe that the maximum sintering rate is achieved exactly at the power peak. At this point, since the real shrinkage of the pellet is non isotropic, the real sintering rate must fall between the two limiting rates just pointed out. In any case, an exceptionally high sintering rate between 400 and 1200×10^{-4} s^{-1} can be determined during the power surge, this being one to three orders of magnitude larger with respect to traditional and even spark plasma sintering processes carried out on pure tungsten carbide [83,97].
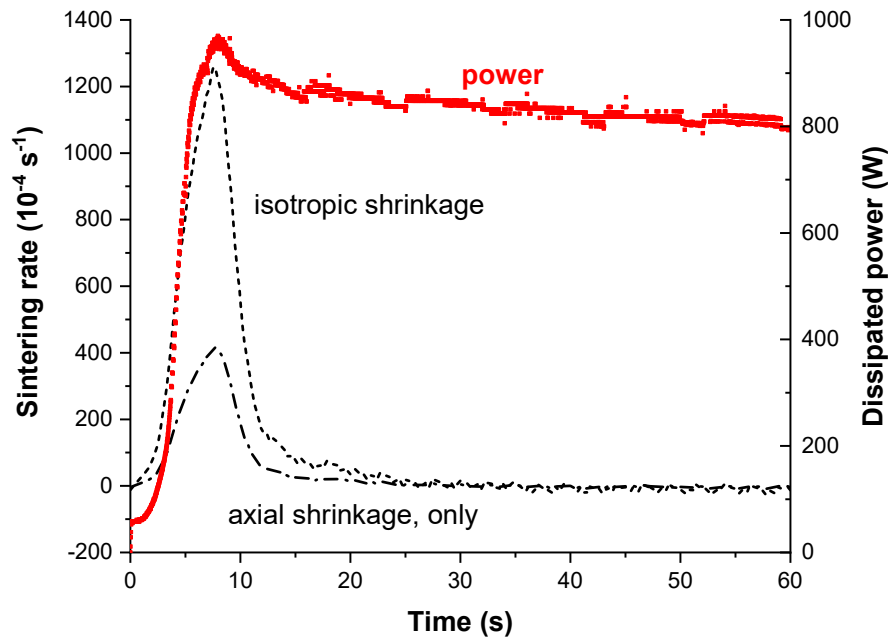
Figure 20. Sintering rate during the process calculated from the vertical displacement recorded by the mechanical testing machine in the hypothesis of isotropic shrinkage and radial constraint; the power dissipated during the test is also shown.

Ultra-fast firing, where heating rates approach 10^{4}°C/min, like in the present situation, has been demonstrated to increase sintering rates by two or more orders of magnitude [83,98,99]. The extremely rapid temperature upsurge, in concomitance with the electrical power peak generated by a non linear drop in the material resistivity, suggests the occurrence of an electrical runaway of Joule heating phenomenon like in flash sintering of ceramics [47,49,80,82,95,100,101]. Nevertheless, a profound difference has to be pointed out between typical flash sintering of ceramics and the phenomenon of interest here because the former has been identified on materials characterized by negative temperature coefficient (NTC) for resistivity while tungsten carbide shows an opposite behaviour.

Conditions for the flash sintering in a PTC ceramic

Figure 21 (a) shows the evolution of resistivity as a function of temperature for bulk tungsten carbide, the data at low temperature having been collected from the literature [102]. A clear PTC behaviour is shown, the resistivity increasing from 2.2×10^{-7} to 1.5×10^{-6} Ω m from room temperature up to 1550°C. Differently from typical metallic materials, the resistivity of bulk WC follows an Arrhenius like temperature trend according to the relationship (Figure 21(b)):

$$\rho = \rho_0 \, e^{\frac{Q}{RT}} \tag{6}$$

where Q is the activation energy for conduction, equal to -6151 (J/mol) and $\rho_0 = 2.13 \times 10^{-6}$ Ωm the pre-exponential factor.
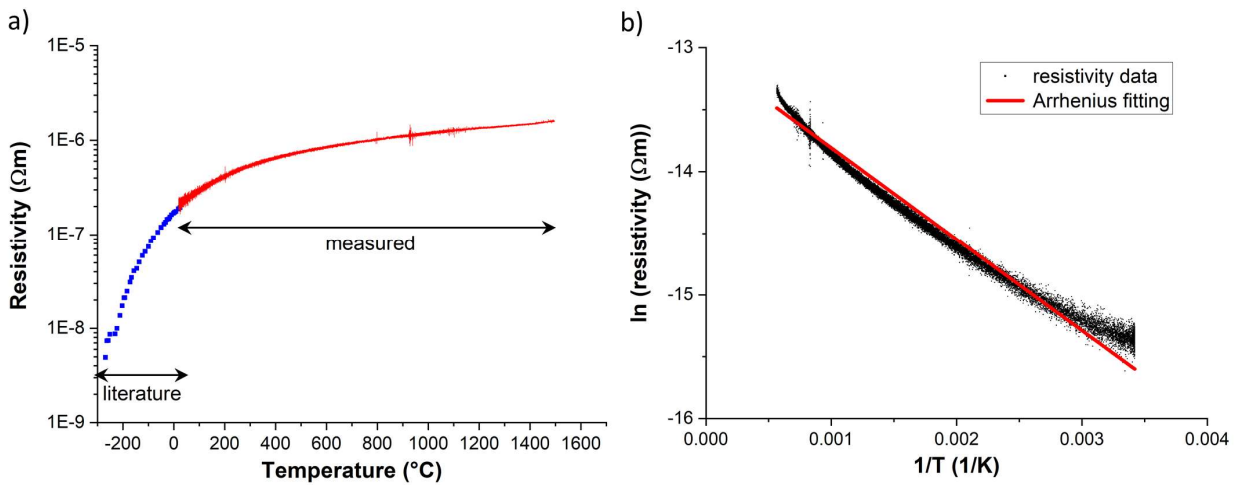
Figure 21. Electrical resistivity of dense tungsten carbide (a): data in red are measured from 25 to 1500°C on a sample produced by SPS while those in blue are taken from the literature [102]. *The log form of the Arrhenius equation is shown in (b) by plotting log(resistivity) vs. 1/T.*

At this point, the energetic model proposed by Todd et al. [82] and Zhang et al. [81] to describe the thermal balance between the heat generated by Joule heating, "W_{in}" (current flow through the material), and the heat dissipated by radiation, "W_{out}", through the specimen surface as a function of the "furnace, T_0" and "sample, T " temperature can be considered:

$$W_{in} = \frac{E^2 \pi r_0^2}{\rho_0} \, e^{\left(-\frac{Q}{R(T_0 + \Delta T)}\right)} \tag{7}$$

$$W_{out} = 2\pi r_0 \sigma \varepsilon ((T_0 + \Delta T)^4 - T_0{}^4) \tag{8}$$

where the "sample" temperature is expressed as $T=T_0+\Delta T$, r_0 is the radius of a cylindrical specimen, σ the Boltzmann constant and ε the emissivity.

As shown qualitatively in Figure 22 (a), the PTC for resistivity identified for WC is always responsible for an equilibrium condition between the two said power forms which allows the sample to reach a specific and finite temperature value that strongly depends on the applied voltage or current. This is substantially different with respect to the behaviour shown by materials characterized by NTC for resistivity. In this case, as shown in Figure 22 (b), a critical condition can be reached at a specific combination of electric field (E) and furnace temperature, corresponding to the thermal runaway for Joule heating, which determines an abrupt increase in the "sample" temperature and accounts for very rapid sintering of the material.
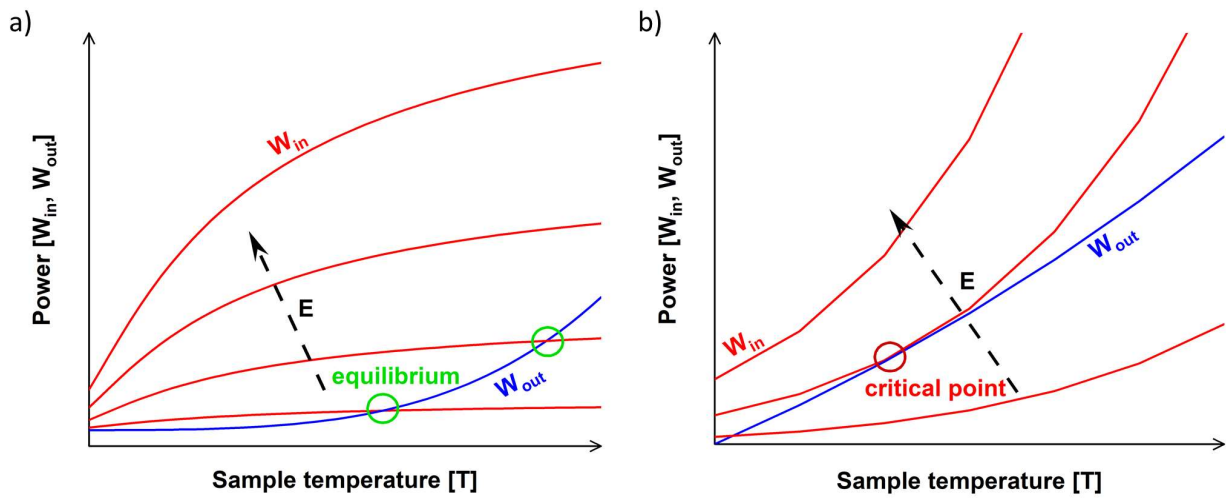
Figure 22. Evolution of the heat generated by Joule heating (W_{in}) and of the heat dissipated by radiation (W_{out}) as a function of the sample temperature at increasing applied electrical field for (a) PTC and (b) NTC ceramic. W_{out} is evaluated in the former case considering only radiative losses and furnace temperature equals to room temperature.

According to the considerations previously reported, it is possible to point out that in the present work the resistivity evolution with temperature is the key to activate a thermal runaway phenomenon [47–49,82,103].

Figure 23 shows how the resistivity of the green WC pellet changes with temperature during heating, the diagram indicating a clear NTC behaviour, differently from the behaviour previously observed for the bulk material (Figure 21). The electrical resistivity decreases from 10^{-3} Ω m down to 10^{-5} Ω m as the temperature increases from about 100°C to 900°C. The largest resistivity drop is recorded below 900°C, well before densification (1050°C) occurs: more in detail, an initial decrease is observed between 200 and 800°C followed by a steeper reduction between 800 and 900°C. When the sample starts to shrink, resistivity drops further this being accounted for by a porosity diminution corresponding to a density increase of about 7%. Upon cooling, the resistivity is affected only by a temperature dependence,

reaching a final value of 1.8×10^{-6} Ω m. It is interesting to observe the relatively small difference between the resistivity of 40% dense material (as it was obtained after the thermal cycle in Figure 23) and fully dense WC, i.e. from 10^{-6} Ω m to 10^{-7} Ω m.
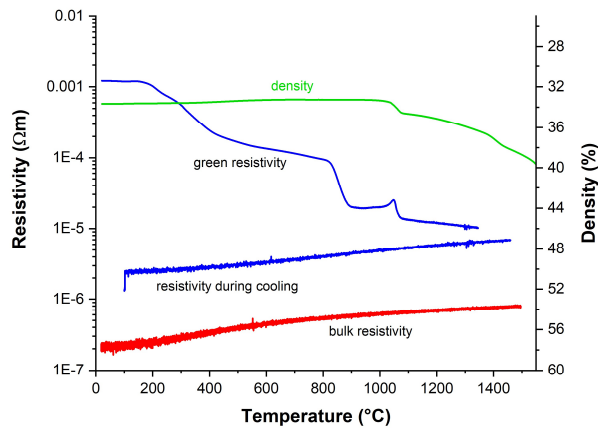
Figure 23. Electrical resistivity and linear shrinkage (density curve) of a green WC pellet measured in a push rod dilatometer, increasing the temperature from 25°C up to 1550°C (10°C/min) in Ar atmosphere. Resistivity was measure during both the heating and the cooling schedule.

The results pointed out according to Figure 23 can lead to the following conclusions: i) a significant drop in resistivity occurs in WC nanoparticles green compact upon heating and ii) the effect of porosity on electrical properties is limited. Very likely, the non linear evolution of resistivity determined during the ERFS experiment (Figure 18) can be related to the nature of the electrical contact points among WC nanoparticles. Two hypotheses can be advanced for such considerable resistivity reduction before sintering: (1) the contact areas among particles increases due to surface diffusion phenomena (according to the constriction theory for small electrical contacts [104]) or (2) tungsten carbide surface chemistry changes with temperature because of the evolution of possible surface contaminants or oxides acting as resistive surface layers.

According to the first hypothesis, also a larger applied pressure affects the electrical contacts among particles and reduces the resistivity of the WC pellet in the zirconia die as shown in Figure 24, the effect being independent on the pellet thickness (from 3.5 to 7.5 mm). The results in Figure 24 confirm the very high initial green resistivity, with a difference between the green and bulk resistivity as high as four orders of magnitude at low pressure. A precise evaluation of the green resistivity is also crucial to determine a suitable contact pressure to minimize arc events and contacts overheating, thus homogenizing the current flow [63]. The initial resistivity of 40% dense green pellets is about 7.5×10^{-4} Ω m at pressure of 4 MPa, as it was used in the experiment shown in Figure 18. Such pressure minimizes the contact resistance with the Mo electrodes and helps to establish a good electrical contact during the ERFS process. The analysis of tungsten carbide surface chemistry and its possible role on the activation of the runaway event will be investigated in the next paragraph (2.2 Role of surface carbon nanolayer on the activation of flash sintering in tungsten carbide).
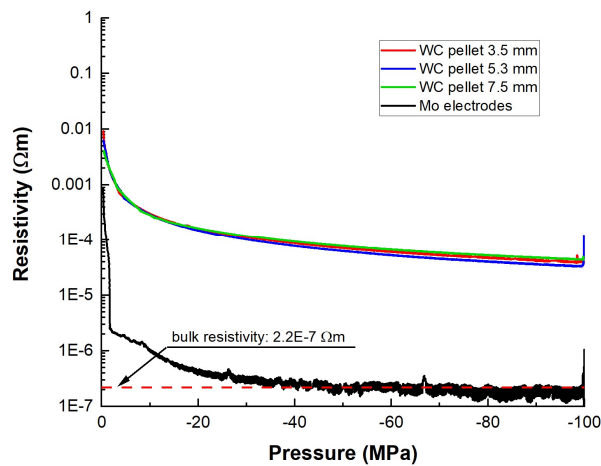
Figure 24. Evolution of the electrical resistivity of green WC pellets with the applied uniaxial pressure. Values for different initial pellet thickness and the contact resistivity of the Mo electrodes are also reported.

The resistivity evolution during the first ERFS stages can explain the ultrafast densification of pure WC nanoparticles shown in Figure 18. The initial NTC behaviour of the green pellet below 900°C (Figure 23) results in a very rapid resistivity reduction when an electrical current is applied (Figure 18). Correspondingly, the superior resistivity of the sample shown in Figure 23 accounts for the thermal runaway to occur for a certain transient period, thus determining an ultrafast temperature increase and sintering.

The data presented so far demonstrate that a "flash event" can therefore be triggered in metal like conductors in case of a transition in the conduction behaviour, from NTC to PTC. Unlike the flash behaviour of NTC ceramics, where the power supply limits the voltage or current, in the present case the process is controlled directly by the material nature and its structure. The power surge extinguishes by itself because of the different thermal runaway behaviour controlled by the high resistivity among particles and porosity. The avalanche phenomenon is continuous only for a particular combination of resistivity reduction and temperature increase. However, this iteration stops at a certain temperature, when the material passes from NTC to PTC behaviour, thus generating a self-extinguishing feature (See paragraph 2.3 for the Finite Element Method (FEM) simulation of the flash event).

How to achieve full densification

In order to analyse the phenomenology of the sintering process further, two regimes are identified during the entire sintering cycle as shown in Figure 25 where the dissipated power plot previously described (Figure 18) is reported. The initial one, whose duration is only a few seconds, is labelled as flash sintering (FS) regime, it being characterized by sudden evolution of resistivity, temperature and shrinkage. The second one, lasting for about a minute, is called electrical resistance sintering (ERS) regime, the material being Joule heated here under a constant current. The energy absorbed in the two regimes can be

evaluated if one integrates the dissipated power in the time domain. The effect of the energy dissipated in the two regimes (FS and ERS) was analysed by changing the thickness of WC green pellets, applied voltage, pressure and time.
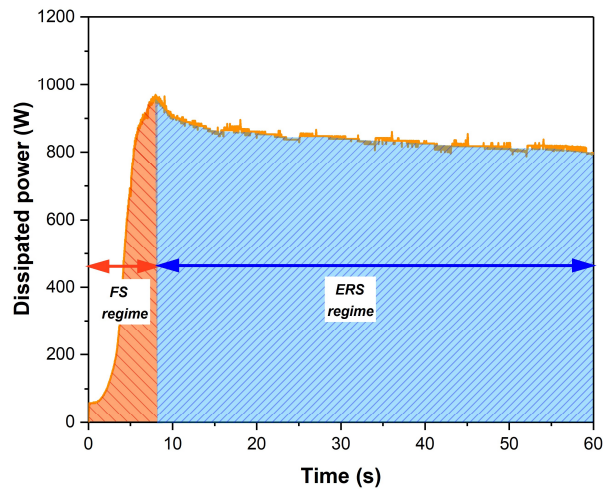
Figure 25. FS and ERS regime as parts of the whole ERFS process.

Figure 26 shows how the thickness of the specimens influences both processing parameters (dissipated power, resistivity and temperature) and shrinkage upon the ERFS process. The fundamental parameters collected and calculated from the diagrams in Figure 26 together with density and porosity measured on the sintered materials are reported in Table 2. The power peak is substantially constant, corresponding to a power density decreasing with the sample volumes, from 9700 down to 4400 mW/mm^3. Conversely, the density sensibly increases, from 57% to 73%, as the relative power peak diminishes. The recorded shrinkage and the microstructure analysed by SEM confirm an improvement in the densification as the sample thickness increases. As previously shown in Figure 24, there is no difference in the resistivity of samples with various thicknesses which could justify the dissimilar densification. The only difference among the three flash events in Figure 26 is the temporal occurrence of the power peak, which increases the resistivity and temperature evolution time scale. For 3.5 mm and 5.3 mm thick specimens, a maximum

temperature around 1600°C is reached at the power peak. For 7.5 mm sample, temperature increases over 1720°C, as also proven by the thermocouple tip melting. This higher temperature advances the sintering to the II stage, with an evolution from the open porosity shown in Figure 26(a, b) to the interconnected one of Figure 26(c). This fact can be explained by comparing the energy consumed in the different sintering regimes. The total electrical energy is similar in the three cases (Table 2), this resulting in a lower specific energy available for thicker samples. Nevertheless, thicker samples reach larger density. The electrical energy fraction dissipated during the FS regime with respect to the total energy (Flash/total energy) increases with the duration of the power surge (FS regime duration in Figure 25) as shown in Table 2: it appears clear that denser materials are obtained when a larger "Flash/total energy" is dissipated during the flash, this also corresponding to higher maximum temperature during the cycle. These observations also suggest a different efficiency of the energy dissipated during the power surge (Flash regime) with respect to that consumed upon the constant current regime (ERS regime). Therefore, the total energy is not the key factor for densification; conversely, it is the energy involved during flash regime which is somehow fundamental for the ERFS process.

Table 2 Electrical parameters, relative density and apparent porosity for samples with different thickness subjected to ERFS.

Initial thickness	mm	3.5	5.3	7.5
Power peak	W	985 (±11)	963 (±5)	949 (±17)
Relative power peak	mW/mm3	9748 (±250)	6477 (±181)	4448 (±460)
Current density‡	A/cm2	3092 (±61)	2967 (±31)	2806 (±67)
Flash energy†	J/mm3	12 (±1)	15.4 (±0.3)	24 (±4)
Total electric energy	J/mm3	471 (±7)	326 (±1)	216 (±23)
	kJ	47.6 (±0.4)	48 (±1)	46 (±1)
Flash/total energy	%	3 (±1)	6 (±2)	13 (±4)
Density	%	57 (±6)	62 (±5)	73 (±3)
Apparent porosity	%	42 (±5)	33 (±6)	21 (±8)

†) total energy provided to the material during the flash event (<10s), calculated from the power integral up to the peak

‡) maximum current density recorded during the current control regime (>10s)
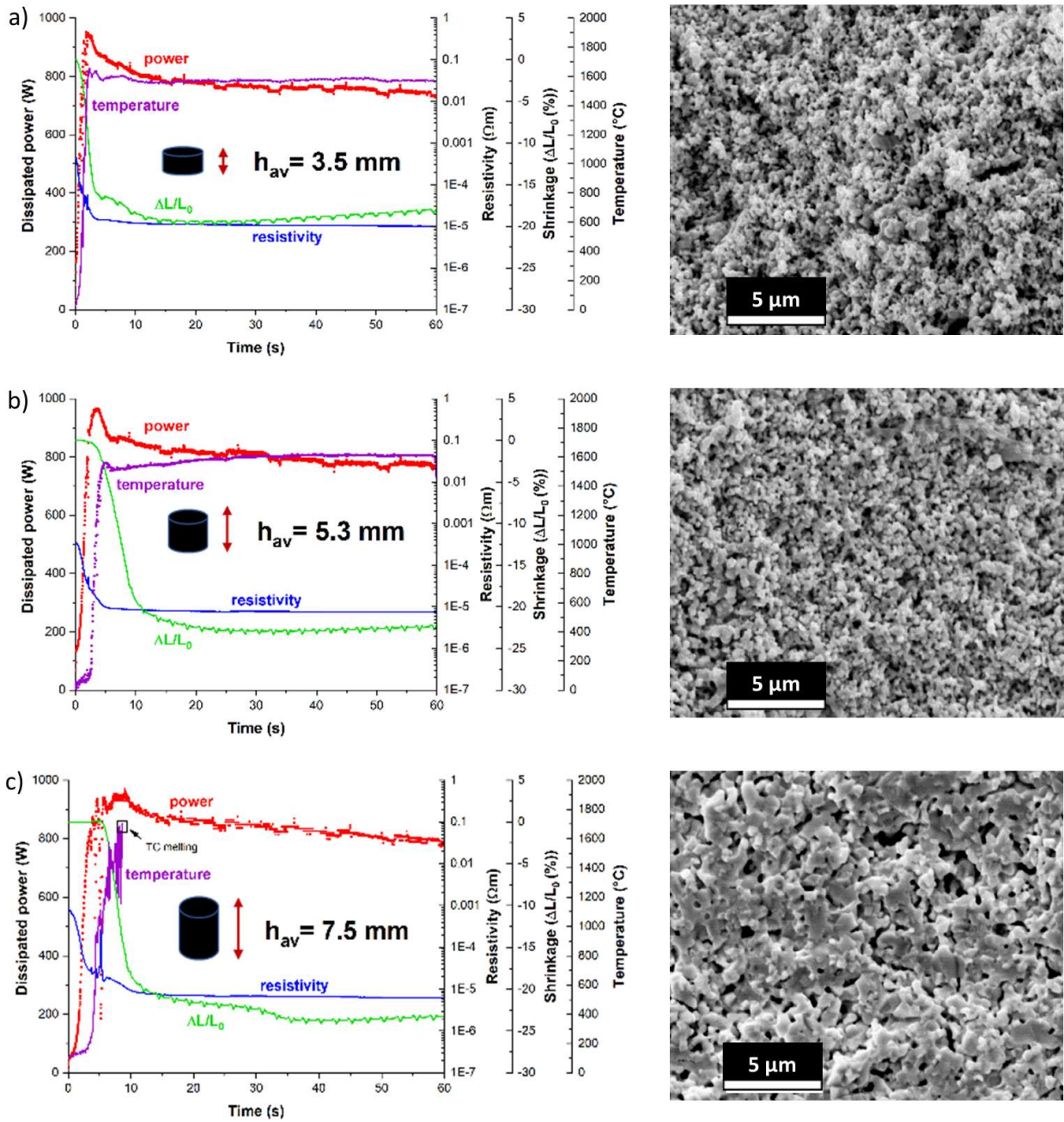
Figure 26. Processing parameters and final microstructure of samples subjected to ERFS tests (3 V and 4 MPa) with initial thickness (h_{av}) equal to (a) 3.5 mm, (b) 5.3 mm and (c) 7.5 mm.

The presence of a temperature peak as shown in *Figure 26* was also recorded in conventional flash sintering experiments [47–49,95,105]. Nevertheless, not in all scenarios the temperature peak arises in concomitance with the power peak. Ji et al. [83] found a maximum in temperature during the power surge before entering the constant current state, corresponding to the ERS regime in our case. Conversely, Raj et al. [95] modelled the flash temperature to occur just in the constant current regime, by accounting the energy generated during the power surge to be absorbed by the sample's heat capacity. Reasonably, for WC, the higher power achieved is no more comparable with its heat capacity (0.28 J/g K) and the heat generated during the power surge increases temperature to a maximum value before entering the steady state.

During the FS of NTC ceramics, the separation of field effects on matter transport phenomena from those related to the very fast heating rates is rather complicated. In the present work, the electric field is so weak that its effect, if any, is negligible. Ji et al. carried out an interesting work to separate the effects of electric field and heating rate, and they demonstrated an acceleration in the sintering rate by orders of magnitude for heating rates in the range 10^3- 10^4°C [83]. The higher efficiency of the electrical energy dissipated during the FS regime, where a thermal runaway occurs, can be connected to the exceptional heating and densification rates also measured in the present work. An extension of the flash period results in a higher sintering temperature and longer sintering time in the stage where the heating rate is accelerated. Zhang et al. [53] compared the effect of conventional and controlled FS experiments on zinc oxide, and they pointed out the importance of ultra-high heating rates during the flash regime and the lower efficiency of the electrical energy dissipated in the steady current regime. Longer sintering times and more intense electrical energy generated by ramping up the current, step by step, did not increase the final density.

Figure 27 shows the electrical parameters and shrinkage together with SEM micrographs taken on the cross section of materials sintered under different pressure and voltage. Quite surprisingly, the pellet subjected to high pressure is much less dense (Table 3). Nevertheless, such result can be explained based on previous arguments: i) the initial green resistivity depends on the applied pressure (Figure 24), which decreases abruptly down to 6×10^{-5} Ω m at 60 MPa with respect to 7.5×10^{-4} Ω m at 4 MPa; ii) the onset time of the power peak is shortened, this resulting in much lower "Flash/total energy" ratio (Table 3). The higher pressure restricts the maximum evolution of resistivity by an order of magnitude and shortens the power surge duration, from 10 s to only 3 s as shown in Figure 27. As reported in Table 3, the final density decreases from 73% to 66% when the pressure is increased from 4 to 60 MPa. The total electrical energy is the same and the only variable, which can justify the lower densification is the reduction in the "Flash/total energy" ratio from 13% to 3% (see paragraph 3.1 Effect of pressure on the electrical resistance flash sintering of tungsten carbide).

A near full dense material is obtained by operating on the voltage (Figure 27(c)). A higher voltage of 4 V doubles the available electric energy from 210 J/mm^3 (3 V) to around 450 J/mm^3 (Table 3), leading 96% dense material. However, due to such higher power, excessive Joule heating causes hot spots in the central part of the sintered pellet, which limit the homogeneity of the final microstructure. It is interesting to point out that also the voltage affects the power surge duration (Figure 27(a,c)) and, accordingly, the "Flash/total energy" ratio decreases from 13% (3 V) to just 4% (4 V).

Table 3 Electrical parameters, relative density and apparent porosity for samples sintered under different pressure and electric field.

		3 V 4 MPa 60 s	3 V 60 MPa 60 s	4 V 4 MPa 60 s	3.5 V 4 MPa 60 s	3.5 V 4 MPa 10 s
Power peak	W	949 (±17)	1032 (±8)	1977 (±12)	1585 (±25)	1519 (±20)
Relative power peak	W/mm^3	4448 (±460)	4675 (±15)	9504 (±150)	7259 (±70)	7260 (±50)
Current density‡	A/cm^2	2806 (±25)	3282 (±37)	4566 (±32)	3940 (±33)	3678 (±42)
Flash energy†	J/mm^3	24 (±4)	6 (±1)	19 (±1)	36 (±2)	30 (±2)
Total electric energy	J/mm^3	216 (±23)	209 (± 14)	443 (±17)	369 (±11)	55 (±2)
Flash/total energy	%	13 (±4)	3 (±1)	4 (±1)	10 (±2)	55 (±3)
Density	%	73 (±3)	66 (±1)	96 (±1)	97 (±1)	95 (±2)
Apparent porosity	%	21 (±8)	31 (±2)	2 (±1)	1.5 (±0.5)	4.0 (±0.5)

†) total energy provided to the material during the flash event (<10s), calculated from the power integral up to the peak

‡) maximum current density recorded during the steady-state, current control regime (>10s)
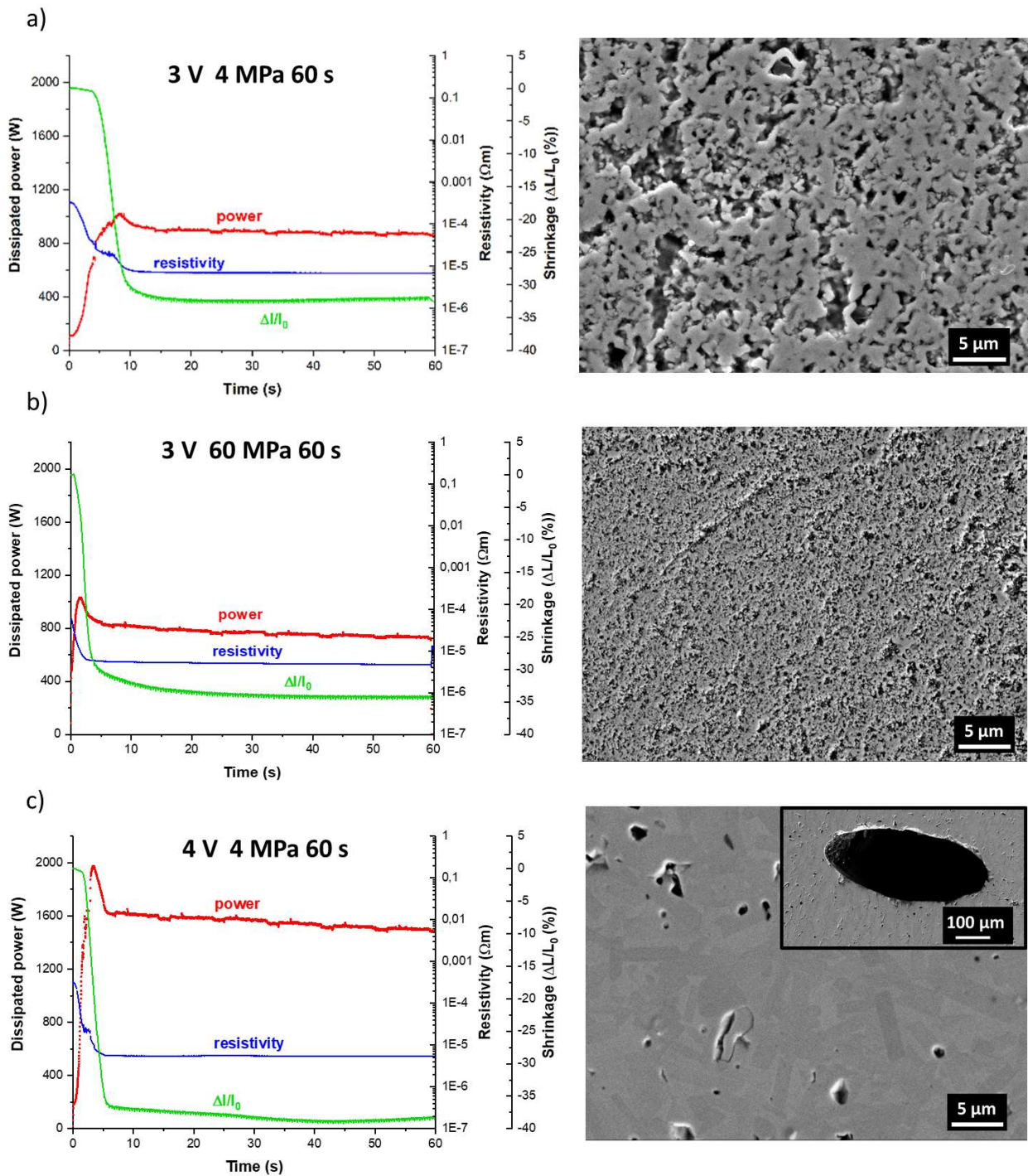
Figure 27. Processing parameters and final microstructure of specimen subjected to 60 s-long ERFS tests by using different pressure and sintering voltage. An example of "hot spot" as formed in the central part of the pellet after sintering under 4 V is shown in the inset of (c)).

52

Three variables are therefore found to affect the "Flash/total energy" ratio: i) pellet thickness, ii) applied pressure and ii) maximum voltage. Figure 28 shows the microstructure of a 7.5 mm thick pellet sintered with an intermediate voltage of 3.5 V under 4 MPa pressure. Sintering with less intense voltage prevents the occurrence of hot spots, improves the homogeneity and allows to reach density as high 97%. To further prove the importance of the flash regime (FS) over the resistive heating one (ERS), the same experiment was carried out with duration of about 10 s, i.e., just after the flash event occurrence. The interruption of the current after the power peak increases the "Flash/total energy" ratio to 55% (Table 3), leading to a material with very high density (95%), limited porosity (4%) and homogeneous microstructure. This result confirms the different sintering behaviour in the FS regime with respect to the ERS one. The majority of the densification occurs during the power surge (Figure 25) in the FS regime, during which the material behaves as a NTC ceramic and sintering occurs under a thermal runaway phenomenon. Densification slightly proceeds during the ERS regime where the material is characterized by a PTC behaviour and a more traditional resistive sintering takes place. These results agree with the previous hypothesis of higher efficiency of the electrical energy spent during the thermal runaway event, taking advantage of the ultra-high heating rates, which boost the sintering rates by orders of magnitude. For comparison, sintering rate in the last case (Figure 28) is about three times larger with respect to that estimated for the experiment in Figure 18 ($900\text{-}3000\text{x}10^{-4}\,\text{s}^{-1}$ vs. $400\text{-}1200\text{x}10^{-4}\,\text{s}^{-1}$). Such higher sintering rate coupled with a reduction of sintering time, from 60 to 10 s, is also much more energy efficient. If one compares the samples sintered under 3.5 V (60 s) and 3.5 V (10 s), the required energy enormously reduces from 369 J/mm3 to just 55 J/mm3 while the density only decreased from 97% to 95% (Table 3).

The results achieved so far allow to propose a new processing route for the consolidation of tungsten carbide products, with important differences with respect the state of the art and, in particular, SPS process. It is worth to observe that the heating rate achievable during the flash regime in the ERFS process

studied here is one two orders of magnitude higher than in SPS process where it is usually around 50-1000°C/min [92]. Accordingly, under the right flash conditions, the sintering rate is here at least ten times larger (0.2 s⁻¹) with respect to SPS (0.005 – 0.01 s⁻¹) [10]. The way in which the electric current interacts with the powder points out the differences between the two processes. In spite of some similarity, densification occurs here at a different time scale, leading to a great reduction in the time and the energy required for sintering.
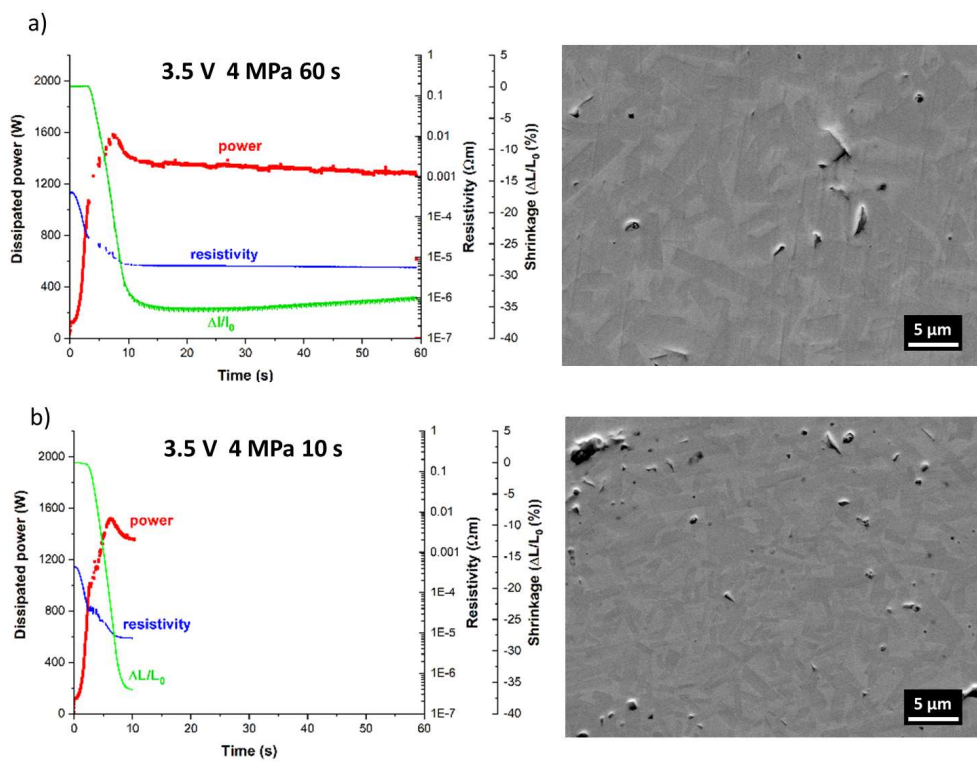
Figure 28. Processing parameters and final microstructure of specimen subjected to ERFS tests at 3.5 V, 4 MPa after different sintering time of 60 s (a) and 10 s (b).

2.1.4 Conclusions

The application of high currents at moderate voltages to tungsten carbide green compacts is shown to induce nearly instantaneous densification of the material. The phenomenon responsible for such event is accounted for by a "flash event" where a thermal runaway phenomenon can be triggered thanks to the transition from NTC to PTC behaviour with temperature. Therefore, pure tungsten carbide can be densified up to 95% in less than 10 s. Pressure, electrical power, pellet thickness and sintering time have a prominent role in pure WC densification behaviour. Although the density does not reach 100% during the experiments carried out in the present work, the results demonstrate the possibility to sinter pure tungsten carbide in very short time and successive optimization procedures could guarantee to obtain fully dense materials. The possibility to obtain variable final microstructures by tuning the operating conditions appears challenging, as well. Finally, some differences can be pointed out here between the flash behaviour of NTC and PTC ceramics: i) the specific power peak values are here one two orders of magnitude larger, ii) the first stage of flash sintering is absent as no incubation time is necessary to initiate the current flow in a conductive powder and iii) the power surge event has a self-extinguishing character.

2.2 Role of surface carbon nanolayer on the activation of flash sintering in tungsten carbide

Isacco Mazo[#], Lia E. Vanzetti [ξ], Jon M. Molina-Aldareguia [§, †], Alberto Molinari [#], Vincenzo M.

Sglavo[#‡]

\# Department of Industrial Engineering, University of Trento, via Sommarive 9, Trento, Italy

ξ Micro Nano Facility (MNF), Bruno Kessler Fundation (FBK), via Sommarive 18, Trento, Italy

§ Department of Mechanical Engineering, Universidad Politécnica de Madrid, 28006 Madrid, Spain

† IMDEA Materials Institute, C/ Eric Kandel 2, 28906, Getafe, Madrid, Spain

‡ INSTM, National Interuniversity Consortium of Materials Science and Technology, Trento Research

Unit, Via G. Giusti 9, 50123 Firenze, Italy

Graphical abstract
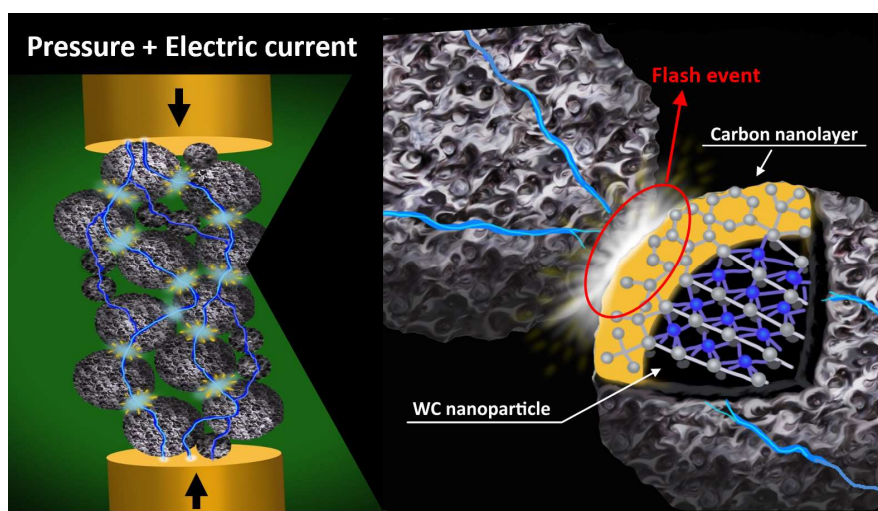
ABSTRACT

Flash sintering has been recently successfully activated also in conductive ceramic like tungsten carbide (WC). The present work aims at understanding how the WC particles surface chemistry can influence the electrical properties of the material and play a fundamental role in the flash sintering phenomenon. An electrical contact resistance (ECR) model was developed to understand the role of resistive surface layers on the electrical behaviour of WC green compacts under different applied pressures during the initial stages of the processes. It is established that the large resistivity measured on green compacts can be attributed to the sole presence of an ultrathin carbon layer on the particles' surface. A carbon nanolayer with a thickness of about 1-2 nm, as detected by XPS and HRTEM analyses, is found to be responsible for the high resistance reached at the particles' contact points while evolving during the flash event. Flash sintering conditions can be achieved during the electrical resistance flash sintering (ERFS) process in WC nanoparticles covered by such carbon layer and independently of the presence of W oxides.

2.2.1 Introduction

Tungsten carbide (WC) is a material of wide interest due to its intense use in many crucial industrial applications, ranging from metal machining to wear and friction resistant components. More recently, it has found also applications as possible precious metal alternative to catalyze hydrogen evolution processes (electrocatalysis). The surface chemistry of WC nanoparticles is of fundamental importance for hydrogen evolution reactions (HER) and its study became the focus of several research activities. Lin et al. demonstrated the potential to increase HER activity of transition metal carbides encapsulated by N-doped carbon nanolayers [106]. The carbon layer encapsulation of Mo_2C showed an unprecedentedly high electrocatalytic activity due to the peculiar electronic interaction of the transition carbide with the

57

C nanolayer [107]. Based on this idea, Liu et al. and Han et al. tested the HER performance of carbon-encapsulated tungsten carbide nanoparticles [108,109]. Raman spectroscopy and X-Ray Photoelectron spectroscopy (XPS) analyses revealed an electronic transfer mechanism between the carbide and the carbon layer, thus pointing out a special chemical and electronic affinity between the two materials. Yannik et al. studied the nature of the C layer on W films after carburization into WC [110]. The peak located at 285 eV in the C 1s XPS core level was successfully addressed to adventitious carbon, being easily removable after Ar ion sputtering. In addition to the carbide C-W peak (282.7 eV), a third species was identified as graphite, even if the peak position shifted from 284 to 284.3 eV. The shift in surface carbon was addressed by Yannick et al. to a larger graphitization degree of the non-carbide surface carbon, according to an increase in the layer thickness. The increase in the graphitization degree with the layer thickness suggests an initial different nature of the surface carbon, being neither fully graphitic nor carbide carbon. Warren et al., working on the oxidation behavior of WC, revealed the existence of non-carbide C 1s carbon peak after a complete cleaning of the surface by ion etching [111]. In addition, they discovered the possibility to passivate the WC surface after exposure to water, inhibiting further oxidation. The passivation can not be addressed to a continuous layer of tungsten oxides, these being non protective by nature [112] and soluble in water [113]. Warren et al. hypothesized the possibility of a rearrangement of the C atoms in the outermost atomic layer after the partial oxidation of incompletely bonded W surface atoms. With this assumption the carbon layer is composed of covalently bonded C atoms and not of graphitic carbon, resulting in a broad C 1s C-C peak shifted by less than 0.5 eV from the graphitic carbon peak. More recently, Krasovskii et al. demonstrated how the surface carbon enrichment over the bulk stoichiometry is a common feature across different WC systems; traces of C can be found even after a hydrogen decarburization of WC to $WC_{0.98}$ [114]. A spontaneous segregation of carbon towards the (1000) surface was also reported after sputtering and vacuum annealing [115].

Recently, the interaction of an electric current with carbonaceous materials has been exploited by Luong et al. for the production of "flash graphene" [116]. In the process, an extraordinarily high temperature of about 3000 K was reached in only few milliseconds, with the immediate transformation of carbon/graphite in turbostratic graphene layers. Starting from this peculiar phenomenon and from the hypothesis that WC nanoparticles tend to be covered by a surface carbon layer, the behaviour of green WC pellets under the effect of electrical current/field was studied. Flash sintering of tungsten carbide was attained by exploiting the interaction of an electric current with the pressed powdered materials, electrically insulated within a ceramic die [117]. Full densification could be achieved in a matter of seconds during electrical resistance flash sintering (ERFS) experiments, due to an abrupt increase of power dissipation and temperature. The vast acceleration in the sintering kinetics was accounted by the peculiar evolution of the green resistivity, changing from a negative to a positive temperature dependence, thus allowing a transitory thermal runaway phenomenon to occur.

The present work aims at investigating the presence and nature of surface carbon on WC nanoparticles and, more importantly, its role on the ultrafast sintering. In the previous work, flash sintering conditions were identified for WC powders in the presence of a small amount of oxides (WO_3/WO_4H_2) [117]. For this reason, two different powders were investigated here to discriminate the effect of an oxide/carbon layer: one partially oxidized (identical to that used in the previous works [117,118]) and a purer one. The presence of oxides was assessed by XRD, thermal analysis and field-emission scanning electron microscopy (FESEM). The carbon nanolayer presence and nature were investigated through high-resolution transmission electron microscopy (HRTEM), XPS and Raman spectroscopy. Based on the acquired information, an electric contact resistance model (ECR) was developed to analyze the electrical properties of green WC compacts under the application of an external pressure i.e., at the beginning of the ERFS experiments. The role of surface chemistry on the resistivity measured at different applied

pressures was modelled by considering three fundamental aspects: (i) the internal resistance of the particles, (ii) the contact resistance due to the constriction of the electrical contacts and (iii) the presence of a resistive layer. Finally, the two powders were tested under the same ERFS parameters to identify their different flash behaviour.

2.2.2 Materials and Methods

Powder properties. Tungsten carbide nanopowders were purchased from Inframat Advanced Materials® (product number #74N-0601) [119]. The powder was divided into two batches, exposing the first to open atmosphere for 12 months while storing the second one sealed and under vacuum; they were labelled as ox-WC and pure-WC. Powder morphology and chemical composition were analyzed by FESEM and energy dispersive X-Ray spectroscopy (EDXS) (ThermoFischer® Apreo 2S LoVac equipped with Ultim® Max 40 EDS detector); EDXS oxygen maps were acquired at 10 kV and 6.3 nA normalizing the colour palette on the maximum intensity by Aztec software (Oxford instruments). Phase composition of powders and sintered materials was determined by X-ray diffraction (XRD) (PANalytical EMPYREAN), generating an X-Ray beam of Cu-Kα1 (1.54060 Å) radiation at 45 kV and 40 mA in a line focus configuration. The measurement was accomplished in a Bragg-Brentano configuration with a PIXcell 1-D detector, with step size of 0.012° and a scan step time of 100 s. XRD data were processed with HighScore Plus® software to refine the peak profile with the Rietveld method. The crystallographic phases used for the refining were selected from the International Center for Diffraction Data (ICDD) database using the PDF-4+ software: ICDDs cards correspond to 00-032-1395 for WO_3, 04-011-6930 for $WO_3(H_2O)$, 01-085-4030 for $WO_2(OH)_2H_2O$, 01-084-5996 for WC, 00-035-0776 for α-W_2C and 00-020-1316 for cubic WC_{1-x}. The evolution of the oxides with temperature was analyzed by differential scanning calorimetry (DSC) and thermogravimetric analysis (TGA) (NETZSCH® Geraerebau GmbH STA 409 thermobalance) in the range of 25-1500°C (10°C/min) in inert atmosphere (Ar) to prevent the oxidation of the carbon species. Oxygen and carbon content were determined by IR analysis of the powders' combustion products using TC-400 oxygen/nitrogen (LECO®) and CS-800 carbon/sulfur (ELTRA®) analyzers.

XPS analysis were carried out with a mono Al Kα primary energy beam of 1486.6 eV (Kratos Axis Ultra), take off angle 90°, on both powders in an area of 300x700 μm^2. The samples were analyzed before and after an Ar ion etching treatment at 3.8 kV for different sputtering times within the XPS chamber. The carbon species were characterized by Raman spectroscopy (RENISHAW), using green laser (532 nm) and 50x optical magnification. A rapid survey was acquired in the range 100-3200 cm^{-1} and higher precision analysis was carried out in the range of the carbon peaks, between 1150-2800 cm^{-1}, increasing to 16 the accumulation times. High resolution TEM micrographs were acquired at 200 kV (FEI Talos F200x); the powders were dispersed in isopropanol by sonication method and deposited onto a Cu grid with a lashed carbon film. Before TEM observations, the samples were treated for 30 s inside a plasma cleaner (FISHIONE Model 1020) using a mixed atmosphere 25% O_2 and 75% Ar to remove any existing carbonaceous debris. In addition, only particles in between the carbon filaments of the lashed TEM film were magnified to avoid the artificial redeposition of C on the WC nanoparticles from the film.

Resistivity of green compacts at different pressures. Tungsten carbide powders (1.3 g) were compacted in cylindrical pellets (Φ=6 mm) by an uniaxial press (Specac®) at 350 MPa using a hardened steel anvil (Figure 29(a)). The compacted sample was transferred in an insulated die, made of zirconia, where two conductive cylindrical electrodes close the circuit with an external data collector and apply at the same time a uniaxial pressure (Figure 29(b)). Raw resistance data were recorded with a high precision digital multimeter (DMM6500 6 ½ digits), sensitivity 1 $\mu\Omega$, frequency 20 readings/s at an increasing uniaxial pressure from 0 to 100 MPa. Results were corrected by subtracting the resistance measured by directly placing the two electrodes in contact. The resistivity was evaluated by measuring the thickness of the pellets with a precision digital micrometer (±0.001 mm) before being inserted in the zirconia die.
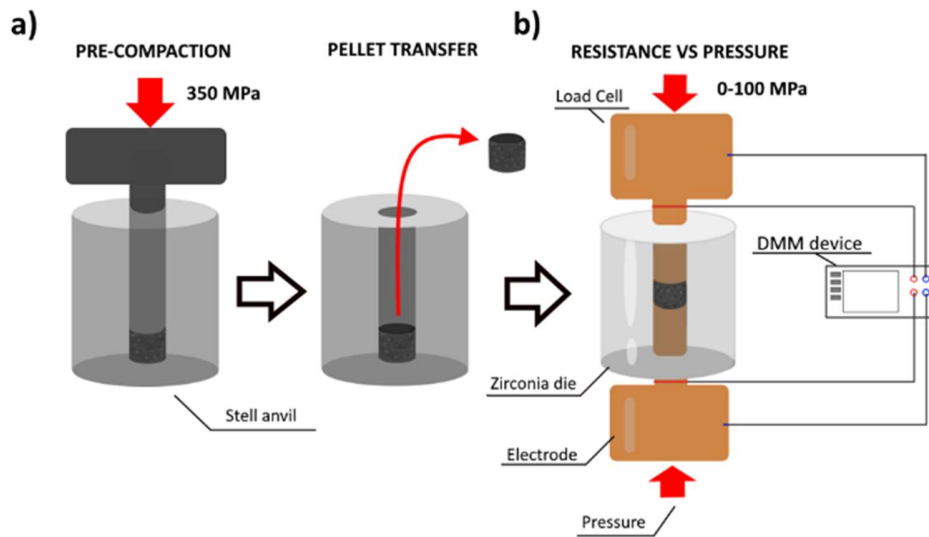
Figure 29 Schematic of the pellet preparation (a) and of the electrical resistance measurement under different applied pressure (b).

Sintering experiments. Electrical resistance flash sintering (ERFS) experiments were performed by a specifically realized apparatus (University of Trento, Department of Industrial Engineering, Italy) [117,118]. The process consists in the application of a low AC voltage in combination with the minimum required pressure (4 MPa) to maintain the electrical contact with the electrodes (Figure 30). The electrical power was applied by controlling the voltage and current below maximum values equal to 3.5 V and 1400 A, respectively. The sintering took place within an insulating ceramic die in open air conditions. The complete sintering procedure lasted approximately 10 s.
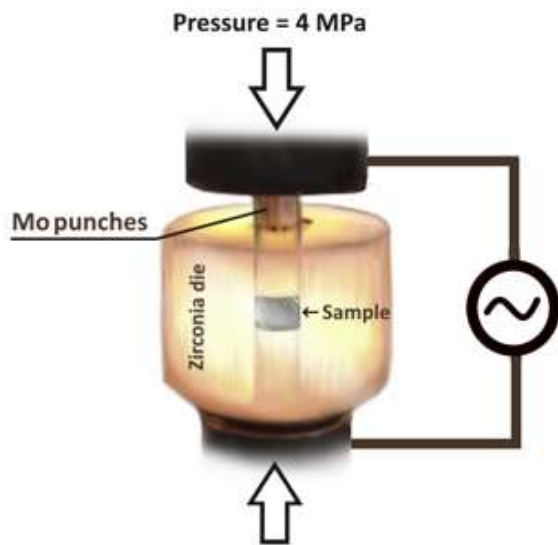
Figure 30 Schematic of the Electrical Resistance Flash Sintering (ERFS) process.

2.2.3 Theory & Calculations- Electrical contact resistance (ECR) model

Conceptualization. The ECR model's concept is focused on the electrical properties of a green ceramic sample prepared by uniaxial compaction (Figure 29(a)). The core of said model is based on the work of Chaim [120], who developed a theoretical approach to explain the particle size effect on the flash sintering temperature of oxide ceramics. Chaim's model for the electrical resistance of a granular compact is adapted to a metallic ceramic, like WC, by incorporating the influence of the particles surface resistive layer [121]. The ECR model assumes the pellet, i.e., the granular compact used for the determination of the resistivity under pressure of Figure 29(b), as composed of identical spherical particles. The overall resistance of the body is simulated as a string of resistors connected in series, the electric field (E) being applied between the flat top and bottom surfaces (Figure 31(a)).

Three effects are considered to contribute to the overall resistance of the sample: (i) the internal particle resistance, (ii) the constriction resistance at the contact points and (iii) the presence of surface resistive layers.
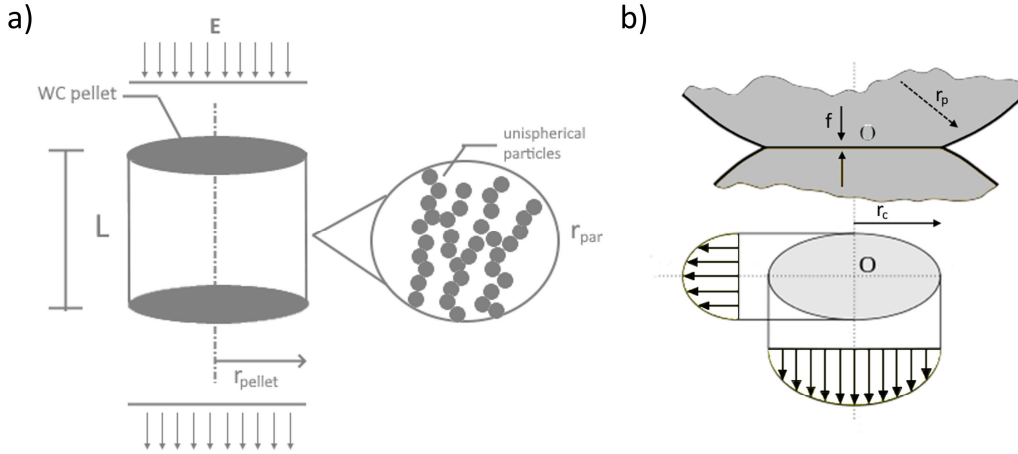
Figure 31 Schematic of the WC powder compact used in the ERFS test (a) and of the contact region between two WC particles (b).

Contribution to the overall resistance. The electrical resistance for a spherical particle can be assumed equal to:

$$R_{part} = \frac{\rho_{bulk}}{\pi r_{contact}} \tag{9}$$

where ρ_{bulk} is the resistivity of the bulk material and $r_{contact}$ the radius of the electrical contact (Figure 29(b)). The contact resistance developed between two nanoparticles is a crucial factor to be evaluated. It depends strongly on the type of conductor and on the scattering probability of free electrons (mean free path of electrons, λ_e). If the contact radius developed during the test (Figure 31(b)) is comparable or larger than λ_e, the Holms limit for the contact constriction should be used [104]:

$$R_{cont}^{H} = \frac{\rho_{bulk}}{2r_{contact}} \qquad (10)$$

Conversely, when the contact radius is lower than the mean free path of electrons, λ_e, a quantum constriction effect arises due to the increased scattering probability caused by the striction at the contact point, this being described as the Sharvin limit for the contact resistance [104]:

$$R_{cont}^{S} = \frac{\lambda_e \, \rho_{bulk}}{\pi (r_{contact})^2} \qquad (11)$$

The contribution of a possible resistive surface layer (carbon/oxides) can be expressed according to its resistivity (ρ_{layer}) [121] by:

$$R_{layer} = \frac{2\rho_{layer}\tau}{\pi (r_{contact})^2} \qquad (12)$$

Following the formalism of Chaim the overall resistivity of the pellet results:

$$\rho_{pellet} = \frac{4\pi}{9} r_{par} \left(R_{part} + R_{cont}^{S/H} + R_{layer} \right) \qquad (13)$$

Mean free path of electrons in tungsten carbide. Data regarding the mean free path of electrons in WC are rather scarce and there is not a precise value in literature. For metals, this value varies from around 5 nm (nickel) up to 54 nm (silver) [122,123]; for metallic tungsten it was estimated around 15.5 nm by first principles calculations [124]. The mean free path of electrons for non-stoichiometric transition carbides, MC_{1-x}, is much lower due to the wide presence of vacancies (responsible for higher scattering probability) and it is around 50 Å [125]. Therefore, for tungsten carbide it should have an intermediate value also considering the order of magnitude which differentiates the resistivity of WC from that of its metallic counterpart: 5.8×10^{-8} Ω m (tungsten) vs. 2.2×10^{-7} Ω m (tungsten carbide). However, there is not a direct relation between the two quantities, since in the microscopic Ohm's law the resistivity is connected to λ_e by:

$$\rho_{macro} = \frac{mv_F}{ne^2\lambda_e} \tag{14}$$

where m is the electron mass, v_f the Fermi speed, n the density of free electrons, e the electron charge and λ_e the mean free path of electrons. This latter can therefore be calculated from the bulk resistivity, the Fermi speed of conduction electrons and their density.

For simple metals, the density of free electrons, n, can be easily calculated according to the number of free electrons per atoms, Z, as:

$$n = Z \frac{N_A \, density}{atomic \, mass} \tag{15}$$

For a compound like WC, characterized by an unknown number of free electrons per atom and complex bands of hybridized C_{2p}-W_{5d} states [102,126], a different route may be found in the energetic part of the Schrodinger equation:

$$E_f = \frac{h^2}{8m}\left(\frac{3n}{\pi}\right)^{\frac{2}{3}}\frac{1}{e} \tag{16}$$

For the Fermi level, E_f, a value of 1.12 Ry or 9.2 eV can be used for the calculation, according to the work of Alekseev et al. [127]. Being h the Planck constant the free electron density will result, $n = 26.95 \times 10^{28}$ electrons m^{-3}. Starting from the Fermi level, also the Fermi speed can be evaluated as:

$$v_f = \sqrt{\frac{2E_f}{m}} = 2.32 \, x10^6 \; m \, s^{-1} \tag{17}$$

Therefore, by using Eq. 14, the electron mean free path is $\lambda_e = 1.4 \, nm$.

Deformation regime at the particles' contact points. The correct selection of the constriction resistance Eq. 10 or Eq. 11, (Sharvin or Holms) requires the study of the deformation regime (Figure 31(b)) reached at the WC nanoparticles contact points during the test of Figure 29(b). The application of a compaction load, F, results in an average contact force on each particle equal to:

$$f = F \left(\frac{r_{par}}{r_{pellet}} \right)^2 \frac{2}{3\rho_g} \tag{18}$$

where ρ_g is the green density and r_{par} the particle radius (*Table 4*).

According to the Hertzian theory, the total displacement, δ, experienced by a particle with respect to its dimension r_{par}, is:

$$\delta^3 = \frac{9(1-v^2)^2 f^2}{16E^2 r_{par}} \tag{19}$$

The contact radius is directly connected to δ by:

$$r_c^{elastic} = \sqrt{r_{par}\delta} = \left[\frac{3(1-v^2)}{4E} r_{par} f \right]^{\frac{1}{3}} \tag{20}$$

According to Eq. 20, the contact radius (r_c) between two particles increases from 1 to 10 nm (Figure 31(b)) when the pressure increases from 1 to 100 MPa (Figure 29(b)). Being the minimum contact radius of the same order of the estimated mean free path of electrons ($\lambda_e = 1.4$ nm) no quantum effect arises in the constriction resistance. The Holms' Eq. 10 can be used in the evaluation of the average contact resistance and, substituting Eqs. 9, 10 and 12 in Eq. 13, the final electrical contact resistance (ECR) model becomes:

$$\rho_{pellet} = \frac{4\pi}{9} \frac{r_{par}}{r_{contact}} \left(\frac{\rho_{bulk}}{\pi} + \frac{\rho_{bulk}}{2} + \frac{2\rho_{layer}\tau}{\pi r_{contact}} \right) \tag{21}$$

Table 4 Mechanical and physical properties for tungsten carbide powders and pellet used in the evaluation of the deformation regime.

Property name	Symbol	Unit	Value
Elastic modulus	E	GPa	700
Poisson's ratio	ν		0.22
Average particle radius	r_{par}	nm	120
Pellet radius	r_{pellet}	mm	3
Green density (WC pellets)	ρ_g	%	40 ± 1

2.2.4 Results and Discussion

Powders characterization – carbon and oxygen species

The ThermoFischer Apreo 2S LoVac, featuring the Ultim Max 40 EDXS detector, is an advanced scanning electron microscope (SEM) that excels in precise elemental analysis, including for light elements like oxygen. The TruQ® (Figure 32Figure 33) functionality reliably eliminates variations caused by peak overlaps and background intensity, while the larger 40 mm sensor sizes of Ultim Max effectively capture a greater portion of low energy X-rays, enhancing sensitivity for light elements. With the Ultim Max's exceptional sensitivity, it swiftly generates ample counts to achieve quantitative errors for oxygen of less than 0.1wt% level and a detection limit of 0.3 wt%. EDXS analyses estimate an oxygen content more than double onto ox-WC powder, (

Figure 32(a)), with respect to pure-WC, (Figure 33(b)) and the two oxygen maps show the accumulation of such element only on certain particles. This non-uniform distribution suggests that only some particles

are prone to form oxidation products, although these are not directly observable by FESEM analyses (Figure S. 1 in Supp. mat.).
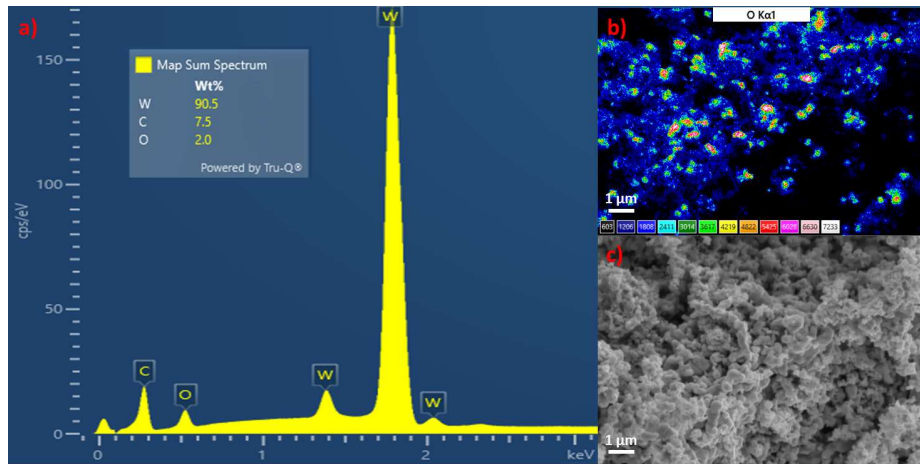
Figure 32 EDXS analysis of ox-WC powder: spectrum and chemical composition (a), oxygen map (b) and corresponding powder micrograph (c).
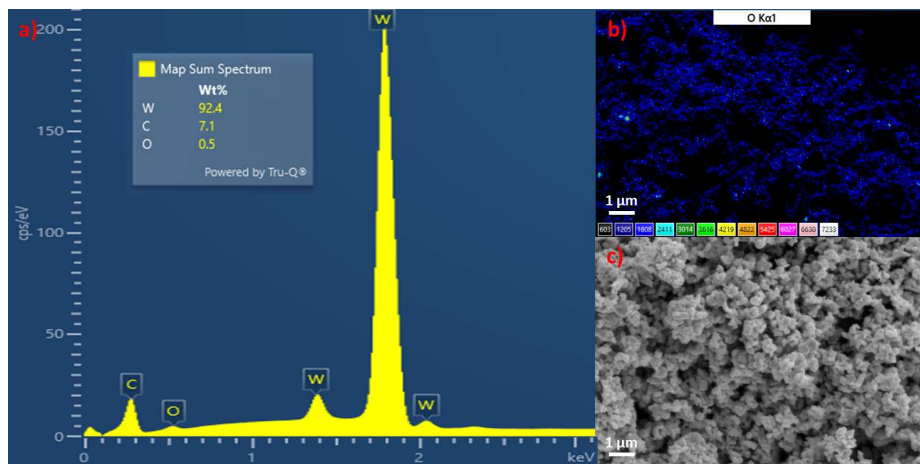
Figure 33 EDXS analysis of the pure-WC powder: spectrum and chemical composition (a), oxygen map (b) and corresponding powder micrograph (c).

XRD analyses of Figure 34 reveal the presence of low angle peaks only in the ox-WC powder. Peaks at 16° and 26°, that are sharp and high in intensity, can be assigned with a high level of confidence to a hydrated species of tungsten oxide, $WO_3(H_2O)$, also known as tungstite. The other low intensity peaks

at 23°, 27°, 52° and 56° are more difficult to be indexed since they are characteristic of different W-oxide species. Nevertheless, the peak at the very small angle, 12°, identifies the presence of very distant interatomic planes, typical of highly hydrated species. Hydrotungstite, $WO_2(OH)_2H_2O$, is found to best fit the remaining peaks of the recorded spectrum. A total of 5 ±1 wt% of oxides are present in the ox-WC powder (Rietveld method), while no oxide peaks are detectable in pure-WC.
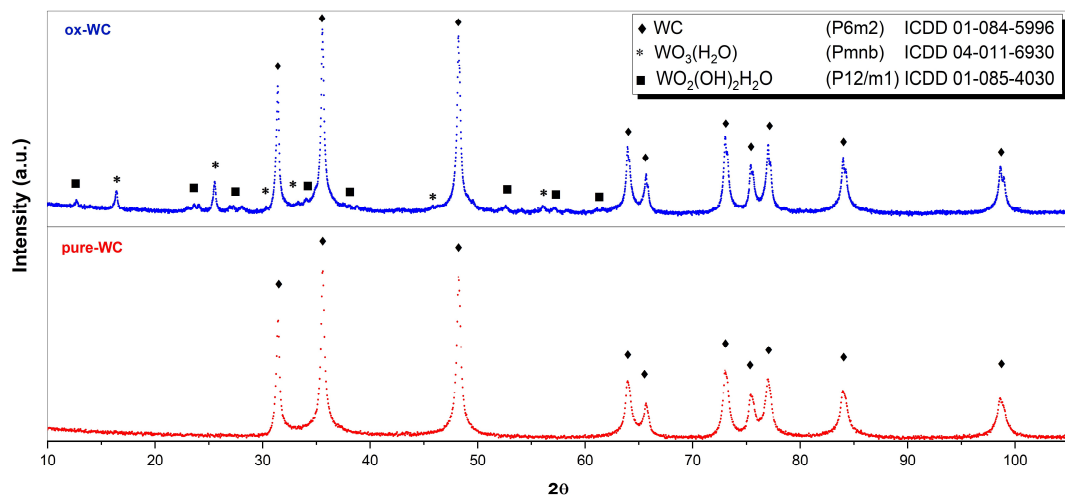
Figure 34 XRD spectra of the WC powders; the structures and the diffraction cards used for the Rietveld refinement are shown in the legend.

The IR analyses of the combustion products of the two powders are shown in Table 5; a larger amount of oxygen is detected in the ox-WC powder with respect to pure-WC one. The analysis revealed a concentration of 1.21 (±0.01) wt% and 5.46 (±0.03) wt% of O and C, respectively; carbon is largely sub-stoichiometric (6.13 wt% theoretical C concentration for WC) and a remarkable amount of oxygen is detected. As expected, the pure-WC powder contains a limited amount of oxygen, 0.28 (±0.01) wt%, in agreement with the EDXS results. It is also characterized by a large amount of carbon, which is well above the stoichiometric ratio. Such surplus can not be present in the carbide lattice and should be identified as residual graphite or amorphous carbon which remains after the powder production process.

As shown by the DTA/TGA diagrams (Figure 35), the powder containing hydroxide species undergoes a mass loss of around 2-3 wt% at 1100°C while heated in inert atmosphere, the evolution corresponding to an endothermic reaction. This reaction, which occurs only for the oxidized power (Figure 35(a)), can be addressed to the high temperature decomposition of the oxide species. The endothermic reaction at 1100°C is comparable to the decomposition temperature of tungsten trioxide (WO_3) [22,128]. In addition, the oxides species can also react with the carbon present in the WC lattice [129] causing the evolution of CO_2 gasses and the mass loss observed. The small perturbation of the DTG curve at about 200°C of Figure 35(a), could be related to the water loss from the hydroxides species.
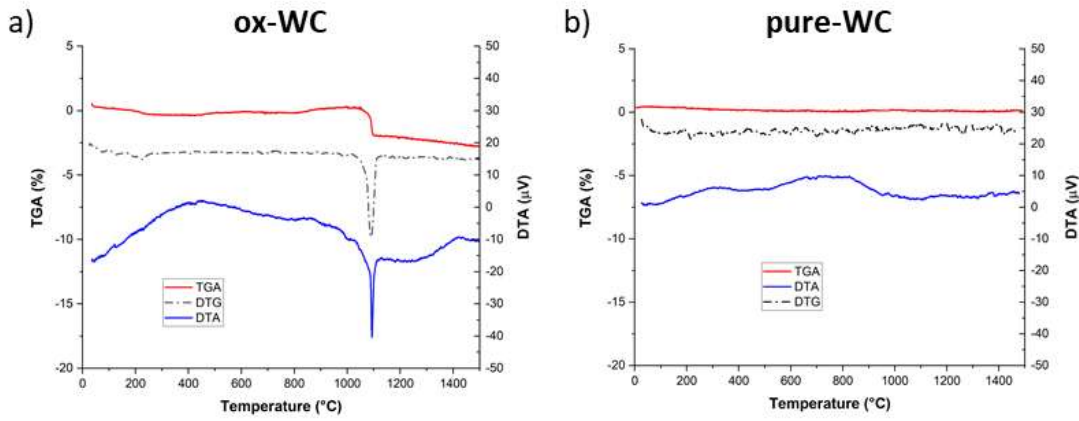
Figure 35 DTA, TGA and DTG (=dTGa/dT) plots for ox-WC and pure-WC powders.

Table 5 Oxygen and carbon content, as evaluated by IR spectroscopy analysis on the WC powders combustion products.

	ox-WC	pure-WC
O (wt%)	1.21 (±0.01)	0.28 (±0.02)
C (wt%)	5.46 (±0.03)	6.43 (±0.02)

The surface chemistry of WC powders was determined from the deconvolution of the XPS signals (Figure 37), by using the RxpsG software [130]. The interaction depth of Al Kα photoelectrons is about 96 Å (≈10 nm) for oxidized WC specimens [131], according to that 95%+ of the signal intensity derived from this region below the particle surface.
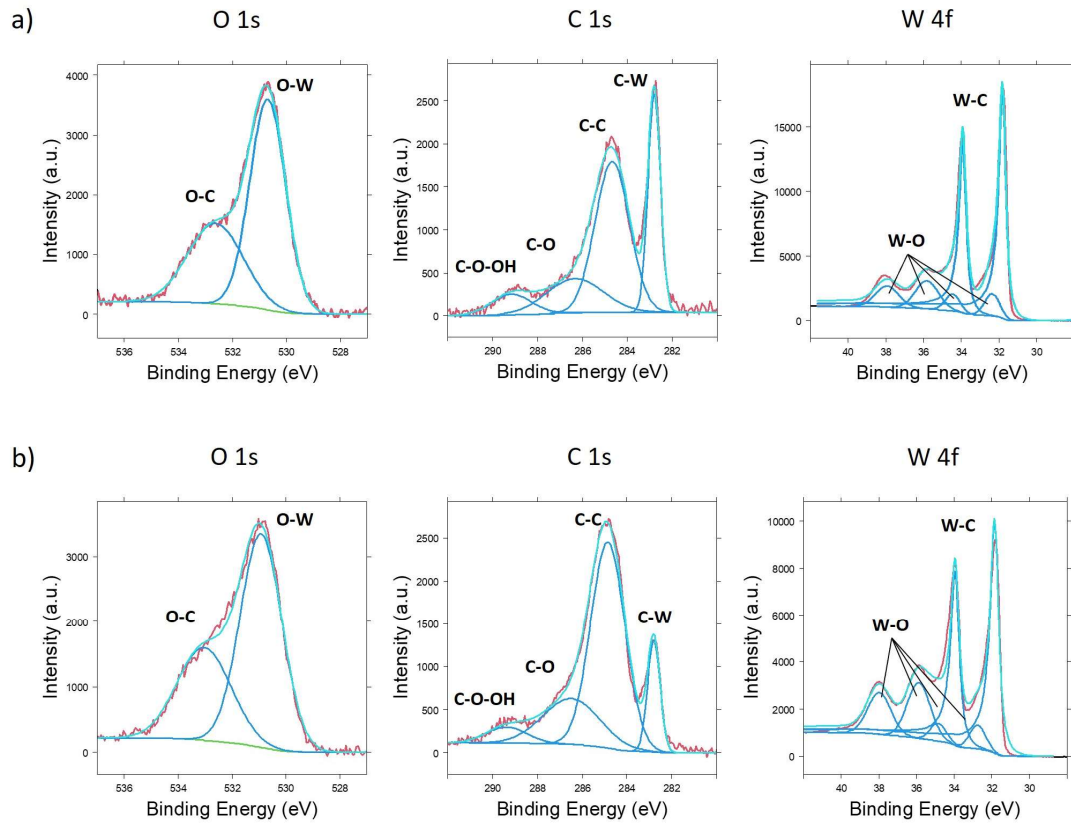
Figure 36 Deconvolution of XPS peaks for the 'as-received' ox-WC (a) and pure-WC (b) powders.

The peak at 530 eV (O 1s) is related to the presence of surface oxides (O-W bonds) while the small shoulder at slightly higher energies is associated with contamination products (C-O bonds). In the C 1s spectrum, the peak located at 282.8 eV belongs to the carbide, while the broad peak at 284-285 eV represents different hybridizations of carbon [132,133] (amorphous/graphitic species) which are too close in binding energy (BE) to be separated effectively without affecting the result by personal interpretations. The small shoulder at 286 eV identifies C-O bonds and that at 288 eV is due to the

presence of hydroxides species (C-O-OH) also bonded with carbon; both can be considered as adsorbed surface contaminants [134]. The deconvolution of the W 4f core level allows the separation of three duplets, corresponding to the three W electronic states of: WC, WO_2 and WO_3, indicated as W-O in Figure 36 for simplicity. WC powders were demonstrated to be reactive in contact with the atmosphere even at room temperature [111,112,135], forming a very thin oxide layer on their surface. More carbon is present on the surface of pure-WC (Figure 36(b)) with respect to ox-WC (Figure 36 (a)), 58.8% vs 54.3% (Table 6), according to overall C concentration previously reported (Table 5). In the first 10 nm below the surface there is more carbon in the C-C bonds than carbide carbon (C-W) and such carbon concentrations are unconventionally high for being a typical XPS contamination [114].

The correct interpretation of the real nature of the carbon present on the WC particles detected by XPS is complicated by the small gap in BE among the different carbon species [133,136]. Krasovskii et al. [114] assigned to 284.55 ± 0.06 eV the position for sp^2-C (graphite) and Diaz et al. [132] reported an increased graphitization degree of a-C films by the shifting in the C-C peak to lower BE. According to the state of the art for the C 1s XPS interpretation, the peak for sp^2 carbon should be separated by less than 0.6 eV from the sp^3 one, which is located at the same binding energy than adventitious carbon (285 eV) [133,137]. Lantsev et al. recently suggested a tendency of WC nanoparticles to form monolayers of surface carbon [70]. Carbon tends to segregate on the surface of the particles from the bulk even in the presence of sub-stoichiometric structural carbon (C < 6.13 wt%) like in our case (Table 5), in search of restoring the equilibrium with the surface oxidized layer [114]. Oxidation studies by Warren et. al suggested the incomplete bonding of surface W atoms, which once oxidized lead to a layer of carbon atoms. These free carbon atoms are not stable and, in the search to restore the disturbed WC crystalline diamond structure, will form covalent bonds with the carbon atoms in the second layer, possibly forming a partially amorphous carbon layer with a fraction of sp^3 hybridized carbons [111]. Warren measured the

composition of the contamination layer of oxidized W and WC before and after an ion etching treatment. C-H, C-O and C-OH peaks were present in both materials before the ion treatment, while C-C was found only on WC samples. After the etching, no C 1s contamination peaks remained onto pure W powder and only C-W and C-C peaks remained in tungsten carbide powder, enforcing the hypothesis of the peculiar rearrangement of carbon atoms on the WC disturbed surface.

To separate the adventitious carbon contribution to the broad peak at 284.8 eV, the two powders were subsequently treated with an in-situ Ar ion etching process within the XPS instrument (Figure 37).
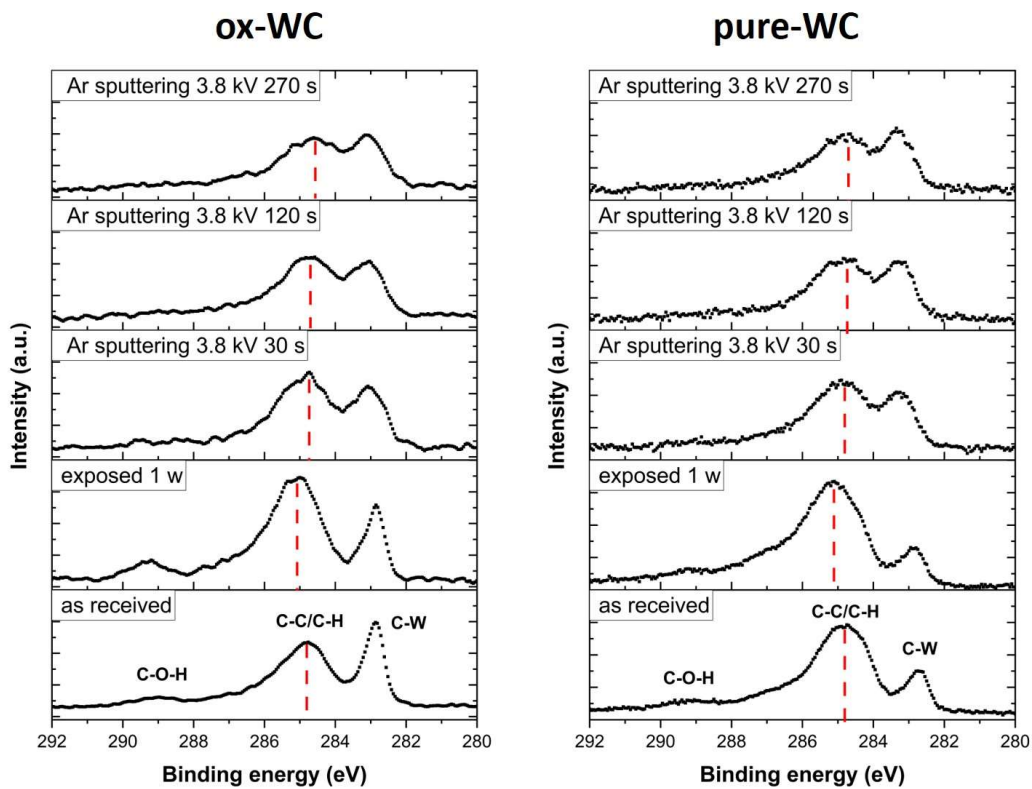
Figure 37 XPS spectra for ox-WC and pure-WC powders: C 1s core levels are acquired at different sputtering conditions and after 1 week of exposure to the atmosphere. The red lines highlight the shift in the C-C peak at different test conditions.

The etching procedure effectively removes the surface contamination, as proven by (i) the complete removal of hydrocarbon contamination (C-O-H bonds), (ii) the reduction in the intensity of the C-C peak and, finally and (iii) the removal of the W-O peaks in the W 4f core level and the decrease in the O 1s shoulder at 533 eV (C-O bonds) (Figure S. 3 in Supp. mat.). Of particular importance is the modification occurring to the carbon peaks in the C 1s level for both powders, the C-C peak identified before as a convolution of multiple species undergoes a deep modification (Figure 37). Its intensity decreases at prolonged etching times and its position shifts towards lower BE: from 284.8 eV to 284.6 eV. This can be explained by the removal of only a portion of the surface carbon species, the adventitious carbon contamination located at 285 eV [134], in spite of other species located in the range of 284-284.5 eV. This is also supported by the analyses on the sample exposed again to the atmosphere after the etching ('exposed 1 w'). The cleaned surface reacquires oxygen and carbon contaminants, concurrently the intensity of the (C 1s) C-C peak increases again with respect to the C-W one and even more importantly shifts to higher BE, from 284.8 eV to about 285.1-285.2 eV, so towards the position of the adventitious carbon located at 285 eV. A re-oxidation of the powders surface is also proved by the increase in the W-O peaks intensity, those corresponding to the oxides in the W 4f core level (Figure S. 3 in Supp. mat.).

Similar to the C-C peak, also the C-W is strongly affected by the Ar etching procedure; the intensity reduction and the conspicuous broadening suggest a partial amorphization of the WC structure. Figure 37 shows how, even in the presence of a severe damage to the C-W lattice generated after an intense etching at 3.8 kV, the C-C peaks retain a large portion of their initial intensity. This result suggests the presence of a carbon layer firmly bonded to the WC sublattice and characterized by C-C bonds with a strength of the same magnitude and similar in nature than the C-W ones.

The carbon and the oxide layer thickness can be estimated according to the formalism described by Nylund and Olefjord [111,138]:

$$\tau_{oxide} = \lambda_W^{ox} sin\theta \ln \left(1 + \frac{I_W^{ox} S_W^{met} D_{wc}}{I_W^{met} S_W^{ox} D_{wo3}} \right) \qquad (22)$$

$$\tau_{carbon} = \lambda_C^{elem} sin\theta \ln \left(1 + \frac{I_C^{carbon} S_C^{carb} D_{wc}}{I_C^{carb} S_C^{carbon} D_c} \right) \qquad (23)$$

where the above quantities are: $\theta = 90°$ the take-off angle, I the measured intensities (integrated peak area), S the experimental atomic sensitivity factors and D the atomic density. W-C and W-O intensities, in W 4f core levels (Figure S. 3 in Supp. mat.), were used to evaluate the thickness of the oxide Eq. 22, while C-C and C-W intensities, in the C 1s, were utilized in Eq. 23.

The results are 14 Å for carbon and 18 Å for the oxide layer in ox-WC and 27 Å for carbon and 23 Å for the oxide layers in pure-WC powders. The resulting layer thicknesses can be incorporated in the ECR model (Eq. 21) to estimate their contribution on the electrical properties. It has to be noted that since the penetration depth of Al Kα in C is almost half of that in WC the relative intensity W-C vs W-O peaks is lower in the W 4f of Figure 37(b), overestimating the real amount of oxides is pure-WC.

Table 6 XPS quantitative analysis.

ox-WC powder	total amount	O-W	O-C/C-O-OH	C-C	C-W
O (%)	25.8	16.2 (O 1s)	9.6 (O 1s)	/	/
C (%)	54.3	/	14.0 (C 1s)	25.9 (C 1s)	13.8 (C 1s)
W (%)	19.9	5.1 (W 4f)	/	/	14.8 (W 4f)
pure-WC powder					
O (%)	26.8	17.2 (O 1s)	9.6 (O 1s)	/	/

C (%)	58.8	/	23.0 (C 1s)	35.5 (C 1s)	7.1 (C 1s)
W (%)	14.4	4.7 (W 4f)	/	/	9.7 (W 4f)

The graphitic character of the carbon layer was further investigated by Raman spectroscopy, in the range 1200 - 2800 cm^{-1} (Figure 38). Carbon species can be identified according to the intensity, position and broadening of the D and G bands. Both bands originate from the vibrational modes of carbon atoms with sp^2 hybridization, but different vibrational modes activate them. The D band, located around 1350 cm^{-1}, corresponds to the A1g breathing mode of carbon aromatic rings, which can be excited only in the presence of defects in graphite layers. Fully amorphous carbon and pristine graphite do not show the D band, since sp^2 carbon rings are either not present or not Raman active. Conversely, the G band, located around 1581 cm^{-1}, corresponds to the E2g stretching of sp^2 carbons and it is always Raman active either in fully amorphous or graphitic carbon.
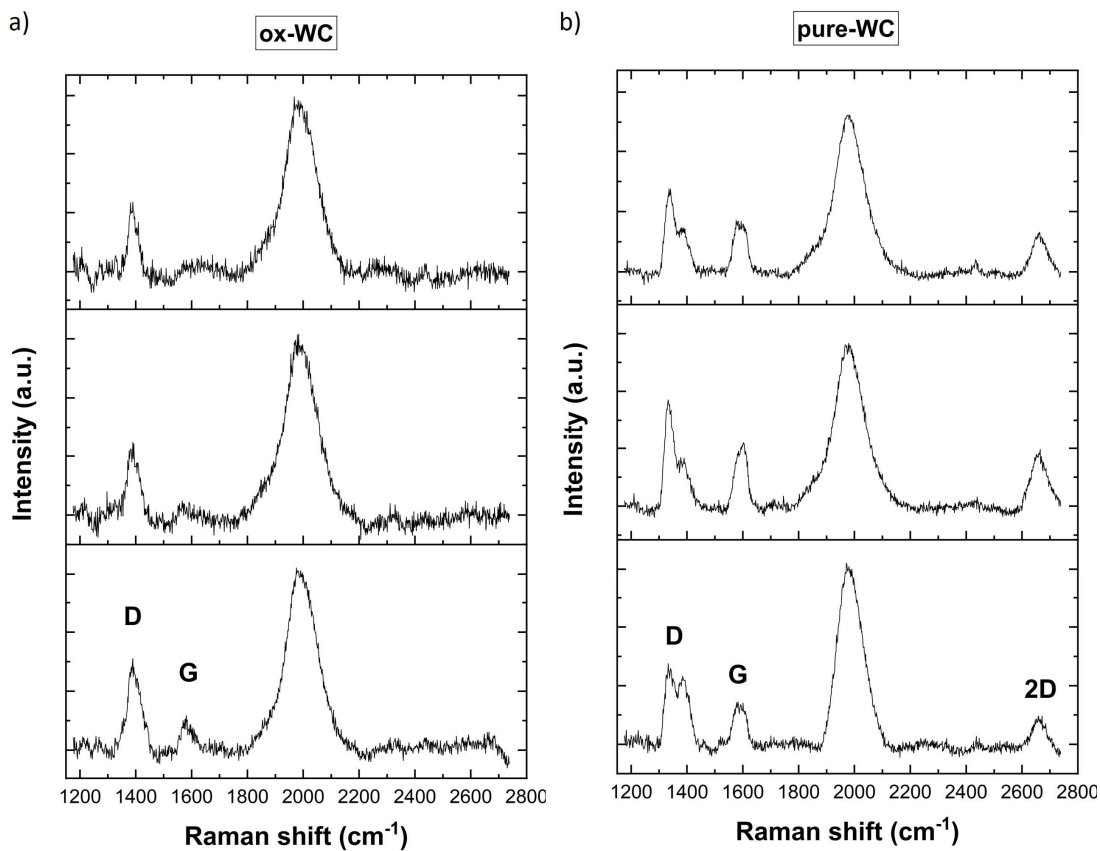
Figure 38 Raman spectra of the ox-WC (a) and pure-WC (b) powders in the region between 1200 – 2800 cm-1. The plot reports the analyses acquired on three different spots on the powder.

According to the work of Ferrari and Robertson [139], the type of carbon can be assessed by comparing the position of the two bands with respect to their intensity ratio I(D)/I(G). The introduction of an in-plane disorder, which corresponds to a reduction of the correlation length (L_a) in graphitic layers, increases the G band position, from 1581 to 1600 cm^{-1}, and the intensity of the D peak. On the other side, the amorphization of graphite with the loss of aromatic rings and the increase in the sp^3 bonds character lowers the I(D)/I(G) ratio towards zero. The D peak is present in both powders (Figure 38 (a) and (b)), with an intensity always higher with respect to the G band. This excludes a priori the presence of fully amorphous carbon, either low sp^3 (a-C) or high sp^3 (ta-C) content species, and of pristine graphite [140].

More in detail, for ox-WC the G band is very broad and shifts from 1581 up to 1594 cm^{-1}. The high I(D)/I(G) ratio coupled with the broad G band position above 1580 cm^{-1}, typical of pure graphite, suggests the presence of a highly defective nanocrystalline graphite (NC-g) with a very low in-plane correlation length ($L_a < 20$ Å) [139]. Similar D and G band positions and intensity ratios are present in the Raman spectrum of pure-WC (Figure 38(b)), which suggest the presence of NC-g also in this sample. It is worth to be noted that for the pure-WC powder, the G peak is composed of two convoluted peaks, around 1577 and 1600 cm^{-1}. The shift in the G peak can arise from a different degree of clustering and/or band disorder of the sp^2 bonds, this pointing out the presence of two different types of graphite. The peak around 1600 cm^{-1} is characteristic of NC-g as described for the previous powder, the peak at 1575 identifies a graphite layer with a higher order. In line with these facts, pure-WC is richer in carbon with respect to the ox-WC one, as identified by XPS (Figure 37) and IR analyses of the decomposition products (Table 5).

The band located around 2000 cm^{-1} for both powders, is rarely observed in carbon containing compounds. Milani and Ferrari [140,141] associated the bands between 2000-2100 cm^{-1} to linear carbon chains with sp1 hybridized carbon. However, the presence of carbon wires on the surface of WC nanoparticles does not have any other experimental evidence. The band located around 1980 cm^{-1} can be more simply ascribed as an overtone of the band at 985 cm^{-1} (Figure S. 2 in Supp. mat.), as it occurs for the D and 2D band, which has been already observed by Cheong et al. [142] on WC nanoparticles in the presence of a carbon layer.

A closer observation of the particles' surface by HRTEM revealed the presence of a well-defined layer on both powders, with morphology and crystallinity clearly in contrast with the WC structure (Figure 39-Figure 40). In both images the ordered arrangement of atoms in the WC lattice is interrupted to an apparently amorphous material near the surface. A thicker amorphous layer is observed in the pure-WC powder, in agreement with the more intense C-C peak of the corresponding XPS C 1s level (Figure 37).

The lack of any crystalline pattern in the observed layers, in contrast to the highly crystallinity of the oxides (Figure 34) and the non-uniform concentration of oxygen on the powder (

Figure 32), leads to the conclusion of the presence of a carbon nanolayer, with a highly disordered structure, on the surface of the WC particles. In addition to the thicker surface carbon layer, pure-WC powder (Figure 40) is also characterized by a second carbon species. The bright particles shown in Figure 40 were identified as nanocrystalline graphite by SAED analysis.
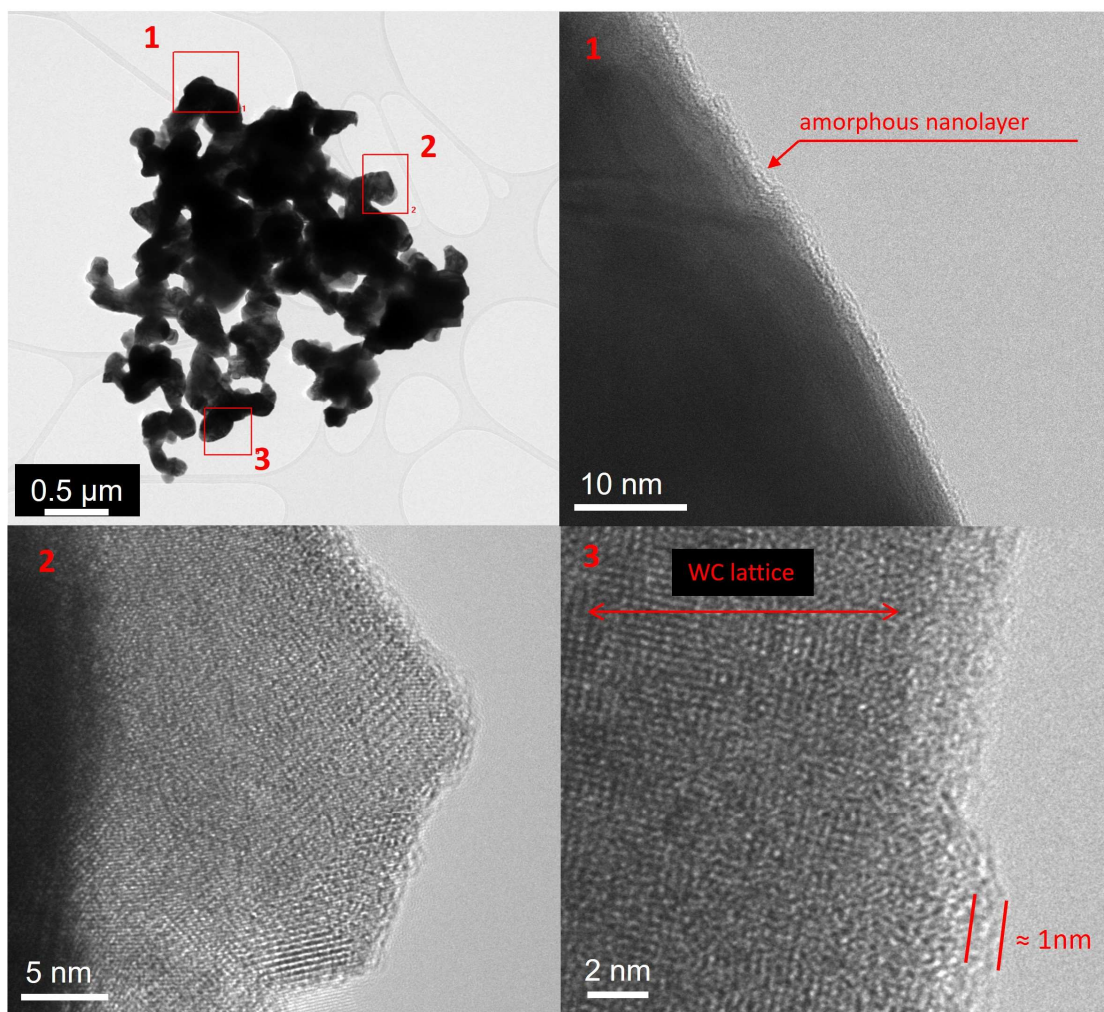
Figure 39 HR-TEM micrographs of ox-WC nanopowders. The particles' surface was analyzed in three different spots, with the nanoparticles located in between the TEM support film.
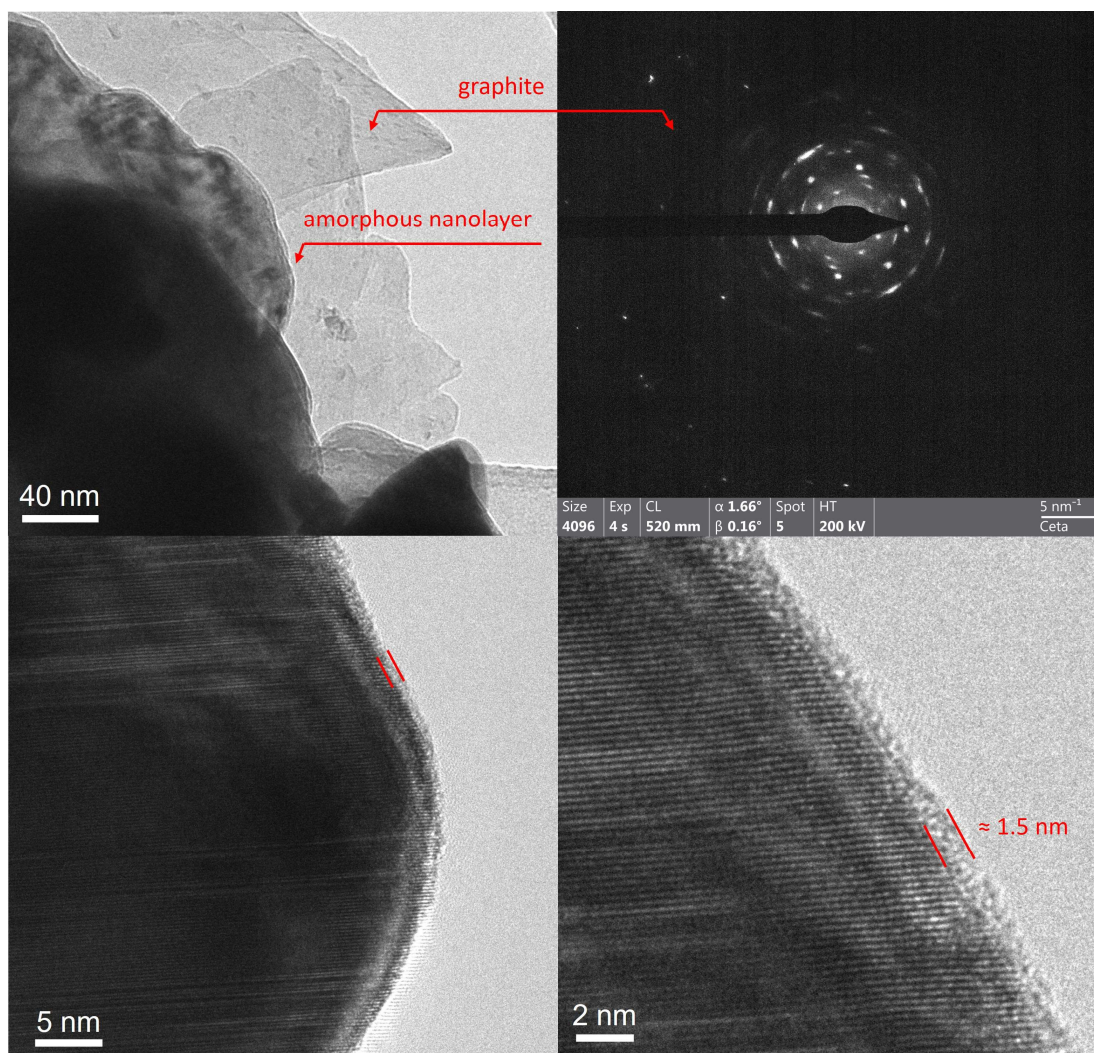
Figure 40 HR-TEM micrographs of pure-WC nanopowders. The particle surface was analyzed in different spots, with the nanoparticles located in between the TEM support film.

Green compacts resistivity and applied pressure

Figure 41 shows the experimental and the modelled resistivity of a WC pellet at different applied pressures. The electrical contact resistance (ECR) model Eq. 21 was used to represent different situations: (i) considering only particles resistance (PR) of Eq. 9 and the constriction resistance (CR) of Eq. 10 (ii) adding the presence of an oxide layer Eq. 12 or (iii) in the presence of a surface carbon layer. The modelling of only the particle resistances and the contact constriction (PR+CR) does not fit the experimental data, resulting in a granular compact with a very low resistivity. The presence of tungsten oxides, with the thickness estimated from XPS surface analyses (Figure 37), was included in the model considering a resistivity of 50 Ω m [111,112,143]. The resulting values exceed the measured ones by six orders of magnitude, showing that oxides do not influence the electrical contacts among particles.

Figure 32(b) shows how the oxidation is not homogeneous and occurs only on certain WC particles, thus the remaining particles can still form a conductive path in the pellet. Moreover, tungsten oxide and its hydroxides were non-protective in their oxidation nature, forming weak and fragile oxidation products [135]. One can hypothesize the breakage of the oxide layer during the pellet pre-compaction at 350 MPa (Figure 29(a)). The effect of the incorporation of a 14 Å and 27 Å thick carbon nanolayer, with a resistivity of $4x10^{-5}$Ω m [144], in the ECR model (Eq. 21), as estimated from the XPS analyses of ox-WC and pure-WC powders Eq. 23 is shown in Figure 41. The incorporation of the carbon layer in the ECR model perfectly matches the experimental data for both powders; thus, the electrical properties of WC particles in contact are determined by the presence and the nature of the particles surface carbon. According to this finding, the larger experimental resistivity of the pure-WC (Figure 41(b)) with respect to ox-WC (Figure 41(a)) can be explained for by the higher overall carbon content, as detected by thermal analyses (Table 5), by XPS (Figure 37) and by HRTEM (Figure 40).
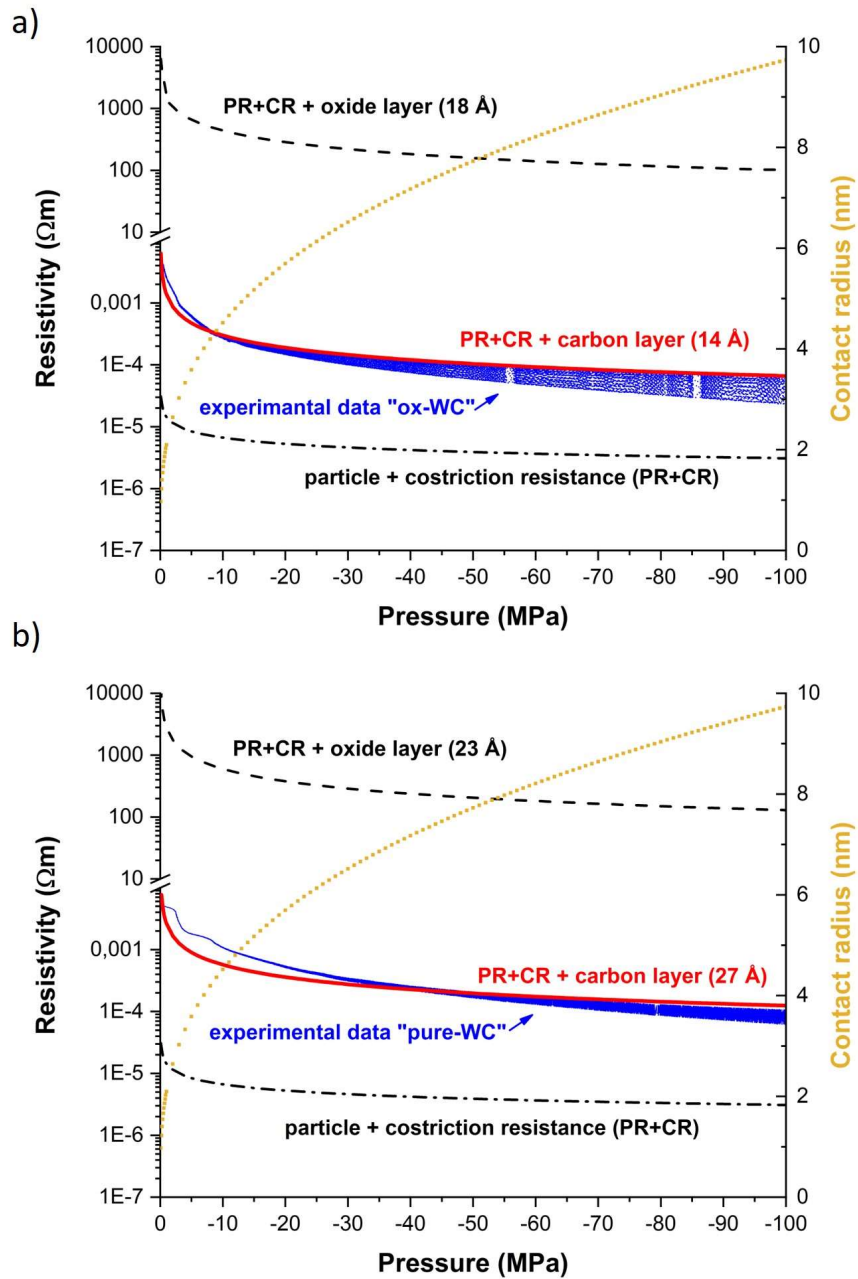
Figure 41 Electrical resistivity of green pellets produced with "ox-WC" (a) and "pure-WC" (b) powder, measured with the setup of Figure 29(b). The contact radius among particles Eq. 20 and the resistivity evaluated with the ECR model Eq. 21 as a function of the applied pressure are also shown.

The fit between the model and the measured green resistivity is maintained for all applied pressures, from 4 to 100 MPa. This suggests the retention of the carbon layer at the high pressures of the test, hence surface carbon influence the electrical properties of the particles in contact up to 100 MPa of pressure. This fact further demonstrates a strong chemical interaction between the layer and the tungsten carbide lattice, supporting the hypothesis of Warren et al. [111] on the rearrangement of surface carbon atoms which form covalent bonds with the carbons in the WC lattice. The shape of the resistivity curve vs. pressure is connected to the evolution of the contact radius (Figure 31(b)), which increases sharp with the applied load and determine a noticeable resistivity drop between 0 and 4 nm.

Effect of W oxides during the ERFS process

Both powders can be consolidated up to very high density (95+%) during the ERFS process, as showed by the microstructures of Figure 42 (a) and (b) only small pores remains in the sintered products. Tungsten oxides, as present in the ox-WC powder, react with the carbon content in the WC lattice, at the high temperature of sintering, promoting a decarburization phenomenon [70]. Indeed, the initial oxide content of about 5 wt%, as detected by XRD (Figure 34) for ox-WC, will generate sintered bodies formed by 37 vol% of W_2C. Decarburization still occurs during the ERFS process also for the pure-WC since it operates in open air condition. Although, in this case, a much smaller portion of lattice carbon is lost at high temperature of sintering leading to the formation of about 5 vol% of a carbon deficient phase denoted as WC_{1-x}, which is characterized by a cubic crystalline system.

Role of the carbon layer on the activation of flash sintering in pure WC

As previously reported, the flash event in pure WC is activated by a thermal runaway of Joule heating, triggered by the evolution of the powder compact resistivity with temperature [117]. During such event,

the electrical power dissipated in the WC green body increases exponentially and determines an almost instantaneous densification. The electrical power evolution during the ERFS process is reported in Figure 43(a) for the powders tested in this work, and the occurrence of a power surge indicates that an identical phenomenon occurs in the two powders' compacts. The resistivity of both powders decreases by several orders of magnitude upon the application of the current during the first 10 s of the process, this indicating the same negative dependence of green resistivity with temperature.
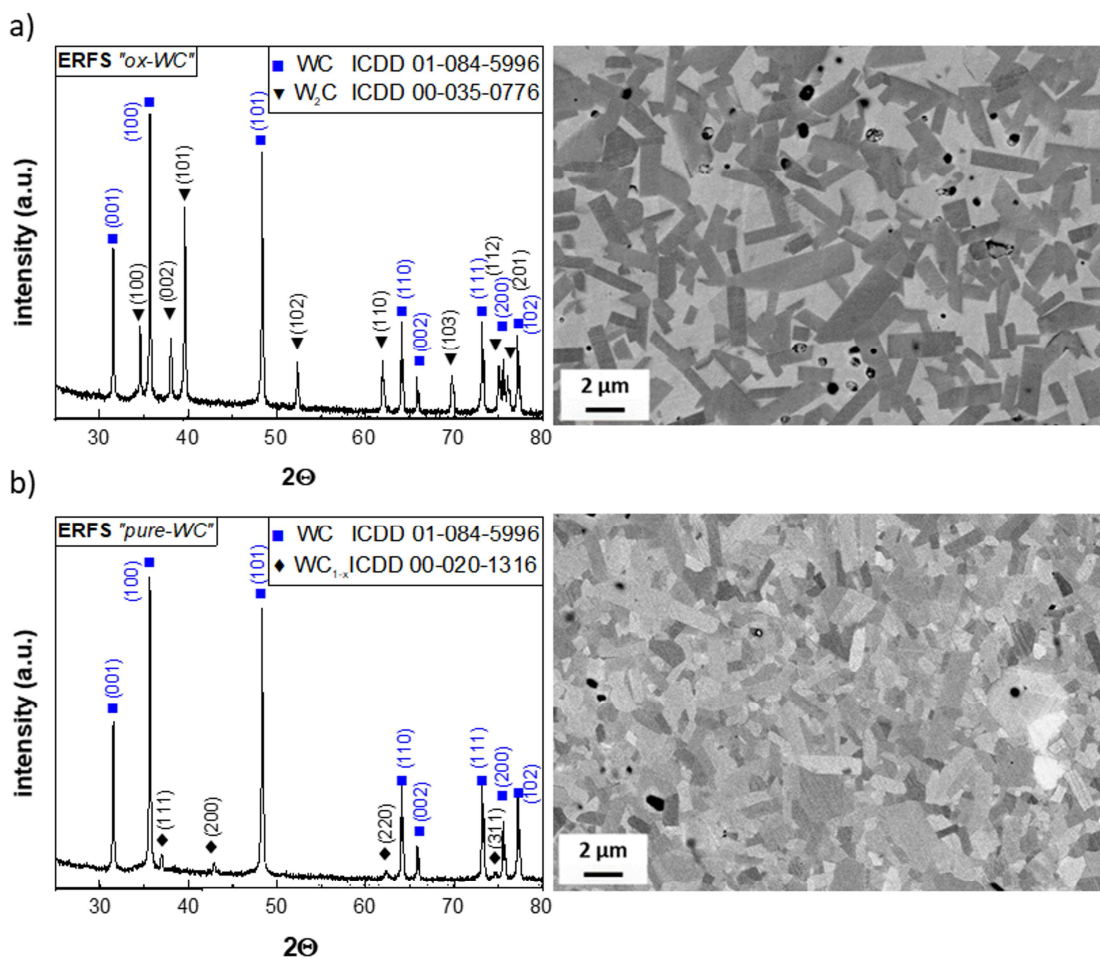
Figure 42 XRD spectrum and corresponding back-scattered SEM micrographs of samples sintered by ERFS using ox-WC (a) and pure-WC (b) powder.

Figure 43(b) clearly shows how the powder characterized by a thicker carbon layer, pure-WC, possesses an initial resistivity of $1.4x10^{-3}$ Ωm, almost on order of magnitude higher to the ox-WC ($4.3x10^{-4}$ Ω m). The higher initial resistivity measured during ERFS agrees also with the experimental data and with the ECR model of Figure 41(b), in which it increases in the presence of a larger amount of surface carbon.

.
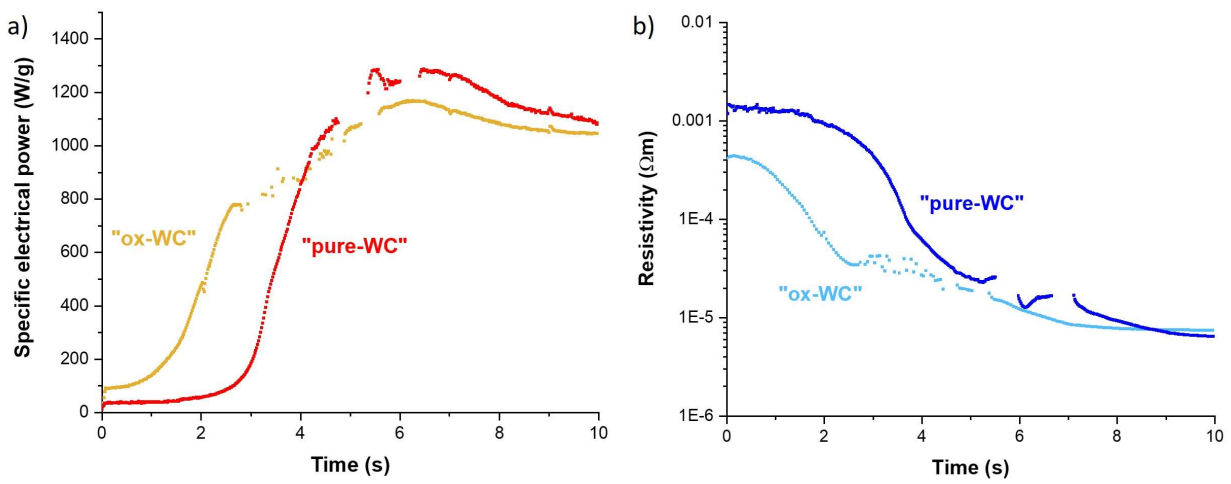
Figure 43 Evolution of WC pellet resistivity (a) and of dissipated electrical power (b) during the ERFS process.

The more abundant surface carbon in pure-WC influences its flash behaviour: since the initial green resistivity is higher, more time is required to trigger the thermal runaway phenomenon (incubation time), thus postponing the occurrence of the power surge (Figure 43(a)). Since the ERFS process operates at an initial constant voltage, a more resistive green material lowers the initial power dissipated by the Joule heating effect and, therefore, longer time is required to reach a temperature which activates the runaway event.

In summary, the flash event can be activated in WC powders regardless of the presence of oxides and Figure 41 suggests that W oxides do not contribute at all to the electrical properties of WC granular compacts. Conversely, the electrical properties of WC particles in contact are affected by an ultra-thin

carbon layer, which acts as a resistive layer since bulk WC is a material with a very high conductivity. In the absence of this layer, the resistivity developed for a green compact can be estimated from Figure 41 to be about 10^{-5} Ω m. A value likely to be too close to the bulk resistivity (10^{-7} Ω m) to activate a thermal runaway phenomenon. This consideration is also supported by the evolution of the resistivity during flash sintering (Figure 43(b)), where values close to 10^{-5} Ω m are reached when the flash event stops by itself. Thermal runaway is a fundamental phenomenon in the flash sintering of ceramics, and its activation requires a material resistivity that decreases by several orders of magnitude with temperature [50]. In this framework, the carbon nanolayer grants both characteristics to the WC green compacts: (i) it increases the resistivity between particles to about 10^{-3} Ω m, a value five orders of magnitude higher than that of the bulk (10^{-7} Ω m) and (ii) it allows the material to have a transitory negative dependence of its resistivity with temperature. The latter is connected to the data, previously reported, regarding the evolution of the WC green resistivity with temperature [117]. It was demonstrated that its resistivity decreases with temperature, even in the absence of an electric current. A large drop was measured between 600 – 900°C, a temperature range well below those suitable to activate sintering mechanisms in WC. This was attributed to the chemical reaction of surface contaminants, which decreases the electrical resistance between the particles after being degraded.

Based on the experimental data acquired in the present investigation and the data presented in [117,118], one can propose the following sequence of events taking place during the flash sintering of WC:

1) Initially, the powder is present in the form of a pre-compressed pellet within a ceramic insulated die (Figure 30(b)), with an initial resistivity that depends on the applied pressure (Figure 41).

2) The application of a limited pressure during sintering, e.g., 4 MPa as in Figure 30(b), will guarantee the retention of a high resistivity at the particles' contact points (Figure 41) associated with the constriction resistance effect and the resistive carbon layer.

3) Soon after the application of the current, a very high temperature is very probably reached at the particles' contacts due to the concentration of the current in those small areas.

4) It is hypothesized that the heat generated during the rapid heating of the powder compact [117] will promote the degradation of surface carbon, since the process operates in open air. According to Figure 41 the absence of the carbon nanolayer will result in a much lower overall resistivity, this being also observed experimentally during the ERFS test (Figure 43(a)) and previous results [117].

5) After the removal of surface carbon, clean WC particles are found directly in contact. The high temperature generated in the ERFS process [117] will promote the activation of surface diffusion and the formation of particle-particle necks. This will inevitably increase the particle contact areas, reducing the constriction resistance contribution (Eq. 10) to the resistivity.

6) As the temperature increases further, two opposite effects on the pellet resistivity remain active: the native PTC behaviour of WC and the effect of porosity, which has a marginal role on the electrical properties [117].

The avalanche reduction in green resistivity is thus limited and will advance only to a certain degree. When the resistivity inverts its dependence with temperature, passing from NTC to PTC character, the thermal runaway phenomenon stops and so does the flash event.

In conclusion, the most significant role on this transitory thermal runaway event is given by the surface nanolayer of carbon, since the drop in green resistivity from 10^{-3} Ω m to 10^{-5} Ω m, the same that takes place during the flash event of Figure 43, was registered before the onset of sintering and therefore, before the decrease in porosity and in particle-particle neck formation [117].

2.2.5 Conclusions

WC nanopowders are covered by an ultrathin carbon layer, with a thickness evaluated from XPS analyses, and directly observed by HRTEM, of about 1–2 nm. The in-situ XPS sputtering process separates two components out of the C 1s C-C peak: (i) adventitious carbon, which can be easily removed by the ion cleaning, and (ii) a carbon layer firmly bonded to the WC substrate. This carbon species differs from the conventional adventitious carbon and is situated at 284.6-284.7 eV instead of 285 eV. Such surface carbon can not removed during intense etching procedure, thus pointing out chemical affinity and strong bonding with the WC lattice. The presence of said surface carbon layer accounts for the measured high electrical resistivity of green compacts and its dependance on the applied pressure, thus promoting the activation of flash sintering conditions.

A flash event can be successfully activated in pellets produced by using different WC nanopowders regardless the presence of initial surface oxides and high density (95+%) materials can be produced in very short time (10 s).

2.3 Flash sintering in metallic ceramics: finite element analysis of thermal runaway in tungsten carbide green bodies

Isacco Mazo[#], Barbara Palmieri [ξ], Alfonso Martone [§], Michele Giordano [ξ], Vincenzo M. Sglavo[#‡]

Department of Industrial Engineering, University of Trento, via Sommarive 9, Trento, Italy

ξ Institute for Polymers, Composites and Biomaterials, National Research Council of Italy (CNR) P. le E. Fermi, Portici (NA), Italy

‡ INSTM, National Interuniversity Consortium of Materials Science and Technology, Trento Research Unit, Via G. Giusti 9, 50123 Firenze, Italy

ABSTRACT

Flash sintering is a powerful tool for the ultrarapid consolidation of green ceramic compacts, although its activation mechanisms in electrically conductive PTC (Positive Temperature Coefficient for resistivity) materials' is poorly understood. It was argued that a flash event can be initiated and sustained for a transitory period in certain PTC ceramics because of an initial negative dependence of the green material resistivity with temperature. The thermal runaway phenomenon and its activation conditions on tungsten carbide (WC) green bodies are investigated in the present work by numerical simulations using finite element methods (FEM). The flash event is recreated and studied within the COMSOL Multiphysics software at the macroscale, i.e., considering the flash as an electrical power surge driven by an increasing sample's conductivity. During the flash, very high temperatures in the range of 1800-2000ºC can be reached in the WC green sample in a few seconds. The accurate numerical simulation of

such event results in heating rates exceeding 1000ºC/s, this being a condition that theoretically brings a powder compact at temperatures high enough to accelerate and prioritize sintering densifying mechanisms over non-densifying ones. It is therefore shown that the sample's regions where the maximum sintering temperature is reached more slowly, because of thermal contacts with the electrodes, remain highly porous at the end of the process.

2.3.1 Introduction

Flash sintering (FS) allows a remarkable reduction of temperature and especially time required to consolidate a vast group of ceramic materials. When a green sample is exposed to the right combination of electric field and furnace temperature, an ultrafast diffusion phenomenon allows densification to take place in few seconds. This very quick nature is connected to the abrupt increase of conductivity in the green ceramic body internally subjected to intense Joule heating. For this reason, the flash sintering phenomenon has been primarily attributed to the thermal runaway of the ceramic's electric resistivity [145]. Theoretically, this condition hinders the applicability of said technology to materials, like metals, which possess positive temperature coefficient (PTC) for resistivity or, in other words, when the electrical conductivity decreases with temperature. In addition, conductivity variation with temperature in PTC materials is also weak to allow a burst in the electrical power dissipation and consequently induce a flash event [49].

Very few works reported the effects of an electric current applied to PTC green samples, in "flash sintering" configuration to allow the current to interact exclusively with the powdered material. Lagos et al. [146] and Montes et al. [147] implemented an electric-current assisted sintering (ECAS) process on metals (Fe) and hard-metals (WC-Co), forcing very high currents (4-10 kA) through the green materials. Mei et al. [148] sintered a silver paste under a high direct current of 6 kA by similar ECAS process. Very

high current densities applied to low melting point materials favour a liquid phase which greatly boosts the diffusion during sintering. These previous works showed remarkable short-term sintering (1-2 s) but did not discuss any relation between the accelerated sintering and the evolution of the material resistivity. In a more conventional FS experiment, Al particles were partially consolidated at high electric fields (175-330 V/cm), during a transition of the material conductivity, probably due to the presence of an oxide (Al_2O_3) film [149].

Only recently, pure WC powders were demonstrated to densify in a few seconds by using ECAS/FS route, the green sample being placed under a limited pressure between two electrodes [117,118]. A similar flash sintering setup was implemented for the consolidation of yttria-stabilized zirconia cylindrical samples [150]. In WC, a transition in the material conductivity was registered under the application of low voltages (3-4 V) and moderate currents (1000-2000 A), this generating exceptional heating and sintering rates. The absence of any liquid phase in pure WC, the burst in the dissipated electrical power and its ultrafast densification demonstrate how a thermal runaway can be responsible for the accelerated sintering in a PTC material [117]. It was argued that such a phenomenon is related to the dependence of the green material's resistivity on temperature, it being negative (NTC) rather than positive (PTC) up to a certain temperature.

The present work aims at studying by numerical simulation using finite element methods (FEM) the relationship between the material electrical properties and the possibility of activating a thermal runaway phenomenon in WC green bodies. An electrical-thermal simulation is carried out to analyse the temperature evolution during the current application and the physical conditions, if any, for the thermal runaway / flash onset in a material (WC) with metallic-like electrical behaviour. The simulation results are then compared and verified with the experimental results obtained from flash sintering tests carried out using WC nanopowders.

2.3.2 Materials and Methods

The sintering apparatus implemented for the electrical resistance flash sintering (ERFS) experiments (*Figure 44*, a) was modelled into a 3D object by CAD software (*Figure 44*, b) and imported into the simulation environment of COMSOL Multiphysics ver. 5.6. The (ERFS) apparatus consists of two cylindrical molybdenum electrodes placed in contact with the green sample within an insulating cylindrical zirconia die. The molybdenum elements are connected to an external power supply (TECNA® Item 3484) through thick copper electrodes. The entire system is mounted on a mechanical testing machine which serves as a servo-hydraulic actuator, thus allowing to control the axial displacement of the two electrodes in contact with the sample under a given pressure. A typical sintering cycle consists in: (i) insertion of the green ceramic sample (disk or cylinder) inside the zirconia die, (ii) placement of the electrodes in contact with the specimen at a specific pressure, (iii) application of the electric current to the sample through the electrodes to induce sintering and (iv) cooling and extraction of the sample from the die. The flash sintering procedure starts when the two electrodes are in contact with the sample and current is turned on and typically finishes 10 s after the application of the current. The entire process takes place in an air. More details can be found in a previous work [117].

In the present work, the flash sintering process was modelled at the macroscopic scale [151] by coupling the equations governing the heat generated by the electric current with those of the heat transfer in solids. Three types of heat losses were considered: (i) conductive heat flux through materials adjacent to the WC sample (zirconia die and molybdenum/copper electrodes), (ii) convective heat flux between the hot surfaces and surrounding air with a heat transfer coefficient h=5 W/(m^{2}K) and (iii) radiative heat flux with the emissivities reported in Table 7. The simulated heat source consists of the Joule heating developed by an electric current flowing between the terminal and the ground, the initial voltage and the

maximum current being the two fundamental variables. The current was controlled by COMSOL with the AC/DC module, which set the electrical boundary conditions to apply either a current or a voltage to the sample. The simulation of a flash event required to model the behaviour of a power supply which must switch dynamically from voltage to current controlled power output during the abrupt increase of the sample conductivity [48,101]. In COMSOL environment, this dynamical switch could be implemented by means of the "Events interface" module [152], which is capable to model a power source driving a system that exhibits variable resistance. A real power supply can provide a constant current up to some peak voltage or a constant voltage up to some peak current. Therefore, the Events interface operated a switch between constant-voltage to constant-current mode when either the maximum voltage or current (I_lim) was reached. The experiment was initially subjected to voltage control, i.e., a certain voltage (V_app) was applied. Then, as the sample's conductivity increased, a limiting current (I_lim) was selected to prevent the uncontrolled generation of heat (Figure 45). The FEM simulation was performed on the 3D CAD model in Figure 44 (b) by using the material properties reported in Table 7. The mesh was built by the COMSOL software using the physics-controlled built-in module, selecting a "Fine-mesh" settings (Figure 49, a). The physical problem was solved in the time-dependent domain, from 0 to 10 s, and the simulated results were stored with an integration time step of 0.1 s. The microstructure of a real WC sample consolidated by the ERFS process at 3.7 V and under a maximum current of 1000 A was investigated by FESEM analysis (ZEISS® Supra40). Cross-sectional images were obtained by cutting a flash sintered WC sample in the direction of the applied current and after subsequent grinding and polishing sequences with diamond pastes down to 1 μm. Different FESEM images were acquired on the cross-section and the microstructure was compared with the gradient of temperature as evaluated from the simulation results.
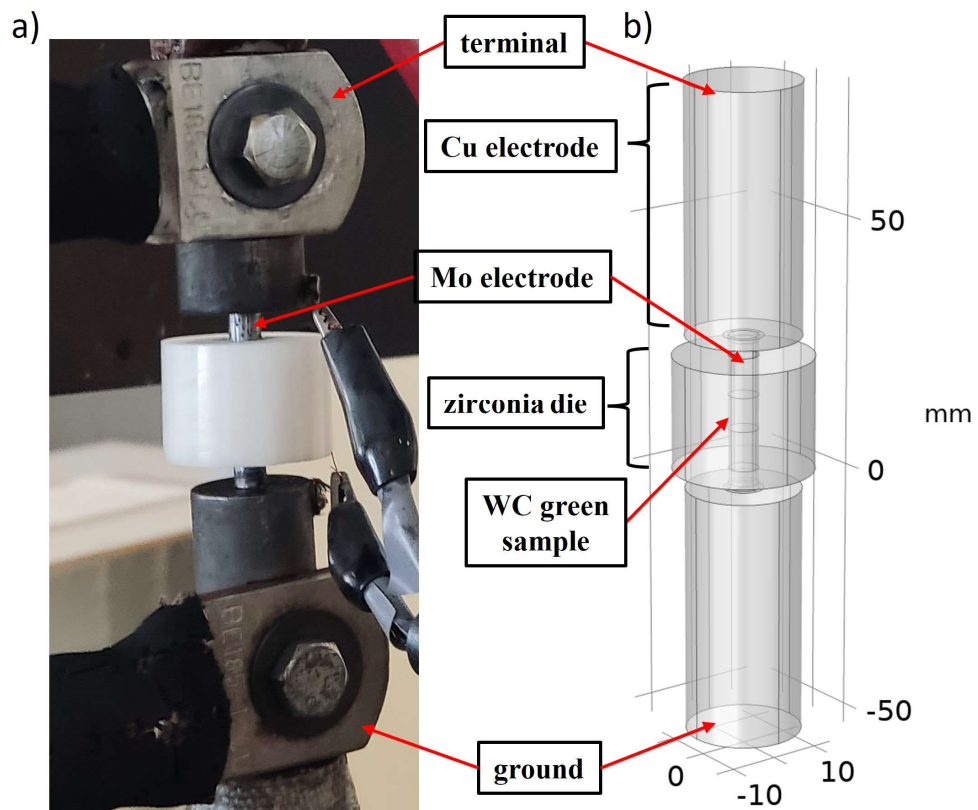
Figure 44 Sintering apparatus for ERFS experiments (a) and its 3D CAD model (b).
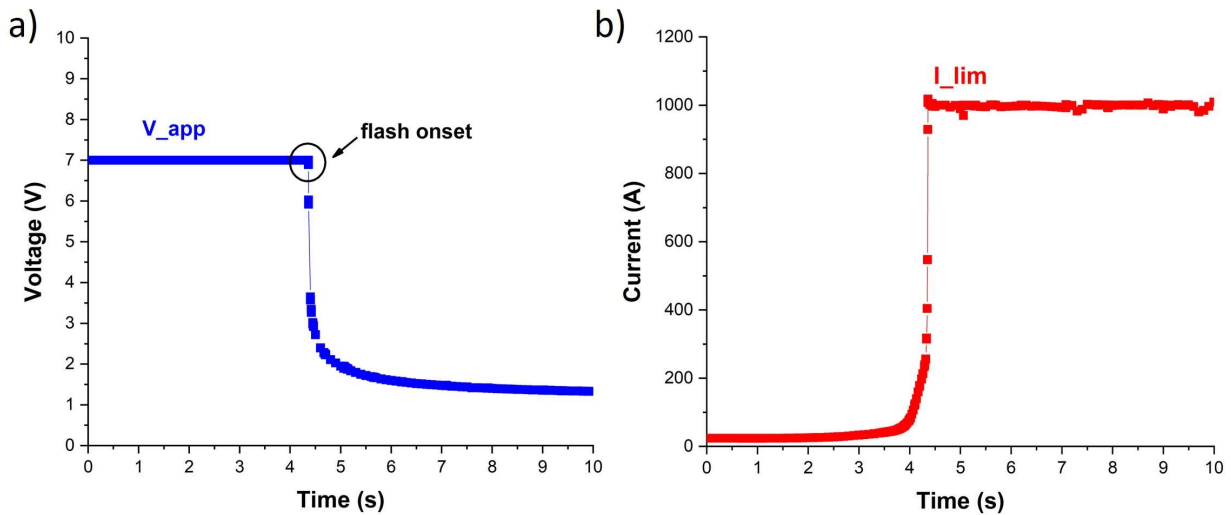
Figure 45 Example of transition from voltage (a) to current (b) controlled sintering regime by using the

COMSOL Events interface (simulation results at 7 V).

Table 7. Materials parameters used in the simulation.

Material	Properties	Value	Reference
Copper (Cu)	Emissivity	0.3	[153]
	Electrical resistivity†	$1.6E^{-8}$ (Ωm) §	[154]
	Thermal conductivity†	400 (W/mK) §	[155], *
	Heat capacity†	388 (J/kgK) §	[155], *
	Density	8700 (kg/m³)	*
Molybdenum (Mo)	Emissivity	0.1	[156]
	Electrical resistivity†	$3.8E^{-8}$ (Ωm) §	[154]
	Thermal conductivity†	140 (W/mK) §	[155], *
	Heat capacity†	220 (J/kgK) §	[155], *
	Density	10200 (kg/m³)	*
Zirconia	Emissivity	0.95	[153]
	Thermal conductivity†	2.5 (W/mK) §	[155], *
	Heat capacity	450 (J/kgK) §	[155], *
	Density	6050 (kg/m³)	*
Tungsten carbide (green)	Electrical resistivity†	$1E^{-3}$ (Ωm) §	[117]
	Thermal conductivity†	110 (W/mK) §	[157][158]
	Heat capacity†	180 (J/kgK) §	[157][158]
	Density	6252 (kg/m³)	[117]

†value dependent on temperature; § value at room temperature (T=20 ºC); * COMSOL 5.6 Materials library

2.3.3 Results and Discussion

Simulation of the flash event

Previous flash sintering experiments on WC green pellets under 3.5-4 V initial voltage and 1000 A limiting current showed almost complete densification of the material [117,118]. Such electrical parameters together with the evolution of the material resistivity (Figure 46) as a function of temperature were used as the starting point for the FEM simulation. Figure 47 shows the different attempts carried out to simulate the flash event for increasing initial voltage (V_app) from 3 V to 7 V.
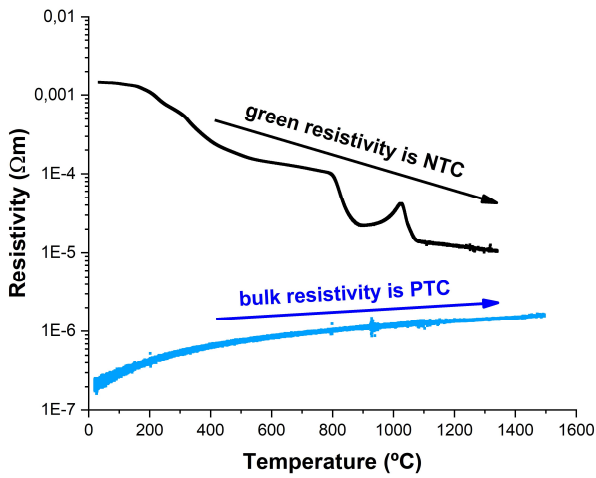
Figure 46 Dependence of the WC electrical resistivity on temperature. Results are reported from [117] *for the material in the green and bulk state.*

The application of an increasing voltage results in an evolution of the material's temperature only between 6.3 V and 7 V (Figure 47, a). For example, under 6.5 V the sample temperature increases slowly for 6 s and then it abruptly reaches about 1600-1700°C (Figure 47, a). Heating occurs at an exceptional rate (around 1000°C/s) and corresponds to a drop in the material resistivity by several orders of magnitude (Figure 47, b). To better understand the nature of the phenomenon generating this ultrafast heating, the energy balance between the heat generated by Joule heating (Figure 49, b) and the heat lost from the WC sample by conduction, convection and radiation (Figure 49, c) is reported in Figure 48. The corresponding values (W_{in} and W_{out}, respectively) are integrated over the volume and the surface domains of the specimen.
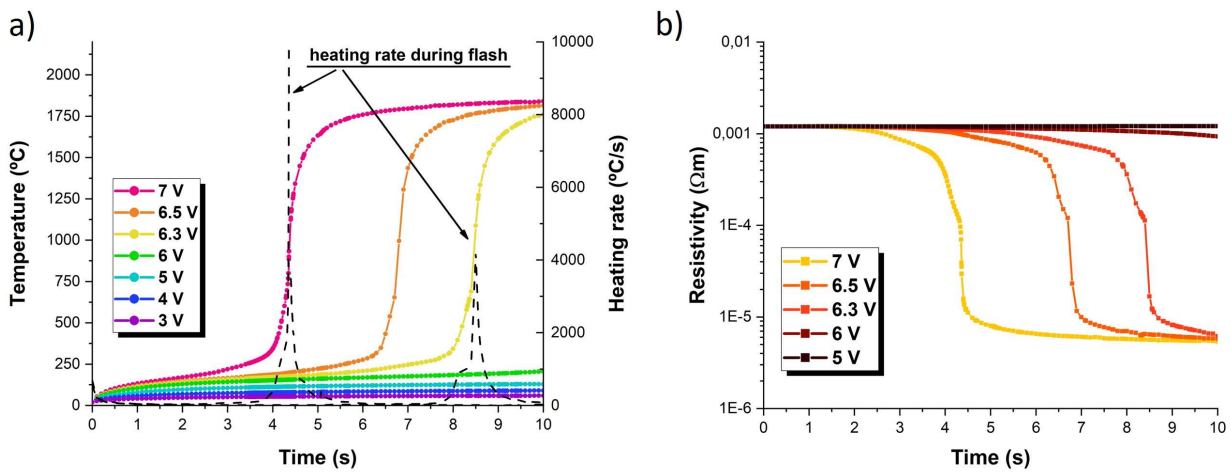
Figure 47 Simulation results of the average temperature and heating rate in the WC pellet under different applied voltage (a) and corresponding material's resistivity evolution (b) as a function of time.

The heat generated by Joule heating, W_{in}, depends almost exclusively on the interaction of the electric current with the specimen (Figure 49, b) since the green body resistivity (Figure 46) is orders of magnitude larger than that of the electrodes (Table 7). The heat losses, W_{out}, are instead dominated by the direct contact of the electrodes with the sample (Figure 49, c). The zirconia die strongly limits the lateral heat losses, this resulting in a large temperature gradient across the ceramic die (Figure 48, c). When the current is supplied to the system, the sample starts to heat up with a limited rate, in a regime where $W_{out}>W_{in}$ (Figure 48, a), i.e., the heat losses from the sample are larger than the power generated by Joule heating. This contributes to increase the temperature in the zirconia die and the molybdenum electrodes. This situation evolves slowly for about 6 s while the sample temperature gradually increases up to about 300ºC where there is the inversion between the two power curves ($W_{out}<W_{in}$). Such temperature (≈300ºC) corresponds more or less to the value at which the WC green resistivity starts to decrease (Figure 46), thus creating the condition for a thermal runaway of Joule heating. During said

event, the heat generated within the sample largely increases because of the higher conductivity (Figure 48, a), up to the point where it cannot be dissipated quickly enough through the electrodes [159]. The condition for the flash onset can be correctly addressed to the intersection of W_{out} and W_{in} curves after 6 s simulation time. In this time frame, the sample temperature increases at a huge rate with respect to the system as shown in Figure 48 (b and c). The temperature continues to increase very quickly up to 1600ºC when the conductivity of the sample is so high to allow the maximum current of 1000 A to flow through the material (Figure 45, b).

At around 9 s and with a sample temperature above 1800ºC, the resistivity reaches a value around 4×10^{-6} Ω m (Figure 47, b), very close to that of bulk tungsten carbide at high temperature (Figure 46). At this condition, the material resistivity does not possess a NTC characteristic anymore and the thermal runaway / flash event spontaneously terminate.
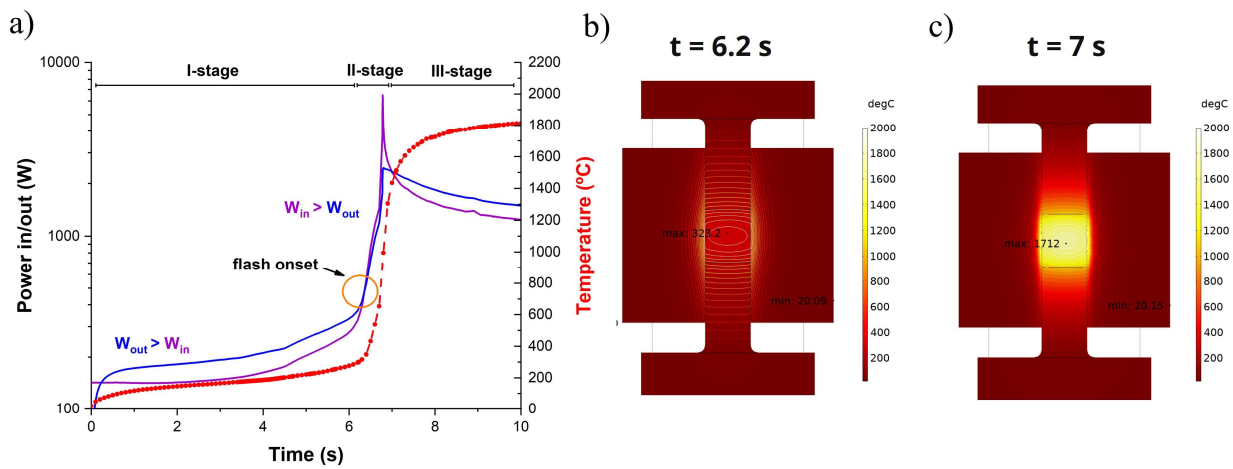
Figure 48 Balance between the power generated by Joule heating, Win, and the dissipated one, Wout.

Temperature distribution within the zirconia die before (b) and after the onset of the flash event (c).

The end of the runaway event at the maximum allowed current of 1000 A slows down the heating process; the system is again characterized by the inversion between W_{out} and W_{in} curves and this results in a slow increase of temperature above 1600ºC. It is worth pointing out the strong similarity between the present flash sintering experiment and those more traditionally performed on free standing ceramic powder green compacts [84,160]. Even if this flash sintering setup operates in open-air conditions and at room temperature, the typical three stages of flash sintering can be identified in Figure 48 (a). During stage I (incubation time) the sample temperature increases slowly due to the limited amount of Joule heating; in stage II (flash onset) an abrupt escalation of the material conductivity occurs, and it allows a surge in the dissipated electric power; during stage III (constant current regime) the maximum current limit is reached and the sintering continues with a moderate temperature increase.
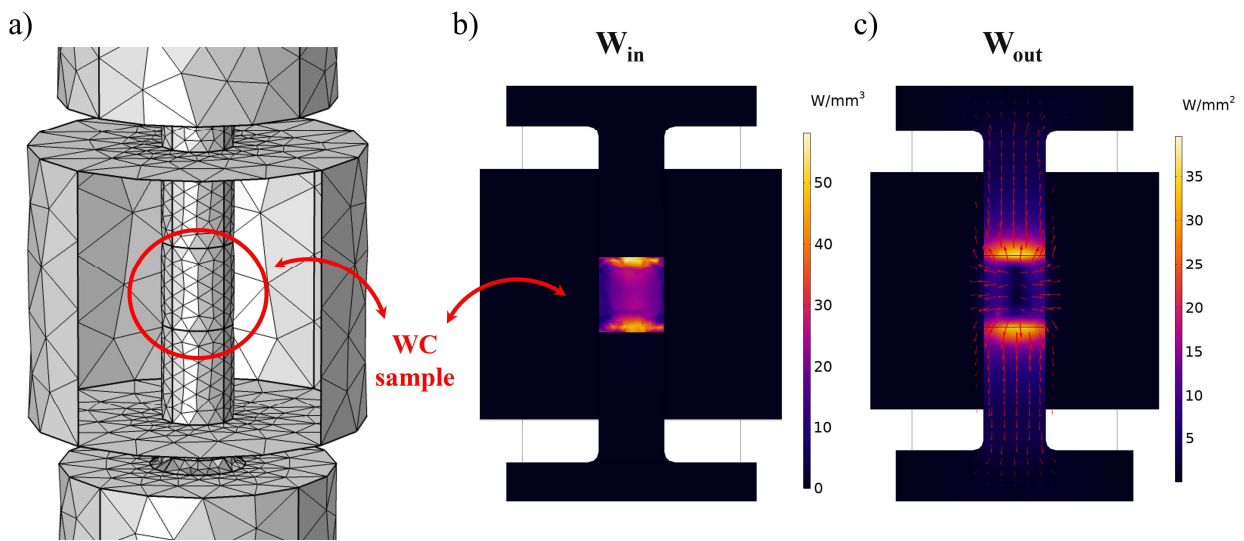
Figure 49 Detail of the mesh within the zirconia insulating die (a) and its cross sections (b, c) showing the simulation results at 6.5 V during the flash event (t=6.8 s). Win = heat generated in the WC sample by Joule heating (b); Wout = heat losses (conduction, convection and radiation) (c).

Flash sintering of WC green samples is achievable in a specific sintering setup, where the heat losses from the ceramic sample are partially limited due to a combination of material properties and high current density supply. The conductive nature of tungsten carbide requires a huge amount of current to sustain the flash phenomenon and to reach the high temperature necessary to sinter the material. As shown in Figure 48 (a), the activation of the flash sintering phenomenon on tungsten carbide opens the possibility to reach very high temperature (1700-1800ºC) with an incredibly fast heating rate (10^3 ºC/s), this resulting in an ultrafast consolidation of the starting powders [117,118]. The applicability of FS to conductive refractory materials and to ultra-high temperature ceramics (UHTC) can offer a valid alternative to more complex FAST/SPS processes, which require complex equipments and far more processing energy [161].

The activation of a thermal runaway event was therefore successfully simulated for a conductive ceramic although a significantly higher voltage (6.3 V) was shown to be required to activate the flash event with respect to the experimental evidence (3.7 V) (Figure 51). This discrepancy will be analysed in detail in the following section, introducing the concept that a powder compact does not behave like a homogeneous material when it is crossed by an electric current. Heat is not generated homogeneously, as simulated by FEM, but it is localised in the region of higher resistance, like particle-particle contacts [151,162].

Two-dimensional disks concept for modelling the particle surface overheating

As shown in Figure 51 and also reported in the temperature evolution plot in Figure 47 (a), the simulated flash event requires a higher initial voltage (6.3 V) to be triggered with respect to the experimental data (3.7 V). The green sample is composed of particles with an average size of about 240 nm, their direct simulation by FEM analysis being almost technically impossible, considering that the specimen contains millions of single elements. Alternatively, the local interaction of the electric current at the particle-particle contacts can be represented by analysing the electrical effect generated at such contact points (Figure 50, d). The particle-particle contacts are characterized by the nanometric size and the surface chemistry of WC nanoparticles. To simplify the problem, a 2D disk model can be developed to study the overheating occurring at the interfaces between the WC particles (Figure 50). The model considers a green pellet consisting of N number of cylindrical disks, where each disk is composed of two regions: an internal one, representing the resistivity developed within a WC particle ($\rho_{particle}$) and an outer one characterized by the increased resistivity at the contacts points ($\rho_{contacts}$).
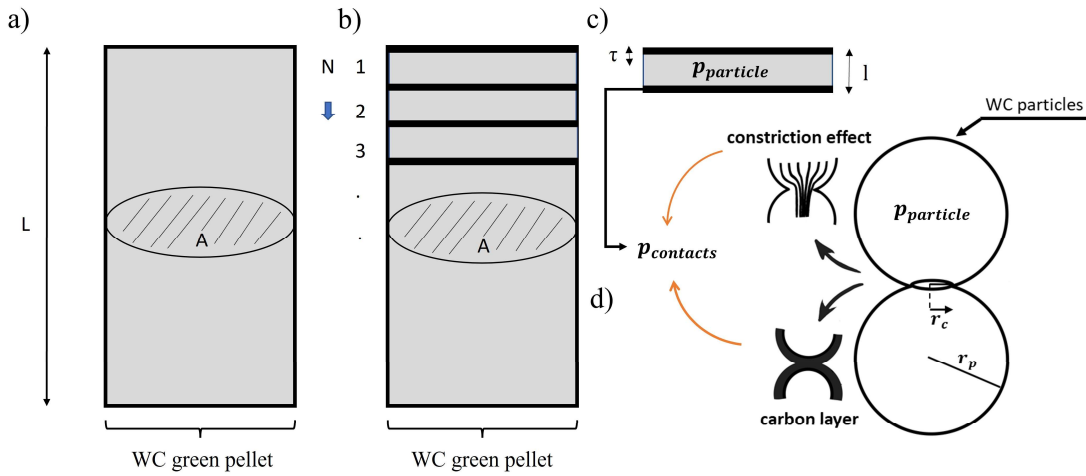
Figure 50 Schematics of the 2D model used for studying the overheating in the WC sample: pellet with homogeneous electrical properties (a) and pellet sectioned in disks with resistive interfaces (b). Every disk is characterized by two regions with low and high resistivity (c) where the former represents the internal resistivity of WC nanoparticles ($\rho_{particle}$) and the latter characterizes the higher resistivity at the contact points ($\rho_{contacts}$)(d).

Every disk contains two layers of higher resistance where the heat is localised upon the current flow. The thickness of these layers (τ) and their resistivity are evaluated in such a way as to simulate the real effect of the localisation of the current between nanometric particles. The effect of heat localisation on the flash onset conditions requires that the average electrical power dissipation (P_{avg}) between the two pellets of Figure 50 (a) and (b) are identical. Therefore:

$$P_{avg}^{hom} = P_{avg}^{disk} \tag{24}$$

where:

$$P_{avg}^{ho} = RI^2 = \rho_{exp}\frac{L}{A}I^2 \tag{25}$$

is the average power dissipation for the homogenous pellet (Figure 50, a) and

$$P_{avg}^{disk} = \sum \rho_{particles} \frac{(l - 2\tau)I^2}{A} + \sum \rho_{contacts} \frac{\tau}{A} I^2 \qquad (26)$$

is the average power dissipation for the pellet sectioned in N disk (Figure 50, b), ρ_{exp} being the experimental resistivity of a green pellet (Figure 46), L the height of the pellet, A the cross-section area of the pellet, l the height of the single disk and τ the thickness of the layer (Figure 50, c). If one considers that that $N = \frac{L}{l}$, Eq. 24 becomes:

$$\rho_{exp} = \frac{N}{L} \left(\rho_{particle}(l - 2\tau) + \rho_{contacts}\tau \right) \qquad (27)$$

which, by simple rearrangement, yields:

$$\tau = \frac{L}{2N} \frac{\left(\rho_{particle} - \rho_{exp} \right)}{\left(\rho_{particle} - \rho_{contacts} \right)} \qquad (28)$$

The particles ($\rho_{particle}$) and the contacts ($\rho_{contacts}$) resistivity can be evaluated according to the theory of small electrical contacts [121], and to the model developed by [163] for the contacts size effect on the flash sintering of ionic nanoparticles. In addition, WC nanoparticles as reported in section 2.2 are natively covered by a carbon nanolayer which influences the electrical contacts and, consequently, the overall resistivity of the green pellet [164]. The overall resistivity of a WC green pellet (ρ_{exp}) can be related to the bulk resistivity of tungsten carbide (ρ_{bulk}) and to the resistivity of surface carbon (ρ_{carbon}) according to the following equation (see Eq. 21 in section 2.2):

$$\rho_{exp} = \rho_{tot,pellet} = \frac{4}{9} \pi \frac{r_{particle}}{r_{contact}} \left(\frac{\rho_{bulk}}{\pi} + \frac{\rho_{bulk}}{4} + \frac{2\rho_{carbon} thickness}{\pi r_{contact}} \right) \qquad (29)$$

where thickness is referred to the depth of the surface carbon layer previously reported in [164]. The overall resistivity of a granular pellet can be split into two parts: (i) the internal contribution of the particles ($\rho_{particles}$):

$$\rho_{particle} = \frac{4}{9}\pi \frac{r_{particle}}{r_{contact}}\left(\frac{\rho_{bulk}}{\pi}\right) \tag{30}$$

and (ii) the contributions of the constriction resistance and that of the surface carbon layer ($\rho_{contact}$):

$$\rho_{contact} = \frac{4}{9}\pi \frac{r_{particle}}{r_{contact}}\left(\frac{\rho_{bulk}}{4} + \frac{2\rho_{carbon}thickness}{\pi r_{contact}}\right) \tag{31}$$

After the evaluation of $\rho_{particles}$ and $\rho_{contact}$, the simulation can be solved according to Eq. 28 for a WC pellet consisting of an arbitrary number of disks (N), N being the input parameter, for an output represented by a specific value of τ. The thickness of the layer (τ), which represents the modification of the local electrical properties at the contact points ($\rho_{contact}$), requires that the average resistivity of the two pellets (Figure 50 (a) and (b)) is the same, because of the imposed condition, $P_{avg}^{hom} = P_{avg}^{disk}$. This means that, by average, the same Joule heating occurs in the two pellets during the flash phenomenon, although in the model composed of N disks more heat is generated at the contact points between the disks with respect to the internal part. This is the same as having a non-homogeneous temperature distribution, in the form of a local overheating during the flash event, thus representing better the real phenomenon occurring between two particles in contact. The accuracy of such model can be refined indefinitely by increasing the parameter N, resulting in a layer thickness (τ) as small as required. Potentially, with adequate computational power, N can be set high enough to reach an interface thickness (τ) similar to the interaction length among the real nanoparticles.

Effect of heat localisation on the flash onset conditions

The simulation results with N equal to 10 (Figure 52, b) show how the 2D disk model successfully simulates a flash event at the same voltage recorded experimentally (Figure 51). The flash event can be triggered at 3.7 V (Figure 51) in the pellet that models the localisation of Joule heating at the interfaces. This means that the pellet with an increased interface resistivity allows to reach, locally, temperatures high enough to have a drop in the material resistivity and to initiate a thermal runaway phenomenon at lower applied voltages. This can be also proven by the temperature evolution plotted in Figure 52 (a) for the two pellets of Figure 52 (b) and (c). The average temperature of the two pellets remains almost the same along the process, the difference regarding the flash event starting time is connected to the effect of the initial voltage on the flash onset time, because a higher initial value shortens the heating incubation time (Figure 47, a).
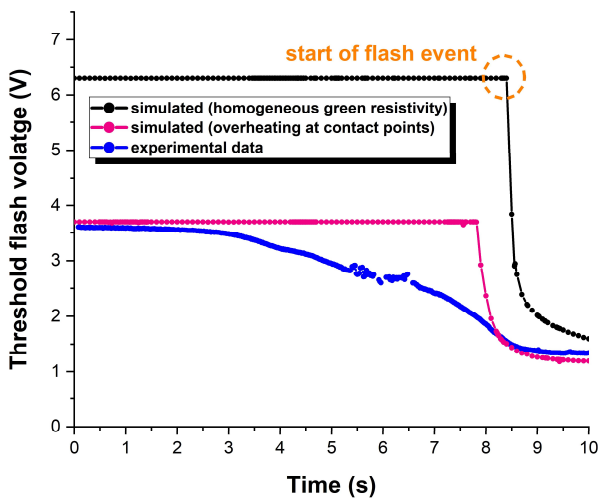
Figure 51 Comparison between experimental and simulation results: threshold flash voltage required for triggering the runaway phenomenon.

Figure 52 shows the important contributions of the overheating at the particle-particle contacts on the flash phenomenon. The rapid temperature increase at the higher resistance regions contributes to

lowering the voltage and so the electrical power consumption for starting the runaway event. This is remarkable since the application of a lower overall electrical power allows a very similar temperature evolution in the material during the test (Figure 52, a).
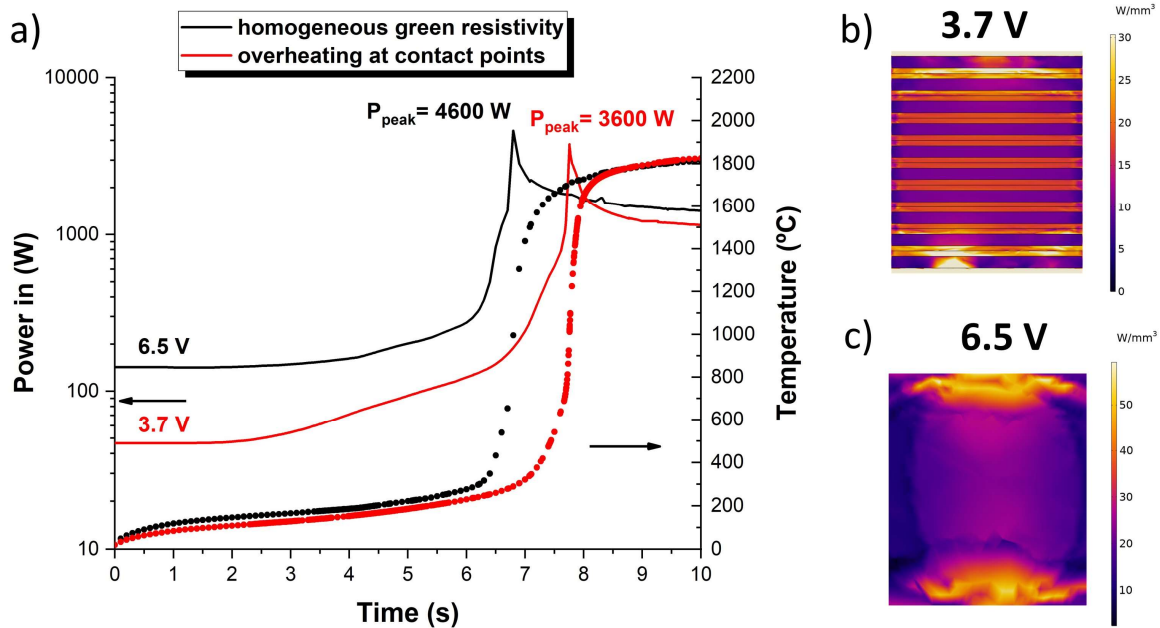
Figure 52 Simulation results of the dissipated electrical power and temperature generated during the flash experiments: (a) Joule heating generated in the WC sample in the case of the 2D disk model (N=10) and (b) for a pellet with homogeneous resistivity (c).

As a proof of concept, the use of the 2D disk model (Figure 50, b) for simulating the particle overheating effect was validated for different N values. Figure 53 shows the results for the power consumption and temperature generated in the WC green pellet for different N values. It is possible to verify how, by increasing the number of disks (N), similar results can be obtained without the appearance of any trend, the position of the power peak (Figure 53, a) not changing with N. This result is in line with the concept of the 2D disk model, where the layer thickness (τ), depending on the parameter N, imposes that the average pellet resistivity equals the average dissipated electrical power (Figure 53, a).
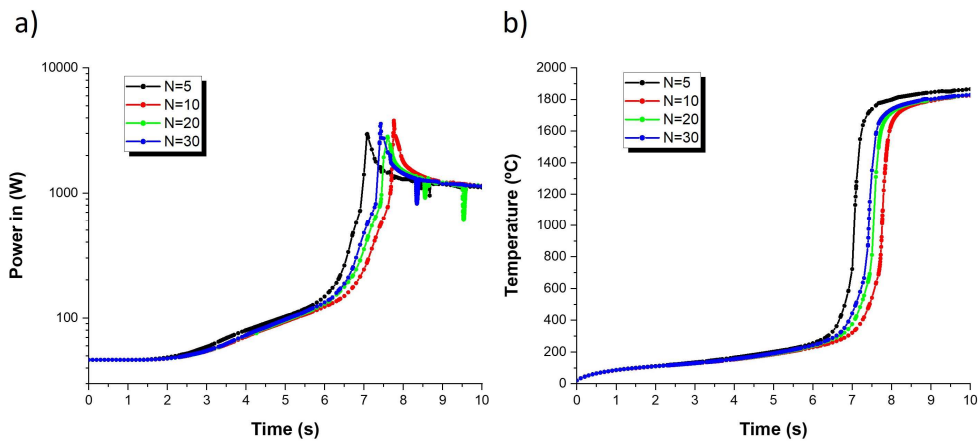
Figure 53 Simulation results showing the electrical power dissipation (a) and the corresponding temperature generated (b) by simulating the particle overheating with different N values.

Temperature distribution effect on WC sample densification

Figure 49 (b) and (c), which show the heat generated and lost in the WC samples, point out an intense heat exchange, during the flash event, in correspondence of the interfaces between the pellet and the electrodes. The high thermal conductivity of molybdenum (Table 7) is indeed the major contribution to the heat loss from the pellet, this generating a strong temperature gradient during the sintering process. To better visualize this gradient and to understand its influence on the densification phenomenon, Figure 54 compares the simulated temperature reached in the pellet cross-section with the microstructure of a real WC sample obtained by flash sintering. As already discussed in previous works, the densification rate of WC is accelerated during the power surge, when the heating rate is maximum (Figure 54, a). It is possible to consider that the temperature distribution achieved during the flash event, hence the sintering stage with maximum densification rate, is related to the final density of the material. Figure 54 (a) and (b) represent exactly the temperature reached within the WC pellet during the power surge, when the heating rate is maximum. The temperature distribution (Figure 54, b), soon after the power peak, is for sure related to the final microstructure (Figure 54, c). The top and bottom portions, in contact with the

molybdenum electrodes, look darker in the digital image taken on the polished cross-section of a sintered pellet (Figure 54, c); according to the FESEM analysis, that region possesses a lower density (around 80%). Conversely, the material is almost completely dense (97-98%) in the central part of the pellet, where the highest temperature is achieved. It is also worth comparing the non-homogenous shrinkage of the sintered pellet in the radial direction with the temperature map in Figure 54 (b). Higher temperatures are reached laterally, due to the insulating zirconia die, and this promotes a greater shrinkage during the densification phenomenon with respect to the radial shrinkage near the top and down sides. This difference results in the peculiar concave lateral shape of the pellet after sintering (Figure 54,c).

Figure 54 points out the strict connection between the temperature field, the thermal runaway event and the corresponding densification achieved during an ERFS experiment. The FEM simulation carried out in this work is proven to be a valid tool for studying the flash sintering phenomenon also in non-conventional sintering apparatus, like that presented in Figure 44. In addition, the agreement between the simulated and the real situation allows one to adopt strategies for improving the flash process. For flash sintering of metallic ceramics, like WC, critical is how the powder is connected to the electrical system. The use of cylindrical metallic electrodes was found to be a great strategy to supply the high current density required for sustaining the flash. On the other side, the use of refractory metals, like Mo, with high thermal conductivity (Table 1), strongly affected the homogeneity of the sintered material in terms of density and microstructure (Figure 54).

From the present work one can understand the necessity to find new solutions to supply electrical energy to the material, limiting the heat losses through the electrodes during the flash process.

In order to solve this problem one could select a refractory material with very high melting point (2000ºC or above), being at the same time good electronic conductor but bad thermal conductor. This is big challenge from the material science point of view because in metals electrons carry both heat and

electrical charge, their electrical and thermal conductivities being therefore coupled as defined by the Wiedemann-Franz law [165,166]. Nevertheless, some peculiar materials violate this law, like VO_2, which shows a separation of the phonons from electronic thermal conductivities. Lee et al. [167] reported an anomalous separation of the heat and charge transport mechanisms in VO_2 near its metal-insulator transition. This material possesses a thermal conductivity of about ~ 0.2 W/m K and an electrical conductivity of ~ 8.0×10^5 S/m, this making it a potential candidate to be used as thermal barrier. Since VO_2 electrical conductivity is not as high as metals, being similar to graphite, small cylindrical inserts with a reduced thickness, could be placed between the green sample and the electrodes to reduce the strong heat losses.
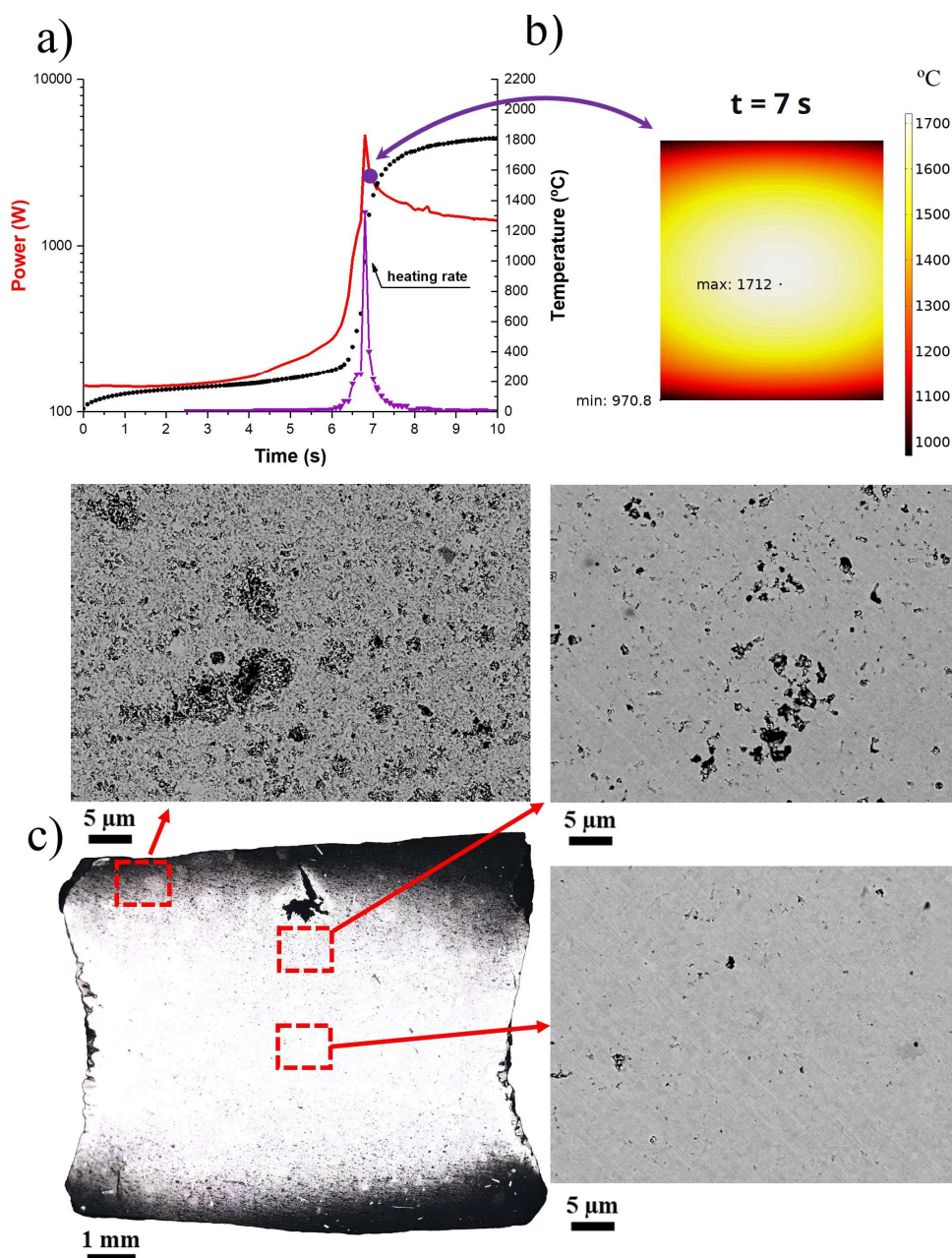
Figure 54 Simulated evolution of dissipated power, temperature and heating rate during flash sintering, measured in the WC sample. The temperature map (b) is shown for a cross-section of a WC pellet at 7 s after the beginning of the simulation, just after the peak in the power dissipation curve (a). The cross-section of a real WC pellet after flash sintering (3.7 V and 1000 A) is shown (c) together with FESEM micrographs taken in three areas (red squares) of different density.

2.3.4 Conclusions

In the present study a coupled Electromagnetic–Heat transfer finite element model was set-up to predict the flash sintering process of conductive ceramics, like WC. The proposed analysis reproduces consistently the physical phenomenon when compared with experimental data.

At the macroscopic scale, the flash event can be represented as a thermal runaway event driven by the evolution of the material's resistivity when the heat generated exceeds the dissipated one. The present work confirms that a thermal runaway event is achievable also for PTC conductive ceramics if one considers that the material in the green state is initially NTC.

More specifically it is possible to conclude that:

- A drop of three orders of magnitude in the resistivity, from 10^{-3} to 10^{-6} Ω m, is sufficient to activate a thermal runaway, this leading to a burst in the temperature up to more than 1800ºC in a few seconds;

- the localisation of the electric current at the nanometric particle-particle contacts has a prominent role on the onset conditions for the flash event; the overheating at the contact regions of increased electrical resistance allows to initiate the runaway event at lower applied voltage;

- the temperature gradient achieved during the electrical power surge is directly related to the homogeneity of the sintered material; the regions in contact with the electrodes experienced a slower heating and, accordingly, are affected by a higher porosity once the sintering process finishes.

Chapter 3

Methods to control the flash-sintered microstructures

Paragraph 3.1 reports how the modification of the flash event, prompted by the sintering conditions of pressure, voltage and time, affects the consolidated materials' microstructure. Specifically, the paragraph investigates the reasons behind the negative effect of pressure on the sintered density as previously reported in 2.1. (Published in Journal of European Ceramic Society, 2022, 42, 2028-2038). The next paragraph 3.2 investigates the possibility to form and stabilize a metastable second phase (WC_{1-x}), during the ERFS process, by selecting WC powders with different oxides contents. (Published in Journal of Material Science, 2023, 58, 1829-1848).

3.1 Effect of pressure on the electrical resistance flash sintering of tungsten carbide

Isacco Mazo[#], Alberto Molinari [#], Vincenzo M. Sglavo[#‡]

\# Department of Industrial Engineering, University of Trento, via Sommarive 9, Trento, Italy

‡ INSTM, National Interuniversity Consortium of Materials Science and Technology, Trento Research Unit, Via G. Giusti 9, 50123 Firenze, Italy

Graphical abstract
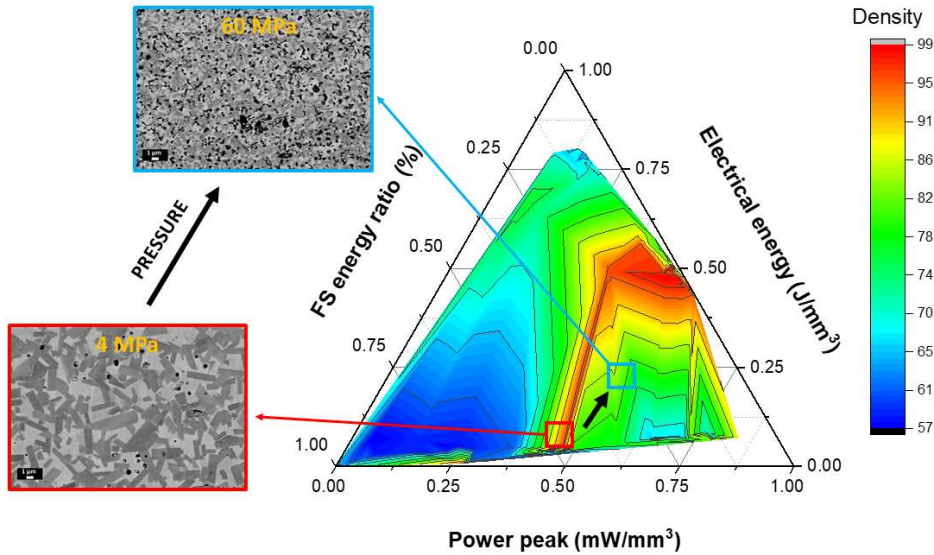
ABSTRACT

The application of external pressure during the Electrical Resistance Flash Sintering of tungsten carbide (WC), a "metallic ceramic" with positive temperature coefficient (PTC) for resistivity, results in a limited densification of the powder. In the present work, the effect of pressure on the ultrafast sintering of WC is analysed in detail. In particular, the application of pressure at different stages of flash sintering is studied by varying independently the processing parameters i.e., voltage, time and pressure. Microstructural characterization performed by FE-SEM and XRD identifies biphasic structures of WC and W_2C, which compositions result almost unchanged for different sintering parameters. Increasing the external load from 4 up to 100 MPa leads to microporous materials, limiting the attainable final density. Pressure is demonstrated to control the flash phenomenon directly by affecting the flash duration and intensity, thus controlling the electrical energy dissipated during the power surge with respect to the overall process.

3.1.1 Introduction

In the context of powder consolidation methods, electric resistance flash sintering (ERFS) can be classified as a field-assisted sintering technique (FAST) with the absence of the pulse discharge step [168]. FAST takes advantage of this rapid discharge to activate the particles surface by removing surface oxides and impurities that hinder the diffusion during sintering. An additional electric resistance sintering (ERS) step is usually required to complete the densification, during which an additional energy for sintering is provided by pressure and Joule heating. The application of ERS process to pure tungsten carbide nanopowders was shown to be characterized by the occurrence of a flash event [117] during which the internally generated Joule heating increases exponentially in the first seconds upon the application of the current. Despite the absence of a pulse discharge step, electrical resistance flash sintering (ERFS) of pure tungsten carbide (WC) revealed an acceleration in the sintering rate during the flash event, promoting an almost instantaneous densification. For this reason, ERFS is characterized by two stages: (i) a flash regime in which an abrupt increase in the current is connected with an almost instantaneous shrinkage and (ii) the ERS regime where the material is Joule heated under a constant current. The setup implemented for the ERFS process shares some similarities with the flash spark plasma sintering (FSPS), where SPS apparatus is used without the usual graphite mould [50]. Uniaxial pressure can be applied during electric current flow to facilitate densification further and maintain electrical contact between the punches and the sample.

It is worth to point out that the usual SPS instruments work at low voltages (10-12 V), this limiting the possibility of testing highly resistive ceramics [105,169]. Francis and Raj (2012) arranged a pressure-assisted flash sintering experimental apparatus equipped with an external furnace and a high voltage power supply [170]. Flash sintering experiments were performed on tetragonal zirconia (3YSZ) samples at different uniaxial stress levels. A higher applied pressure significantly decreased the threshold

temperature for flash sintering, this allowing full densification of 3YSZ at lower furnace temperatures, without directly affecting the sintering rate. The electric field has the same effect on the flash onset temperature and, for this reason, the authors accounted for such behaviour with an innovative electro-chemo-mechanical mechanism where the applied stress induces an electrical potential in the free surface of zirconia [171]. More recently, Chaim (2018) modelled the electrical resistance of a green granular compact to study its influence on flash temperature [120]. The compaction pressure applied during an electrical sintering test affects the contact particle radius, which, at low pressures, determines a green resistivity more than three orders of magnitude higher. Chaim's model agrees with the experimental data of Francis et al.: the flash temperature decreases with an increasing neck-to-particle ratio and hence pressure. Our previous work has shown the same dependence of green resistivity on the applied pressure [117]. Conversely, in the flash sintering of conductive ceramic, such as tungsten carbide (WC), a higher green conductivity, as increased by pressure, seems to affect the overall densification negatively [117]. This discrepancy in the effect of pressure during a flash event suggests a different role of the initial sample conductivity in the activation of the flash event between ceramics with positive temperature coefficient for resistivity (PTC), such as WC, and those with negative temperature coefficient (NTC), like 3YSZ. Pressure was proposed as a possible solution to reduce current localization and hot spot problems in flash sintering of NTC ceramics [172]. Furthermore, its fundamental role in electrical resistance sintering (ERS), hot pressing and spark plasma sintering (SPS) processes is well recognised in the literature [59,63,64,173–177]. Besides that, pressure-assisted flash sintering experiments on WC have revealed a possible connection between pressure and power surge duration and, hence, the flash duration. The present work aims to clarify the effect of applied pressure during the ERFS of pure WC. To separate the effect of an external load on the two different ERFS regimes, the flash and the ERS ones, sintering experiments are performed varying pressure, sintering time and maximum applied voltage independently.

117

3.1.2 Experimental Procedure

Tungsten carbide powder with nominal purity of 99.95%, average particle size around 150-200 nm and crystallite size of 40-70 nm was purchased from Inframat Advanced Materials. Electrical resistance flash sintering (ERFS) experiments were performed on pressed pellets with 1.3 g height, 7.5 mm nominal thickness, 6 mm nominal diameter and relative green density equal to 40%. The samples were pre-compacted within a steel die by uniaxial pressing by a hydraulic press (Specac). Then, the pressed specimen was inserted inside an electrically insulating cylindrical die (φ = 6 mm), made of zirconia, where the two molybdenum electrodes applied a certain pressure and a voltage, simultaneously (Figure 55). The sintering tests were performed in air atmosphere. An AC current was applied directly to the green sample by means of a step down high current transformer (TECNA item 3870). The power supply output was controlled between 30 and 40% of the maximum power of the transformer, this corresponding to an initial applied voltage between 3 V and 4 V. The evolution of electrical parameters in the WC specimen during the test was measured with a multichannel data acquisition system (DAQ NI USB 6211). Voltage (V) and current (A) were sampled simultaneously, thus allowing the evaluation of the dissipated electrical power during the ERFS experiment [117]. Sintering tests were performed at pressure variable from 4 to 100 MPa and sintering times of 10 s and 60 s. Each combination of the processing parameters (voltage, pressure and time) was tested in triplicate to evaluate the repeatability of the experiment.
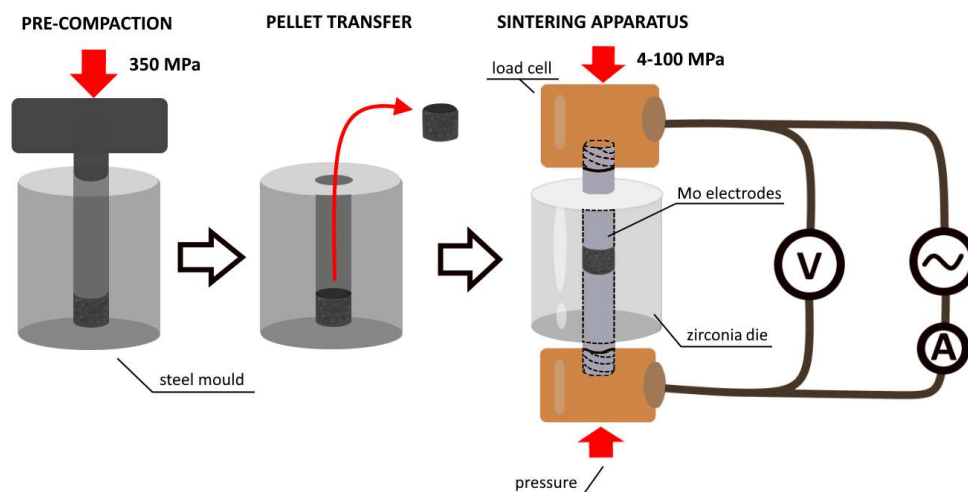
Figure 55 Schematic of the pre-compaction procedure and ERFS setup.

The density of the ERFS sintered pellets was measured by the Archimedes' method (ASTM C373-17) using a digital balance (KERN ALJ 310 4A) with sensitivity of 0.1 mg and distilled water as immersion liquid. The sintered pellets were sectioned in the direction of the applied pressure with a diamond blade and the microstructure was analysed on the obtained cross sections. The samples were mounted in resin and then grinded and polished with diamond abrasives down to 1 μm, reaching a mirror-like surface. The mineralogical composition was determined by X-ray diffraction (XRD) on the polished surface; the diffractometer (Rigaku® IIID MAX) was equipped with a Cu-Kα (λ = 1.5405 Å) X-ray source excited at 40 kV, 30 mA. Peaks identification and quantitative phase analysis from the diffraction pattern were carried out using the Rietveld refinement method using MAUD® software. High-resolution FE-SEM equipped with an angle selective backscattered electron (AS-BSE) detector (Carl Zeiss® SUPRA 40) was used to determine the microstructure (porosity, phase composition and grain size) of the polished samples.

3.1.3 Results and Discussion

The two stages of the ERFS process: FS and ERS regimes

The application of an AC current across the WC green compact generates a rapid increase in the electrical power dissipation concurrent with a steep decrease in resistivity. As shown in Figure 56 the occurrence of a power surge is a feature of the ERFS of pure tungsten carbide [117], it occurring in a considerable interval of pressure and maximum applied voltage. The power dissipation curves follow the same trend in all tests: they increase rapidly up to a maximum value and then decrease slightly towards a plateau when the electrical resistivity reaches a constant value. This power surge separates the ERFS process into two stages, the flash regime (FS) and the electrical resistance sintering regime (ERS).

120
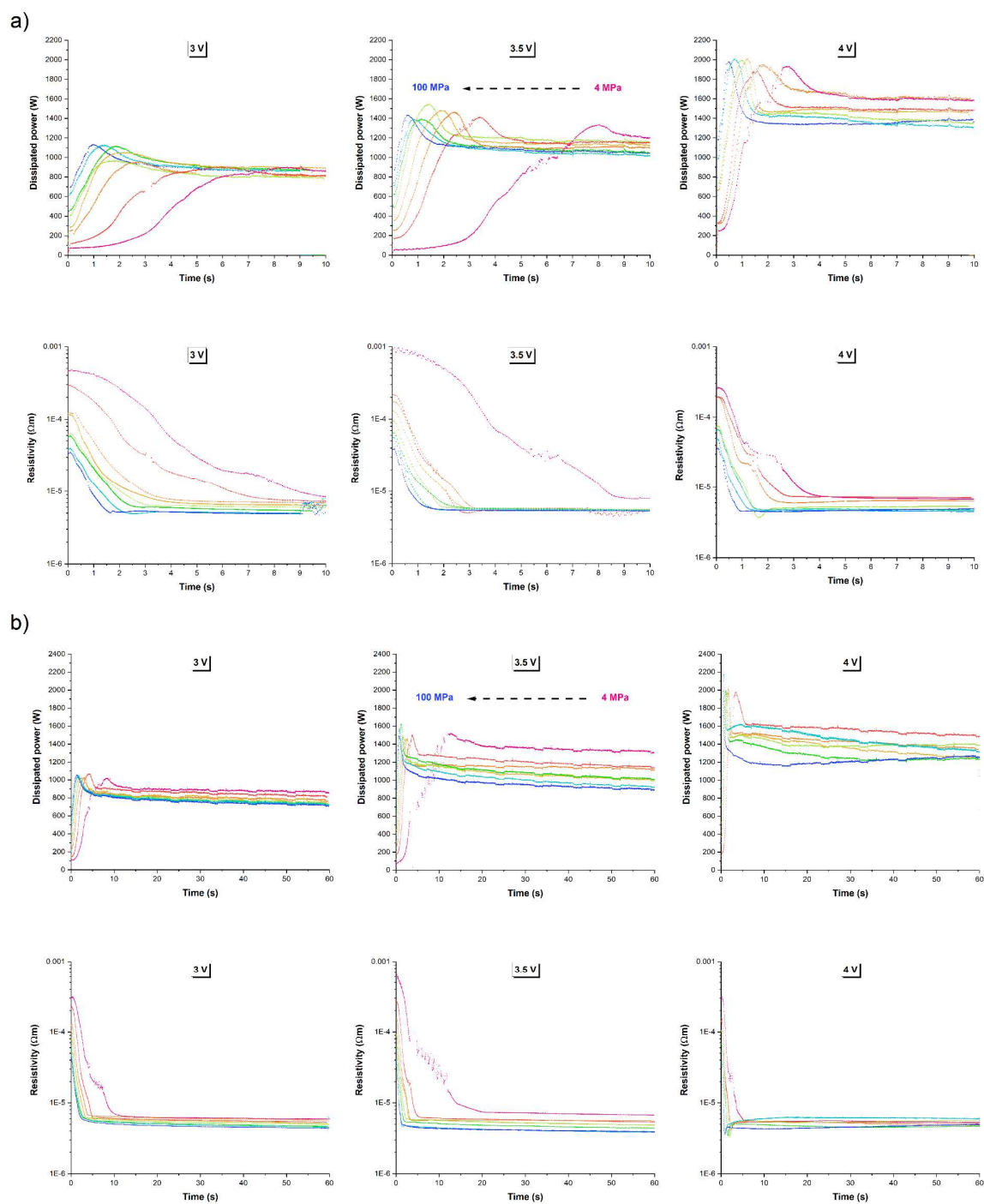
Figure 56 Evolution of dissipated power and resistivity during 10 s (a) and 60 s (b) ERFS of WC pellets under different applied pressure and maximum applied voltage.

The electrical power and the energy involved in the two regimes are summarized in *Figure 57* for different applied voltage and pressure. When the current is applied for longer time, dissipated power and resistivity evolution does not change significantly, while the overall energy dissipated in the ERS regime increases (*Figure 56* and*Figure 57*). During the FS regime, the electrical power peak is clearly affected by the applied pressure and the maximum voltage. A higher voltage increases the current flowing initially through the WC compacts, this resulting in a much higher peak in the power dissipation. Moving from 3 to 4 V, the maximum power reached in the flash event almost doubles, from 1000 up to 2000 W, achieving a value for which resistive heating generates an uncontrolled temperature increase, sometimes causing the local melting of WC (melting temperature 2870°C). The power peak time occurrence is affected by the applied voltage and pressure, the latter having a more pronounced effect. At both sintering times (10 s and 60 s), a higher voltage restricts the temporal occurrence of the power surge; this can be easily observed from data in Figure 56 if the sintering tests at the same pressure are compared.
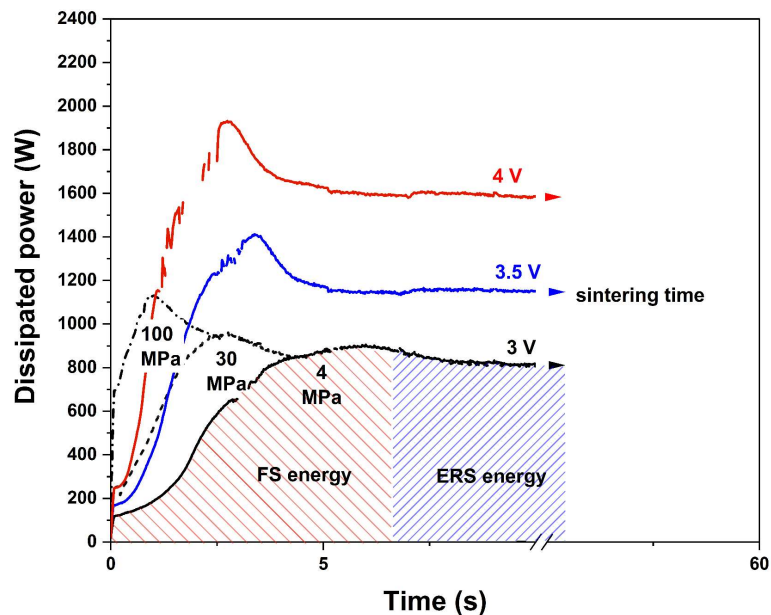
Figure 57 Effect of the input parameters (pressure, time and voltage) on the power and energy dissipated in the two ERFS regimes.

Pressure, green resistivity and power surge intensity

Higher external pressures during the ERFS process decrease the initial resistivity of the WC pellet (Figure 58), the trend being clearly observed in all tests (Figure 56). It is reasonable to explain this resistivity reduction by a better electrical contact among the WC nanoparticles at higher pressures, which increases the overall green's conductivity and allows the flow of larger current in the first instants of the process. It is worth to observe that such conductivity increment is very probably connected to wider contact area among particles subjected to elastic deformation and not to higher green density. The lower pressure used during the sintering tests (4-100 MPa) with respect to the pre-compaction one (350 MPa), can not result in further green density growth (Figure 55). According to this increased green conductivity, the power dissipated when the sintering process starts (at time zero) increases, shifting the power curves' starting point to the top. Therefore, the resistivity reaches the plateau in a shorter time, thus limiting the time at which the material experiences a nonlinear resistivity evolution and, accordingly, reducing the power surge extension. In all tests, the pressure is found to restrict the period for the flash event to occur (Figure 59), thus lowering the amount of electrical energy dissipated during the FS regime with respect to the ERS one (Figure 57 and Figure 60).
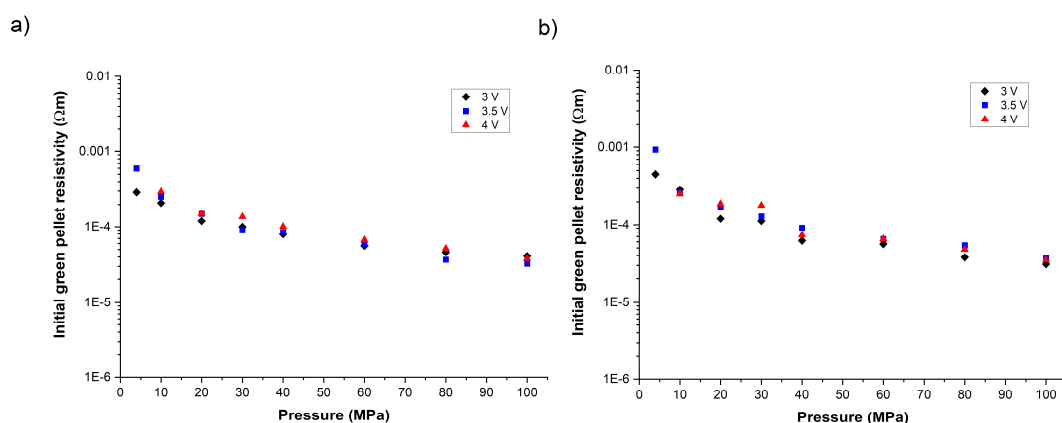
Figure 58 Effect of the applied pressure on the initial resistivity of the green WC pellets for sintering tests of (a) 10 s and (b) 60 s.
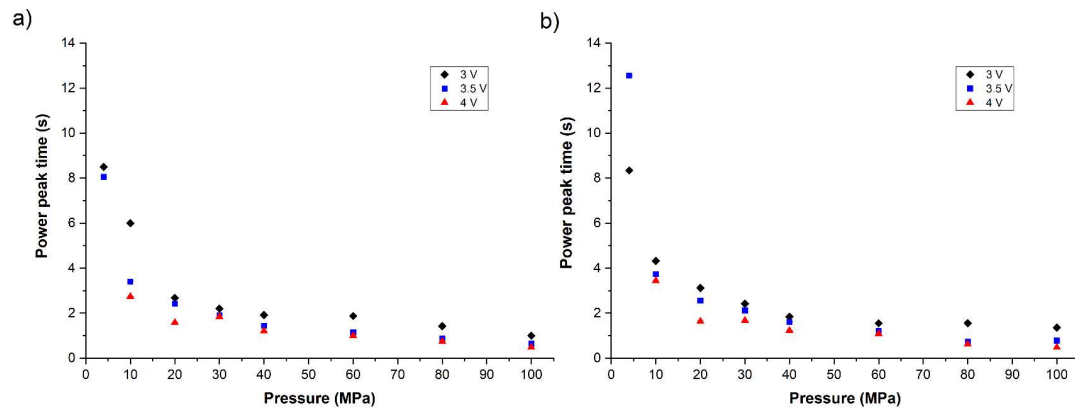
Figure 59 Effect of applied pressure on the time at which the maximum dissipated electrical power is reached for test duration of (a) 10 s and (b) 60 s.
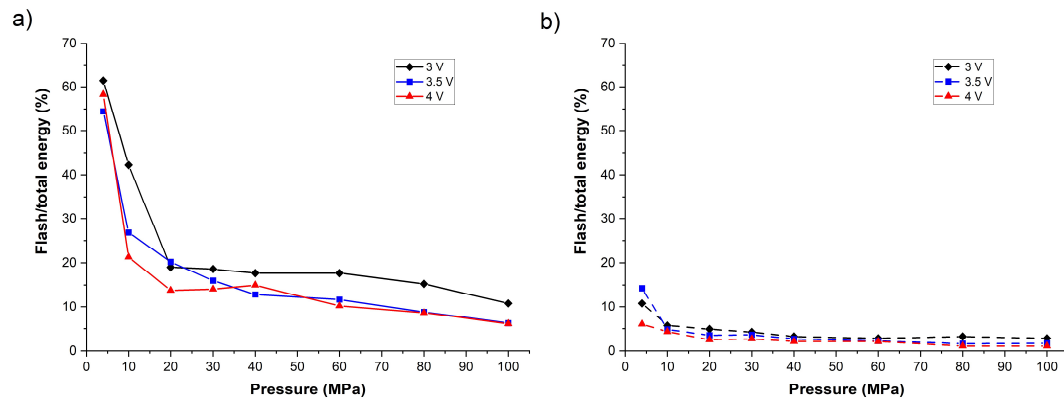
Figure 60 Effect of applied pressure on the ratio of electrical energy dissipated during power surge with respect to the overall process for sintering tests of (a) 10 s and (b) 60 s.

The three tested parameters, i.e., (i) external pressure, (ii) applied voltage and (iii) sintering time have a prominent effect on the final density achieved by the ERFS processed WC (Figure 61). Among them, the most effective for densification is the applied voltage, which allows to reach almost the highest values; indeed, it affects the maximum power peak reached during the flash sintering regime and increases the overall energy available for the densification process (Figure 57). Figure 61 shows that for both 10 s and 60 s duration, the lowest density is recorded at the minimum voltage of 3 V. Quite surprisingly, the

pressure decreases the overall density in almost all tested configurations. The most substantial effect can be observed at the intermediate voltage of 3.5 V where, for 10 s sintering, the final density decreases from around 94% (4 MPa) to 70% (100 MPa). This behaviour disagrees with the expected results since, theoretically, pressure is known to increase the driving force for densification [41]. Some exceptions are observable when high pressure values between 60 and 100 MPa are reached; in such cases, a small benefit of an increased pressure on the final density is shown. Besides that, in all cases the final density achieved at 100 MPa is never greater than that reached at the lowest value of 4 MPa. An exception is found for the highest voltage of 4 V and 60 s sintering when the material densifies up to 95% independently of the used pressure.
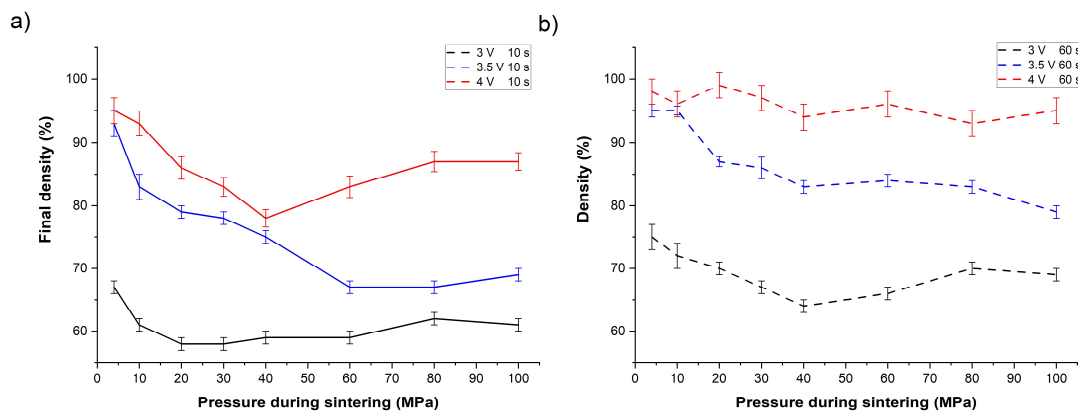
Figure 61 Density measured on the ERFS samples processed under different pressure, voltage and sintering time.

Effect of the sintering parameters on the microstructure

The microstructures obtained for ERFS experiments carried out with different processing parameters are represented in Figure 62, Figure 63 and Figure 64. In most cases, it is possible to observe large darker prismatic grains embedded in a light grey matrix. Accordingly, the XRD analysis performed on the cross section of different samples always resulted in the presence of two well-defined crystalline phases of the W-C system (Figure 65)[178]. One is the hexagonal primary phase of WC (symmetry P-6m2), while the

other one is identified as the trigonal W_2C (P-31m), also known as sub-carbide [179]. W_2C is formed upon sintering due to an insufficient amount of carbon to retain the 1:1 stoichiometric W/C ratio of the parental WC phase this being accounted for either by the presence of oxides in the starting powders or by a rapid oxidation at high temperature [72,180,181]. In this specific case, the ERFS process leads to a biphasic tungsten carbide microstructure, where the darker prismatic grains can be assigned to WC (density 15.63 g/cm^3) and the light grey phase to W_2C according to the larger atomic mass (density 17.1 g/cm^3).
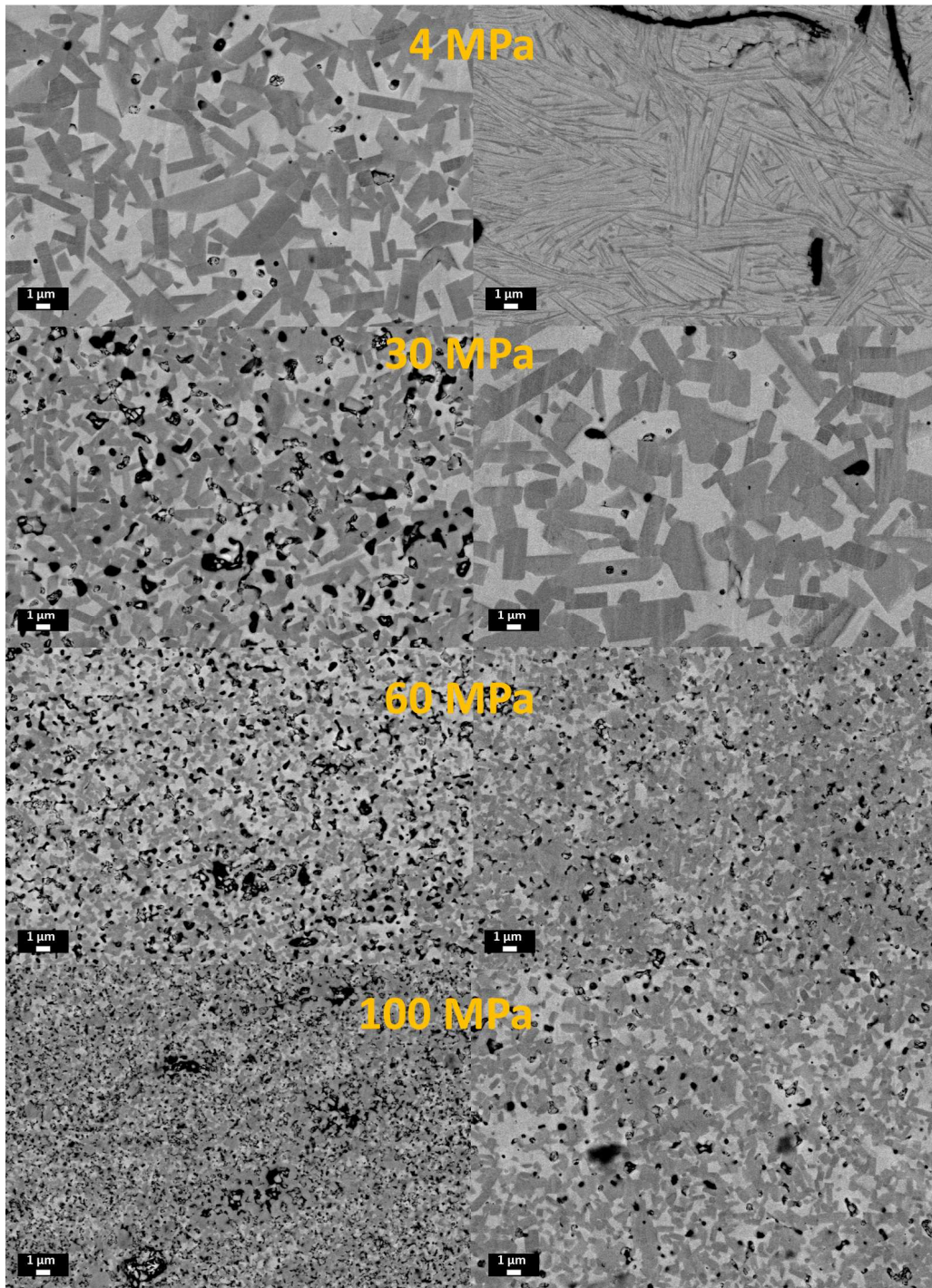
Figure 62 FE-SEM images (BSE mode) taken on polished cross sections of ERFS WC pellets processed under different pressures and voltages with an overall sintering time of 10 s.
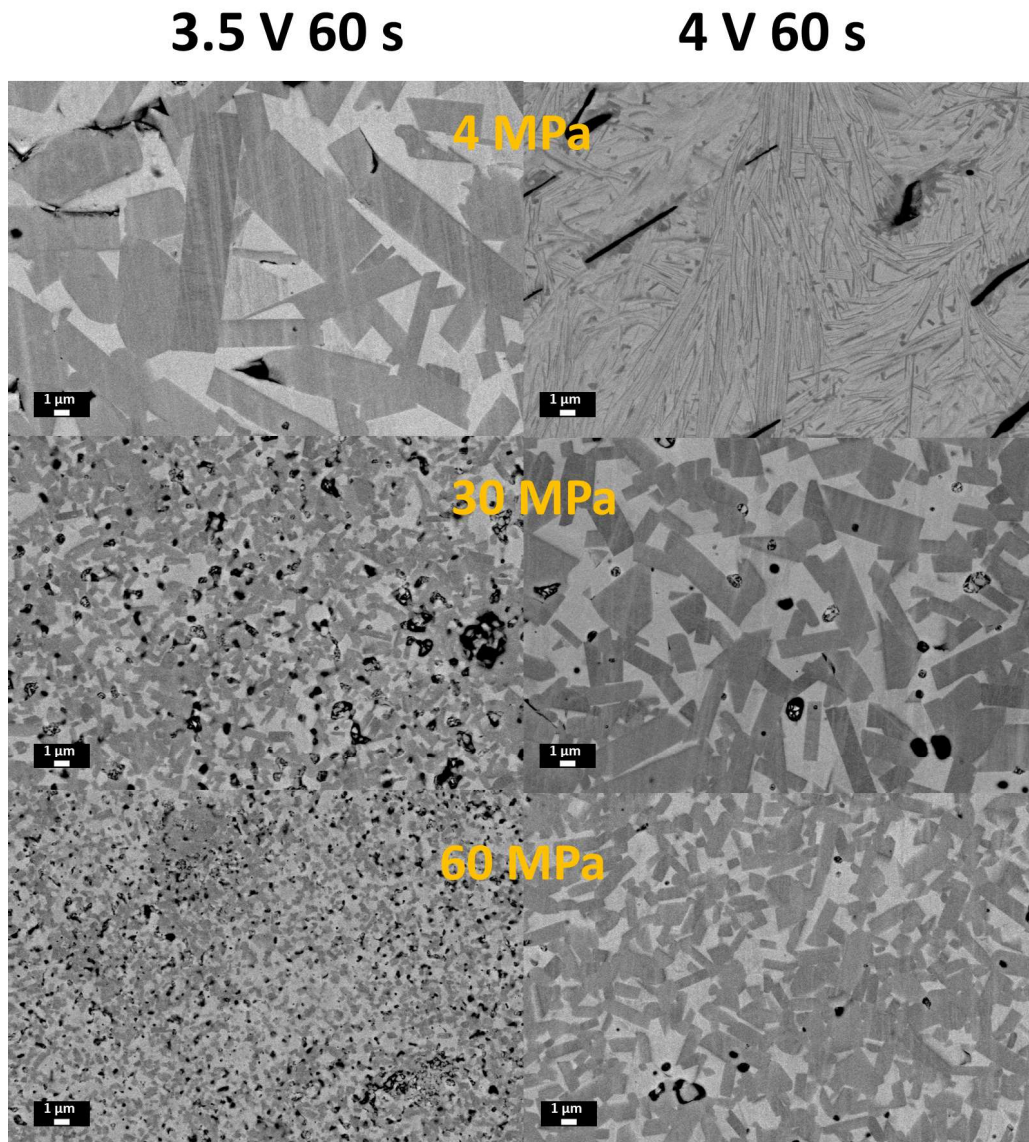
Figure 63 FE-SEM images (BSE mode) taken on polished cross sections of ERFS WC pellets processed under different pressures and voltages with an overall sintering time of 60 s.

The FE-SEM images, as taken on the polished cross section of the pellets, well compare with the density measured by the Archimedes' method. The applied pressure results in a strong decrease of the final density. In the sample sintered under 3.5 V (Fig. 8) the evolution of the microstructure of this biphasic WC material as a function of the external load is very evident. Pressure limits densification during ERFS

and leads to a final microporous material. The retention of a significant fraction of pores, smaller than 1 µm when 100 MPa are applied, greatly reduces grain growth [41]. This trend is typical for all samples sintered for 10 s and for those sintered at 3 and 3.5 V for 60 s. According to Figure 61, high density can be reached in spite of the pressure magnitude when a sufficiently high voltage is applied for a prolonged time, this case being represented in Figure 64 for the material sintered under 4 V for 60 s. Under the maximum tested voltage (4 V) and time (60 s), the pressure is beneficial in reducing the grain size of WC without decreasing the overall density.
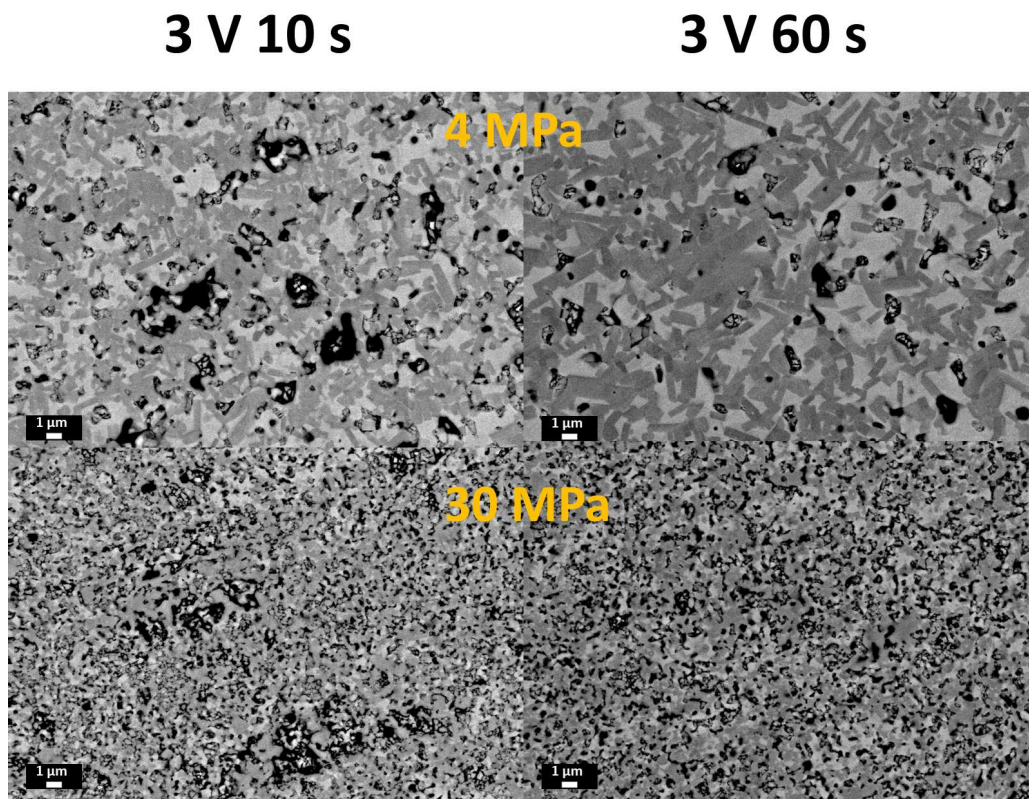
Figure 64 FE-SEM AS-BSE images taken on polished cross sections of ERFS WC pellets processed under different pressures and sintering times with an overall voltage of 3 V.

As introduced before, sintering of WC nanopowders at 4 V generates an enormous amount of electrical energy capable to increase locally the temperature up to the melting point of WC; this was observed in two cases corresponding to the lowest applied pressure (4 MPa) (Figure 62 and Figure 63). In such situations, the microstructure detected by FE-SEM images is completely different with respect to the others: one can observe the presence of larger fraction of W_2C phase (light grey regions) and elongated and very narrow WC grains (darker grey regions). Also, the porosity morphology is different and the microstructure resembles more a solidification structure than that resulting from solid-state sintering of powders. In previous works, Nayak and co-workers pointed out the development of WC/W_2C mixtures with a lamellar/acicular microstructure similar to that discussed just above when tungsten carbide was processed by arc plasma melting [182–185]. The peculiar microstructure originates from a martensitic transformation due to the very fast cooling of WC from the molten state. Similar conditions are very likely reached in the present work because of the very small sample volume which allows an almost immediate cooling. Accordingly, Figure 65 shows the XRD patterns acquired on samples with the two characteristic microstructures. The diffraction pattern of sample processed at 4 V, 4 MPa in 10 s and at 3.5 V, 4 MPa in 10 s (Figure 62) were used as a reference to compare the two microstructures, since very similar patterns were recorded in the other ERFS materials in agreement with the microstructure shown by the FE-SEM micrographs. The two diffraction patterns were successfully refined by the Rietveld method with two crystalline phases, WC and W_2C (corresponding to the ICCD cards No. 01-084-5996 and 00-020-1316). The fitting revealed a large difference in the average phase composition, corresponding to 63 vol% WC and 37 vol% for the biphasic microstructure (3.5 V, 4 MPa, 10 s) and to 46 vol% WC and 54 vol% W_2C for the acicular one (4 V, 4 MPa, 10 s). In the cited paper by Nayak and co-workers, the arc-melting of tungsten carbide resulted in the growth of the sub-carbide phase (W_2C) in favour of a reduction of the hexagonal WC phase. In addition to the difference in phase composition,

Figure 65 also points out a possible preferential orientation of the WC phase in the acicular microstructure. This can be clearly observed by the different intensity of the (100) with respect to the (001) and (101) peaks between the two considered materials.
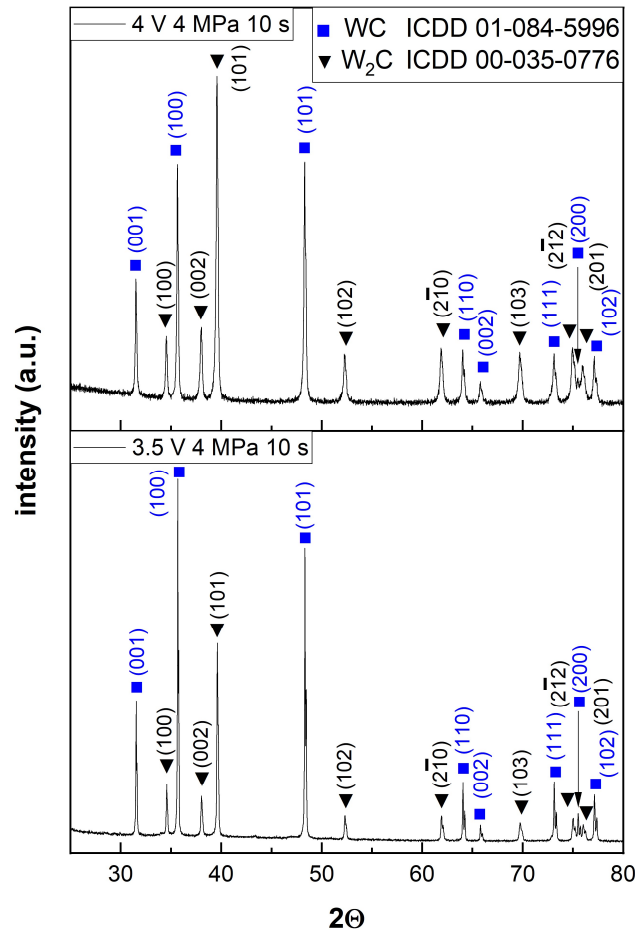
Figure 65 Exemplary XRD diffraction pattern of WC samples sintered by the ERFS process. The samples processed at 4 V, 4 MPa and 10 s and 3.5 V, 4 MPa and 10 s are used to compare the acicular and biphasic microstructure respectively (Figure 62).

The results obtained so far agree well with our previous work [117] where the concept of two different sintering regimes (FS and ERS) as part of the ERFS process was introduced. Pure tungsten carbide can be densified close to full density in less than 10 s; this can be achieved when the right combination of

voltage and pressure is applied to the green compact inside an electrically insulated ceramic die (Figure 62 and Figure 63). As a matter of comparison, other advanced sintering techniques such as hot pressing (HP) or spark plasma sintering (SPS) require several minutes and much larger amount of energy to reach similar densities [33,186]. Hot pressing requires temperature in the range of 1900-2000°C for several hours to reach full density [143]. Cha and Hong and Nino et al. succefully sintered binderless WC by SPS by applying a >1000 A pulsed current and an external pressure of 50 MPa for more than 15 min [176,187]. The flash event is responsible for this large increase in the densification rate, which is activated by the evolution of the electrical properties of the green compact upon the application of the current. A thermal runaway phenomenon can be activated when WC possesses a negative coefficient for resistivity (NTC) while in the green state. If the thermal runaway is assumed as responsible for boosting the sintering rate necessary to achieve the material's densification in a few seconds, the application of an external pressure affects the intensity and the duration of such electrical runaway. Pressure is found to affects the runaway phenomenon in three ways: (i) decreasing the initial resistivity when the material is in the green state (Figure 59), (ii) reducing the duration of the event (Figure 60) and, accordingly, (iii) reducing the electrical energy dissipated in the runaway process in favour of a pure resistive heating (Figure 61). The thermal runaway in a conductive ceramic with native PTC behaviour can be activated only because of the initial NTC behaviour of the green compact. Pressure can partially suppress this phenomenon, the negative evolution of the material resistivity being limited both in duration and in magnitude. Since the non-linear evolution of resistivity with temperature is the key to activate flash sintering in ceramics [49,81,82,95], in the case considered here pressure partially suppresses flash sintering and the densification which can be achieved during such event. In addition, flash sintering for WC has a self-extinguishing behaviour since it lasts until there is an avalanche reduction of the material resistivity after which the material is electrically characterised by its intrinsic PTC behaviour. This occurs concurrently

with the end of the FS regime, where most of the densification occurs. In this perspective, when the sintering time is prolonged from 10 s to 60 s, the density shows only a limited improvement by prolonging the ERS regime. Following such explanation, one can explain the different effect of pressure in said two regimes. The application of an external pressure during the ERS regime, where the electrical properties of the material and the power produced by the Joule effect are constant, is very similar to what happens during hot pressing (HP) or spark plasma sintering (SPS). Pressure has the beneficial effect of providing an additional driving force for densification while suppressing grain growth. In HP and SPS the material is pressed at high temperatures, this allowing a strong reduction in the sintering time from hours to minutes. Such situation is approximated when the highest electrical power is used for a duration of a minute and when the duration of the flash regime is very limited, hence for high pressure levels and for high applied voltages. Indeed, FE-SEM micrographs show that the pressure positively affects the microstructure when these conditions are reached (4 V and 60 s), i.e., when the material is kept at the highest temperature for a longer period.

Flash sintering energy ratio

Since pressure, sintering time and applied voltage affect differently the two ERFS regimes (Figure 57), three sintering parameters are proposed to discriminate the effect of the two regimes on sintering: (i) power peak intensity, (ii) total electrical energy and (iii) ratio of the electrical energy dissipated during the flash event with respect to the total one. The input parameters used in the process are directly correlated to such variables, since pressure affects the FS energy ratio as shown in Figure 60, sintering times influence both the FS energy ratio and the total electrical energy, while its effect on the power peak is negligible (Figure 60 and Figure 66) and voltage acts on both total electrical energy and power peak (Figure 66). The use of said parameters make it possible to build a sintering map as in Figure 67, where the contribution for each regime (FS and ERS) is shown. The 4-D plot reports all sintering data of Figure

56 together with the density results collected in Figure 61. The maximum density can be achieved under two processing conditions: (i) almost pure resistive heating and (ii) flash sintering condition. The pure resistive heating region, highlighted by the blue circle, corresponds to the situation where the FS energy is minimised and the electrical energy is dissipated at a sufficiently high power level. Density decreases if a higher electrical energy is dissipated since it corresponds to a reduction in the power peak level, which can be achieved by prolonging the sintering time at a lower power output; the material is kept at lower temperature for a longer period of time. On the other hand, when the FS energy ratio is increased, corresponding to applied pressure reduction, and the power peak is kept constant, pure WC can be sintered at the same density with an enormous reduction of the required electrical energy. The reduction of the total energy at the same power peak corresponds to shorter sintering time, since the power peak depends only on the applied voltage. In conclusion, the flash regime allows a much faster sintering of the material with respect the ERS counterpart, decreasing significantly the time and, consequently, the energy required to the consolidation process. For example, one can sinter pure WC under 3.5 V (corresponding to a power peak of 6800 mW/mm^3) to about 95% density with a total energy consumption of 68 J/mm^3 instead of 240 J/mm^3 by extending the energy dissipated during the power surge from 3% up to 30%.
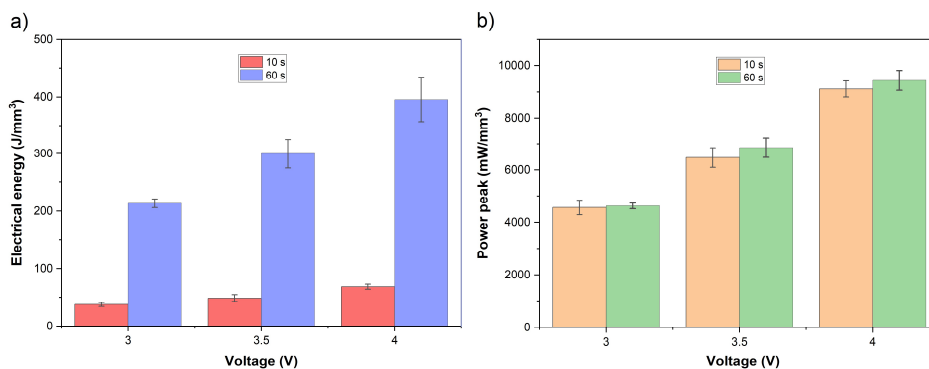
Figure 66 Total electrical energy dissipated during the ERFS process (a) and power peak (b) as function of the applied voltage.
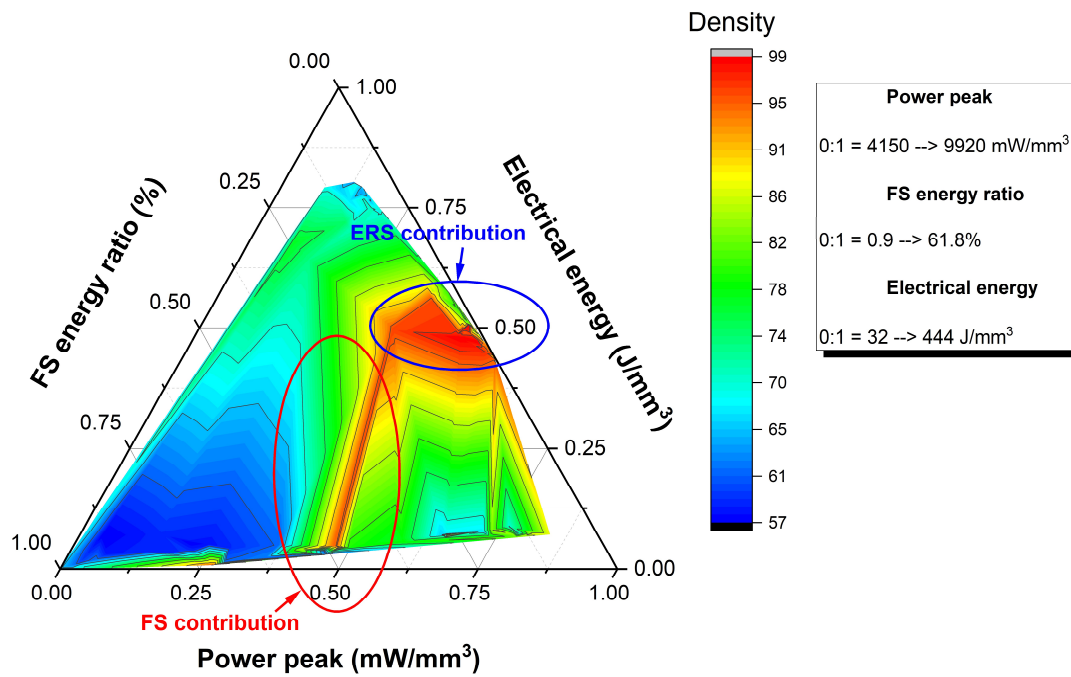
Figure 67 Sintering map in terms of final density for ERFS of pure WC: contribution of the flash sintering regime vs. the electrical resistance one on densification. The parameters are normalized between 0 and 1 as represented in the inset.

3.1.4 Conclusions

The application of increasing pressure during the electrical resistance flash sintering of tungsten carbide inhibits its densification, resulting in a body with microporous structure. A higher applied load modifies the electrical properties of the WC in the green state, limiting the contribution of the electric thermal runaway to ultrafast sintering. Pressure decreases the initial resistivity of the green material, the temporal occurrence and the magnitude of its evolution thus resulting in a shorter power surge duration. The positive effect of the pressure on the microstructure and sintering kinetics starts to become important at longer sintering times and higher voltages. The ERFS process can be classified depending on the maximum power peak reached during the flash regime and by the energy portion dissipated during such event. When these two values are high enough, it is possible to completely sinter pure WC in less than 10 s due to the exponential increase of the electrical power consumption. Prolonging the sintering after this point is shown to have a little effect on the residual porosity closure while promoting the abnormal growth of hexagonal WC grains.

3.2 Room temperature stability, structure and mechanical properties of cubic tungsten carbide in flash sintered products

Isacco Mazo[#], Jon M. Molina-Aldareguia [§, †], Alberto Molinari [#], Vincenzo M. Sglavo[#‡]

\# Department of Industrial Engineering, University of Trento, via Sommarive 9, Trento, Italy

§ Department of Mechanical Engineering, Universidad Politécnica de Madrid, 28006 Madrid, Spain

† IMDEA Materials Institute, C/ Eric Kandel 2, 28906, Getafe, Madrid, Spain

‡ INSTM, National Interuniversity Consortium of Materials Science and Technology, Trento Research

Unit, Via G. Giusti 9, 50123 Firenze, Italy

Graphical abstract

Unique microstructure after flash sintering

New mechanical properties

room temperature plastic deformation

active slip planes (111)
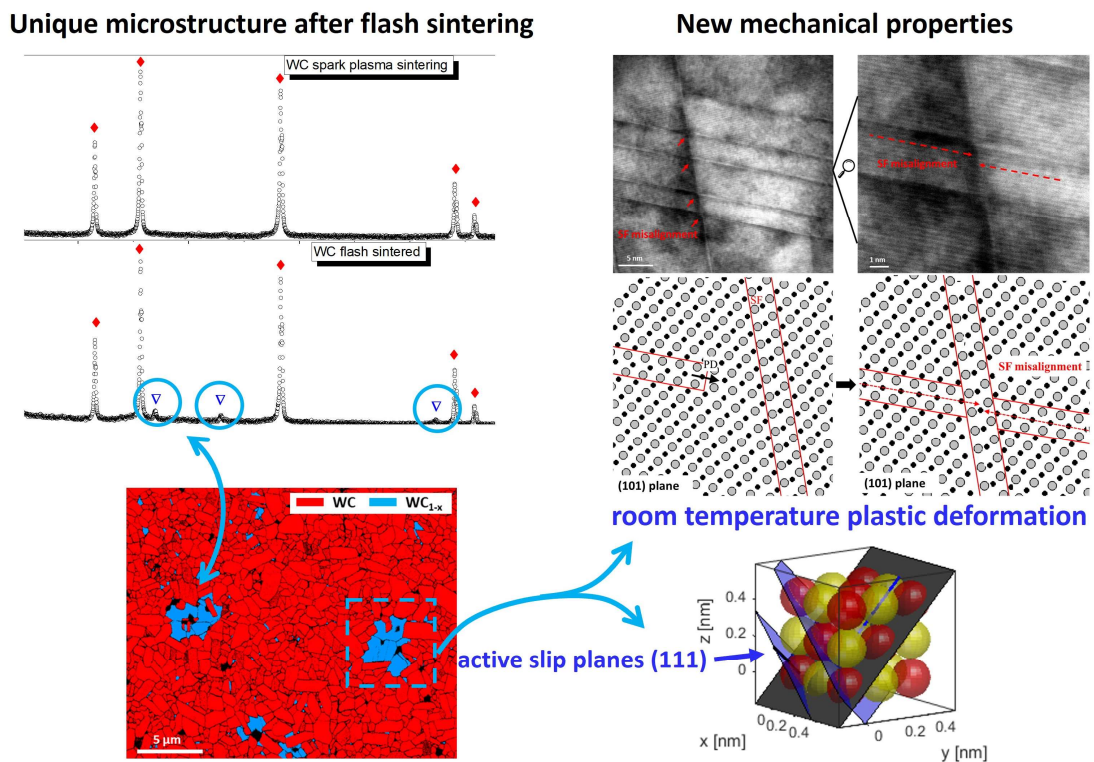
ABSTRACT

This work explores the possibility to obtain the metastable cubic tungsten carbide phase (WC_{1-x}) during the rapid and the ultrarapid consolidation of hexagonal WC nanopowders. Spark plasma sintering (SPS) and flash sintering (FS) techniques are implemented to study the formation and the stability of WC_{1-x} during sintering. A biphasic ceramic material, corresponding to cubic-WC/hex-WC (10/90 vol%), can be obtained uniquely with the flash sintering process. The ultrafast sintering of powders containing Cr and V impurities results in a peculiar cubic-WC quaternary phase $(W_{0.87}Cr_{0.12}V_{0.09})C_{0.71}$ which retains the crystalline structure, Fm3m {225}, and the metastable character of WC_{1-x}, decomposing into the thermodynamically stable hexagonal phases (WC and W_2C) after vacuum annealing at 700°C and 1100ºC. Structural features of the composite are analysed by HRTEM and Transmission Kikuchi Diffraction (TKD), which pointed out the activation of room-temperature plastic deformation mechanisms in cubic WC grains. Such behaviour is connected to stacking faults interacting with partial dislocations on {111} planes, similarly to FCC metals. Nanomechanical indentations were also used to map the elastic modulus and the hardness of the cubic phase, which shows a noticeable softer character with respect to the hexagonal matrix. These results suggest flash sintering as a new strategy for producing WC/WC_{1-x} composite materials with tailored elastic modulus and hardness/toughness ratio.

3.2.1 Introduction

The high-temperature cubic tungsten carbide phase, WC_{1-x}, is thermodynamically stable only between 2789 and 3028 K and in sub-stoichiometric carbon concentration condition (37-50 at%) [22]. This phase was found to remain stable at room temperature only in peculiar conditions of very fast cooling rate or quenching from the molten state; Zhang et al. suggested that a cooling rate as high as 10^8-10^{11} K/s is necessary to stabilize the cubic lattice [188]. Cubic WC_{1-x} nanopowders were successfully synthesized by Pak et al. by discharge plasma jet [189]. Tanaka et al. exploited the high temperature and speed generated by the electrical explosion of a W wire immersed in a paraffin bath [190]. Evidence of this metastable phase was also found after high energy laser/ion beam surface treatments of WC components [188,191]. Lian et al. proposed a novel approach to produce ultrafine WC_{1-x} particles (3-4 nm) by simply pyrolysis of dicyandiamide mixed with ammonium metatungstate at 800°C [192]. Besides the important achievements reported in the production and study of this metastable phase, the knowledge about its physical and mechanical properties is rather scarce if not absent at the moment. Its further study is limited by the absence of a proper route to produce the cubic polymorph in bulk components. Although different routes are present for the production of WC_{1-x} in form of nanopowders, their sintering inevitably leads to the transformation of the WC_{1-x} into WC and W_2C products. The thermal stability of WC_{1-x} layers obtained by magnetron sputtering was studied by Abad et al. who pointed out its phase transition around 700°C, well below a suitable temperature for sintering [193].

Flash sintering (FS) offers a new opportunity for the retention of metastable phases at room temperature, ultrafast heating rates and non-equilibrium generation of lattice defects allowing the consolidation of out-of-equilibrium materials [74][194]. Flash sintering conditions have been very recently achieved in tungsten carbide during electrical resistance sintering (ERS) experiments, thus opening the possibility to study the conditions of existence of cubic WC_{1-x} in the sintered products [117]. The use of WC powders

containing small amount of oxides (5 wt%) allowed the generation of biphasic WC/W_2C (60/40 vol%) sintered bodies. Oxide species were shown to be responsible for a carbon loss at high temperature, associated with prominent decarburization of the stoichiometric WC lattice. The carbon stability range of the cubic phase sits in between the two hexagonal phases, WC and W_2C [22]. Therefore, the FS process was used in the current work to sinter commercial WC powders with lower oxygen content trying to avoid the generation of W_2C in favour of the WC_{1-x} phase. This work aims at pointing out how flash sintering can induce the formation of the metastable high-temperature phase, WC_{1-x}, for opportune carbon concentration. Structural features are analysed by HRTEM and Transmission Kikuchi Diffraction (TKD) and nano-indentations are used to determine elastic modulus and the hardness of the cubic phase to be compared with the mechanical properties of the hexagonal one.

3.2.2 Materials and Methods

Tungsten carbide nanopowders were purchased from Inframat Advanced Materials®, product number #74N-0601 [119]. The chemical composition of the starting powder was characterized by EDXS (ThermoFischer® Apreo 2S LoVac) at 20kV and 3.2nA. The phase composition of powders and sintered products was determined by X-Ray diffraction (PANalytical EMPYREAN), with Cu-Kα1 (1.54060 Å) radiation generated at 45 kV and 40 mA in a line focus configuration. The samples were analysed in a Bragg-Brentano geometry, by using an angular step size of 0.012° and an accumulation time of 100 s. The 1-D diffraction patterns were refined by the Rietveld method (HighScore Plus® software) using the following ICDD diffraction cards as reference patterns: 01-084-5996 for WC, 00-035-0776 for α-W_2C and 00-020-1316 for cubic WC_{1-x}.

The electrical resistance flash sintering (ERFS) process was performed in a specifically realized apparatus, were the sample, in the form of an uniaxially pressed pellet, is sintered by the direct application of an AC current. The sintering process takes place inside a hollow zirconia die, where the pellet sample is pressed between two cylindrical electrodes to maintain the electrical contact. In this work, 1.3 g of powders were pressed into cylindrical pellets, inserted in the zirconia die and flash sintered for 10 s under 4 MPa of uniaxial pressure by controlling the voltage and current maximum values to 3.7 V and 1000 A respectively. A more detailed description of the ERFS apparatus and methodology was already reported in previous works [117,118,164].

The same powder was also consolidated by SPS at K4Sint SpA (Pergine Valsugana, Italy) by means of a Dr. Sinter 1050 apparatus. Sintering was carried out at 2100°C, with heating rate of 200°C/min, in low vacuum condition ($5x10^{-4}$ bar) and under 60 MPa uniaxial pressure.

Sintered products were cut in the direction of the applied pressure and the obtained cross sections were grinded and polished with diamond abrasive pastes down to 1µm size. Polished surfaces were analysed by means of FEG-SEM microscope (ThermoFischer® Apreo 2S LoVac) equipped with an EBSD detector for the analysis of the phases and grains orientation.

The thermal stability of the flash sintered samples was evaluated by vacuum annealing experiments in a tubular furnace (Nabertherm RHTH 120-600/16) at the temperatures of 400, 700 and 1100°C with 1 h of holding time. After the thermal treatment samples were tested by means of XRD, with the methodology previously described, to asses any modification in the phase composition.

Mechanical properties in specific areas were evaluated by nanoindentation (Hysitron triboindenter TI950), mapping the elastic modulus and the hardness with a Berkovich diamond tip (BKL-DLC). Preliminary cyclic loading-unloading procedures were performed for the correction of the machine compliance and for the estimation of suitable penetration depth to avoid indentations overlapping. Maps

were acquired in an area of 7.7 x 7.7 μm^2, by using 3 mN maximum load; 22 x 22 indents were produced with a separation distance of 0.35 µm. The indentation map position was calibrated by imaging the surface with the same indenter diamond tip in AFM mode.

The deformation behaviour of the grains at the nanoscale was assessed by preparing an electron transparent lamella of a plastically deformed portion of material. To pursue this scope, firstly, a micropillar was prepared by focused ion beam (FIB) milling within a FIB-SEM dual column microscope (Helios NanoLab 600i). Pillars of 3 µm in diameter and 6 µm in height were then compressed uniaxially by a diamond punch (Ø 15 µm) within the apparatus for nanoindentation (Hysitron triboindenter TI950), with a strain rate of 10^{-4} s^{-1}. The compression tests were stopped after reaching the yield point (ε=0.2%) and before the final brittle failure. A lamella was prepared on the cross-section of the deformed pillar by FIB milling: the current and the accelerating voltage were scaled down from 30 kV and 9.3 nA to 10 kV and 80 pA to reach electron transparency and to limit the ion damage of the material.

High resolution TEM/STEM micrographs and EDXS analysis were obtained from the prepared lamella at 200 kV in a FEI Talos F200x microscope. The orientation and crystalline composition of the grains composing the lamella were finally characterized by the Transmission Kikuchi Diffraction technique, also known as transmission EBSD, in the FEG-SEM microscope. Transmission Kikuchi patterns were obtained following the indication of Suzuki [195]: the lamella was positioned at a WD of 5 mm between the electron beam and the EBSD detector, with a tilting angle of 25° with respect to the horizontal axis. The pattern was acquired with an accelerating voltage of 30 kV and a step size of 0.025 µm.

3.2.3 Results and Discussion

Powder composition

The tungsten carbide nanopowders used in the present work show a very limited oxygen content (0.34±0.01 wt%), much lower if compared to those previously tested in flash sintering experiments (2–3 wt%) [117]. EDXS analysis (Figure 68) also shows the presence of Cr and V impurities, in very low quantities (0.4 and 0.3 wt%, respectively). These are not homogeneously dispersed in the powder and are present also as small spots. The XRD analysis (Figure **69**(a)) shows the absence of any Cr and V oxide or carbide, thus suggesting the presence of these impurities as single elements dispersed in the WC matrix. Despite these contaminants, the powder is characterized by a very high purity level, 98-99 wt% (Figure 68, a), and composed exclusively of WC hexagonal phase (Figure 69, (a)).
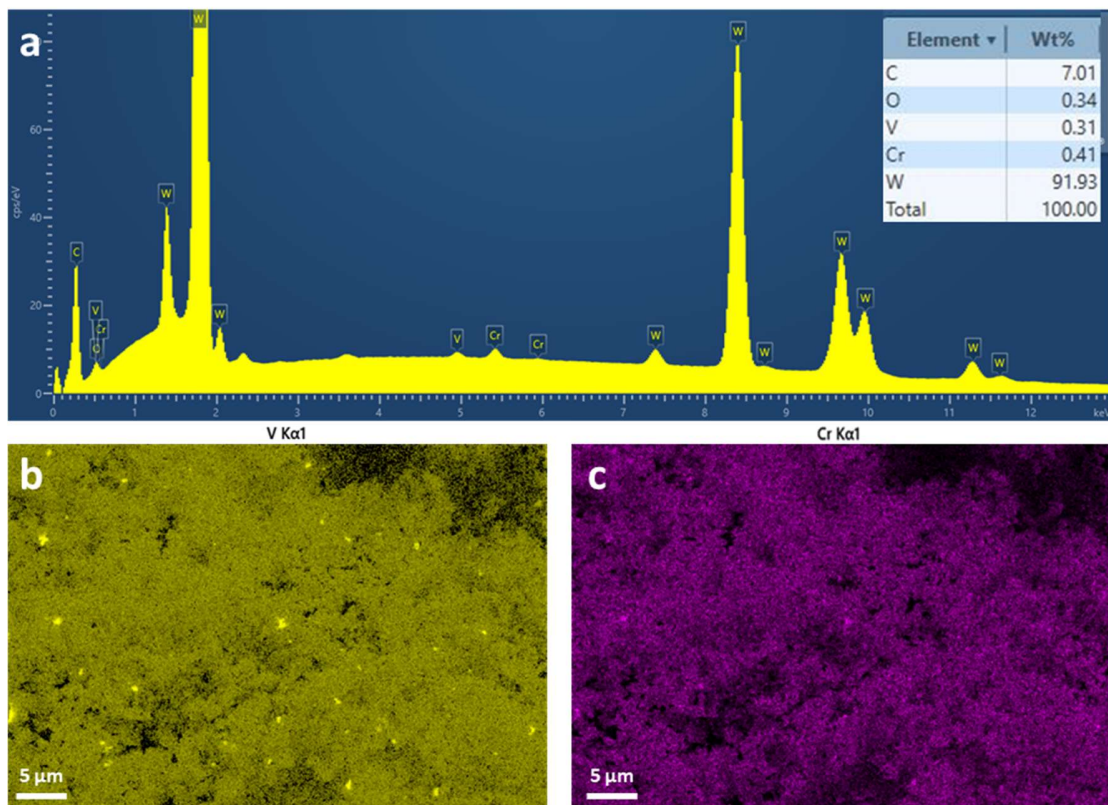
Figure 68 EDXS elemental spectrum of WC powder (a), elemental map of V (b) and of Cr (c).

The phase composition of the samples processed by electrical resistance flash sintering (ERFS) and spark plasma sintering (SPS) is shown in Figure 69 (b) and (c). The low initial oxygen content and the absence of any tungsten oxides in the starting powder avoid the decarburization of WC in the low carbide phase W_2C during the SPS process. This result demonstrates how, by using high purity WC powder, fully monophasic (100% h-WC) sintered products are obtained by SPS. Other researchers reported the necessity to control the decarburization by precisely tuning carbon addition to the initial powders [196].
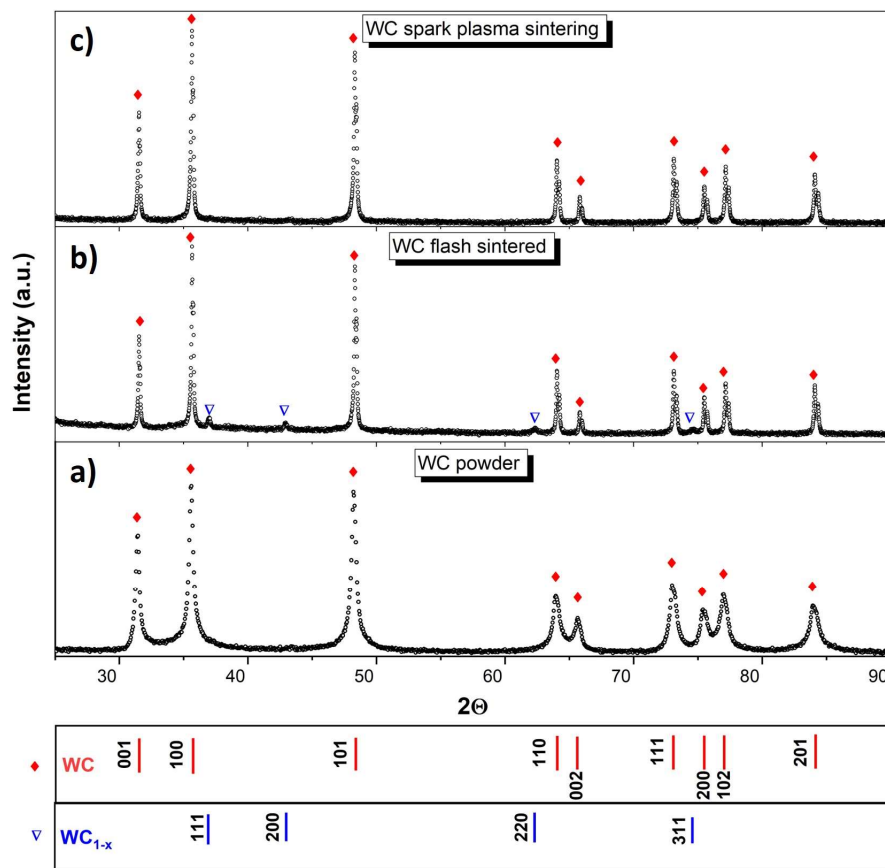
Figure 69 XRD spectra of WC powder (a) and bulk components obtained by flash sintering (b) and spark plasma sintering (c).

Presence and structure of cubic WC$_{1-x}$ phase after flash sintering

The ultra-rapid consolidation by the ERFS process results in the formation of a new phase. Peaks of low intensities appear at 37.0°, 42.9°, 62.4° and 74.6° (Figure 69, (b)) together with typical hexagonal WC reflexes. Said peaks can not be fitted by any W$_2$C polymorph but they correspond to the metastable high-temperature WC$_{1-x}$ cubic phase - space group Fm-3m {225}, being indexed by using ICDD card no. 00-020-1316 (cross-referenced to 04-022-5716), the same card used to characterize cubic WC$_{1-x}$ nanoparticles obtained by discharge plasma jet synthesis [189]. The cubic phase, differently from the hexagonal one, has a broad range stability. This is narrow at the lower transformation temperature (2789 K), corresponding to WC$_{0.58}$ - WC$_{0.65}$, and wider WC$_{0.59}$ – WC$_{0.98-1.00}$ from 3030 to 3055 K [22]. The lattice parameter of the cubic modification was studied accurately by Kurlov and Gusev [22] for several carbon concentrations and the data are well fitted by the following function:

$$a_{WC_{(1-x)}} = 0.4018 + 0.0481y - 0.0236y^2 \ [nm] \tag{32}$$

where y = 1 – x = C/W refers to the C atomic concentration in the cubic lattice. Eq. 32 can be used to estimate the carbon stoichiometry using the lattice parameter evaluated from XRD measurement . The reference lattice parameter of the phase used for the fitting (no. 04-022-5716) is $a_{\mathrm{ref}} = 4.234$ Å, while the Rietveld refining of pattern in Figure 69 (b) gives $a_{\mathrm{exp}} = 4.211$ Å (Figure 71). This lattice constant is lower than every other value reported so far: Pak et al. [189] obtained $a = 4.2536$ Å for cubic WC$_{0.86}$, Rudy et al. determined a value of $a = 4.220$ Å for WC$_{0.61}$ and, according to Sara et al., the lower phase boundary is WC$_{0.59}$. However, the use of Eq. 32 with the parameter measured for the flash sintered WC$_{1-x}$ of Figure 69 (b) results in WC$_{0.56}$, where the carbon content (C=36 at%) is outside the WC$_{1-x}$ phase stability region, between β-W$_2$C and γ- WC$_{1-x}$ (Figure 72) [22]. The discrepancy of the lattice constant

from the data regarding the high temperature phase stability in the W-C system can be explained by the results shown in Figure 70 and Figure *71*.
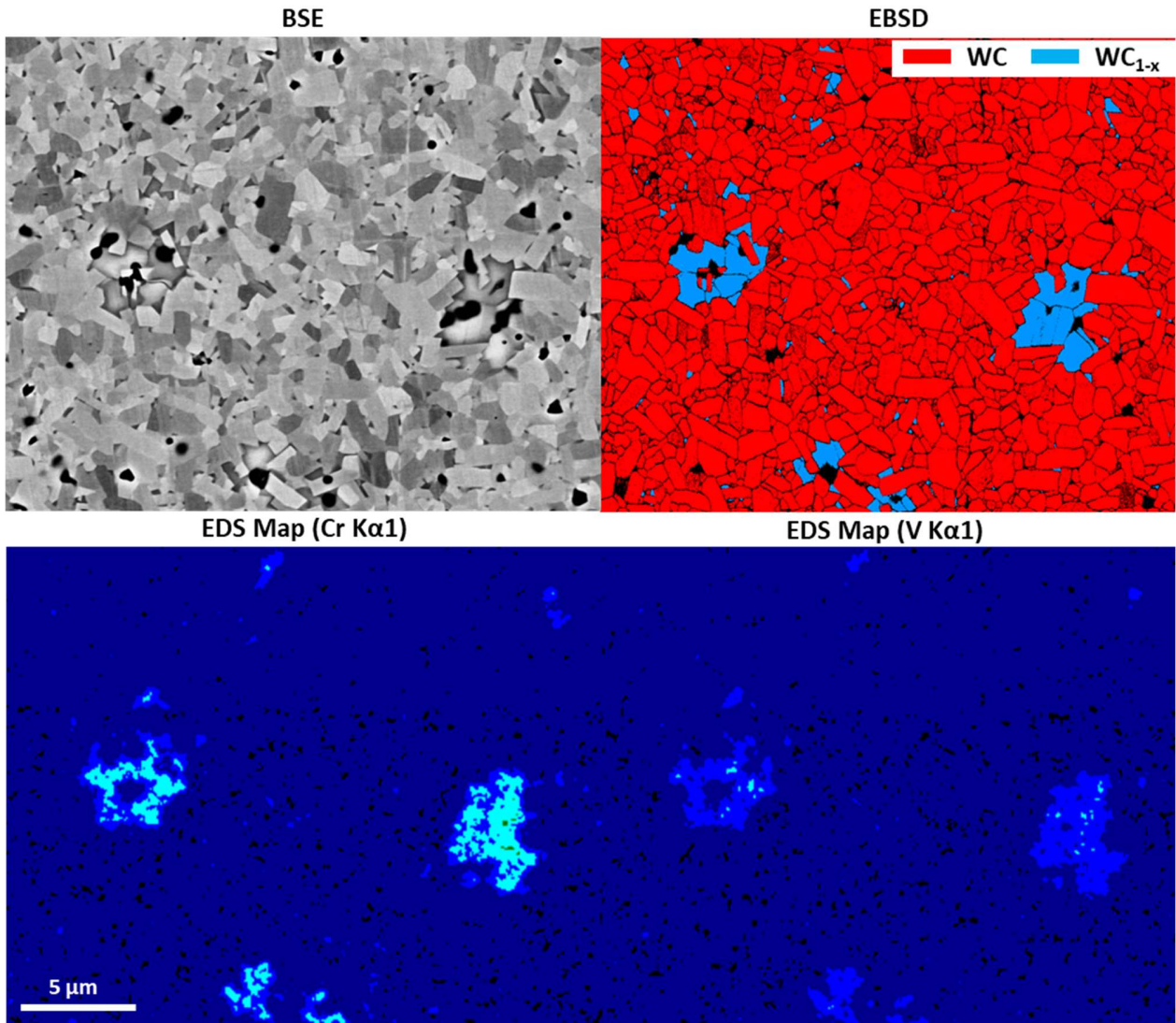
Figure 70 Microstructure analysis of the polished cross-section prepared by the ERFS process. Back-scattered electrons (BSE) image is compared with EBSD and EDS maps to point out the presence and the composition of the cubic phase (WC1-x) in the flash sintered product.

EBSD analysis successfully detects the presence of cubic phase within the WC matrix by using again the pattern no. 04-022-5716 as a reference. Well-developed WC_{1-x} grains are present among the hexagonal WC grains. The micrograph shown in Figure 70 is representative of the entire cross-section, where WC_{1-x} grains are mainly organized in small clusters of 5-12 grains and rarely isolated within the WC matrix. The presence of black spots in Figure 70 indicates missing points in the EBSD phase composition maps. These black spots represent areas where the software cannot determine a crystalline orientation based on the diffraction pattern. In fact, these black spots highlight the existence of grain boundaries, material porosities and surface defects like polishing scratches.

The EDS maps acquired on the same area reveal a certain amount of Cr and V, the same elements identified initially in the powder. Nevertheless, the comparison of elemental maps in Figure 68 (b) and (c) with that of Figure 70 points out the difference in the dispersion of such elements, segregated in specific grains, that, according to EBSD analysis, belong to the cubic phase. This segregation can be for sure ascribed to a very fast atomic diffusion of such two elements in the cubic phase during the flash sintering process. Considering that the entire ERFS process duration is only 10 s and that Cr and V are initially dispersed randomly in the powder (Figure 68), their segregation must have occurred with an unconventionally high diffusional rate. The concentration of these elements in some specific grains can modify the crystalline structure of the detected phase. For this reason, the diffraction pattern of Figure 69(b) was tentatively refined with other cubic phases, symmetry Fm-3m {225}, containing Cr and V, like chromium tungsten carbide ($Cr_{0.4}W_{0.6}C$) and vanadium tungsten carbide ($V_{0.5}W_{0.5}C$). The diffraction lines of these two phases are shown in Figure 71. The most intense peaks can be precisely fitted by the initial pattern of the reference card no. 04-022-5716, although it is possible to observe how the exact peak positions of the detected phase slightly diverge from the WC_{1-x} pattern with a position between cubic $V_{0.5}W_{0.5}C$ and $Cr_{0.4}W_{0.6}C$ phases (Table 8).
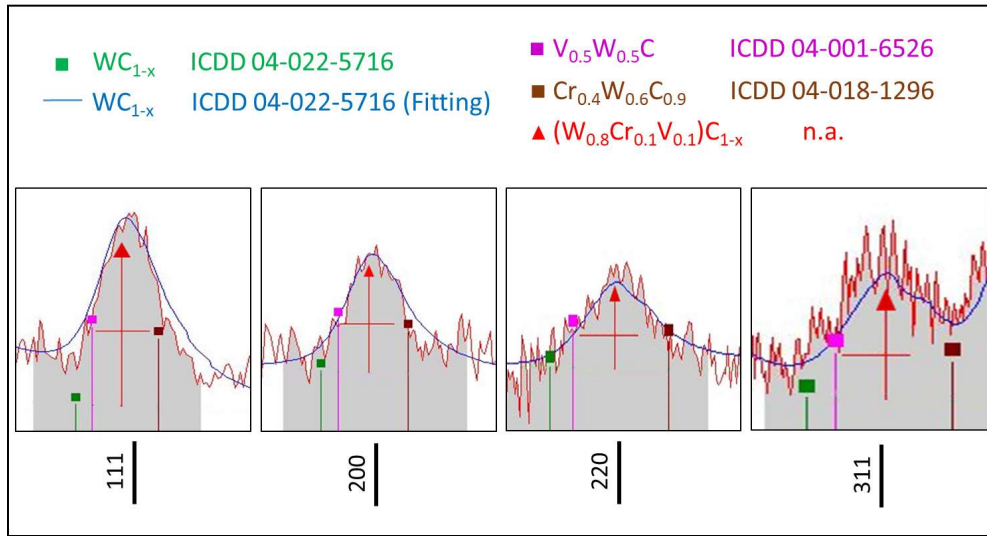
Figure 71 Magnified view of the XRD peaks of Figure 69 (b) for the cubic WC phase. Comparison between the diffraction line positions of the reference patterns shown in the legend and the experimental one.

Table 8 Lattice constant and diffraction lines position of the reference patterns and the experimental XRD data

phase	a [Å]	density [g/cm³]	111 [2θ]	200 [2θ]	220 [2θ]	311 [2θ]
WC_{1-x}	4.234	17.139	36.735	42.674	61.937	74.225
$V_{0.5}W_{0.5}C$	4.226	11.388	36.807	42.759	62.067	74.389
$Cr_{0.4}W_{0.6}C_{0.9}$	4.1935	12.787	37.107	43.112	62.611	75.075
$(W_{0.8}Cr_{0.1}V_{0.1})C_{1-x}$	4.2119	15.055	36.939	42.914	62.304	74.683
Experimental pattern	*4.2110*	*n.a.*	*36.932*	*42.9064*	*62.291*	*74.670*

The substitution of W with Cr or V in the cubic lattice shifts the peaks to higher 2θ values, Cr having the strongest effect on their position and cell parameter (Table 8). The central position of the experimentally determined phase with respect the $V_{0.5}W_{0.5}C$ and $Cr_{0.4}W_{0.6}C$ phases suggests the presence of a new cubic phase in the flash sintered product, belonging to the quaternary system comprising W-C-Cr-V, where Cr and V partially substitute W, modifying the original structure of WC_{1-x}. To support such hypothesis, a new phase was created with the HighScore® software, starting from a space group Fm-3m {225} and a lattice parameter a=4.2110 Å. Cr and V atoms were assumed to be present in the cubic lattice in substitution of W ones. The degree of substitution was assessed by refining (Rietveld method) the occupancy of Cr and V in the W sites. The simulated pattern confirmed the presence of a new phase, where the substitutional degree of Cr and V can be estimated between $(W_{0.8}Cr_{0.1}V_{0.1})C$ and $(W_{0.6}Cr_{0.2}V_{0.2})C$. Figure 71 shows that the new quaternary phase, referred as $(W_{0.8}Cr_{0.1}V_{0.1})C$ for simplicity, matches almost perfectly the 111, 200, 220 and 311 diffraction peaks (Table 8). The segregation of Cr and V during flash sintering affects the WC cubic structure, shifting the peak position and decreasing the calculated density of WC_{1-x} from 17.12 g/cm^3 to 15.05 g/cm^3 (Table 8).

The discrepancy in the result obtained from Eq.1 will be discussed in section 3.4 together with the precise evaluation of Cr, V and C content. It will be shown how the modification in the cell parameter introduced by Cr and V can be included into Eq.1, to correctly estimate the carbon content of the cubic phase.

Formation of WC_{1-x} and its stability

Differently from the sample consolidated under flash sintering conditions, those prepared by SPS (Figure 69, (c)) do not show any presence of this new WC_{1-x} cubic phase. Its absence implies that the phase transformation WC -> WC_{1-x} cannot occur at the SPS sintering temperature or that the cubic phase

decomposes upon cooling. Of the two hypotheses, the former is more likely since (i) the maximum temperature reached during SPS is 2100°C while WC_{1-x} is thermodynamically stable only above 2515°C (Figure 72) and (ii) WC_{1-x} decomposes in multiple products, WC, W_2C and W, which are not detected in the sintered material (Figure 69, (c)). Data regarding the thermal stability of WC_{1-x} are currently limited to thin films, produced by low-temperature sputtering, or to nanoparticles. Abad et al. [193] reported a transformation of WC_{1-x} thin films in W_2C and WC products during vacuum annealing at 700°C and a second reaction at 900-1000°C with the formation of metallic tungsten. Shanenkov et al. [197] showed how the thermal stability under vacuum of WC_{1-x}, in the form of nanoparticles can be extended up to 1500°C in the presence of carbon shell. However, in the same study they revealed how, in the attempt to sinter WC_{1-x} nanoparticles, full decomposition into W_2C and WC products occurred after SPS at 1500°C. The diffusional phenomena during sintering promote the decomposition of WC_{1-x} at lower temperatures. Attempts to consolidate almost pure (94+%) WC_{1-x} nanoparticles at 1500°C by SPS resulted in low density (74%) sintered bodies composed exclusively of WC and W_2C [197]; this leads to the conclusion that SPS is not a viable route for the formation or the retention of cubic tungsten carbide.

Conversely, flash sintering appears capable of producing cubic tungsten carbide phase very similar to WC_{1-x}, namely $(W_{0.8}Cr_{0.1}V_{0.1})C$, simply starting from hexagonal WC nanopowders. In addition, very interestingly, this new phase remains stable, or probably better, metastable, upon cooling down to room temperature. However, its existence in the sintered products requires to discuss the simultaneous presence of Cr and V on the phase stability. Chromium tungsten carbide and vanadium tungsten carbide are known phases in the W-Cr-C and W-V-C systems although, according to the international centre for diffraction data (ICDD), updated to 2021, a quaternary phase comprising W-Cr-V-C has not been reported yet. For this reason, the effect of Cr and V on the thermodynamic stability of the cubic WC_{1-x} was simulated with the CALPHAD method using the Thermo-Calc software (TCNI8 database). The experimentally

determined W-C phase diagram [22] and its simulated counterpart are shown in Figure 72. The W-C phase diagram and the temperature stability range for WC_{1-x} were simulated with a sufficient accuracy by using the cited database, although the simulation lacks of the accuracy of the experimental phase diagram in describing the stability range of WC_{1-x} between 40 and 50 at% C. Figure 73 shows how Cr and V affect the temperature stability range of WC_{1-x} at three different temperatures, 2700, 2850 and 2900 K. Specifically, a small concentration of Cr (1-2 at%) in solid solution suppresses completely the existence of WC_{1-x} in the 2850-2900 K temperature range; conversely, V has the opposite effect, it allowing the retention of the cubic phase also at temperatures lower than 2700 K, below the transformation temperature of the original phase diagram (Figure 72, (b)). However, the attempt to estimate the stability of the quaternary phase, $(W_{0.8}Cr_{0.1}V_{0.1})C$, did not give reliable results due to a lack of information in the available database.

The stability of this phase in the range from 25 up to 1100°C was further determined by vacuum annealing experiments and subsequent XRD analyses of the flash sintered specimen. According to Figure 74, the $(W_{0.8}Cr_{0.1}V_{0.1})C$ phase is stable up to about 700°C and then decomposes to more stable phases. Between 700°C and 1100°C $(W_{0.8}Cr_{0.1}V_{0.1})C$ completely disappears with the formation of W_2C phase. These results well agree with those of Abad et al. [193] who observed that WC_{1-x} decomposes in the same temperature range into WC and W_2C. $(W_{0.8}Cr_{0.1}V_{0.1})C$ is demonstrated to be a metastable phase and, similarly to pure cubic tungsten carbide (WC_{1-x},), it possesses a comparable temperature transformation range and the same decomposition products.
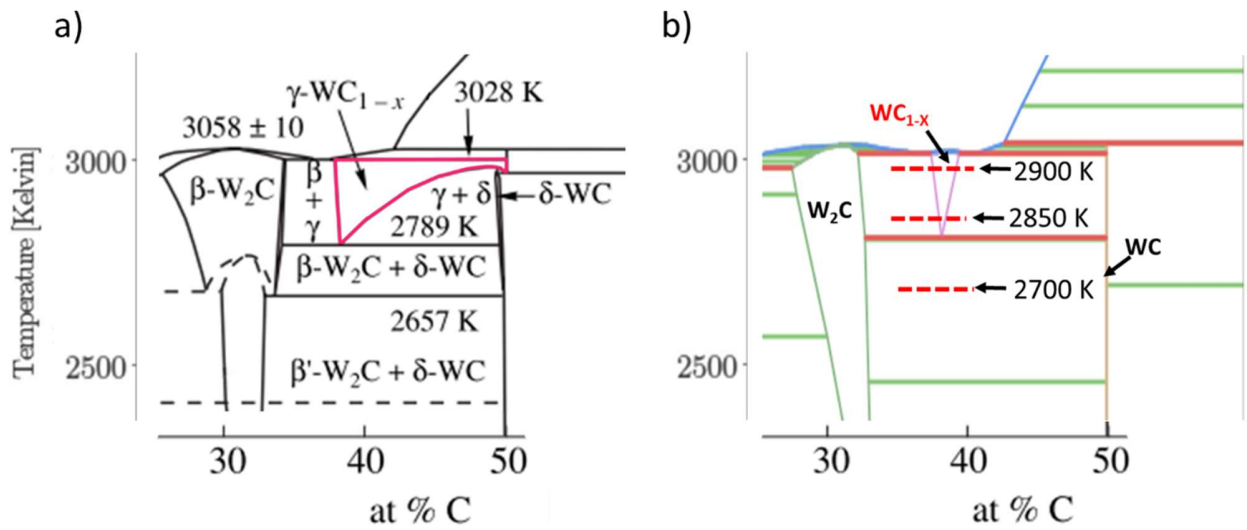
Figure 72 W-C phase diagram corrected with experimental data as reported by Kurlov and Gusev [22] (a) and W-C phase diagram simulated with Thermo-Calc (b).
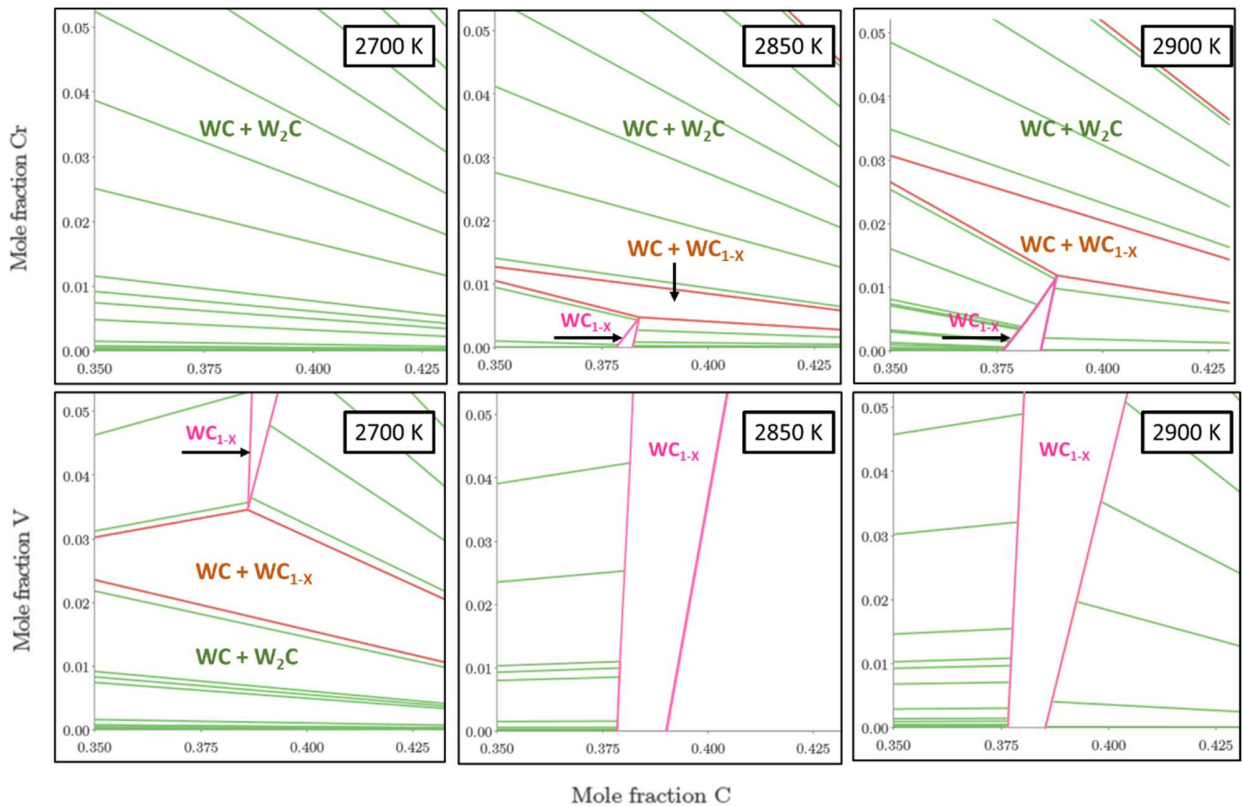
Figure 73 Ternary phase diagrams for W-Cr-C and W-V-C at 2700, 2850 and 2900 K
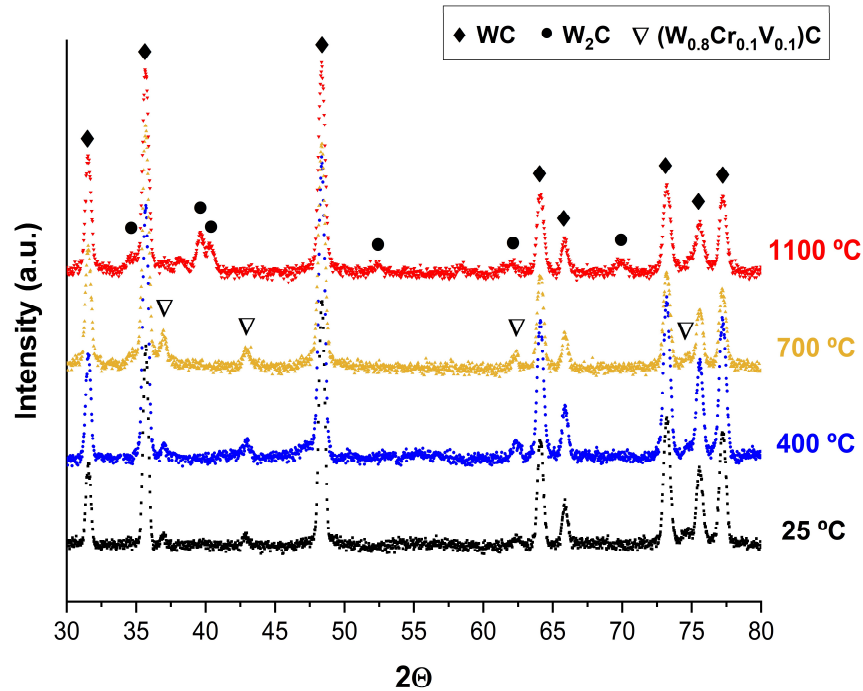
Figure 74 XRD analyses of as-produced flash sintered WC samples and after vacuum annealing at 400, 700 and 1100°C.

Since VC and Cr_3C_2 are well known grain growth inhibitors for WC-based products, several researchers studied the formation of secondary new phases in the W-C-Cr-V system. The simultaneous effect of Cr and V addition in WC products sintered by SPS was studied by Al-Aqeeli and he did not find any presence of other phases in addition to hexagonal WC [198]. Sugiyama et al. evidenced how only few atomic layers, at the WC-Co interface, are affected by V addition, resulting in a $(W,V)C_x$ layer with a NaCl crystal structure [199]. The same evidence for a (Cr,W)C ultrathin layer (1.4 nm) formed on the WC grain surface in contact with the Co-rich binder phase was found by Yousfi et al. [200]. Several researcher proposed that the cubic (Cr, V, W)C layers, occurring at the WC-Co and WC-WC interface, act as grain inhibitors in cemented carbides [201]. Similarly, but in the absence of any additive, Gao et al. pointed out how at WC-Co and WC-WC interfaces the formation of a layer-like cubic WC_{1-x}, of few atomic planes, is energetically favoured and stabilized [202]. WC_{1-x} and its V and Cr alternatives retain

stability due to low surface energy and coherent relationships between the involved interfaces. Based on this background and on the strong similarities regarding crystalline structure, metastability and decomposition products between $(W_{0.8}Cr_{0.1}V_{0.1})C$ and WC_{1-x} (Figure 71, Figure *73* andFigure *74*), the influence of Cr and V on the room temperature stability of cubic tungsten carbide can be excluded. In this perspective, the flash sintering process has a double potential: (i) it allows the transformation WC -> WC_{1-x} to occur during sintering and (ii) it preserves the metastable phase during the cooling process. Flash sintering has been proposed as a defects engineering technology capable of producing new material features and properties by the alteration of the lattice defects equilibrium. Noticeable is the modification of plastic deformation mechanisms driven by the introduction of a vast amount of defects [75,77,78], or the achievement of a non-equilibrium thermodynamic state in entropy-stabilized oxides [203]. In this context, Figure 75 compares the crystal quality (micro-strain) between WC sample and phases obtained during the flash sintering process and during SPS. The quantification of the lattice defects can be accomplished by analysing the line broadening dependency on the diffraction peaks angle in Figure 69. The contribution of size and strain on the overall peak broadening (B_{struct}) can be separated by plotting $B_{struct} \cos \theta$ as a function of $\sin\theta$ according to the equation:

$$B_{struct} \cos \theta = 1.1 \frac{\lambda}{crystallite\ size} + lattice\ strain\ (4 \sin \theta) \tag{33}$$

in the so-called Williamson-Hall plot (Figure 75).

For a correct interpretation of the peak broadening and to exclude the contribution of instrumental broadening, a zero microstrain reference sample was produced: well annealed WC, with average grain size of 20 µm, was obtained after 2 h sintering at 2150°C in a pressure-less vacuum furnace (Astro®). Crystalline defects were quantified by the slope of the lines in the Williamson-Hall plot (W-H) in Figure 75. The conventionally sintered material is certainly a good standard for the microstrain analysis, being

the corresponding line in the W-H plot almost flat. Regarding the hexagonal WC phase, samples sintered by ERFS are characterized by a slightly higher amount of lattice defects (micro-strain) with respect to those obtained by SPS. Conversely, the line corresponding to the cubic phase strongly diverges from the hexagonal phase, showing a vast contribution of post sintering defects to its crystal quality. Hexagonal WC is known to be characterized by an anomalous low concentration of defects in both metal and carbon sublattices. The formation energy of V_C (carbon vacancies) is significantly lower than for V_W and, therefore, any possible deviation from the stoichiometry is mediated by C defects in the form of vacancies. Since in WC the carbon stability range as narrow as a line (Figure 72), very small deviations from stoichiometry are allowed. An anomalous low defect concentration in hex-WC crystals was accurately determined by positron annihilation spectroscopy [204] and by density functional theory (DFT) calculations [1]. Indeed, the flash sintering process only allows the introduction of a limited amount of "extra-defects" in the sintered products compared to SPS. Conversely, the WC_{1-x} phase, which is characterized by its carbon vacancies and by the additional substitutional defects of Cr and V, as previously determined, can accommodate lattice defects much more easily. Correspondingly, the cubic phase results in a defect population one to two orders of magnitude larger than in the hexagonal counterparts.

The metastable character (Figure 74) and the unconventional high density of lattice defects (Figure 75) of the cubic phase $(W_{0.8}Cr_{0.1}V_{0.1})C_{1-x}$ stimulate the idea of a defect-assisted stabilization mechanism of this high temperature phase by the flash sintering process.
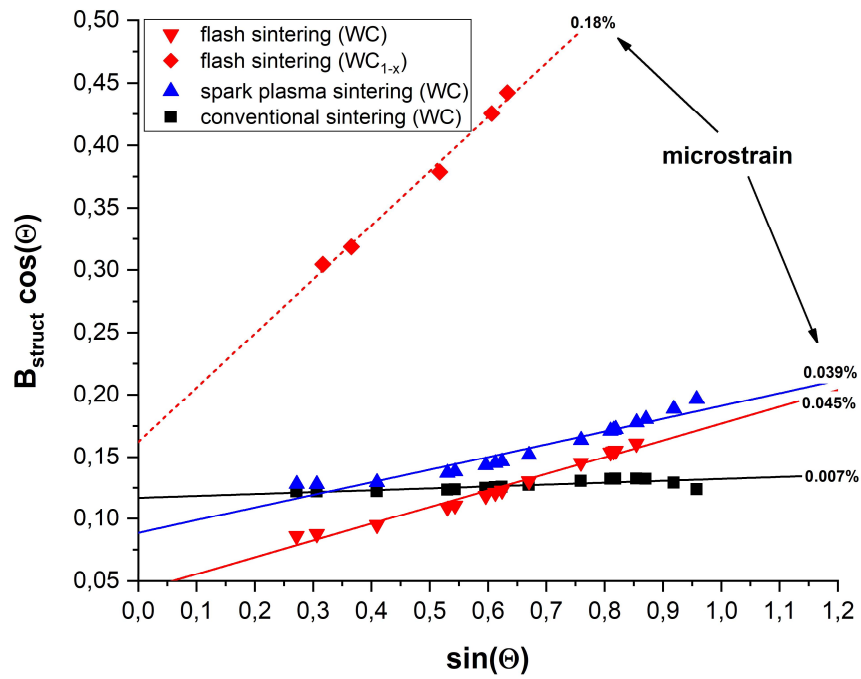
Figure 75 Linear Williamson-Hall plot: discrimination of the size and defects broadening contribution to XRD peaks. The % indicates the level of microstrain in the analysed samples.

TEM & Transmission Kikuchi Diffraction (TKD) analyses

Lamella preparation

An electron transparent portion of the flash sintered material, produced as shown in Figure 76, can be used to refine with high precision the elemental composition of the cubic phase estimated from XRD analysis to be in between $(W_{0.8}Cr_{0.1}V_{0.1})C$ and $(W_{0.6}Cr_{0.2}V_{0.2})C$. The lamella includes several cubic grains, identified as WC_{1-x} in Figure 77 (b) (ICDD card no. 04-022-5716) by analysing the Kikuchi diffraction patterns in transmission mode (TKD). A portion containing this phase was analysed by EDXS within the TEM, which generated the high-resolution elemental maps of Figure 78.
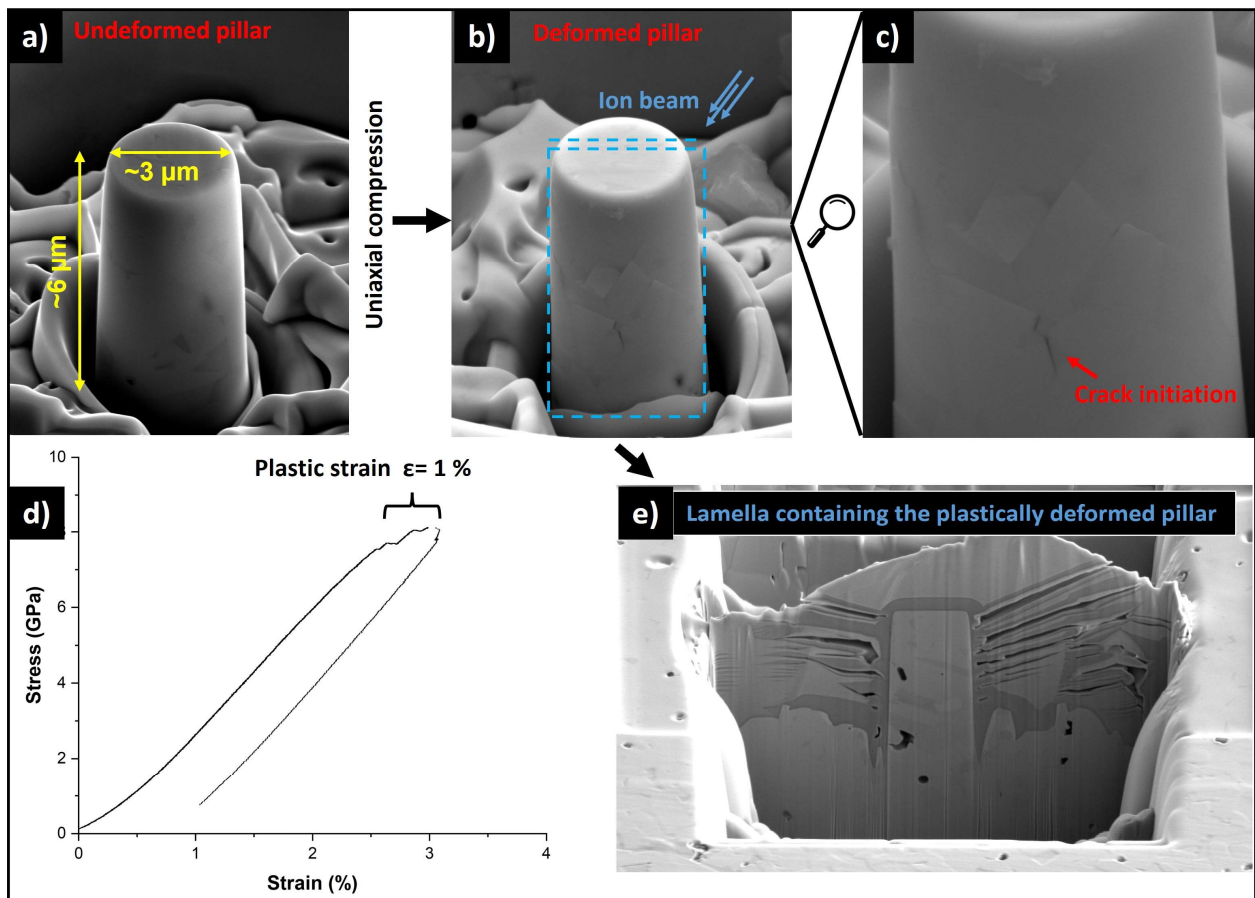
Figure 76 Procedure for studying the small-scale deformation behaviour of tungsten carbide grains. An electron transparent portion of the material, namely a "lamella" (e) was prepared by focused ion beam (FIB) on a pillar (a) which was preliminarily uniaxially deformed (b) above the elastic limit (d). A magnified view of the deformed pillar (c) points out the initial stage of controlled crack propagation in the deformed pillar.
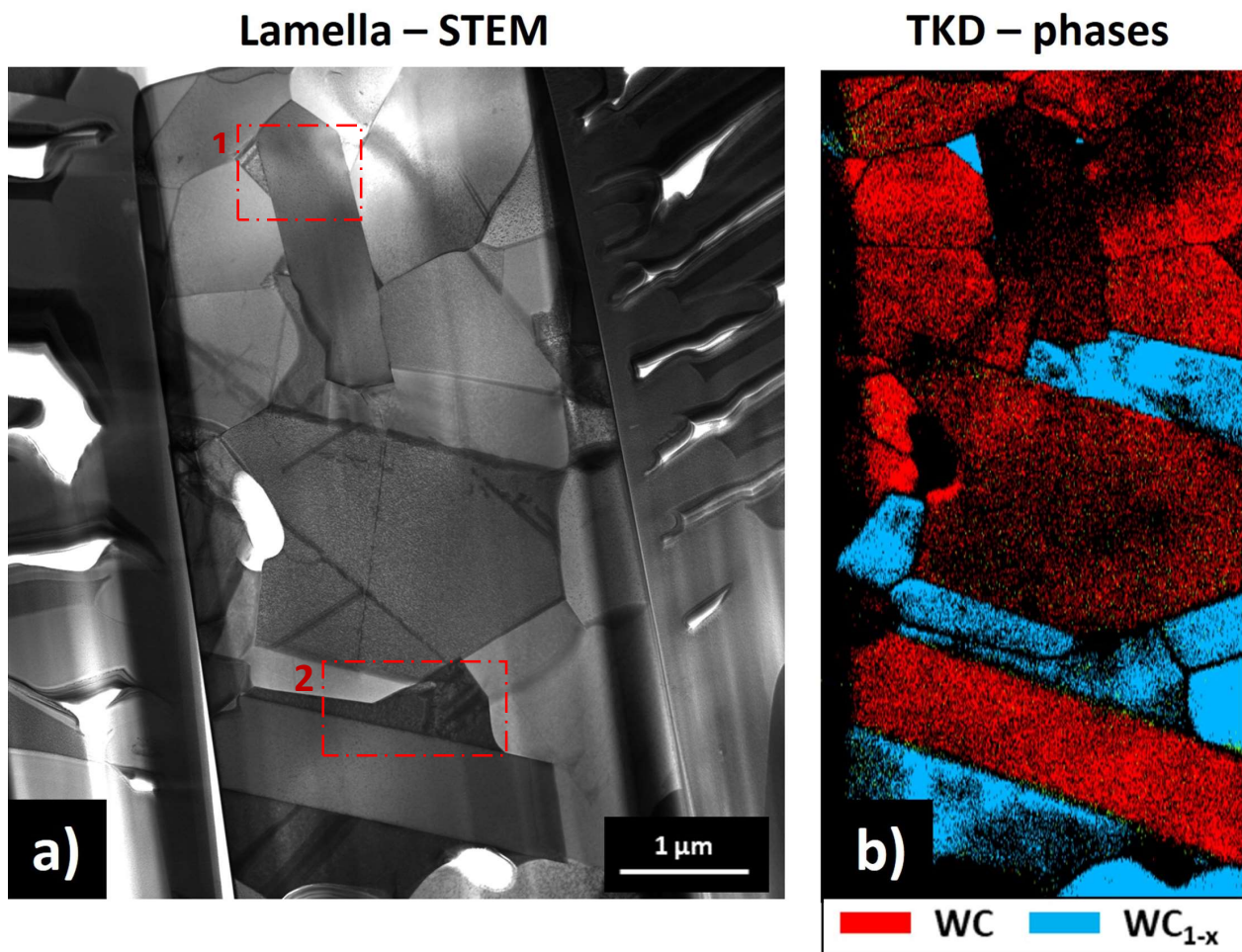
Figure 77 STEM micrograph (a) and TDK analysis (b) of a lamella containing a significant portion of cubic grains. The red boxes (1 & 2) show the areas selected for the successive analyses.

As previously stated, the W atoms are partially substituted by Cr and V in the cubic lattice, the elemental map of Figure 78 (b) clearly showing a lower concentration of tungsten in the grains identified as cubic from the TKD analysis (Figure 77). All cubic grains (Figure 77) contain Cr and V as segregated elements, this confirming the EDXS results of Figure 70 performed on the polished cross section. From the elemental composition, it is possible to determine the average composition $(W_{0.79}Cr_{0.12}V_{0.09})C_{1-x}$, very close to that estimated by fitting the occupancy site in the XRD analyses (Figure 71). The results show that Cr is present in a slightly higher amount than V, in accordance with the higher amount detected in the starting powder (Figure 68) and in the polished cross section (Figure 70).

EDXS analysis of the lamella
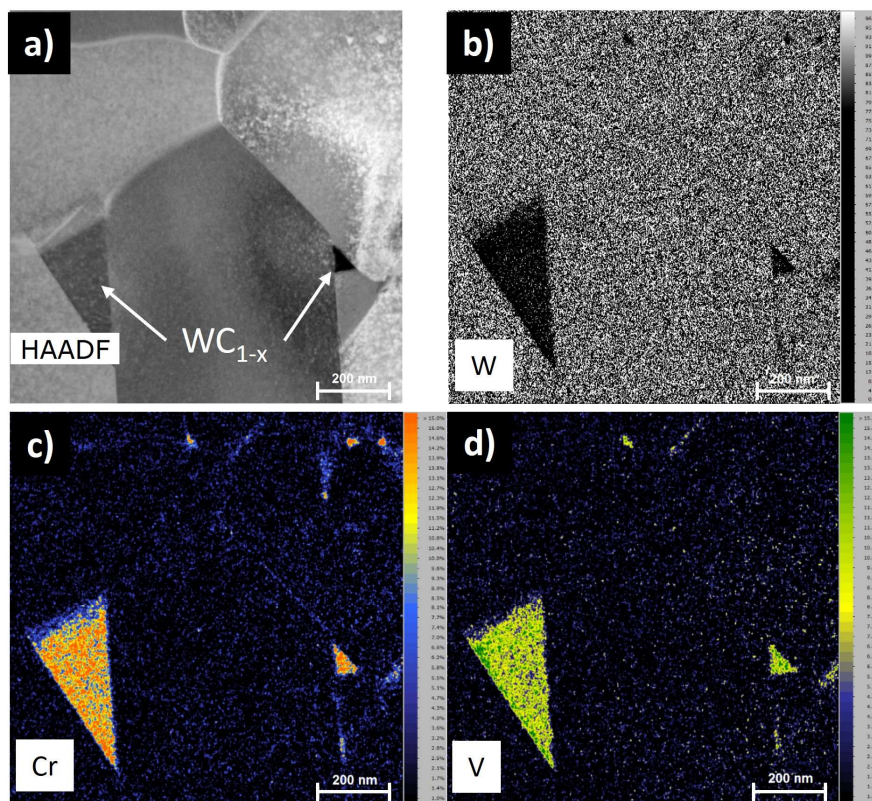
Figure 78 EDXS analysis of the lamella of Figure 77 (box 1). High-angle annular dark-field (HAADF) micrograph of the analysed area (a); quantitative elemental maps of W (b), Cr (c) and V (d).

From the determined composition $(W_{0.79}Cr_{0.12}V_{0.09})C_{1-x}$ it is possible to estimate the effect of Cr and V

on the cubic lattice parameter of WC_{1-x} (Table 8) according to the Vegard's law [205]:

$$a_{A_{(1-x)}B_x} = (1 - x)\, a_A + x\, a_B \tag{34}$$

where the crystal lattice constant of an alloy $(a_{A_{(1-x)}B_x})$ is linearly related to those of its constituent

concentrations, (1-x) for A and x for B.

The lattice constant for $(V_{0.5}W_{0.5})C$ and $Cr_{0.4}W_{0.6})C$ (ICDD cards no. 04-001-6526 and 04-018-1296,

respectively) are considered and the following results are obtained:

$$
\begin{aligned}
a_{(W_{0.5}V_{0.5})C} &= 0.5\, a_{WC} + 0.5\, a_{VC} \rightarrow 0.4226\ (nm) \\
&= 0.5 \cdot 0.426 + 0.5\, a_{VC} \rightarrow a_{VC} = 0.4192
\end{aligned}
\tag{35}
$$

$$
\begin{aligned}
a_{(W_{0.6}Cr_{0.4})C} &= 0.6\, a_{WC} + 0.4\, a_{CrC} \rightarrow 0.4193\ (nm) \\
&= 0.6 \cdot 0.426 + 0.4\, a_{CrC} \rightarrow a_{CrC} = 0.40925
\end{aligned}
\tag{36}
$$

The lattice constant of $(W_{0.79}Cr_{0.12}V_{0.09})C_{1-x}$, in the condition of $C_{1-x} = C_1$ (y=1 in Figure 79), can be

calculated from the values of a_{VC}, a_{CrC} and a_{WC}, this latter being the lattice constant of WC_{1-x} evaluated

from Eq. 32 at y=1. Therefore:

$$
\begin{aligned}
a_{(W_{0.79}Cr_{0.12}V_{0.09})C}(y = 1) &= 0.79\, a_{WC} + 0.12\, a_{CrC} + 0.09\, a_{VC} \\
&= 0.4233\ (nm)
\end{aligned}
\tag{37}
$$

This result can be included in Eq. 32 to consider also the effect of Cr and V on the cubic cell parameter:

$$a_{(W_{0.79}Cr_{0.12}V_{0.09})C_{1-x}} = 0.4015 - \Delta a + 0.0481\, y - 0.0236\, y^2 \tag{38}$$

where $\Delta a = a_{WC_{1-x}}(y = 1) - a_{(W_{0.79}Cr_{0.12}V_{0.09})C_{1-x}}(y = 1) = 0.0026\ [nm]$.
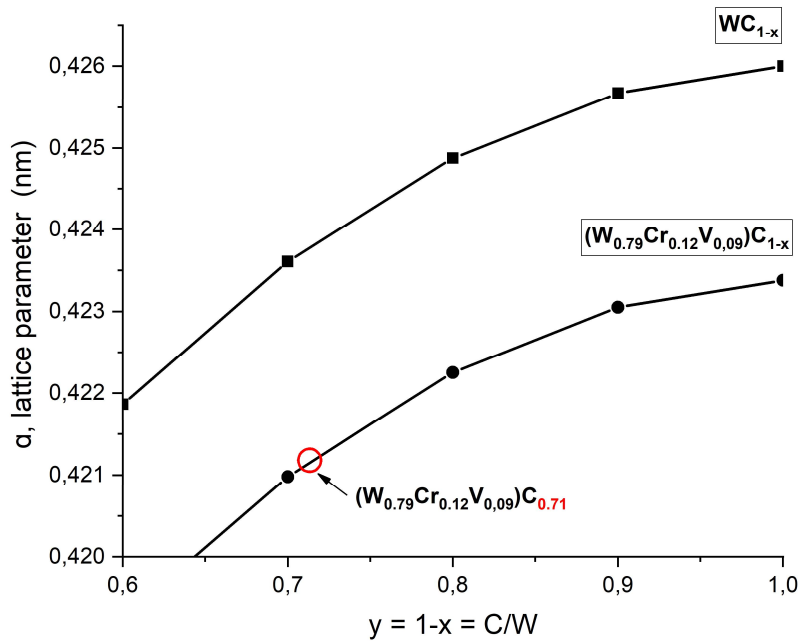
Figure 79 Lattice parameter a as a function of carbon content for cubic tungsten carbides WC1-x (Eq. 32) and the (W0.79Cr0.12V0.09)C1-x modification (Eq. 38). The red circle indicates the resulting carbon content of (W0.79Cr0.12V0.09)C1-x for a lattice parameter of a=0.4211 nm, as evaluated from the XRD pattern fitting (Figure 71).

Figure 79 shows the plot of Eqs 1 and 7. The coupled effect of the substitutional elements (Cr and V) results in a decrease in the WC_{1-x} cubic cell lattice parameter, according to the lower atomic radius of Cr and V with respect to W. The lattice parameter evaluated from the fitting of the experimental diffraction pattern of this new cubic phase (Figure 71), a= 0.4211 nm, can be used in Figure 79 to estimate the actual carbon content of the $(W_{0.79}Cr_{0.12}V_{0.09})C_{1-x}$ phase which, from Eq. 38, is equal to 0.71. The carbon content of $(W_{0.79}Cr_{0.12}V_{0.09})C_{0.71}$ corresponds to 41-42 at%, a value which now sits correctly within the carbon stability range of the cubic-WC phase of Figure 72 (a) [22].

Plastic deformation behaviour of cubic tungsten carbide

The portion of the WC grains embodied in the electron transparent lamella of Figure 77 experienced a high level of stress as shown in Figure 76 (d), the original pillar having been subjected to a maximum compressive load of about 8 GPa.

During the compression of the WC pillar (Figure 76), the stress is high enough to overcome the elastic limit of the material, as shown from the stress-strain curve (Figure 76 (d)). The advantage of this small-scale compression test lies in the possibility of reaching the high stress level required to activate plastic deformation mechanisms in WC before its catastrophic failure [206]. The lamella produced in Figure 76 (e) contains plastically deformed grains, both hexagonal and cubic, as revealed by the TKD analysis (Figure 77 (b)). The grains in the lamella exhibit some evidence of dislocation activity as demonstrated by several straight dark bands in hexagonal and cubic grains. It is of interest for this work the deformative mechanism active in the cubic lattice at room temperature, not reported in the literature. For this reason, the cubic grain in area 2 of Figure 77 (a), characterized by high density of such dark bands, was selected for further analyses. This cubic grain (Figure 80, (a)) is oriented very close to the zone axis (101) as evaluated from the IPFZ map in Figure 80 (b). The grain appears completely tilted towards the zone axis (101) within TEM. This can be proved by indexing the electron diffraction spot pattern of Figure 80 (d), acquired on the oriented grain of Figure 80 (c), with the CrysTBox software algorithm [31] using the cubic crystalline structure ICDD card no. 04-001-6526, as reference (Figure 80, (e)).
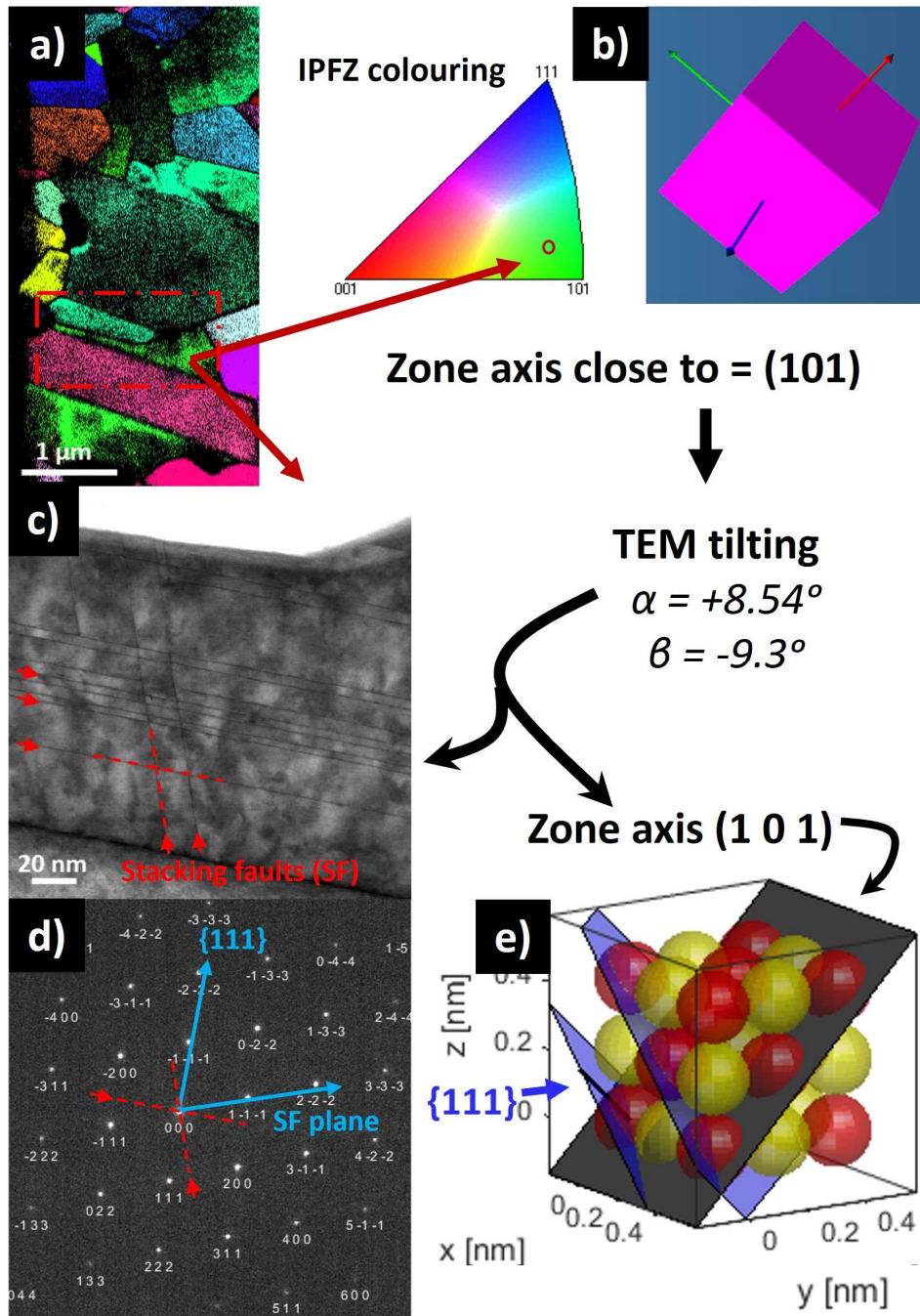
Figure 80 Inverse pole figure zone (IPFZ) map (a) obtained from TKD analysis of the lamella in

Figure 77 (box 2) and (b) orientation of the cubic grain under investigation (red box). STEM

micrograph (c) of the cubic-WC grain and its selected area electron diffraction pattern (SAED) (d)

The oriented grain of Figure 80 (c) contains a large number of very narrow dark bands, whose nature can be better resolved from the high-resolution images of Figure 81 (a & b). The atomic resolution in Figure 81 (b) allows to discriminate the nature of these defects as stacking faults; the stacking sequence of atomic planes is altered when these dark bands cross the lattice. These SF appear so narrow to be visualized as single lines in Figure 80 (c); indeed, in Figure 81 (b), the distorted region seems to be limited to single atomic planes. According to the diffraction contrast in TEM analyses, the faulted planes have to be aligned with the direction of the electron beam and, since the grain is oriented with a zone axis (101), all SF planes in Figure 80 (c) have to be orthogonal with respect to this plane.

The actual SF planes, marked by the red line in Figure 80 (c), belong to the {111} system, as proven by the blue line, drawn at 90º with respect to the red lines, in the reciprocal lattice of Figure 80 (d). Figure 80 (e) shows a sketch of the cubic cell, where the zone axis (101) (black plane) is perpendicular to the SF planes. These SF are actually the results of plastic deformation driven by the movement and interaction of partial dislocations. It is possible to reach this conclusion from the SF network observed in Figure 81 (a & b), when different stacking faults intersect each other's. Following the work of Xiao et al. [207], the SF network is the result of an interaction of partial dislocations with previously formed SF (Figure 81, (c)), when the shear stress is high enough the partial can slip away from the intersected SF leaving a misalignment step (Figure 81, (d)). Thus, the misalignments observed in Figure 81 (b) can be only caused by the movement and interaction of partial dislocations with previously formed SF creating the complex network shown in Figure 80 (c) and Figure 81 (a).
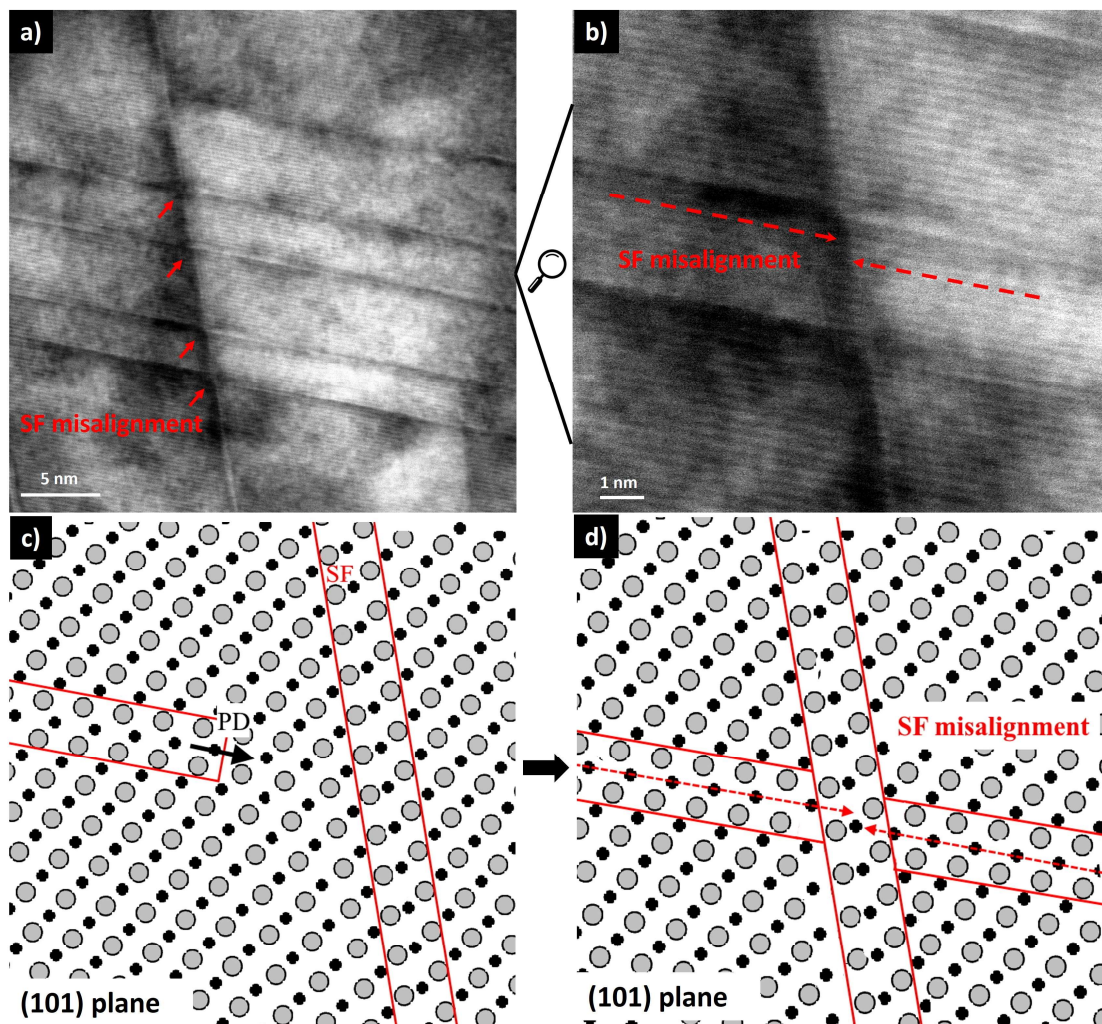
Figure 81 STEM (a) and HR-STEM (b) micrographs of a portion of the cubic WC grain analysed in Figure 80; the red arrows points the misalignment observed in the SF network. The interaction of moving partial dislocation (PD) with pre-existing SF (c), on the (101) plane, and the generation of SF misalignment (d) is also represented graphically

According to these findings, cubic tungsten carbide can be deformed plastically at room temperature through the movement of partial dislocations across {111} planes. For comparison, the system {111} <110> is a well-known primary slip system in FCC metals, although in nonstoichiometric cubic transition metal carbides, such as TiC, VC, ZrC etc., different slip systems result active at room temperature, like {110} <110> or, more rarely, {001} <110> [208]. Several researcher argued that the characteristic brittle-to-ductile transition of these cubic transition-metal carbides is attributed to the activation of the slip system {111} <110> at high temperature, by a partial weakening of the strong directional M-C bonds that limit slip on such a plane [208–211]. In this perspective, cubic WC may possesses a higher room temperature plasticity in comparison to other cubic carbides with similar rock-salt structure.

Nanoscale mechanical properties: hardness & elastic modulus maps

Cubic WC is characterized by a noticeable lower hardness and elastic modulus with respect to the hexagonal phase. The nanoindentation analysis of Figure 82 (1) shows how the elastic modulus (E) of the cubic phase is about 230-310 GPa, considerably lower than that of WC (650-700 GPa). The hardness follows the same behaviour, with a drop from 30 GPa down to 10-15 GPa. Shanenkov et al. obtained similar results (Young's modulus ≈ 300 GPa, hardness ≈ 10-25 GPa) from nano-indentation in pure WC_{1-x} thin film, deposited on a metallic surface by high-speed plasma spraying [212]. The comparison between phase composition and grain orientation discloses the effect of this latter on small-scale properties; elastic modulus and hardness of area-2 show small variations in proximity of small pores, but not between differently oriented grains. In this perspective the noticeable difference in E and H in the region around the cubic grains (Figure 82, (1)) can be only addressed to the presence of cubic grains, which somehow affects the elastic modulus and hardness of the adjacent material.

The atomic force microscope (AFM) maps (Figure 83) shows the condition of the surface reached after the polishing procedure. Directional scratches caused during polishing and small residual pores are present in both area-1 and area-2. In particular, the area containing the cubic phase, $(W_{0.79}Cr_{0.12}V_{0.09})C_{0.71}$, results in a strong contrast in both imaging modes, gradient (μN) and topographic (nm). The dark topographic contrast of area-1 identified as cubic by EBSD (Figure 82, (1)) corresponds to a small depression on the surface, which is absent in the area without the cubic phase (Figure 83 (2)). This can be the result of a larger material removing rate from the surface upon polishing; the cubic phase, being softer than WC, is removed more quickly leaving a small depression on the surface as shown by the AFM images of area-1.
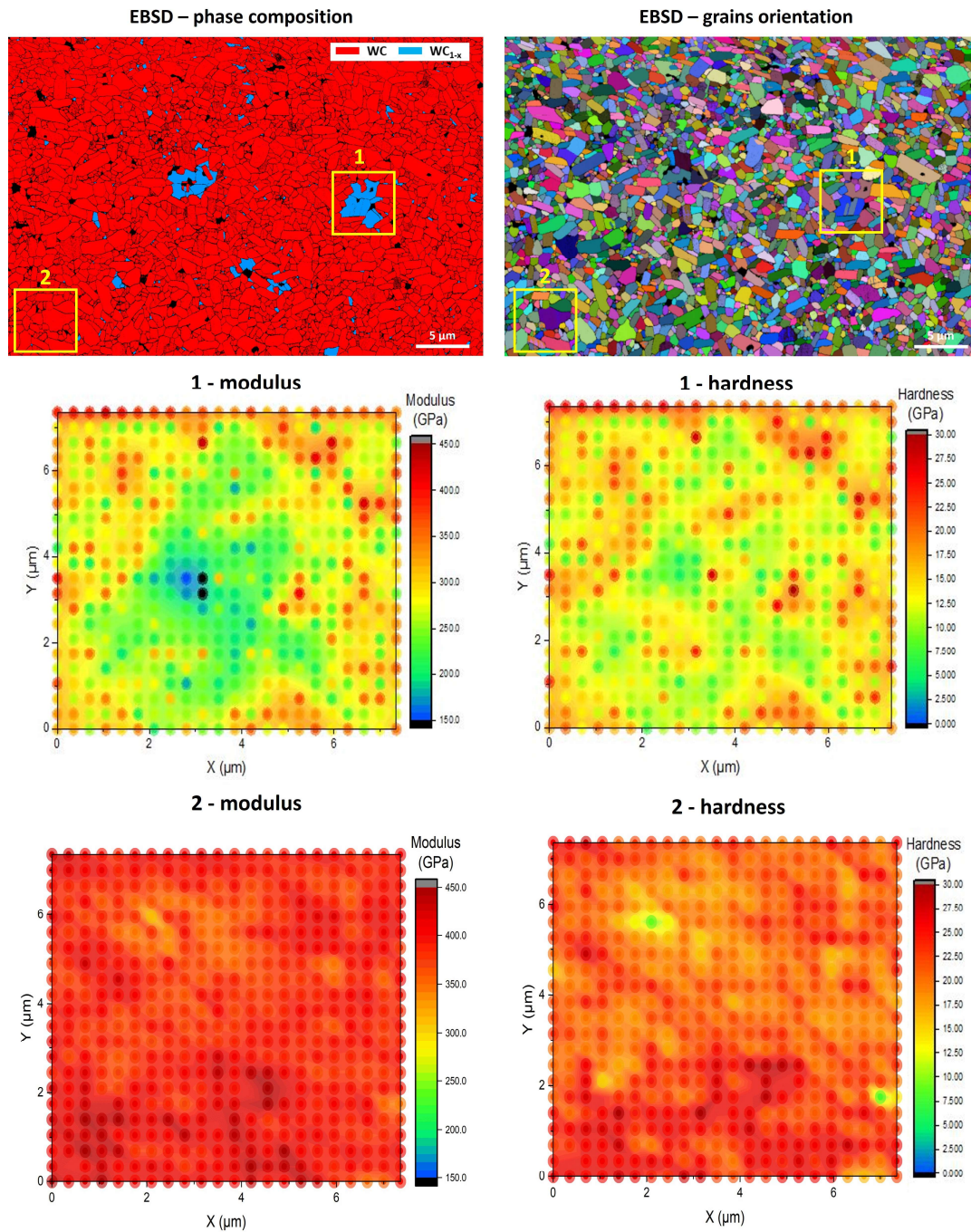
Figure 82 Nanoindentation maps for hardness and reduced elastic modulus acquired on the polished cross section of the flash sintered material; the area analysed by EBSD is a zoom-out view of Figure 70. Two distinct regions are mapped: in the presence of the cubic phase (area-1) and in an area with hexagonal grains, only (area-2)

168

AFM – area 1

Gradient contrast Topographic contrast

area 2

10 µm
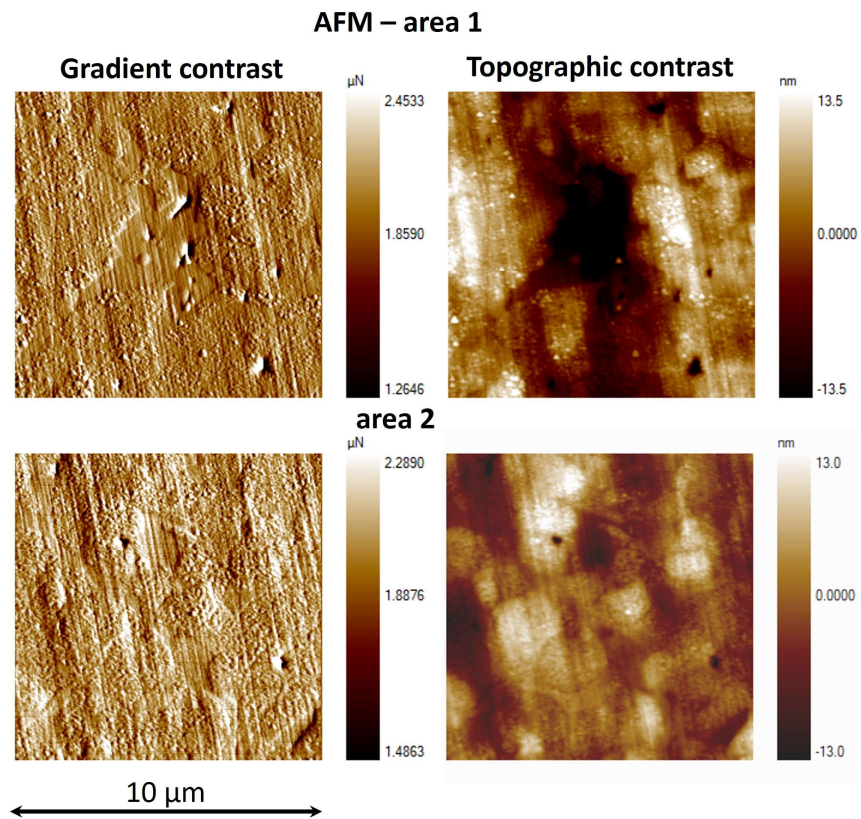
Figure 83 Atomic force microscopy (AFM) images taken in area-1 and area-2 of Figure 82 prior to nano-indentation testing

3.2.4 Conclusions

Cubic tungsten carbide was successfully obtained as a second phase during the electrical resistance flash sintering (ERFS) of commercial WC nanopowders. The low oxygen content in the nanopowders limits the decarburization phenomenon, thus avoiding the WC$\rightarrow$W$_2$C transformation during both SPS and ERFS processes. However, only during the flash process, the limited loss of structural carbon and the unconventional high sintering rate allow to produce and stabilize the high-temperature WC$_{1-x}$ structure rather than W$_2$C.

Cubic tungsten carbide was characterized as (W$_{0.87}$Cr$_{0.12}$V$_{0.09}$)C$_{0.71}$ with a lattice constant of a=4.211 Å, which disagrees with the ICDD card no. 04-022-5716 (a=4.234 Å) due to the presence of Cr and V in solid solution. Phase stability simulation (CALPHAD) of the W-C-Cr-V quaternary systems reveals an opposite role of Cr and V on WC$_{1-x}$ phase stability and their simultaneous presence in (W$_{0.87}$Cr$_{0.12}$V$_{0.09}$)C$_{0.71}$ does not explain its stability. Vacuum annealing experiments determine the decomposition of (W$_{0.87}$Cr$_{0.12}$V$_{0.09}$)C$_{0.71}$ into WC and W$_2$C products in the 700-1100°C temperature range, thus pointing out its metastable character.

The (W$_{0.87}$Cr$_{0.12}$V$_{0.09}$)C$_{0.71}$ cubic phase is softer than WC, with an hardness ranging from 10 to 15 GPa and an elastic modulus of about 230-310 GPa. Cubic grains reveal a high amount of stacking faults arranged in a network of narrow bands perpendicular to each other, this network being the result of partial dislocations interacting with {111} stacking fault planes.

The results reported in this work point out the great advantage of the ERFS process to produce new composite materials based on WC/WC$_{1-x}$. The softer character and the room temperature plasticity, via {111} active slip planes, make cubic WC a potential candidate to optimize the hardness/toughness ratio of tungsten carbides products.

Chapter 4

Mechanical properties of flash sintered WC

Chapter 4 is focused on the mechanical properties of BTC polycrystalline materials consolidated by the ERFS process. To understand if and how the flash event affects the mechanical properties of the consolidated materials the same tests were performed on materials sintered by ERFS and by SPS. This allows a discussion of the effects of fast (SPS) and ultrafast sintering (ERFS) processes on the mechanical behaviour of WC ceramics. Paragraph 4.1 investigates the strength and deformability of BTC sintered ceramics at the small-scale: by performing a micropillar compression study. Conversely, in paragraph 4.2 the study is focused on the macroscopic mechanical properties, such as hardness, fracture toughness and failure mechanisms of bulk samples.

4.1 Room and high temperature deformability of WC micropillars

Isacco Mazo[#], Miguel A. Monclus [†], Jon M. Molina-Aldareguia [§, †], Vincenzo M. Sglavo[#‡]

Department of Industrial Engineering, University of Trento, via Sommarive 9, Trento, Italy

† IMDEA Materials Institute, C/ Eric Kandel 2, 28906, Getafe, Madrid, Spain

‡ INSTM, National Interuniversity Consortium of Materials Science and Technology, Trento Research Unit, Via G. Giusti 9, 50123 Firenze, Italy

ABSTRACT

The study aims to unravel the effect of fast and ultrafast electric current-assisted sintering (ECAS) technologies on the plasticity of ultrahard binderless tungsten carbide (BTC) ceramics. This work explores the small-scale deformation of polycrystalline micropillars made of materials consolidated by Spark Plasma Sintering (SPS) and Electrical Resistance Flash Sintering (ERFS) processes. Micropillars, 3 µm in diameter, were prepared by focused ion beam (FIB) and compressed ex and in-situ at both room and high temperature (700 ºC). Electron-transparent lamellas were milled out from the pillars plastically deformed at different strain levels to carry out Transmission Kikuchi diffraction (TKD) and HRTEM analyses. At room temperature, BTC micropillars show similar mechanical responses under compression, reaching outstanding yield strengths (8-11 GPa) and possibly accommodating limited plastic strains up to 3-5 % because of a dislocation-assisted toughening mechanism. At 700 ºC, the pillar's yield strength drops to around 1.5-2 GPa in both materials, accompanied by the relevant temperature-activated plasticity, as observed by Transmission Kikuchi diffraction (TKD) and HRTEM analyses. However, only the pillars prepared from the flash-sintered ceramic can be homogeneously deformed up to ≈50 % of strain, while the SPS ones fail macroscopically at strains of ≈20-25 % upon localization of plastic strain at shear bands.

4.1.1 Introduction

Binderless tungsten carbide (BTC) ceramics have been recently studied as an alternative to the cemented carbide counterpart. The soft and ductile binder phase, usually Co, is an excellent technological solution to resolve, at the same time, the low sinterability and toughness of tungsten carbide. Although the relatively low melting point and limited chemical, oxidation and radiation resistance of the metal phase limit the applicability of cemented carbide (WC/Co, WC/Ni or WC/Fe) components at high temperature and/or in harsh environments, they have found an extensive use as tool inserts, abrasive and wear resistant parts, high pressure nozzles and sealings in many industrial sectors [213,214]. In addition to those critical applications, BTC components are regaining focus from the research community as neutron shielding material in fast breeder reactors [13] and as a promising candidate for plasma-facing components of fusion reactors [14,16,215]. Despite its intrinsic brittle behaviour, monolithic WC shows unexpectedly higher thermal shock resistance temperature strength than cermets under extreme heat flux conditions (edge localisation and plasma disruption events) [18]. WC and some of its composites (WC/B_4C, WC/TiC, etc.) also combine neutron reflecting and absorbing capability of heavy (W) and light elements (C or B), possibly outperforming metallic W-based neutron shielding materials [14,16]. In the absence of a metallic binder, two are the main challenges for the successful production of BTC products [186]: (i) obtaining highly dense bodies (98-99%+ of relative density) upon sintering and (ii) boosting the inherently low fracture toughness. The extremely limited self-diffusivity of W and C atoms [1] makes pressureless sintering of pure WC powders fairly feasible [216]. Only high pressure-high temperature and fast sintering techniques lead to reasonably good results in terms of density, grain size, phase stability and hardness [37,217,218]. Out of such techniques, the most promising for consolidating BTC powders is spark plasma sintering (SPS) [33], which allows obtaining fully dense bodies with good control of the final microstructure in terms of grain size and semicarbide (W_2C) formation [35,70]. Typically, BTC

products consolidated by SPS achieve 98-99+% density, hardness of about 28-30 GPa and fracture toughness in the range of 4-6 MPa m$^{1/2}$ [36,70], this latter being often too low for most structural applications. Bulk ceramics, BTC components included, are typically characterised by the trade-off relationship between hardness and fracture toughness [36,196]: the harder the material, the less plasticity is available for intrinsic toughening mechanisms [27]. Toughening phenomena can sometimes be activated in BTC using fibers, whiskers or nanotubes reinforcement, grains bridging/interlocking, crack deflection in coarse grain or laminated structures, particles dispersion etc. [196]. Certain oxides are used as alternative binders to increase the material toughness up to 8-9 MPa m$^{1/2}$, introducing crack bridging and deflection mechanisms [11]. Nevertheless, dispersing particles and/or second oxide phases modify the material structure inevitably, impairing not only the native WC hardness, with a drop from 30 GPa down to 18-22 GPa, but especially its thermomechanical [215] and thermophysical [13] properties. Of critical importance is the anomalous high thermal conductivity of monolithic WC [17] (as high as 100-200 W/m K at room temperature [13,19]), essential for high heat flux applications [13,16,219], which decreases promptly when low thermally conducting ceramics are included [16,220]. Thus, using monolithic BTC for structural components requires new strategies to make this material more damage tolerant, which translates into altering the intrinsic toughening mechanisms of WC [27].

Different deformability has been recently reported for some hard ceramics produced by flash sintering [75]. It was argued that the very high mass transport and flow rate during the flash process accounts for the development of shear stresses at the particles' neck, intense enough to overcome the material yield strength at the high sintering temperature. It was then demonstrated that during flash, the high-temperature deformability is significantly enhanced by the athermal effect, which lowers the activation energy for plastic flow [221].

Although the question about the correlation between the flash event and plastic flow is still under debate within the scientific community [222], "post-flash" dislocations were observed in TiO2 [223], Er(Mn,Ti)O3 [224] and yttria-stabilised zirconia (YSZ). In the latter case, shear stresses over 1 GPa were estimated during flash sintering, high enough to allow dislocation pile-up [78]. The copious defects introduced during flash sintering lead to improved plasticity, as reported for YSZ [225], TiO2 [77] and SrTiO3 [226–228]. The application of external electric fields can be used to alter the defect chemistry of oxide ceramics, modifying the oxygen vacancy concentration along grain boundaries [227]. Flash sintering experiments under a direct current (DC) alter the redistribution of oxygen vacancies, promoting their migration towards the negative electrode [226]. This migration was demonstrated to affect the plasticity of SrTiO3 single crystals by favouring the dislocations nucleation over their mobility [228,229]. Within this area of interest, the present work aims at understanding if flash sintering can also affect the deformability of a non-oxide ceramic, like tungsten carbide (WC). This study wants to disclose if the ultrafast sintering of a non-oxide ceramic promoted by low AC electric fields (~5 V/cm) has a role in activating dislocation-induced plasticity at room and high temperatures.

4.1.2 Materials & Methods

Samples preparation. The mechanical properties of materials consolidated by ERFS (ultrafast/flash sintering) and SPS (fast sintering) were studied to understand the difference at the micron-scale. Two different WC nanopowders (Inframat Advanced Materials®) were selected for producing the samples. The powders, as already reported in [164], are characterised by different oxygen content: 1.21 wt% and 0.28 wt% for the oxidised (WC_{ox}) and purest one (WC_{pure}), respectively. Ultrafast (ERFS) and fast (SPS) sintering of said powders produced four different monolithic WC samples, characterised by different mineralogical composition (Figure 85). Sintering of oxidized nanopowders produced biphasic

composites (WC/W$_2$C = 60/40 vol%) [164]. Conversely, single phase material and metastable cubic WC$_{1-x}$ phase embedded in WC matrix were obtained by SPS and ERFS, respectively. Accordingly, the specimens prepared in the present work are labelled as FS$_{ox}$, SPS$_{ox}$, FS$_{pure}$ and SPS$_{pure}$ (Figure 85). The ERFS process and details on the composition and microstructure of the obtained materials have been previously reported [117,118,164]. The SPS samples were consolidated by Dr. Sinter 1050 apparatus at K4Sint Srl (Pergine Valsugana, Italy); 20 g of powder were poured in a 20 mm diameter graphite die and sintered at 2100ºC for 5 min under 60 MPa uniaxial pressure, using a heating rate of 200ºC/min.

Microstructure analysis. The sintered pellets were cut along the direction (axial) of the applied electric current and pressure and polished with diamond abrasive pastes up to a mirror-like surface (1 μm size). The polished surfaces were analysed by EBSD within a FEG-SEM microscope (ThermoFischer® Apreo 2S LoVac). The density of crystalline defects was estimated for the four sintered samples by X-Ray diffraction using PANalytical EMPYREAN diffractometer, with Cu-Kα1 radiation (1.54060 Å) in a line focus configuration. Linear Williamsom-Hall plots were generated from the line-broadening analysis of the corresponding diffraction patterns [230]. Diffraction patterns were acquired in a Bragg-Brentano geometry with divergent optics (FDS 1/8 and 5 mm mask), a Ni-kβ filter and a 1-D detector. The following ICDD diffraction cards were used as reference: 01-084-5996 for WC, 00-035-0776 for α-W$_2$C and 00-020-1316 for cubic WC$_{1-x}$. A zero microstrain reference sample, with average grains size of 30 μm, was prepared by pressureless sintering the WC$_{ox}$ nanopowders at 2150ºC for 2 h inside an Astro® vacuum graphitic furnace.

Micropillars preparation and testing. Micropillars and lamellae were produced on the polished surfaces within a FIB-SEM dual-column microscope (Helios NanoLab 600i) operated at 30 kV. The pillars were produced following a 2-step approach with two concentric rings milling pattern: initially, a high FIB current (9.3 nA) was used to create a circular trench with the pillar at the centre and,

subsequently, at lower current (0.23 nA), the pillar's tapering angle was reduced (Figure 84 (a, b)). On average, pillars with a 3 µm diameter and 6 µm height were produced in a cylindrical trench with a 20 µm diameter.

Room temperature compression tests were carried out on the produced micropillars using a Hysitron triboindenter TI950 equipped with a 15 µm-diameter flat punch diamond indenter (Figure 84, e). Micropillars were compressed under displacement control at rates of 6 nm/s (corresponding to a constant strain rate of $\approx 10^{-3}$ s^{-1}). Most of the pillars were compressed up to failure to evaluate the maximum strain, while some tests were interrupted at different strain levels to observe any evidence of plastic deformation post-compression. High-temperature compression tests were performed to elucidate any difference in the activation of high-temperature deformation mechanisms between FS and SPS samples. High-temperature tests were carried out in-situ inside a Zeiss SEM Evo using a Hysitron PI88 picoindeter (Figure 84c). Micropillars (with a composition corresponding to FS_{pure} and SPS_{pure}) were compressed using a 10 µm-diameter flat punch (Figure 84, d and e) at strain rates of 10^{-3} s^{-1} and different levels of strain at room temperature and 700ºC. The contribution of the machine compliance to the obtained load-displacement curves was corrected by comparing the elastic response of the pillars compressed at room temperature with both systems (ex-situ and in-situ).

Lamellae preparation, TEM and TKD analyses. Electron transparent lamellae were prepared within the FIB-SEM from the pillars previously compressed above their elastic limit, i.e. with maximum strain in excess of 0.2%. The deformed grains contained in the lamellae were observed with a FEI Talos F200x TEM microscope operated at 200 kV. The results were compared with the grains' crystalline orientation and phase composition as acquired by Transmission Kikuchi Diffraction (TKD). TKD analyses were performed by positioning the lamella at a working distance of 5 mm between the electron beam of the FEG-SEM and the EBSD detector, with a tilting angle of 25º with respect to the horizontal axis. The

Kikuchi pattern was acquired at 30 kV with 25 nm step size and processed by AZtecCrystal® proprietary software. The Kernel Average Misorientation (KAM) map is then calculated based on the processed TKD data. KAM represents the average misorientation between each point in the microstructure and its neighboring points within a defined kernel size.
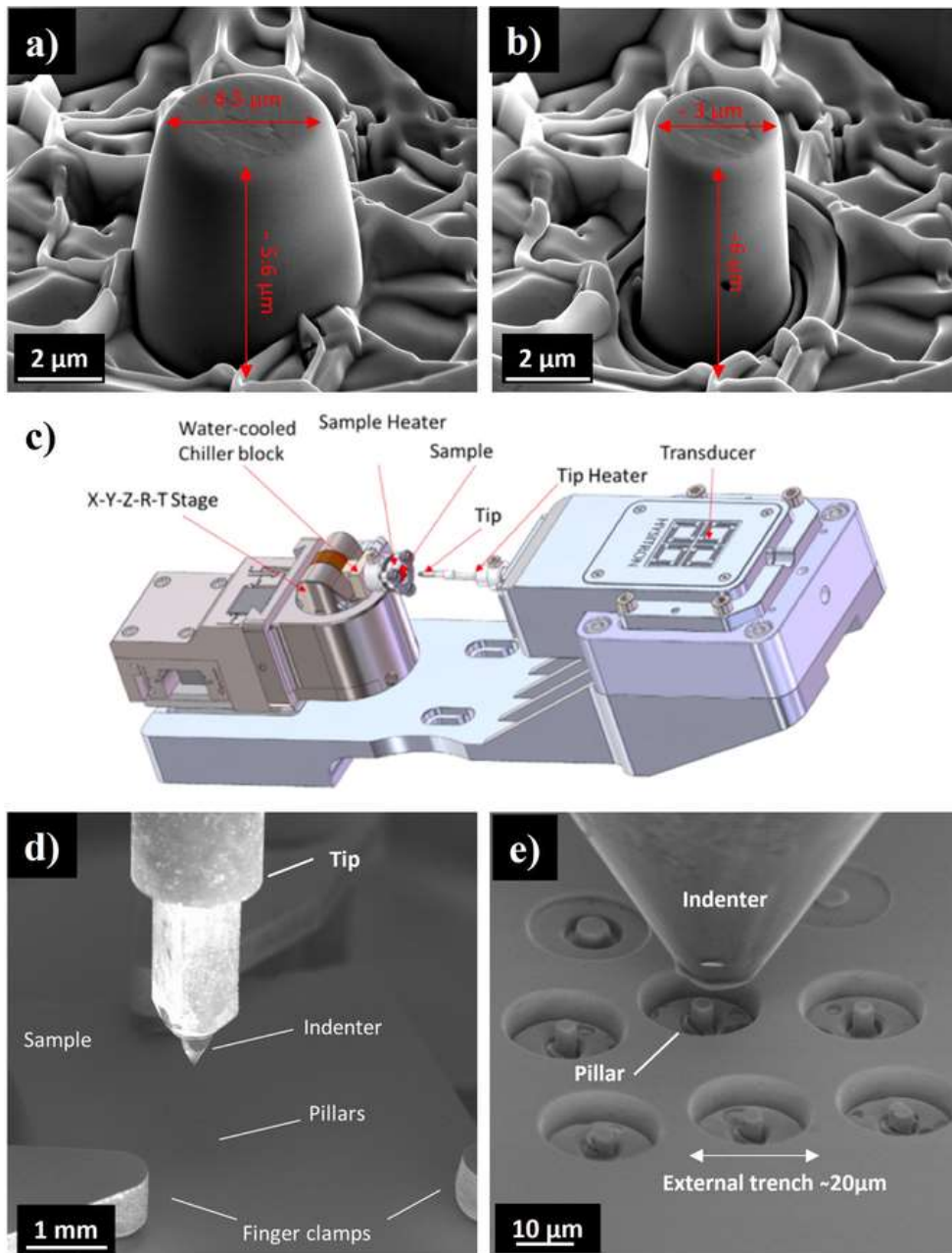
Figure 84 Sample, apparatus and procedure for in-situ compression tests on micropillars. FESEM images of the pillars under preparation: 1st step (a) raw milling of the trench and 2nd step (b) precise milling of the pillar's tapering angles. Picoindeter Hysitron PI88 for room and high temperature in-situ compression tests (c). FESEM images showing the sample mounting (d) and details of the indenter tip and trench diameter (e).

4.1.3 Results & discussion

Microstructure and phase composition

The microstructure and phase composition of the samples as detected by EBDS are shown in Figure 85. As previously pointed out, sintering of the low-oxygen content WC powder produced two materials free from the W_2C phase, but with 6-8 vol% metastable WC_{1-x} phase in the flash product (FS_{pure}). On the other hand, both samples obtained by sintering the oxidised nanopowder are characterised by a biphasic WC/W_2C microstructure (see Figure 2). The SPS_{ox} sample contains a lower amount of W_2C sub-carbide, around 4 vol%, and possesses finer grain size (Table 1) with respect to the FS_{ox} one. It is interesting to observe that the grain size is around 0.5 μm in the case of SPS, despite the material remaining at the high sintering temperature (2100ºC) for 5 min. Conversely, during the flash process, which only lasts 10 s, the grain size increases and, in the presence of the sub-carbide phase, it is higher than 3 μm. Abnormal grains, elongated and with a high aspect ratio, are observable in the two samples containing W_2C. SPS_{ox} sample contains only a few abnormal WC grains randomly distributed among finer WC and W_2C equiaxed grains, while the FS_{ox} is fully composed of such abnormal grains (Table 1).

It is known that W_2C, an hexagonal carbon deficient phase for WC, can accommodate a larger density of defects. Lantsev et al. proposed a relation between the W_2C phase, the occurrence of abnormal grain growth (AGG) and accelerated diffusion kinetics [36]. They experimentally measured a lower sintering activation energy in BTC materials with AGG, leading to the hypothesis of a change in the parameter for grain boundary (GB) diffusion. Since the activation energy for GB diffusion depends on its non-equilibrium density of defects at the boundary, the GB migrating into highly defective W_2C grains can absorb more lattice defects thus boosting its diffusion rate. The strong dependence of GB mobility on the defects density can explain the AGG observed in Figure 85 in the presence of the W_2C phase. The

same argument can also be used to explain the superior grain growth in FS_{ox} with respect to FS_{pure} since they are both produced by flash sintering, but no W_2C phase is present in the latter sample. Another possible explanation for the exaggerated grain growth occurring during flash sintering can reside in the actual temperature developed in the material during the flash event, which, if largely superior to that occurring in SPS (2100ºC), can partially explain the boost in diffusion and also in grain growth kinetic. Unfortunately, the temperature during flash is almost impossible to be measured precisely; the black body model by Raj [95], for a theoretical evaluation of the flash temperature, requires the sample to be inserted in a furnace of a known temperature. Nevertheless, if one considers the temperature issue, the large difference in grain growth between FS_{ox} and SPS_{ox} should also be observable between FS_{pure} and its SPS_{pure} counterpart, whose difference is only about 0.5 µm (Table 9). It is also necessary to remember that SPS operates under high uniaxial pressure of 60 MPa, which is well known to contrast grain growth in favour of densifying phenomena. This contribution is absent in the flash process, which operates at negligible uniaxial pressure (4 MPa). In conclusion, the only effect of the extraordinarily high temperature during flash can not justify the excessive grain growth observed in FS_{ox}; therefore, the presence of W_2C phase, in combination with the larger number of defects generated by flash, must have a role in the occurrence of such phenomenon.
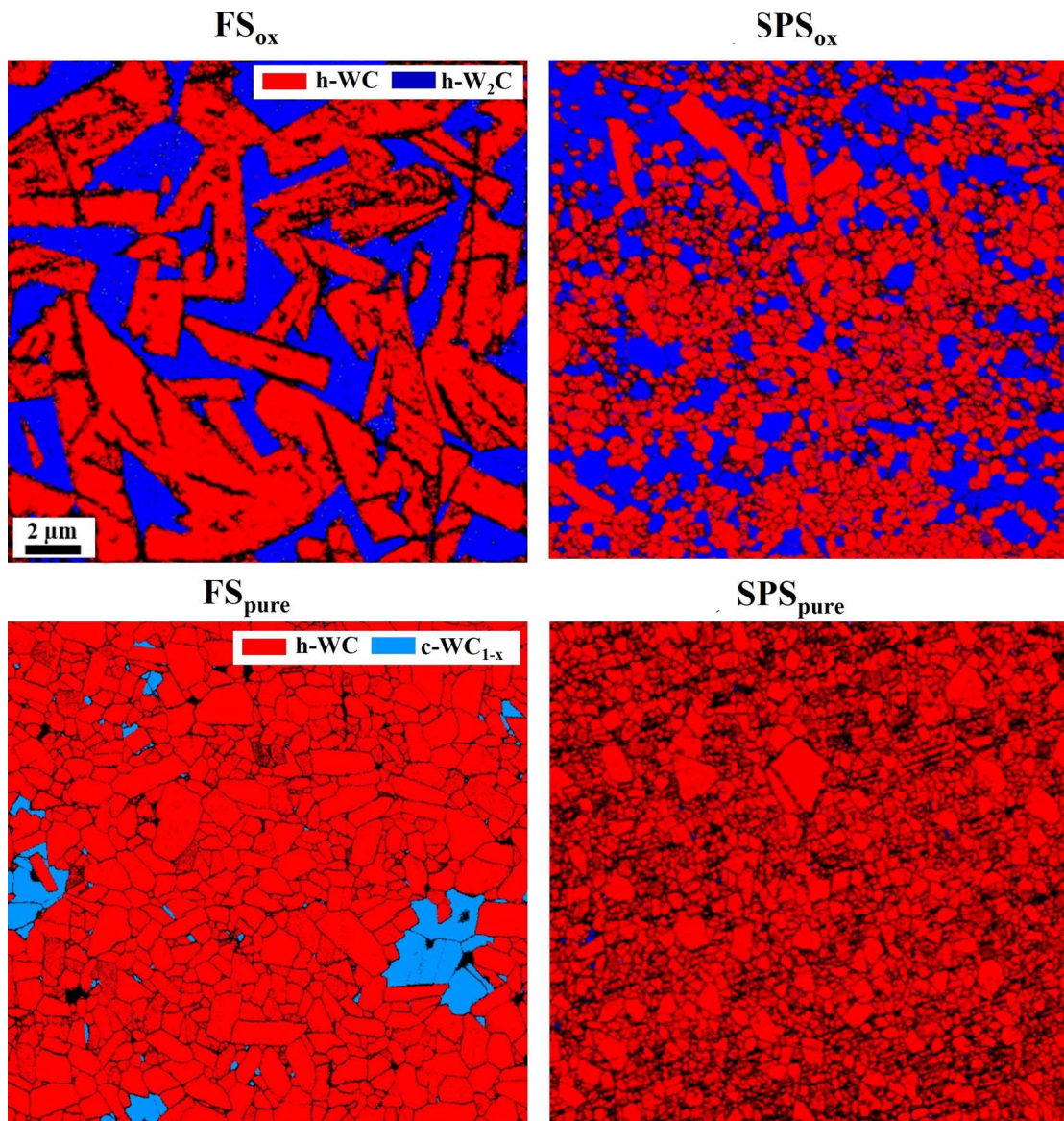
Figure 85 Electron Backscatter Diffraction (EBSD) phase analyses of the different WC samples.
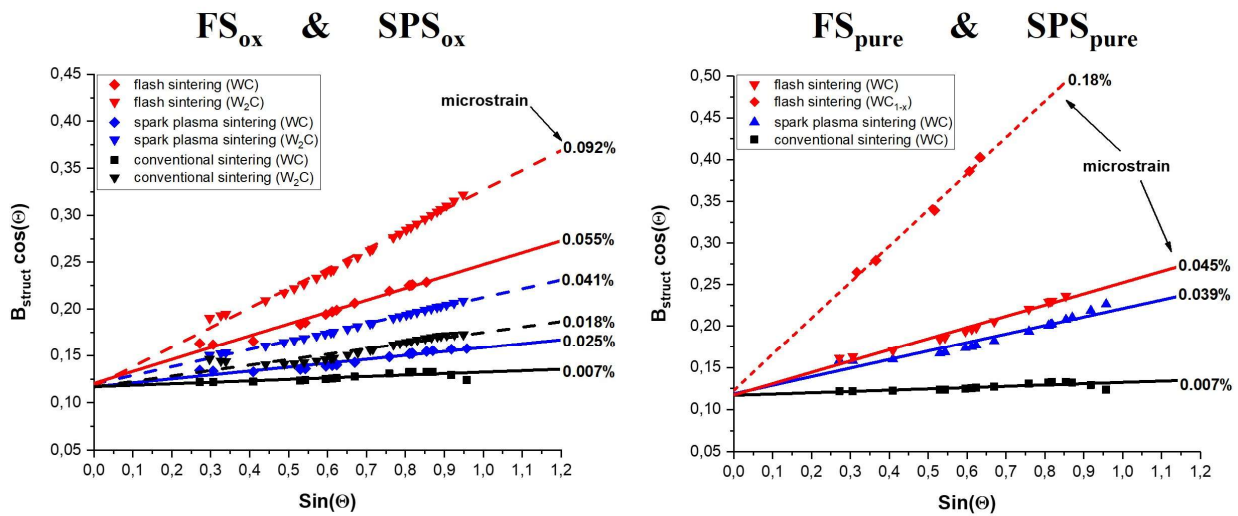
Figure 86 Density of crystalline defects (microstrain %) as estimated from X-Ray diffraction for the different phases present in the bulk samples of Figure 85. Black lines refer to the zero microstrain reference WC sample.

Figure 86 compares the lattice defects (microstrain) of the samples obtained by flash sintering and SPS. The estimation of the lattice microstrain is obtained from the analyses of the line broadening (B_{struct}) dependence of the XRD peaks with $\sin(\theta)$. The lattice strain can be estimated by plotting $B_{struct} \cos\theta$ as a function of $\sin\theta$ according to Eq. 33. The higher the defect concentration in the lattice, the higher the slope of the fitting lines in the two plots of Figure 86. This is the conventional procedure to indirectly estimate the number of defects present in the grains of a sintered material, although the nature of the defects (i.e. 1D vacancies or 2D-dislocations), cannot be differentiated. As previously stated, the W_2C phase, which is present in SPS and FS materials, is characterised by a larger amount of lattice defects with respect to the WC phase. In all cases, a higher microstrain, corresponding to a local distortion of the crystalline order, is measured for FS samples with respect to the SPS ones, being also much higher than the reference sample. The defects density in the FS_{ox} sample is almost double with respect to the SPS_{ox}

one, thus agreeing with the explanation given before for the AGG observed in Figure 85 (1), which represents further proof of the higher number of defects introduced by the flash process.

Table 9 Average grain size (Davg) and aspect ratio of the samples in Figure 85.

	1) FS_{ox}	2) SPS_{ox}	3) FS_{pure}	4) SPS_{pure}
D_{avg} [μm]	3.17	0.65	1.07	0.53
Aspect ratio[§]	4.7	1.7	1.7	1.6
W_2C vol%	38	32	8 (WC_{1-x})	0

[§] Defined as the longest axis divided by the shortest axis of carbide grains.

Room temperature pillars' deformability

Figure 87 shows some FESEM images of the pillars where the different microstructures of Figure 85 are easily recognised. After the FIB milling, the pillars taper angle is reduced to $\approx 3.5°$, as shown in Figure 87; this allows a precise evaluation of engineering stress and strain as:

$$\sigma_{eng} = \frac{F}{A_0} \tag{39}$$

$$\varepsilon_{eng} = \frac{\Delta L}{L_0} \tag{40}$$

from the recorded data of force (F) and displacement (ΔL), A_0 and L_0 being the initial micropillar top diameter and height, respectively. The specific selection of pillar's dimensions allowed to prepare microsamples from both SPS and FS materials almost free of pores (Figure 87). It is worth noting that materials consolidated by flash sintering possess higher residual porosity, around 3-4%, with respect to SPS one; such difference can be significant when mechanical properties are compared at a larger scale

[231]. At the micron scale, a single pillar contains, according to the microstructure of Figure 85, from tens to hundreds of individual grains (Figure 87). This allowed to study the deformability of polycrystalline monolithic tungsten carbide, instead of single crystals, at a size scale small enough to delay the unstable crack propagation and up to stress levels comparable to those required to activate plastic deformation mechanisms.
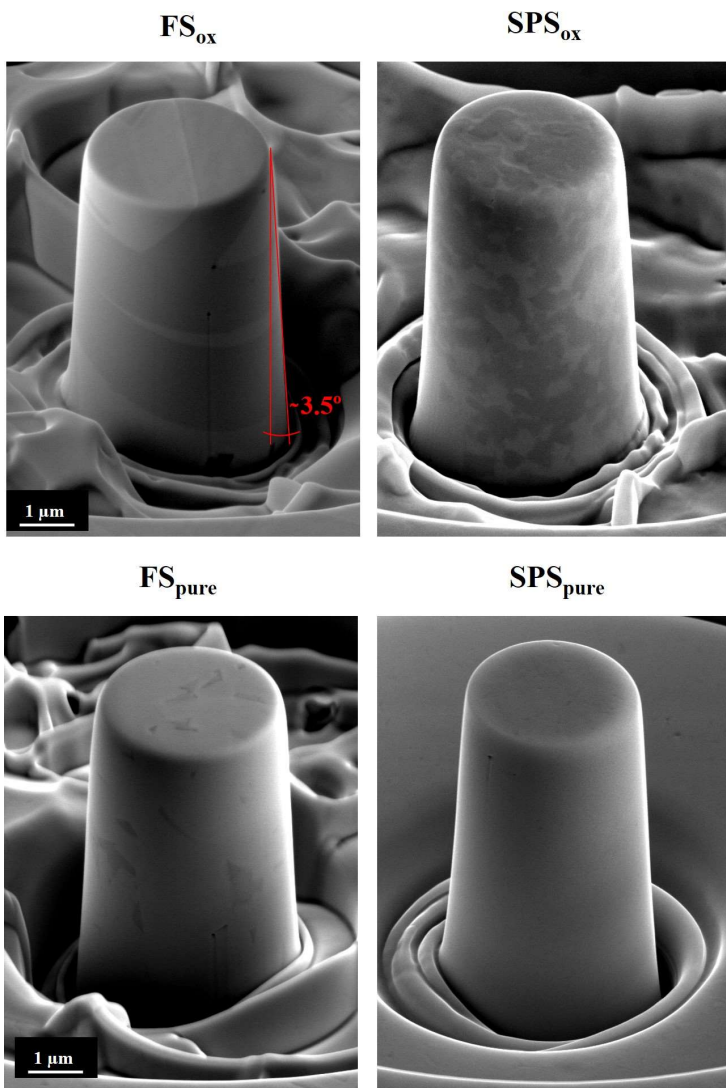
Figure 87 FESEM images, at a tilting angle of 52º, of pillars prepared using circular FIB patterns. The final taper angle reached in the final milling step is indicated for FS_{ox} samples (around 3.5º).

Figure 88 andFigure 89 show the stress-strain curves and post-compression FESEM images of pillars compressed above their elastic limit but before their catastrophic failure. As previously mentioned, the micrometric pillar dimension allows to reach stresses as high as 10-11 GPa, in a condition of stable crack propagation, which is a testament to the strong bonding of the sintered grains; for comparison, pillars prepared from WC single crystals have an ultimate strength in the range of 2-5 GPa (prismatic orientation) and 20-25 GPa (basal orientation) [232]. In almost all the curves of Figure 88 andFigure 89, the pillars did not fail in the elastic regime, and different deformation mechanisms were activated before the final failure accounting for a certain degree of permanent deformation.

Room temperature deformability of SPS pillars

Pillars extracted from SPS samples possess the highest yield stress: 10 GPa for SPS_{ox} and around 11 GPa for SPS_{pure}. The two materials show an elastic behaviour up to higher stress levels when compared to FS pillars. In addition, SPS pillars behave differently after reaching the yield point since they show a partial strain hardening behaviour up to the ultimate strength and a decrease in the stress for increasing strain (strain-softening) up to the failure.

In traditional tensile tests, this is the region of neck formation, where the reduction of the resistive cross-sectional area translates into the apparent strain-softening behaviour in the engineering stress-strain curve. SPS_{ox} and, partially, SPS_{pure} show both strain-hardening and strain-softening regions. It is possible to explain the strain-softening behaviour shown in most SPS_{ox} curves with the same argument used for neck formation in a macroscopic tensile test i.e. with a reduction in the material's resistant cross-sectional area. Post-compression SPS_{ox} pillars (Figure 88, (2, b)) show an extensive microcracking which influences the resistant area i.e. the portion of material supporting the load. As a matter of fact,

compressed pillars in Figure 88 (2, b) show a remarkable increase in the observable microcracking with permanent strain from P2 to P5, this being associated with an extension of the strain-softening regions. It is worth noting that SPS biphasic microstructure (WC/W$_2$C) tolerates a much higher permanent strain with respect to the monophasic SPS$_{pure}$ counterpart (Figure 89 (4, b)), at the expense of a lower maximum strength and a lower stiffness. The W$_2$C phase is generally considered brittle and detrimental in WC products, responsible for lower macroscopic hardness and toughness [180]. However, in the presence of the W$_2$C phase in the WC/W$_2$C composite, the SPS$_{ox}$ pillars reached the highest strain (up to 7%), with a considerable portion of permanent deformation.
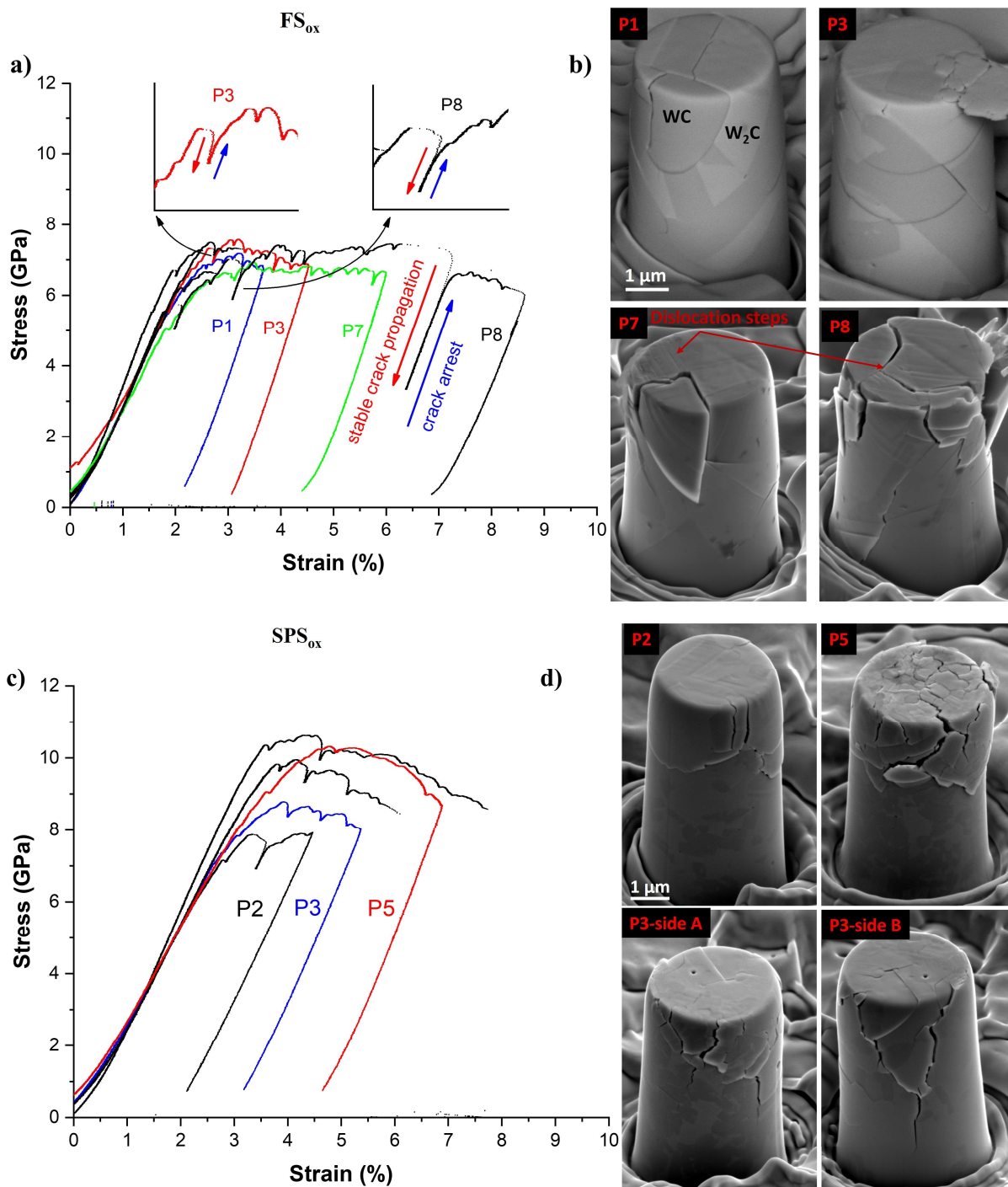
Figure 88 Stress-strain curves obtained from room-temperature compression of FS$_{ox}$ (a) and SPS$_{ox}$ pillars (c) and corresponding FESEM images (b, d) of plastically deformed pillars at different strain levels before final failure. The insets in FS$_{ox}$ (a) show magnified views of crack arrest events.

Plastic deformation occurs simultaneously with crack propagation and is accompanied by stress drops/strain jumps. Jones et al. [232], in their micropillar compression study of WC single crystals, suggested that these instantaneous load drops can be caused by intermittent plastic slip and/or by crack propagation. Evidence of plastic deformation during the room temperature compression of the two SPS pillars is limited to the presence of some dislocation steps on the top surface of pillars compressed at the highest strains (see P6 and P8 in Figure 89 (d).

With the aim to disclose the connection between these instantaneous load drops (red and blue arrows in the insets of Figure 89 (c)) with the activation of plasticity, the cross-section of deformed pillar P6 was analysed by TEM (Figure 90). After the compression test, a lamella was prepared by FIB milling from the deformed SPS$_{pure}$ pillar P6. Such pillar was deformed plastically to about 1% strain, as shown from the unloading curve in Figure 89 (a). Figure 90 (c, d) shows the presence of undissociated dislocations in the deformed grains of pillar P6, which, once reaching the surface, generate the dislocation steps shown in Figure 89 (d). Plasticity, intended as dislocation motion, has a role in the occurrence of such intermittent load drops, and it is very probably competing simultaneously with crack propagation and arrest. The inset in Figure 89 (a) shows several sharp stress drops and jumps during the compression of the P6 pillar, these events being very likely correlated with the crack initiation (sharp drop of the stress) and subsequent arrest (stress surge). This phenomenon occurs several times before the catastrophic failure of the pillar or its unloading. During these multiple crack propagation and arrest events, the material experiences (i) stable crack propagation along multiple paths (microcracking) and (ii) the presence of a minor dislocation activity (Figure 90 (c, d)). This multiple crack arrest mechanism is evident in almost all compression curves (Figure 88 andFigure 89), for both SPS and FS pillars. This is why most of the pillars do not fail in a brittle manner but can be compressed plastically in a condition of stable crack propagation.

In summary, polycrystalline tungsten carbide possesses, at the micro-scale, a toughening mechanism associated with micro-cracking at limited strain levels. Since this mechanism is present in all samples but is activated at different stress levels, it can be used to understand the different deformability of WC products at room temperature. This toughening mechanism is much more active in SPS_{ox} pillars than in SPS_{pure} ones, which is associated with the ability of SPS_{ox} pillars to resist more intense crack extension and, thereby, to reach much higher strain levels before failure. The only difference between the two SPS materials is the presence of the W_2C phase, which must certainly play a role in increasing the efficiency of this toughening mechanism.
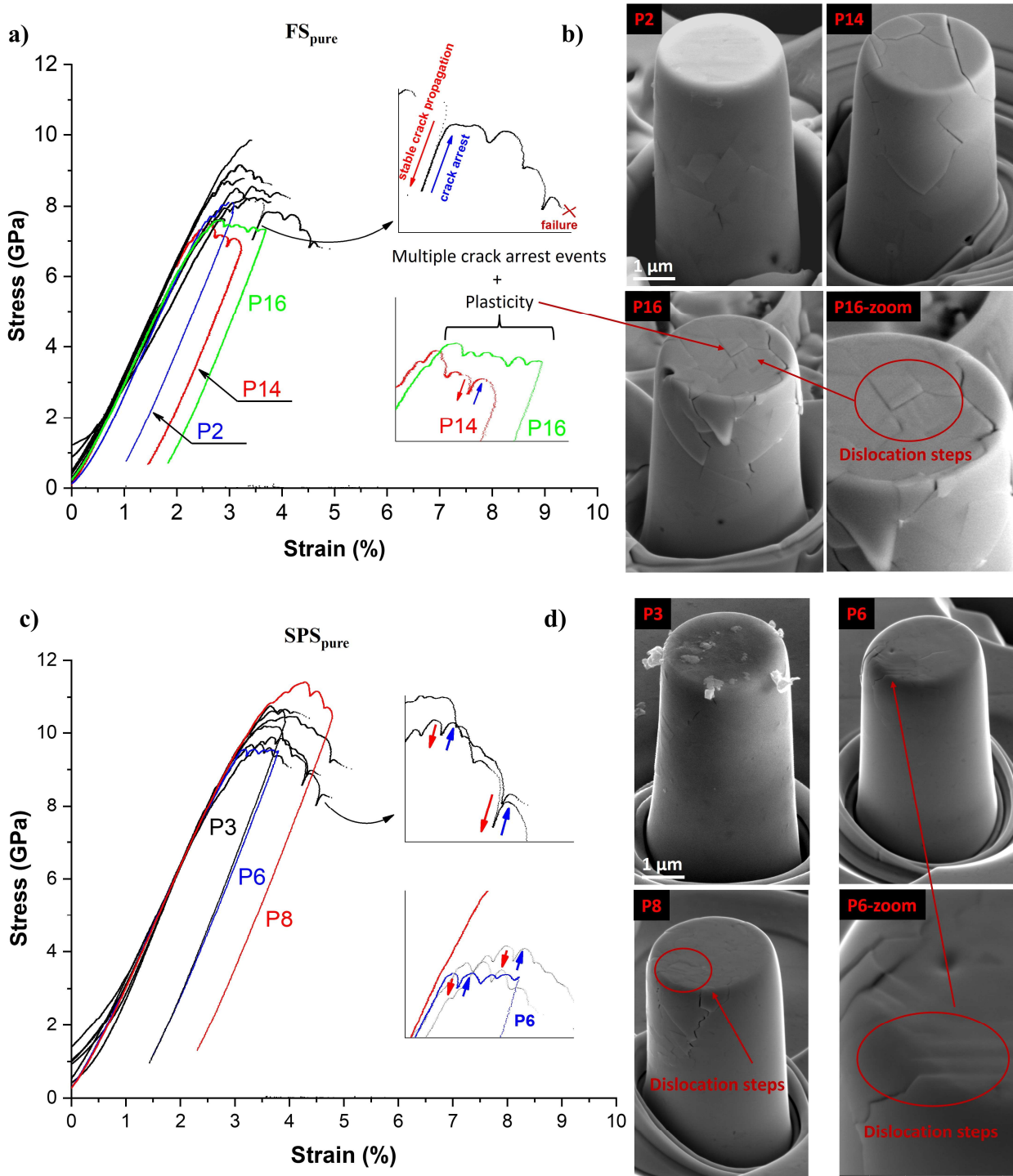
Figure 89 Stress-strain curves obtained from room temperature compression of FS_{pure} (a) and SPS_{pure} pillars (c) and corresponding FESEM images (b, d) of pillars, plastically deformed at different strain levels. The insets show magnified views of crack arrest events.
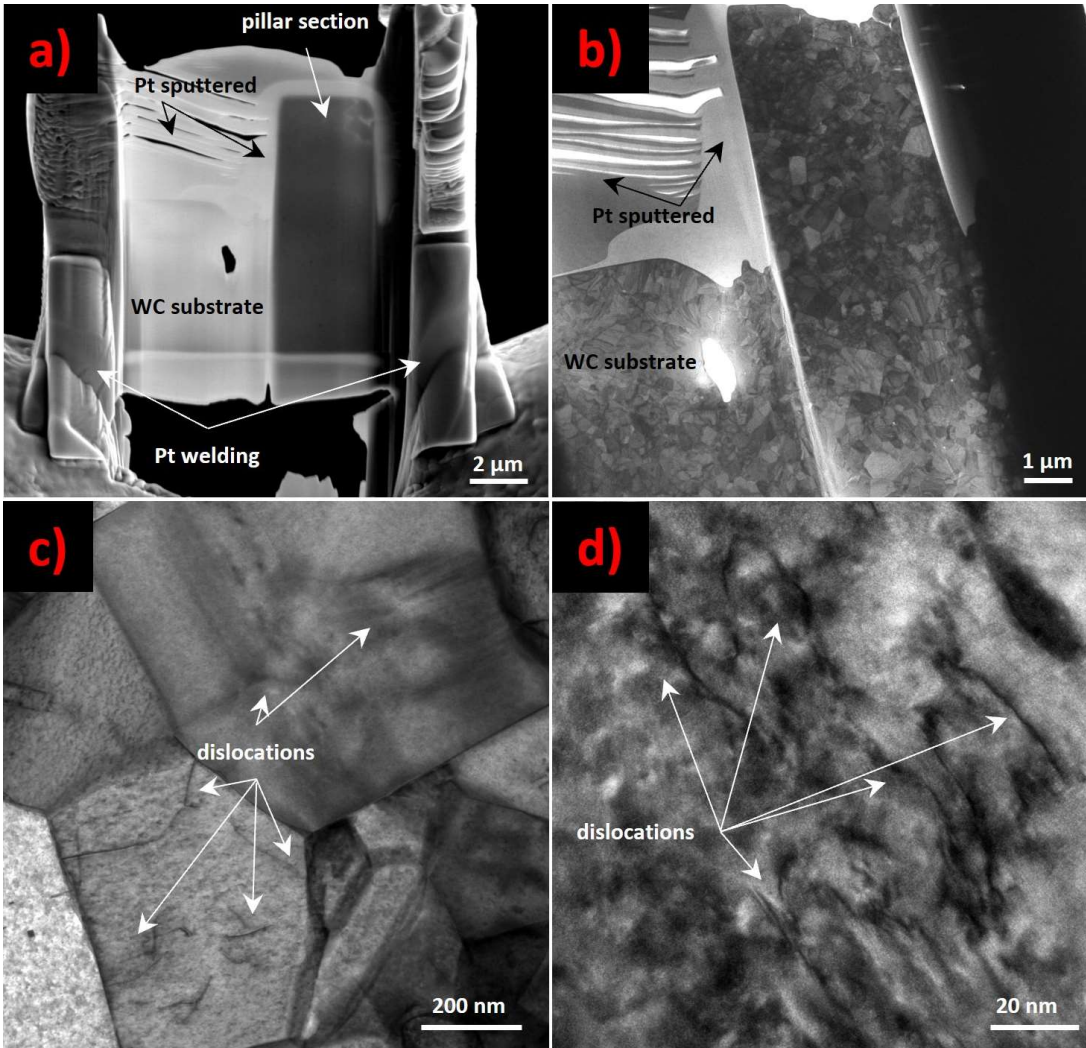
Figure 90 Electron transparent lamella containing a cross-section of the SPS pure P6 pillar. FESEM image of the lamella during its preparation inside the FIB-SEM microscope (a) and its low magnification TEM image (b). HRTEM images of some grains contained in the lamella (c) and (d). White arrows highlight the presence of undissociated dislocations.

Room temperature deformability flash-sintered pillars

The presence of the W_2C phase contributes to reach a larger maximum strain also in flash-sintered FS_{ox} pillars (Figure 88 (a)) with respect to FS_{pure} ones (Figure 89 (a)). For example, P8 sample (Figure 88 (a)) reaches very high strains (about 9%) without failure. Nevertheless, unlike SPS_{ox} and SPS_{pure} specimens, FS_{ox} pillars deform plastically without significant stress drop; in other words, after the elastic region, the curve remains flat without the strain-softening effect observed for SPS pillars. This flat region, corresponding to FS_{ox} pillars undergoing plastic deformation, is again characterised by crack propagation and arrest events. As for the SPS_{ox} counterpart, the nature of these intermittent load drop events is connected with extensive pillar cracking. The compression of FS_{ox} pillars at increasingly higher strain levels (corresponding to 3, 4, 6 and 9% from P1 to P8 (Figure 88 (b)), is accompanied by further crack propagation. However, before being unloaded, such extensively damaged pillars can still sustain stresses of about 6-7 GPa, denoting peculiar high damage tolerance and toughness. This high toughness is associated with the tendency of cracks to split in multiple paths during the irreversible deformation of FS_{ox} pillars and with a dislocation-mediated plastic deformation as observed in P7 and P8 in Figure 88 (b).

The grain size in FS_{ox} is much larger than in SPS_{ox}. This relates to the larger maximum strain and the different shape of the stress-strain curve, which is flat after the material's yield point without noticeable strain hardening and softening behaviour. This is connected to the strong dependence of plasticity on WC grain size [233], which, in turn, is associated with the active slip systems in WC crystals at room temperature. Recently, in-situ compression studies of single crystal WC pillars [232], lattice rotation axis analyses [234], and slip traces coupled with EBSD and HRTEM analyses [233] have found enough evidence to unravel the complexity of the highly anisotropic plasticity of WC grains. At room temperature, the prismatic slip systems $\{10\bar{1}0\}$ are favoured: $[11\bar{2}0](\bar{1}100)$ and $[1\bar{2}10](\bar{1}010)$; while

the basal one, $[0001](01\bar{1}0)$, is considered a secondary slip system. For this reason, grains favorably oriented for prismatic slip deform more easily than those favorably oriented for basal slip. Nabarro et al. predicted, by first-principles density functional theory simulations, that the Peierls stress for the basal dislocations $[0001](01\bar{1}0)$ was twice that for prismatic dislocations on $\{10\bar{1}0\}$ [235,236]. The high anisotropy between prismatic and basal-oriented grains also reflects the huge difference in their nanoindentation hardnesses: 29 GPa (prismatic) against 53 GPa (basal) [237]. This anisotropy was also detected in the transition from a stochastic to deterministic flow stress in basal-oriented WC single-crystal pillars. This transition was observed between pillars with 1 μm and 5 μm in diameter: the former shows a stochastic flow stress, related to the probability of having an already present dislocation in the crystal, while in the latter, all crystals deform in the same way, because the larger pillar/crystal size allows dislocations to pile-up so that the stress levels required to both nucleate and propagate a dislocation are reached [232]. Therefore, the different plastic behaviour of SPS_{ox} and FS_{ox} pillars, which possess the same biphasic WC/W_2C composition, can be mainly related to the exaggerated grain size generated by the flash sintering process: much larger WC crystals in FS_{ox} (3-5 μm with respect to 0.5 μm in SPS_{ox}) can favour the activation of both prismatic and basal slip systems. This increased plasticity is then reflected in the higher ability of the damaged material to resist catastrophic failure because of the more intense activation of the intrinsic toughening mechanism (Figure 88, 1).

FS_{pure} pillars (Figure 89, 1) show an intermediate maximum stress with respect to FS_{ox} and SPS_{pure} ones. They are also stiffer and stronger than FS_{ox} specimens, although the maximum strain is lower. It is difficult to disclose if this reduced maximum strain is due to the absence of W_2C phase or the finer grain size (Table 1). FS_{pure} pillars have inferior mechanical properties with respect to SPS_{pure} ones, in terms of yield/ultimate strength and deformability (Figure 89 (3) & (4)). They also show the largest variability among all the materials tested, some pillars reaching a yield strength of about 7 GPa, and others being

194

loaded elastically up to 8-9 GPa. The compression curves of FS_{pure} pillars show the previously discussed intermittent load drops, together with dislocation steps (like P16 in Figure 89, (1,b)). The majority of FS_{ox} pillars failed catastrophically at unpredictable strain levels and this required to test a much larger number of pillars (up to 16) to be able to save three pillars loaded at increasing strain levels (P2, P14 and P16 in Figure 89 (1,b)). This high variability in the probability of failure can be caused by strong competition between the strain energy dissipation mechanisms, namely crack propagation and dislocation motion. Hence, to better understand when the deformation mechanism is activated with respect to grains orientation and initiation/propagation of the crack, two of the three saved pillars were analysed by TEM and TKD.
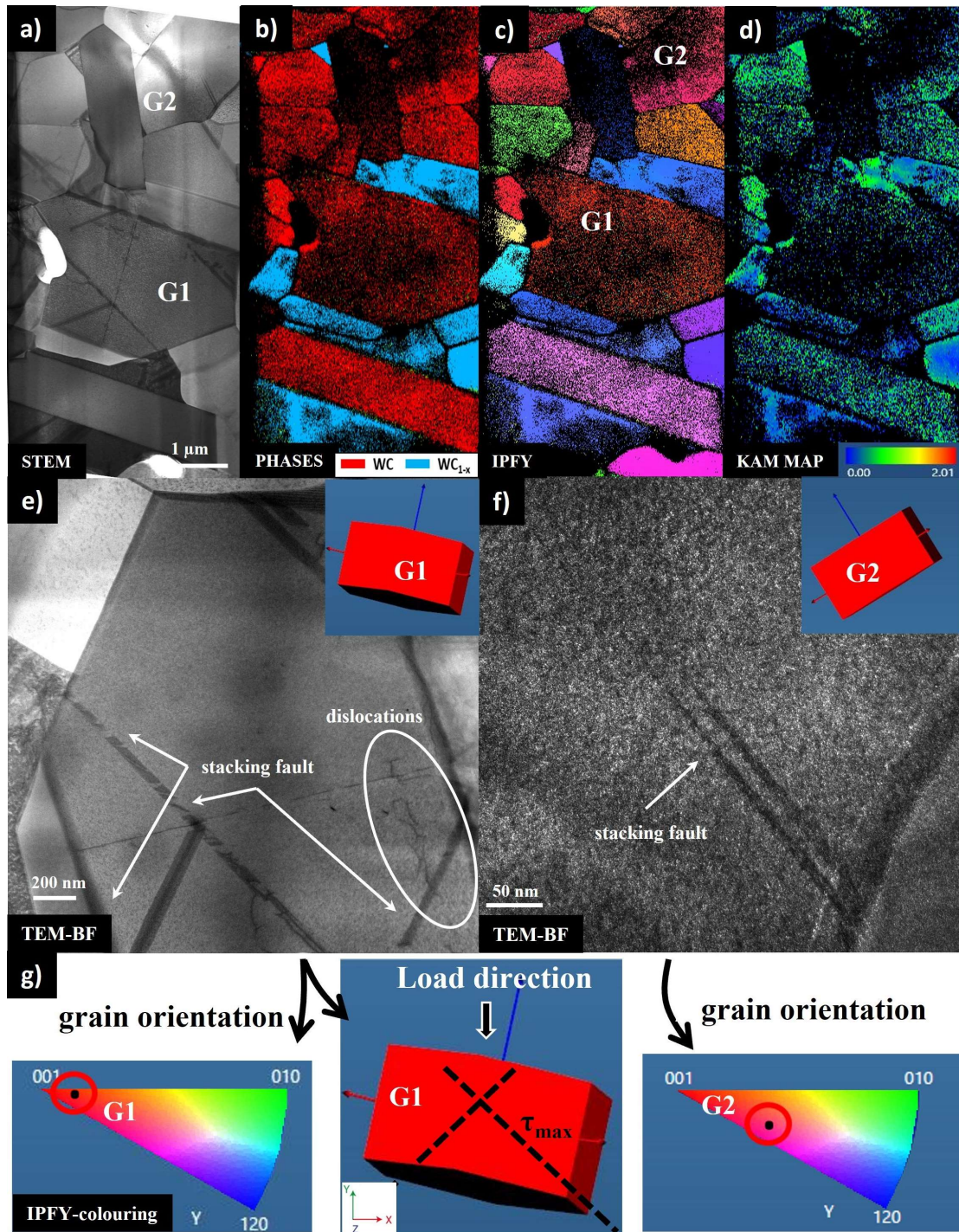
Figure 91 HRTEM and Transmission Kikuchi Diffraction (TKD) analyses of a lamella containing the cross-section of FS_pure P2 pillar after compression. STEM view of the deformed grains contained in the sectioned pillar (a), together with its phase composition (b), orientation analysis (c) and measure of the local strain gradient: Kernel Average Misorientation (KAM) map (d). Bright field (BF) TEM

micrographs of grain G1 (e) and G2 (f) containing stacking faults; the insets represent the grains orientation. Orientation relationship between the IPF-Y map, the load and the maximum resolved shear stress direction (g).

Figure 91 and Figure 92 summarise the analyses of the grains composing two FS_{pure} pillars (P2 and P16 in Figure 89 (1)) deformed at maximum strains of 3% and 4%, respectively. In both pillars, the majority of the dislocations involved in the plastic deformation are partial dislocations hence, several stacking faults (SF) can be observed in the deformed grains. It is possible to conclude that the observed SFs are the result of deformation because: (i) all the SF share the orientation with one of the two directions of maximum shear stress (τ_{max}), as indicated in Figure 91 (g), and (ii) partial dislocations cross a grain boundary between G1 and G2 grains, forming a continuous SF among the two grains, as represented in Figure 92 (e, g). Liu et al. reported that partial dislocations contribute significantly to the plastic deformation and toughness of WC crystals [238].

In P2 specimen (Figure 91), only few grains contain a trace of the movement of partials, i.e. stacking faults. For example, Figure 8 (e,f) show the presence of some SF in two hex-WC grains, denoted as G1 and G2. The low KAM (Kernel Average Misorientation) map intensity confirms such limited dislocations concentration (Figure 91 (d)). KAM is a measure of the local distortion in the orientation of a crystal, and it is directly related to the dislocation density in a crystalline material. The area of high magnitude in the KAM map corresponds to strain concentration, i.e. more deformed material [238]. Comparing the two KAM maps of Figure 91 and Figure 92, which possess the same colour gradient, it is easy to conclude that the grains in P2 sample experienced very modest plasticity. On the other side, grains in P16 specimen, especially those near the top of the pillars, are completely full of SF and, indeed, the KAM map of Figure 92 (d) has a stronger magnitude in correspondence with such grains. The dislocation activity among the two samples differs significantly, while the total deformation of the two

197

pillars, P2 and P16, differ only by 1%. The compression curve for P16 in Figure 89 (1) reaches 4% strain before the pillar is unloaded. We believe that the sample was very close to failing at this strain since the majority of FS_{pure} pillars (Figure 89 (1)) broke at a very similar, if not lower, strain. Also the KAM map in Figure 92 (d) suggests that the strain concentration reached at the grain boundary between grains G1 and G2 is very close to the strain level achieved near the regions of crack propagation. A polycrystalline material requires that slip propagates from one grain to the other to plastically deform in a condition of "easy glide" (absence of strain hardening). Figure 92 shows that this is possible among two h-WC grains only when their orientation does not differ significantly. In Figure 92 (g), partials can cross the GB between G1 and G2 because the orientation difference is lower than 3º, but they cannot cross into G3 since the mismatch is much larger.

(P16) ε_{max}=4%
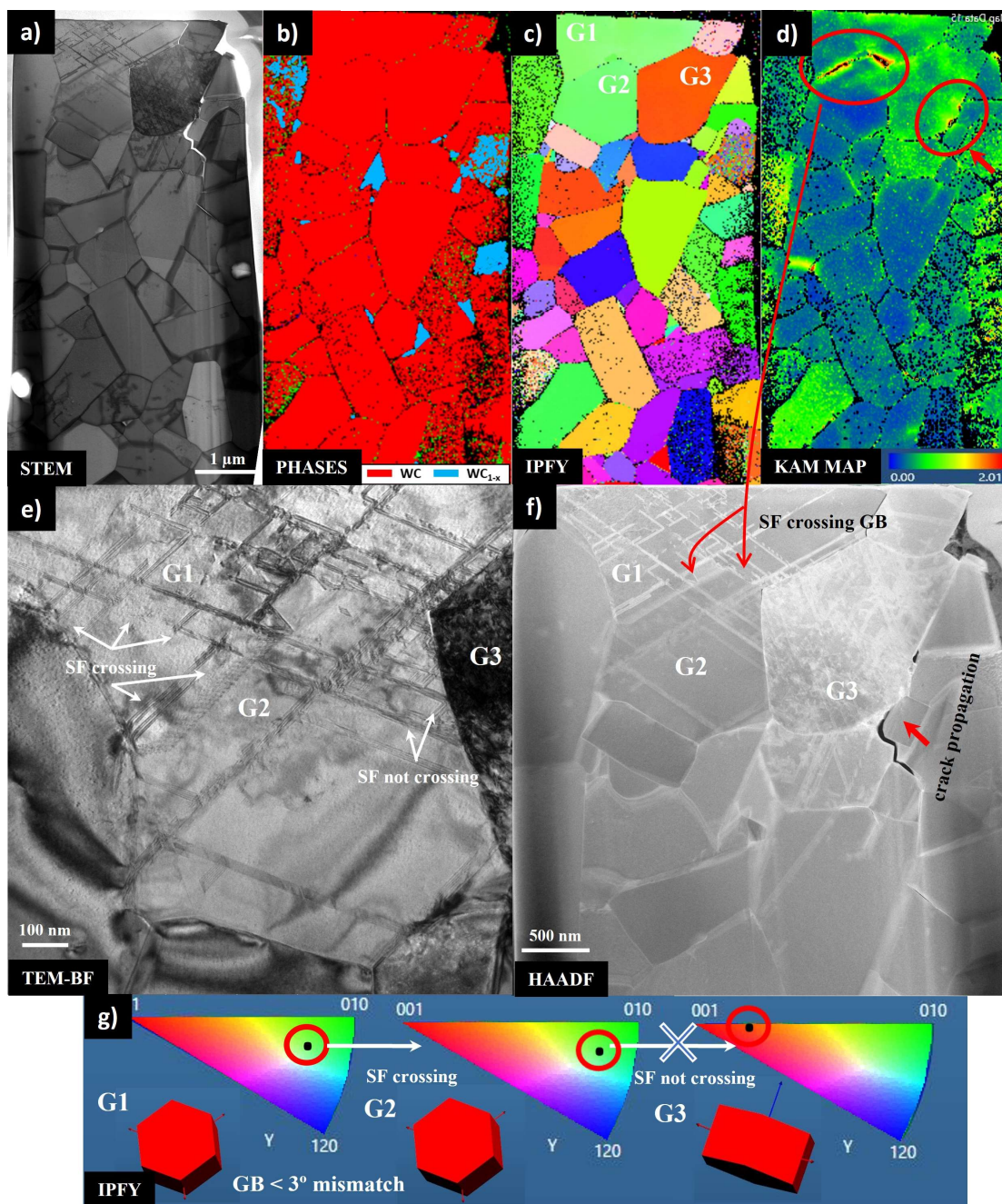
Figure 92 HRTEM and TKD analyses of a lamella containing the cross-section of FSpure P16 pillar after compression. STEM view of the deformed grains contained in the sectioned pillar (a), together with its phase composition (b), orientation analysis (c) and measure of the local strain gradient by KAM map (d). Bright field (BF) (e) and High-angle annular dark-field (HAADF) (f) TEM micrographs of a highly deformed pillar region containing G1, G2 and G3 grains. IPF-Y map and orientation (g) relationship

between G1, G2 and G3 grains, pointing out the mismatch conditions for dislocation to cross the GB between two hexagonal WC grains.
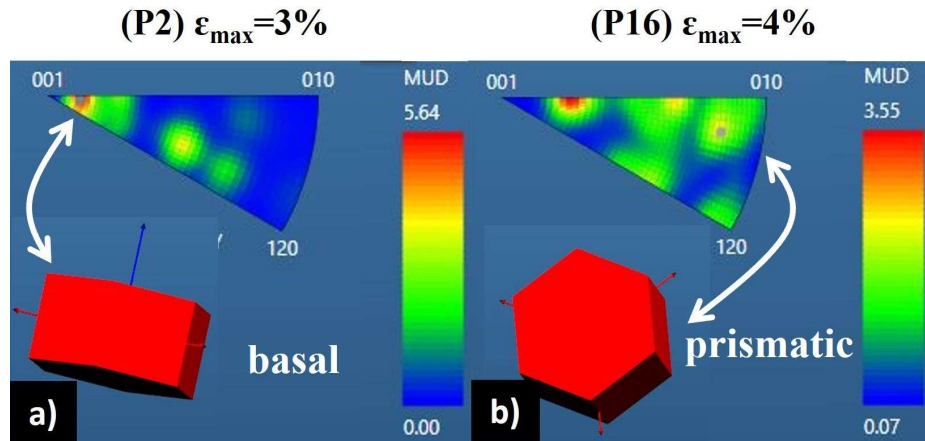
Figure 93 IPF-Y maps coloured according to the MUD scale; MUD>1 represents a preferential orientation of the grains in the lamella. The two maps report the preferential orientation of P2 (a) and P16 (b) pillars of the FSpure series.

The stress required for a dislocation to cross the GB, in the almost perfect condition of two well-oriented grains, is very close to the stress required for a crack to propagate. This can be deduced from the large difference in concentration of SFs between the surface and the middle and bottom parts of the P16 pillar (Figure 92 (a)). SF activity ends by reaching the bottom region of G3 in (Figure 92 (f,d)) where the big crack present competes in releasing the strain energy accumulated during the compression of the pillar (Figure 92 (f)). The analyses reported in Figure 92 represent a good example of why an arbitrary deformation is so difficult in these polycrystalline pillars and why they fail stochastically at different strain levels (Figure 89 (1)). The amount of strain energy required for activating plasticity in the WC grains competes with the mechanisms of energy release operated by the generation of new surfaces by crack advancement. Plasticity in WC crystals is anisotropic and according to the literature previously reported, i.e. on the slip systems active at room temperature, it is favoured in such grains oriented with

the prismatic faces in the direction of the applied load and disfavoured for those with a basal orientation. Figure 93 summarises the different preferential grains orientation for the two pillars analysed in Figure 91Figure 92, and shows how the low dislocation activity in P2 sample of Figure 91 can be attributed to the disfavoured orientation of the grains contained in such pillars, which are almost completely basal oriented. The basal orientation corresponds to the red colour of the majority of grains in the IPFY map of Figure 91 (c), while differently the highly deformed grains contained in the top portion of P16 (Figure 92 (c)) are more coloured towards the green, that corresponds to a prismatic orientation.

In conclusion, the room-temperature deformability of BTC products does not differ significanlty between the materials consolidated by flash sintering and spark plasma sintering. This is being tested in the presence and absence of the W_2C phase, hence between FS/SPS$_{pure}$ and FS/SPS$_{ox}$ samples.

High-temperature pillars deformability

At room temperature, tungsten carbide possesses a limited number of independent active slip systems (lower than 5), making the material extremely hard and brittle. At room temperature, the plastic strain is limited, and the stress-strain curves have a stochastic nature, depending on the orientation of the grains in the pillars and on pre-existing defects. By increasing the temperature, new slip systems become available in WC crystals allowing more intense plastic deformation. A third prismatic slip system $[\bar{1}\bar{1}23](\bar{1}100)$ and the basal one $\{0001\}$ become available at around 600ºC [232]. An additional candidate can be $[11\bar{2}0](0001)$ via a cross-slip mechanism of <a> dislocations from prismatic to basal planes [232]. The increased plasticity in the range 600-700ºC is also reflected in a two to three-fold drop in the hardness of carbide grains [237,239].

The effect of temperature on the increased deformability of polycrystalline tungsten carbide tested in-situ by the Hysitron PI88 picoindeter (Figure 84, c) is reported in Figure 94. Pillars produced from FS$_{pure}$

and SPS$_{pure}$ materials were tested at RT and 700ºC. The RT compression curves are very similar to those reported in Figure 89. SPS$_{pure}$ and FS$_{pure}$ pillars are extremely stiff at room temperature, reaching a maximum strength of about 8 GPa (FS$_{pure}$) and 9.5 GPa (SPS$_{pure}$) in the elastic regime, with very limited plastic deformation. An example of a catastrophic failure event is reported in Video 1 (Supp.mat.) for FS$_{pure}$ pillar tested at room temperature; the failure event is almost instantaneous and ends with the complete shattering of the pillar.

a) FS_pure

b) P1 P2 P3 P4

c) SPS_pure

d) P1 P2 P3 P4
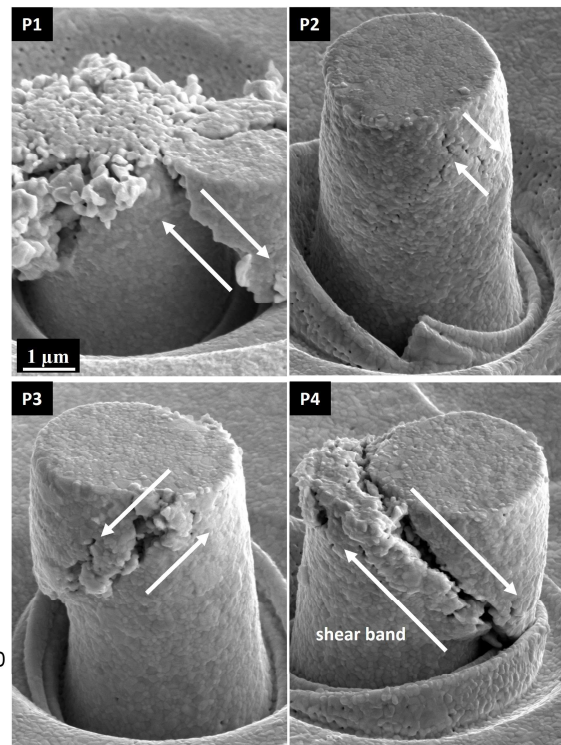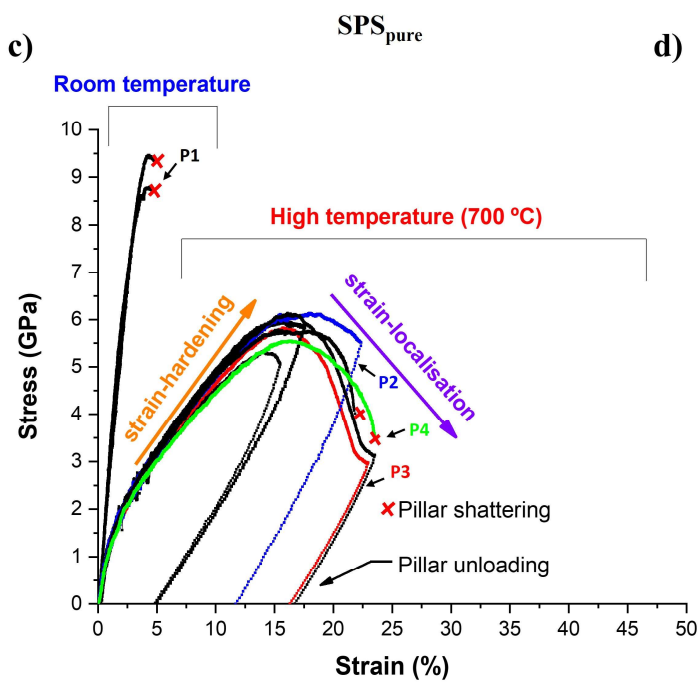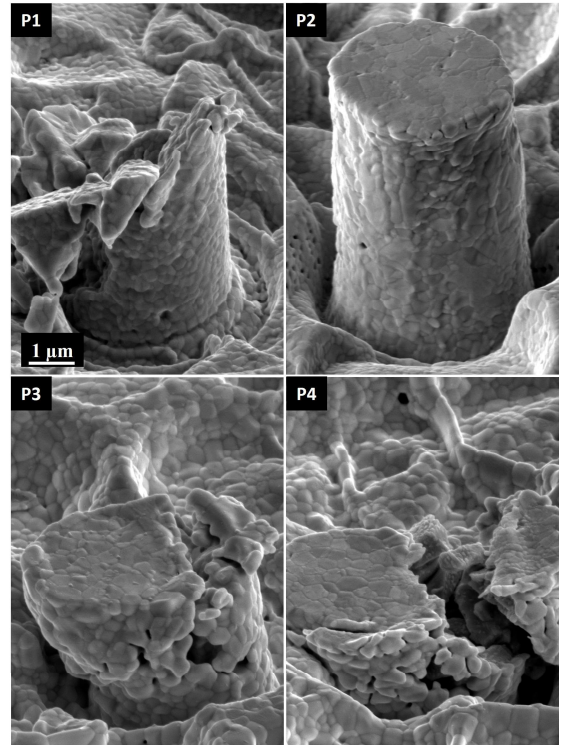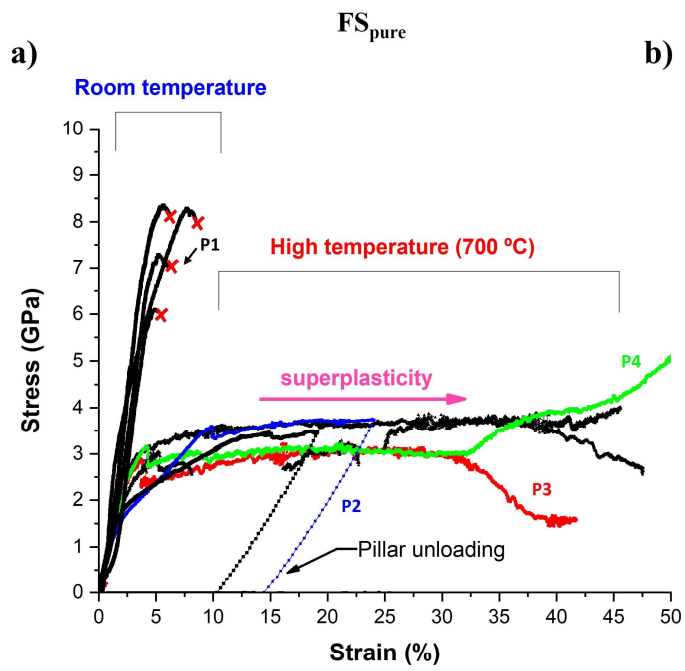
Figure 94 Stress-strain curves obtained from in-situ compression test at room and at high temperature (700ºC) of FSpure and SPSpure pillars (a, c) and corresponding FESEM images (b, d) of pillars, plastically deformed at different strain levels The curves where the load drops instantaneously to zero are indicated with a red cross and refer to the shattering of the pillar.

At high temperature (700ºC), stress-strain curves shown in Figure 94 reveal a significant increase in the deformability of the material along with a substantial reduction in the pillars' strength. SPS_{pure} pillars, characterized by a tensile strength of 8-9 GPa at RT, are plastically deformed at a yield of around 1.5-2 GPa at 700ºC. Similar behaviour is shown by FS_{pure} pillars up to the onset of plasticity. This behaviour can be indeed correlated to the activation of new slip systems in WC crystals in the temperature range 600-700ºC, at which considerable differences in the deformation behaviour between FS and SPS pillars can be observed. SPS_{pure} pillars deform plastically with a strain-hardening behaviour up to their maximum strength (Figure 94, c), the stress then decreasing at larger strain (strain-softening). Images of deformed P2, P3 and P4 pillars (Figure 94, d) clearly show that strain localisation events occur during the strain-softening regime. Shear bands appear at 45º on the surface of the deformed pillars (directions of maximum shear stress), which causes instability in the deformation. This loss of deformation homogeneity leads to catastrophic failure when the resistive cross-section cannot support the high loads. Figure 94 (b) shows the state of a pillar before (P3) and after (P4) this failure event. The top portion of such pillars slides down at the fracture stress and maximum strain that the pillars can support in correspondence with the shear band. All SPS_{pure} pillars tested at high temperature share the same deformation behaviour and fail catastrophically at a maximum strain of around 25%.

On the other hand, FS_{pure} pillars (Figure 94, a) show little strain-hardening and no strain softening behaviour. All the tested pillars were deformed at 700ºC in a condition of almost perfect plastic

deformation, without or with a very limited strain-hardening. For example, FS$_{pure}$ P2 sample shows the pillars' state during the plastic flow, at a strain level of around 20% where there is no evidence of crack propagation events as observed for the SPS$_{pure}$ P2 pillar. These pillars can be deformed up to an outstanding value of maximum strain of 50% without the occurrence of shear-bands (Figure 94, b), hence without the loss of homogeneity of deformation. It is thereby possible to conclude that at 700ºC, the flash-sintered WC material can be plastically compressed up to very high strain levels (50%) without strain localisation events, thus showing a phenomenon known as superplasticity [240].

Superplasticity in flash-sintered pillars & grain boundary (GB) sliding

Superplasticity is an exclusive characteristic of polycrystalline materials, as observed in the high-temperature behaviour of the WC pillars tested in this work, where the primary mechanism allowing the exceptionally large deformability at elevated T is grain boundary (GB) ` phenomenon occurs during high-temperature deformation of fine-grained ceramics, like SiC, Si$_3$N$_4$ and yttria-stabilized zirconia. An essential feature for superplasticity to occur is the presence of accommodation processes compensating for the cavities and cracks inevitably generated during the sliding of the rigid ceramic grains. Thus, superplasticity is, for example, observed in Si$_3$N$_4$ in the presence of a glassy phase at GB. Alternatively, diffusion and dislocation motion can operate as accommodation mechanisms. A closer look at the grains contained in the FS$_{pure}$ pillars (Figure 95) reveals how superplasticity is the result of GB sliding. Red arrows (Figure 95) indicate the areas of the pillars where grains are still connected but shifted from their original positions. Both, SPS$_{pure}$ and FS$_{pure}$ materials (Figure 94) are characterized by clean GBs with minor Cr impurities (Figure S. 4, Supp.mat.); although only the flash sintered pillars (FS$_{pure}$) can be deformed to around 50% strain without failure.
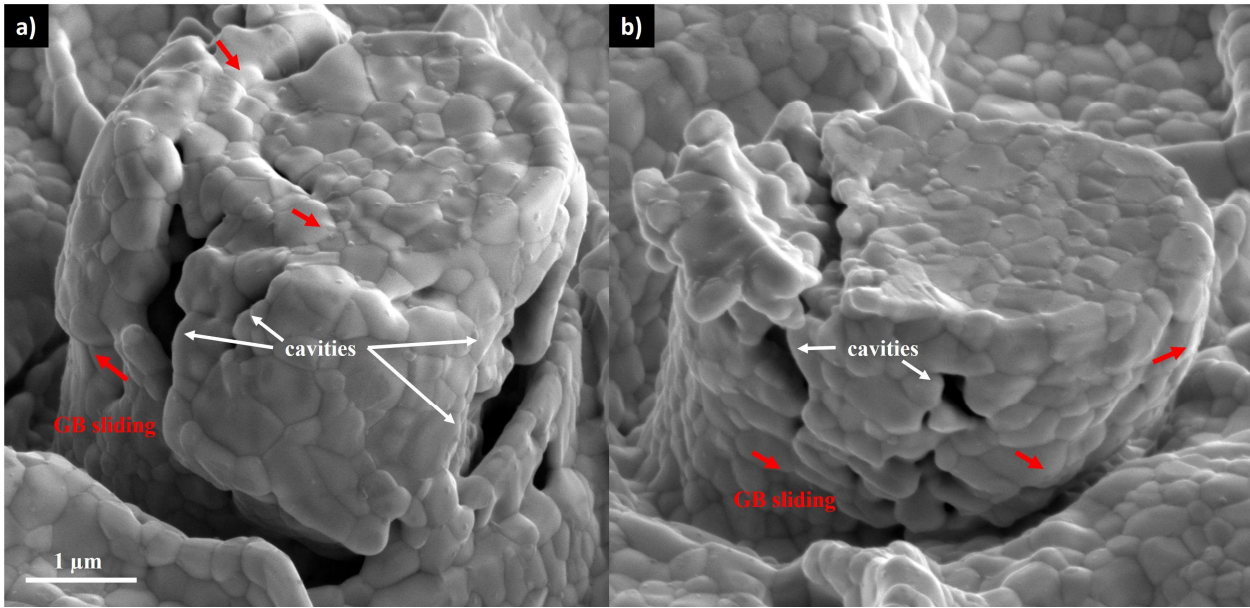
Figure 95 High magnification FESEM images of two FSpure pillars deformed up to 50% strain at 700°C. Grains are visible in the two pillars because the material was exposed to 700°C during in-situ compression in SEM high-vacuum atmosphere. Red and white arrows indicate GB sliding and cavities formation from rigid sliding of ceramic grains, respectively.

In addition, grains in the deformed FSpure pillars (Figure 95) remain equiaxed and appear much finer than in the original FSpure material (Figure 85,Figure 91 and Figure 92). HRTEM analyses in Figure 91Figure 92 do not show any evidence of sub-grains within the WC crystals able to explain the grain refinement observed in the pillar after the high-temperature deformation; therefore, grain recrystallisation must have occurred at 700°C during the severe plastic deformation. Kim et al. reported a refinement of zirconia grain structure after high-temperature superplastic deformation [241]. Ceramic grains are usually considered rigid bodies in superplastic ceramics, and GB sliding is accommodated only by diffusion. Although similar to ZrO_2 crystal, WC possesses slip systems active at high temperature and, therefore, grains can be deformed plastically to some extent. It is possible to argue that the dislocations formed during the superplastic deformation of FS pillars (FS_{pure}) were arranged to form subgrain

boundaries during deformation. According to Kim et al., this dislocation-induced plasticity significantly contributes to the accommodation process of GB sliding, relaxing the stress concentration via grains plasticity as an alternative to diffusion processes. Another consequence of this additional accommodation mechanism is the suppression/reduction of stress and strain concentration generated at GBs. The consequences of this stress relaxation can explain why the deformation remains homogeneous for the flash-sintered pillars up to very high strain levels in contrast to the formation of cracks and shear bands (shear instability) in the SPS pillars (Figure 94). Enhanced plasticity of FS WC grains with GB sliding and the formation of new subgrain boundaries give way to the high-temperature superplasticity effect. The reasons for this high-temperature (700ºC) enhanced plasticity in the flash-sintered grains over SPS ones are still unknown; other research imputed the increased plasticity observed in YSZ [225] and TiO_2 [77] after flash sintering to the introduction of a high amount of defects, like vacancies and/or dislocations. Figure 86 shows how the flash-sintered material, FS_{pure}, which shows the superplastic behaviour, is characterised by a higher density of crystalline defects. In particular, the cubic WC_{1-x} phase in the FS_{pure} material possesses a peculiarly high microstrain. This increased microstrain observed in both h-WC and c-WC phases of FS_{pure} material also found a correlation with the presence of "post-flash" dislocations detected during the TEM observation (Figure S. 5 (c), Supp.mat.). Undissociated dislocations were found in the regions where the material was not subjected to external stress.

4.1.4 Conclusions

Polycrystalline binderless tungsten carbide (BTC) micropillars can withstand a certain degree of permanent deformation while maintaining a relatively high load-bearing capability. During room-temperature compression, micropillars prepared from both SPS and FS processes possess a toughening mechanism associated with stable crack propagation and arrest events. These toughening events

correspond to intermittent load drops/surges within the stress-strain curves of the compressed pillars and permit them to accommodate some degree of permanent deformation. At room-temperature, this toughening mechanism is not affected by the flash sintering process, although it is correlated with the presence of the subcarbide (W_2C) phase within the WC matrix.

On the contrary, at high temperature (700ºC), FS pillars possess a superplastic behaviour reaching deformations of up to 50% of the pillar height without failure. Also the material consolidated by SPS shows increased deformability at 700ºC, although none of the pillars tested in this work survive strains above 25%. The strain is not homogeneous in SPS pillars, causing the material to fail because of a macroscopic slide at shear bands.

Flash sintering is demonstrated to enhance the high-temperature deformability of tungsten carbide. The superplastic behaviour at 700ºC occurs because the flash sintering alters the accommodation mechanism of GB sliding, allowing the material to deform homogeneously up to very high strain levels. In light of such results, it will be crucial to assess in future works how this superplasticity correlates with an increased plasticity and defect concentration of flash-sintered WC grains.

4.2 Hardness and fracture toughness of BTC components

Isacco Mazo[#], Miguel A. Monclus [†], Jon M. Molina-Aldareguia [§, †], Alberto Molinari [#], Vincenzo M.

Sglavo[#‡]

Department of Industrial Engineering, University of Trento, via Sommarive 9, Trento, Italy

† IMDEA Materials Institute, C/ Eric Kandel 2, 28906, Getafe, Madrid, Spain

‡ INSTM, National Interuniversity Consortium of Materials Science and Technology, Trento Research

Unit, Via G. Giusti 9, 50123 Firenze, Italy

4.1.1 Introduction

This work reports the macroscopic mechanical properties of the samples, previously analysed in section 4.1 (Figure 85), with the aim to understand the integrity difference for materials consolidated by electrical resistance flash sintering (ERFS) and spark plasma sintering (SPS). These samples are denoted as FS_{ox}, FS_{pure}, SPS_{ox} and SPS_{pure}, as introduced in 4.1, and they are representative of the type of BTC microstructures resulting from sintering WC nanopowders with a different oxygen content (see section 2.2 for the complete analysis and discussion of these two nanopowders). As summarized in Figure 96 the samples possess a different microstructure in terms of grain size and phase composition, this allowing to understand the effect of the second phase in combination with the sintering technique on the material's mechanical properties.
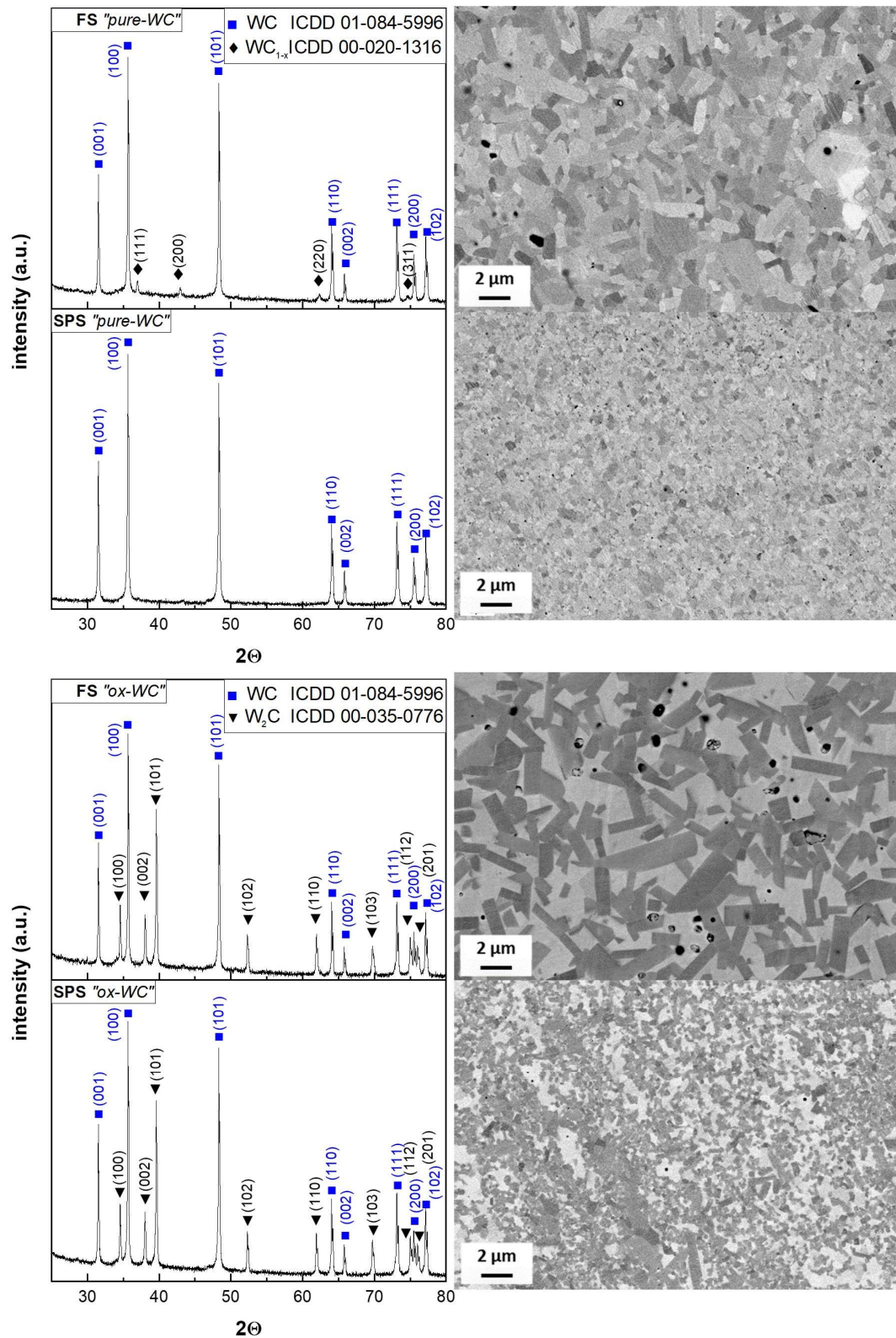
Figure 96 Summary of the phase composition (XRD) and microstructure (FESEM-BSE) of the samples denoted as FS$_{ox}$, FS$_{pure}$, SPS$_{ox}$ and SPS$_{pure}$. (Original figure by Mazo).

4.2.2 Experimental procedure

Berkovich nanoindentations

Elastic modulus and hardness were measured by an instrumented nanoindenter (Hysitron triboindenter TI950) equipped with a diamond Berkovich tip. Figure 97 shows a typical load-displacement curve as acquired during such analysis. The hardness, H, was evaluated from the maximum load P_{max} and the residual area A_r:

$$H = \frac{P_{max}}{A_r} \tag{41}$$

The elastic modulus is instead obtained during the unloading phase of the indentation cycle, when the material's behaviour is purely elastic. However, the slope S in Figure 97, which is indicative of the stiffness of the contact includes the contribution of the tested material and the diamond tip. For this reason, the modulus evaluated from this is curve is usually interpreted as a reduced modulus, E_r, and must be converted in the specimen modulus, E_s, by the following equation:

$$\frac{1}{E_r} = \frac{(1 - v_i^2)}{E_i} + \frac{(1 - v_s^2)}{E_s} \tag{42}$$

where the modulus of the diamond indenter, E_i, equals to 1140 GPa and its Poisson ratio, v_i, is 0.07. Three different maximum loads were used, corresponding to 250, 500 and 750 mN with ten repetition each.
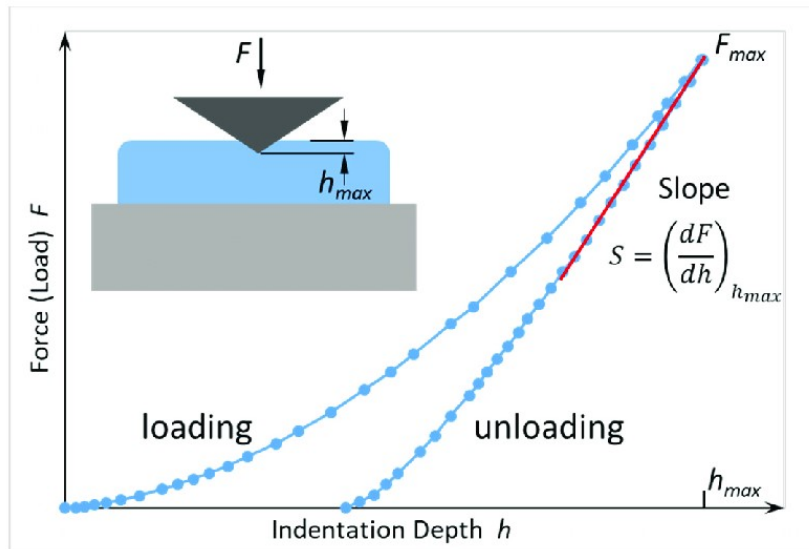
Figure 97 Typical load displacement curve as acquired during a nanoindentation test (Original figure from I. Utke [242]*, licensed under a CC-BY 4.0).*

Elastic modulus and hardness maps were acquired on a specific area of interest performing 22 x 22 indents in an area of 7.7 x 7.7 μm^2, by using 3 mN maximum load and with a separation distance of 350 nm. The indentation map position was scanned by Atomic Force Microscopy (AFM) forming a topographic image of the surface with the same indenter diamond tip (BKL-DLC) in AFM mode.

Vickers indentations

Vickers hardness was measured at five different loads (100, 20, 20, 5 and 2 N) with 10 s holding time and ten replica each. The fracture toughness was measured by the analysis of the radial cracks generated on the surface of the samples upon the indenter unloading.

The imprints were observed after the tests with a digital optical microscope (Olympus DSX1000) for a precise measurement of the radial cracks and further examined in FEG-SEM microscope using a Back-scattered electrons (BSE) detector (ThermoFischer® Apreo 2S LoVac).

212

4.2.3 Results & discussion

Elastic modulus & hardness

Very high hardness of more than 23 GPa characterizes the BTC samples of Figure 99 and Figure 100, this pointing out the high degree of densification and structural integrity of the materials sintered by both techniques. However, the samples sintered by SPS are superior in both hardness and modulus at the three tested loads. Both SPS samples possessed a hardness of around 29-30 GPa, around 7 GPa more than the two FS samples. This difference can be mainly attributed to the finer microstructure and smaller grains size obtained by SPS (Figure 96). On the other side, the large difference in the elastic modulus is more difficult to be explained by considering only the microstructure. SPS_{pure} sample possesses a modulus of about 600 GPa, 70 GPa higher than FS_{pure}, a difference that can not be ascribed to the grain size. In addition, samples with a high second phase (W_2C) content, FS_{ox} and SPS_{ox} of Figure 100, are instead characterized by a similar average modulus of 530-550 GPa; this value is in between the modulus of its two components, 700 GPa for WC [196,243,244] and 440 GPa for W_2C (Figure 101) [183,245]. The larger scattering observed in Figure 100 for the elastic modulus of FS_{ox} can be for sure ascribed to the very coarse microstructure; in other words, the result from the indentation analysis depends on the phase in which the diamond tip tested the material (Figure 101).
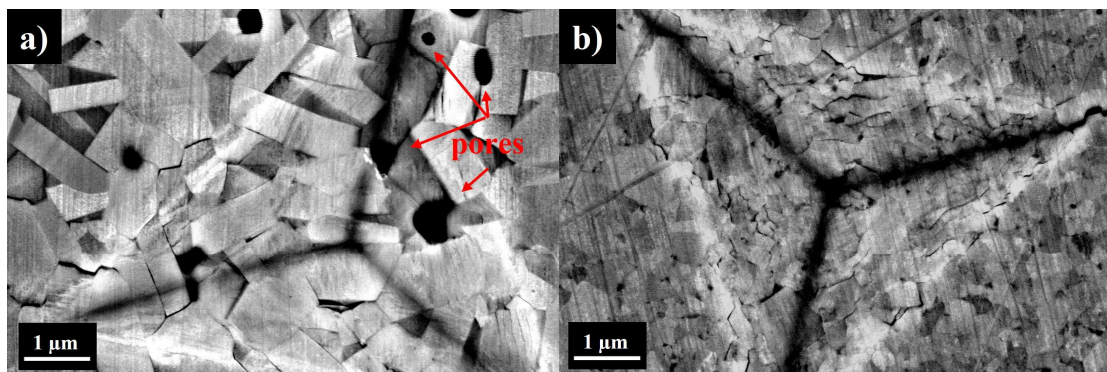
Figure 98 Example of Berkovich imprints, performed on FS$_{pure}$ (a) and SPS$_{pure}$ (b) samples at 750 mN.
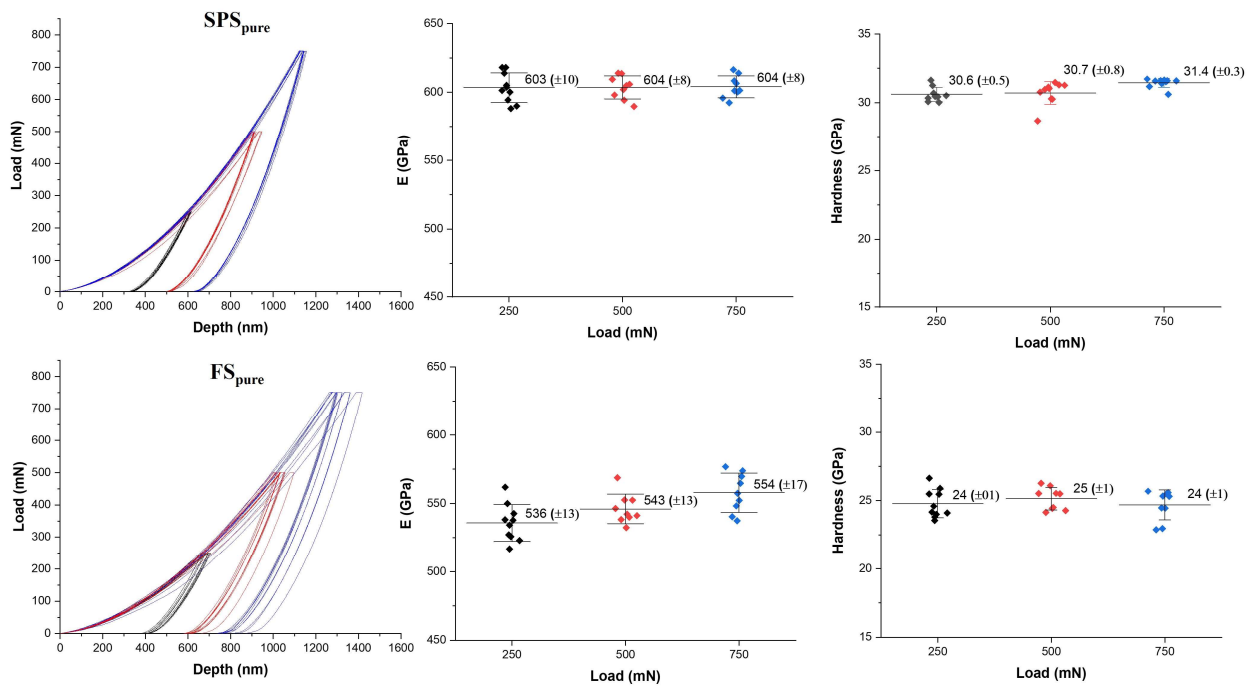
Figure 99 Nanoindentation curves, modulus (E_s) and hardness for SPS_{pure} and FS_{pure} samples acquired at maximum indentation loads of 250, 500 and 750 mN. Error bars refer to the standard deviation.
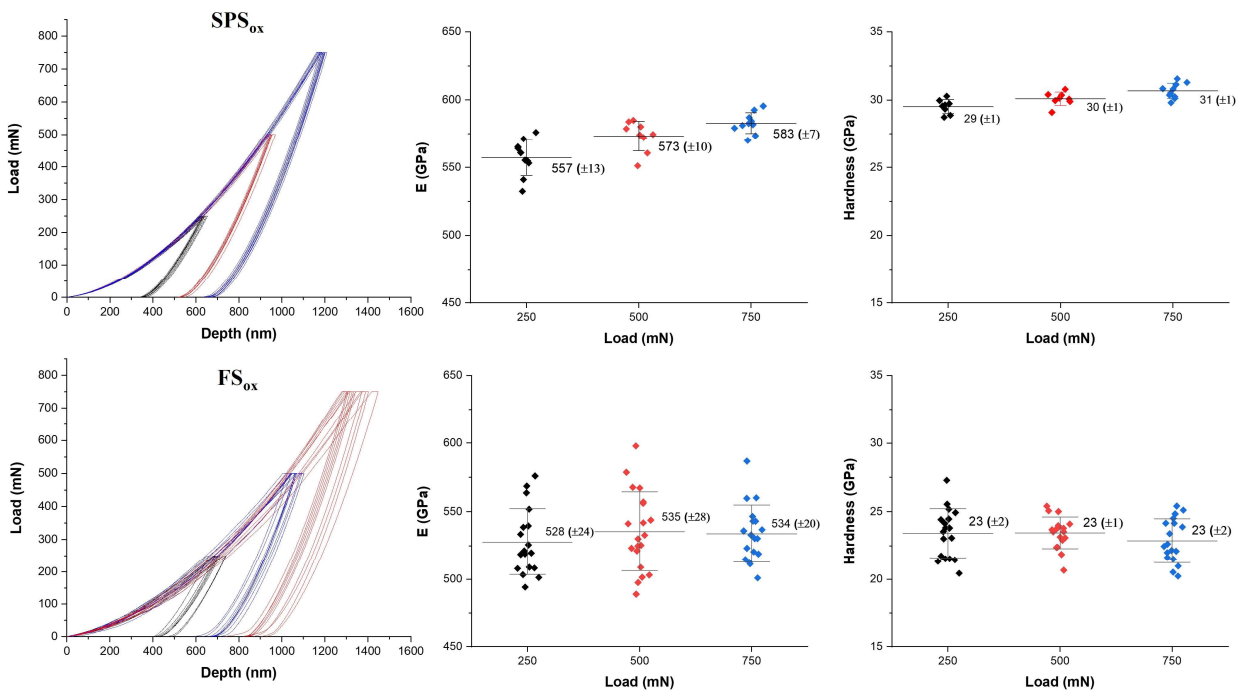
Figure 100 Nanoindentation curves, modulus (E_s) and hardness for SPS_{ox} and FS_{ox} samples acquired at maximum indentation loads of 250, 500 and 750 mN. Error bars refer to the standard deviation.

It is interesting to note that the modulus for the FS_{pure} sample is not larger than in FS_{ox} despite the latter contains 40 vol% W_2C (Figure 96), phase with a considerably lower E (Figure 101). Two are the possible causes for the different elastic response between FS_{pure} and SPS_{pure} samples (Figure 99): (i) the residual porosity of about 3-4 vol% is known to affect the modulus if the indenter size is comparable with the size of the pores; like in the imprint of Figure 98 (a) [231,246]; (ii) the presence of 8-10 vol% of the WC_{1-x} second phase, characterized by a much lower modulus $\cong300$ GPa (Figure 82).
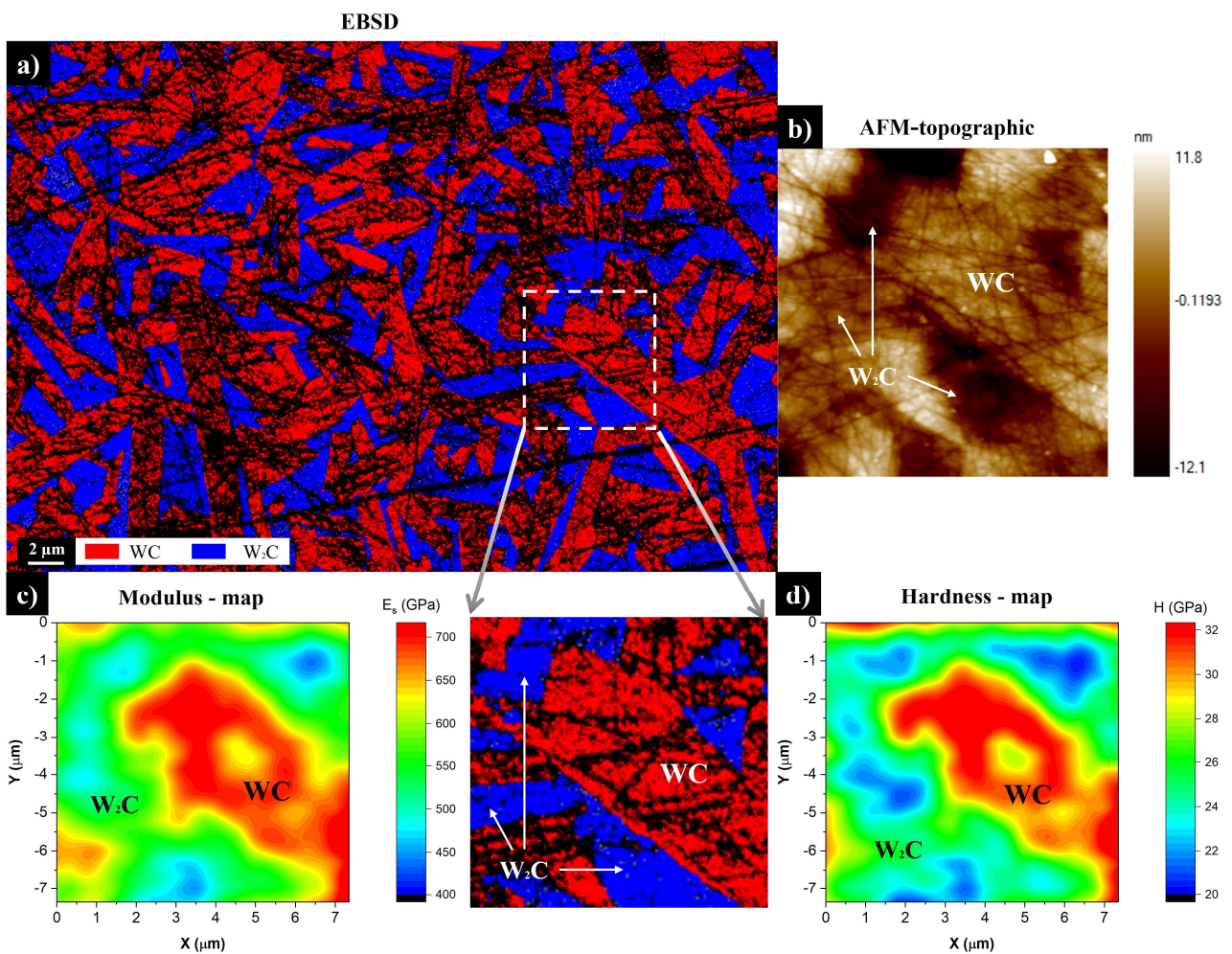
Figure 101 Difference in the mechanical properties between the two hexagonal tungsten carbide phases: WC and W_2C. The EBSD phase composition of FS_{ox} (a) is reported together with the AFM imaging (b) and properties mapping (c, d) of the area highlighted by the dotted white line.

Indentation fracture toughness

The determination of fracture toughness by indentation method requires the correct determination of the crack shape, either Palmqvist or Median-Radial (Figure 102). The type of crack depends on the material, and typically high fracture toughness materials are characterized by Palmqvist cracks, while the Median-Radial is more often observed on brittle ones. Since both crack systems appear the same on the surface, the only way to determine the real system is a direct examination of the cross section. The determination of the system is very important for this kind of analysis since it regulates the correct equation to be used [247]. WC-based materials can show different types of cracks depending on the presence of the metallic binder. WC-Co cermets show Palmqvist crack type, and their indentation toughness is generally measured using the Shetty equation [248]. For BTC materials the situation is more complex and the choice of the equation is not unique among the scientific community; some researcher used the Anstis equation [26] (Median-Radial crack type) [179], while others used the Shetty one (Palmqvist crack type) [20,68]. This result in a certain confusion in the reported fracture toughness values [196], since the two equations can lead to difference in the estimation of the fracture toughness of about 2-3 MPa m$^{1/2}$, which in a brittle material like BTC is equivalent to an error of more than 40%.
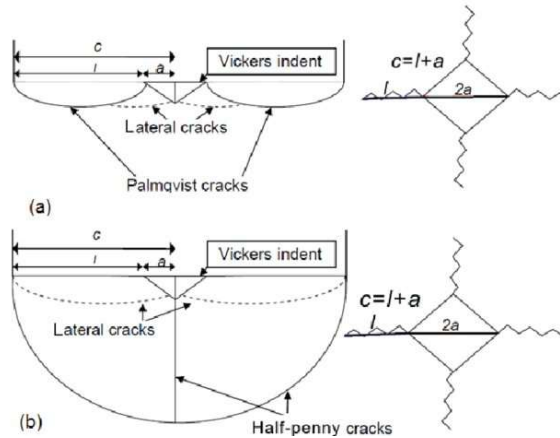
Figure 102 Crack profile comparison between Palmqvist (a) and Median-Radial (Half-penny) crack type (b). (Original figure from Moradkhani et al. [249] *distributed under the terms of the Creative Commons Attribution 2.0 International License).*
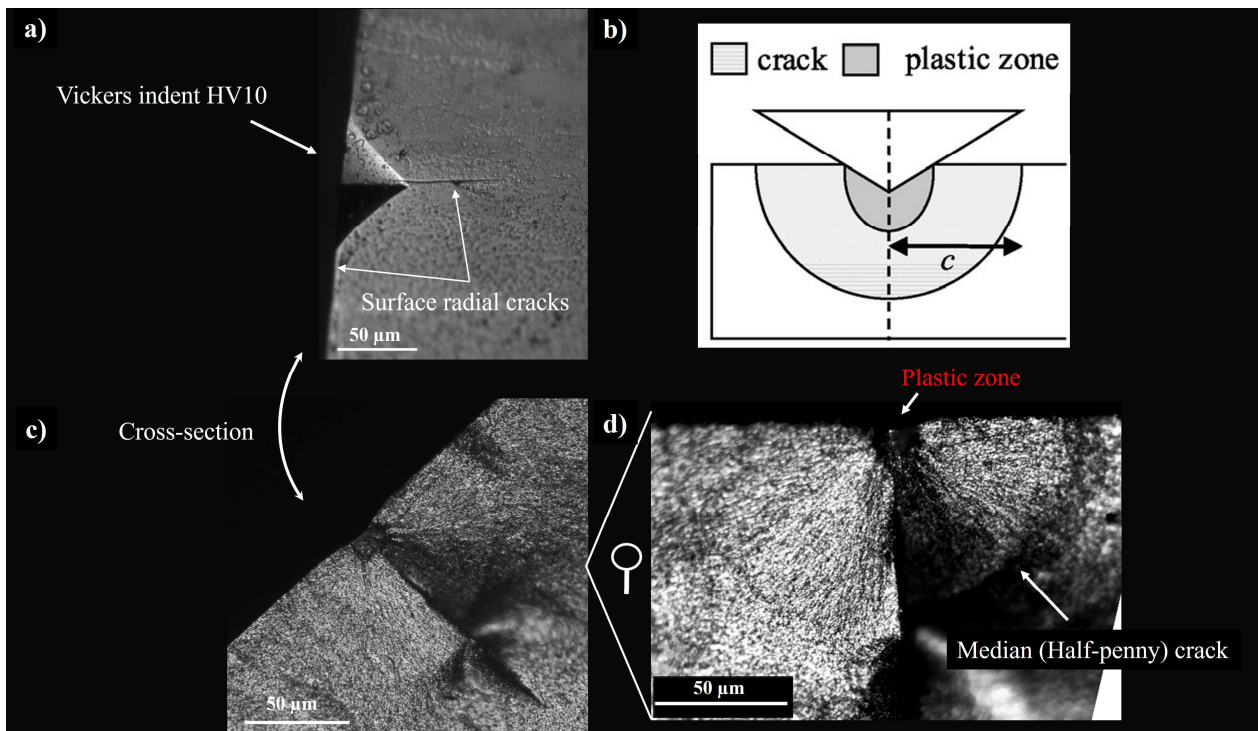
Figure 103 Crack cross-section profile of a Vickers indent performed at 10 kg on the surface of a BTC component: surface of the splitted indentation (a), example (b) and cross sections (c, d) of a Median-Radial (Half-penny) crack morphology (Original figure by Mazo).

In the present study, the choice on the equation was performed by directly observing the crack type generated by manually opening (Figure 103, a) a Vickers indentation. Figure 103(d) clearly shows that the crack generated under the indentation is a Median-Radial (Figure 102). Therefore, the Anstis formalism [26] will be used in the determination of the indentation fracture toughness:

$$K_{Ic} = 0.016 \left(\frac{E}{H}\right)^{1/2} \left(\frac{P}{c^{3/2}}\right) \tag{43}$$

where P is the indent force, c the average crack length (Figure 103 (b)), H the hardness and E the Young's Modulus previously measured from the nanoindentation tests.

Hardness, as measured from Vickers indentation at different loads (Figure 104), shows an increasing trend by the indentation load. This behaviour, known as indentation size effect (ISE), has several possible contributions that depends on the material's plasticity. In very hard ceramics, the deformation under the indenter occurs in discrete bands (Figure 109(a)) rather being continuous. The recovery of the elastic increment of deformation, preceding each new band of deformation, results in the indentation appearing smaller than expected. Since this effects scale with the indentation size, lower is the applied loads and higher is the magnitude of the elastic recovery between two deformation bands [250]. Bull et al. reported that in some extreme cases, when the indentation is in the nano size, the surface flexure will remain elastic and is fully recovered upon unloading, leaving no residual hardness impressions [250]. At the lowest 2 N load, the SPS samples reach a Vickers hardness that is comparable with previous Berkovich tests (Figure 99Figure 100), around 30 GPa for the biphasic SPS_{ox} and above 31 GPa for monophasic SPS_{pure}. Similarly, for the flash sintered samples, the hardness drops to 24-25 GPa for the FS_{pure} and about 21 GPa for biphasic FS_{ox}.

The fracture toughness of SPS samples is found around 4-5 MPa $m^{0.5}$, in agreement with the data reported in literature [251]. Slightly lower values are measured from SPS_{ox}, the sample containing a

larger content of the W_2C phase, which is generally considered a more fragile phase with a $K_{Ic} \cong 3.5$ MPa m$^{0.5}$ [180]. In the biphasic and monophasic SPS samples K_{Ic} is substantially constant with the indentation load. Differently, the FS samples show an overall higher K_{Ic} which increases by decreasing the indentation size. K_{Ic} of FS_{pure} but especially that of the biphasic FS_{ox} samples are considerably higher than the SPS counterpart, reaching values of $\cong$6-7 MPa m$^{0.5}$ and 8-9 MPa m$^{0.5}$ respectively. This difference can be easily visualized from Figure 108, where all the indentation cracks lengths, used for the evaluation of the K_{Ic} (Eq. 43), are reported and compared between the FS and SPS samples.
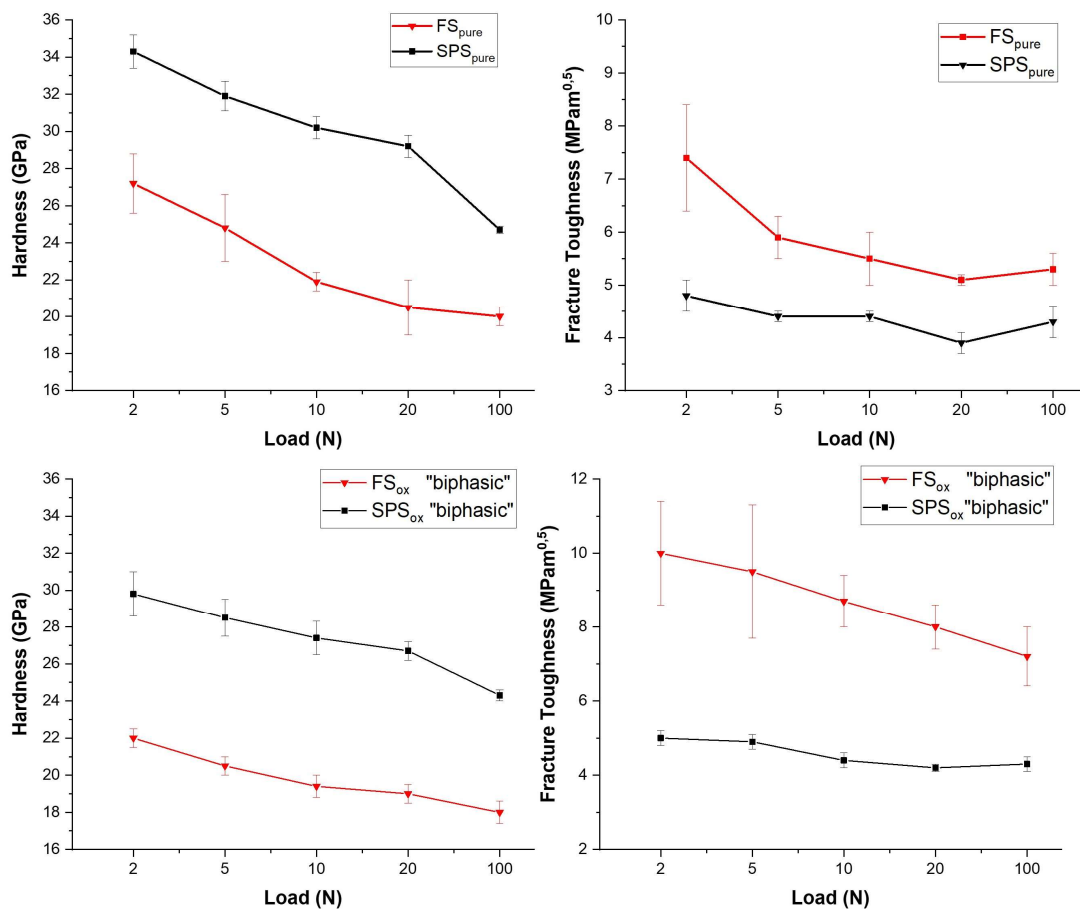
Figure 104 Vickers hardness and fracture toughness of the four BTC samples measured at different loads: 2, 5, 10, 20 and 100 N.

The large difference in fracture toughness between FS_{ox} and SPS_{ox} sample is easily discernible from Figure 105, where the indentation crack length generated by Vickers indentation at 20, 10 and 5 N is compared. Radial cracks in the flash sintered sample are visibly shorter and even more importantly they look distorted and with a high tortuosity. Starting from 5 N and below, radial cracks are not even more generated and according to that the corresponding value of K_{Ic} at low loads in Figure 104 is only estimated from the diameter of the hardness imprint.
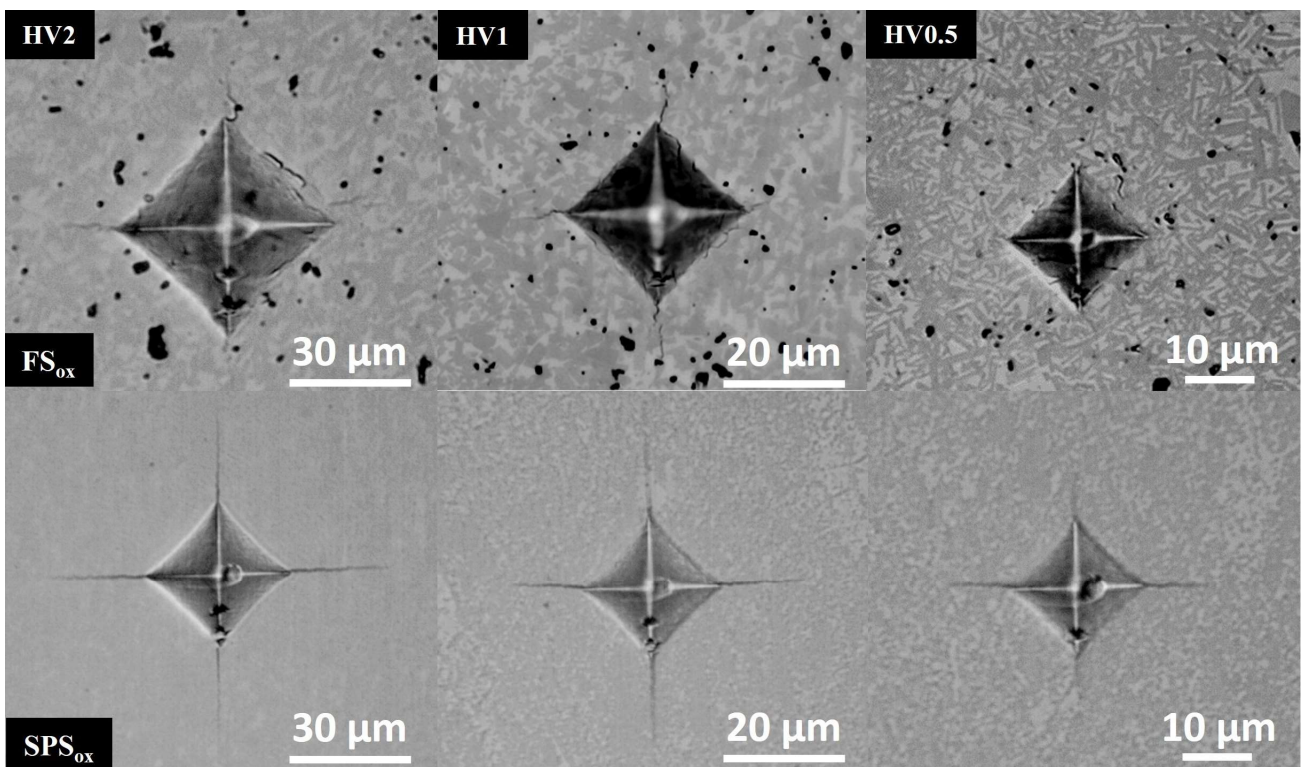
Figure 105 Vickers imprints for FS_{ox} (top) and SPS_{ox} (bottom) at different indentation loads: 20, 10 and 5 N.

The relative large toughness of this WC/W_2C biphasic material was also revealed in Figure 88 (a), where the biphasic micropillars retained a large portion of their strength ($\cong 6$ GPa) up to considerably large deformations (8 % of strain).
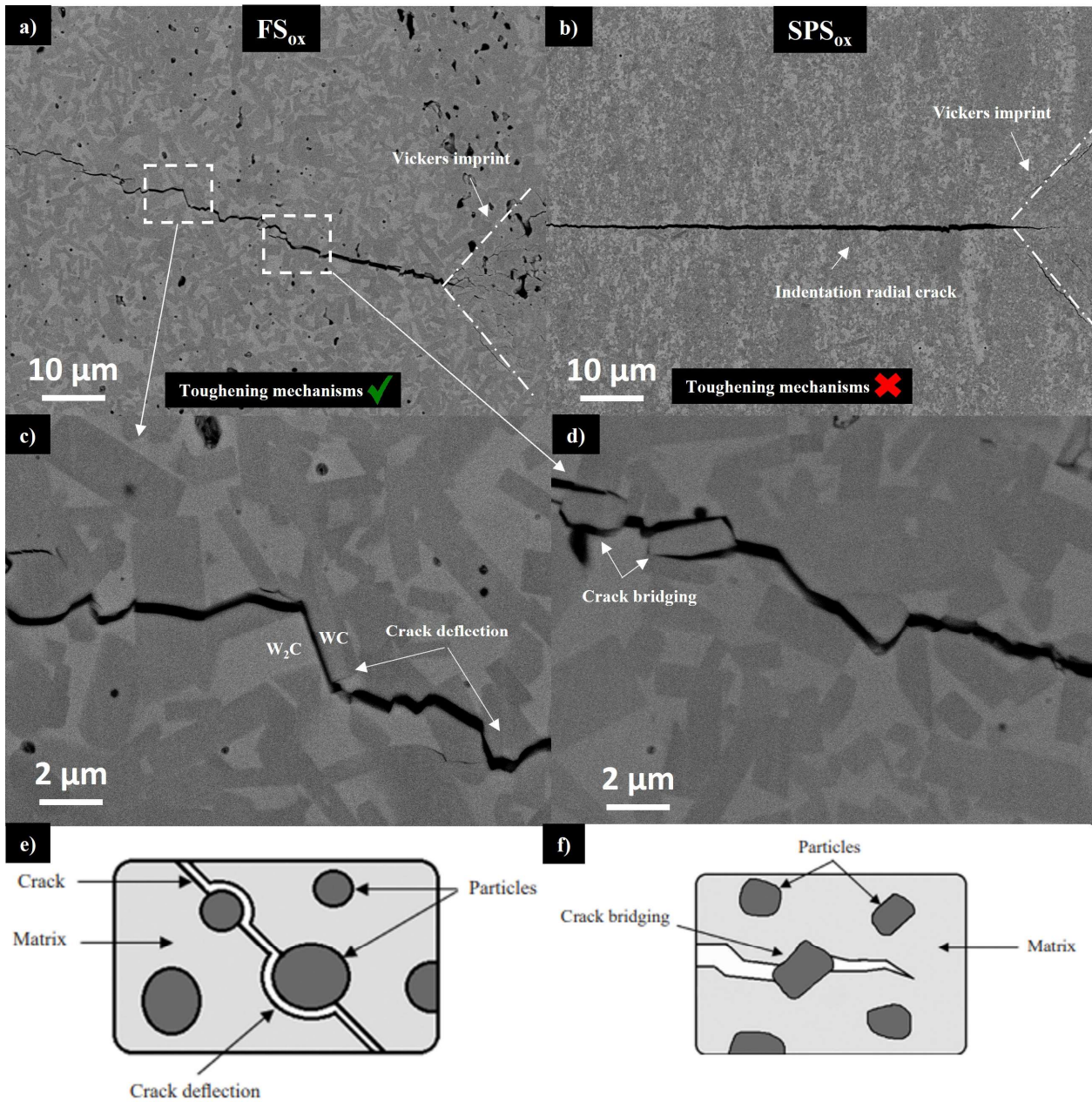
Figure 106 Comparison between the radial crack morphology after 10 N Vickers indentation for FS$_{ox}$ (a) and SPS$_{ox}$ (b) samples. Crack deflection (c, e) and crack bridging (d, f) toughening mechanisms active in the FS$_{ox}$ thanks to the presence of elongated WC grains in a WC/W$_2$C biphasic microstructure.

The capability of FS$_{ox}$ to dissipate a large amount of strain energy for crack propagation is for sure connected with crack deflection and bridging toughening mechanism as shown by SEM micrographs (Figure 106). The difference in the mechanical properties of WC and W$_2$C phases (Figure 101) creates a condition similar to that reported in Figure 106 (e, f); where hard particles are dispersed in a softer matrix.

These toughening mechanisms can only explain a flat increase in the K$_{Ic}$ measured between FS$_{ox}$ and SPS$_{ox}$, but not an increase of K$_{Ic}$ at lower indentations loads (Figure 104). Also for FS$_{pure}$ the higher fracture toughness of Figure 104 correspond to a real difference in the average crack length developed upon indentation (Figure 108) and similarly to FS$_{ox}$, below certain critical loads ($\cong$200 g) no indentation cracks are formed (Figure 107). For accounting these problems, the next paragraph will investigate the origin of an indentation size effect for fracture toughness and the connection, if present, with the increased toughness of the FS samples.
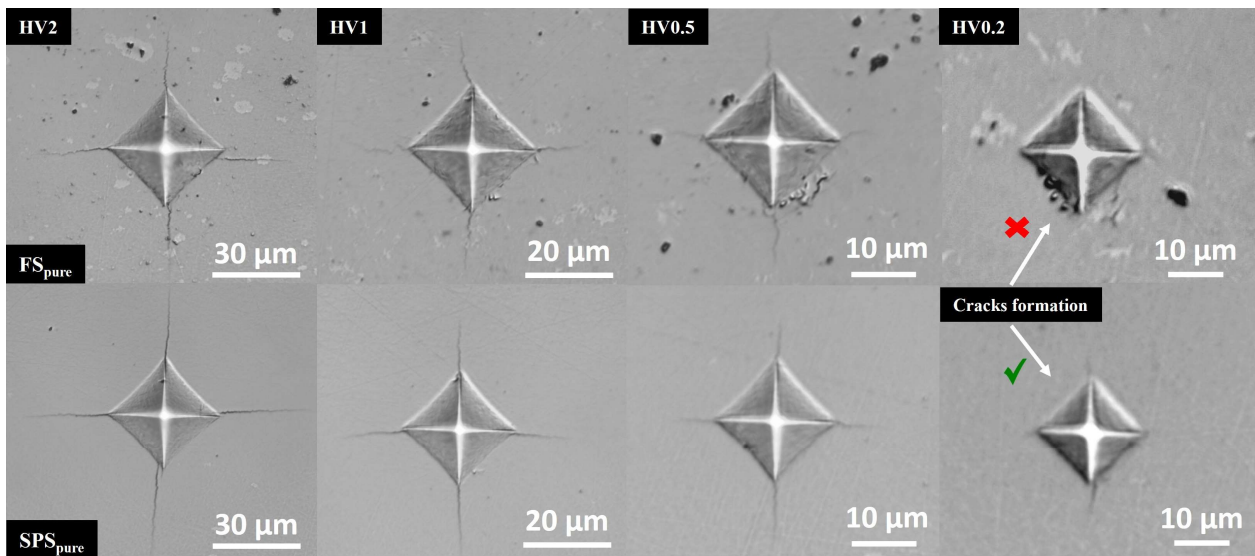
Figure 107 Vickers imprints for FS$_{pure}$ (top) and SPS$_{pure}$ (bottom) at different indentation loads: 20, 10, 5 and 2 N.
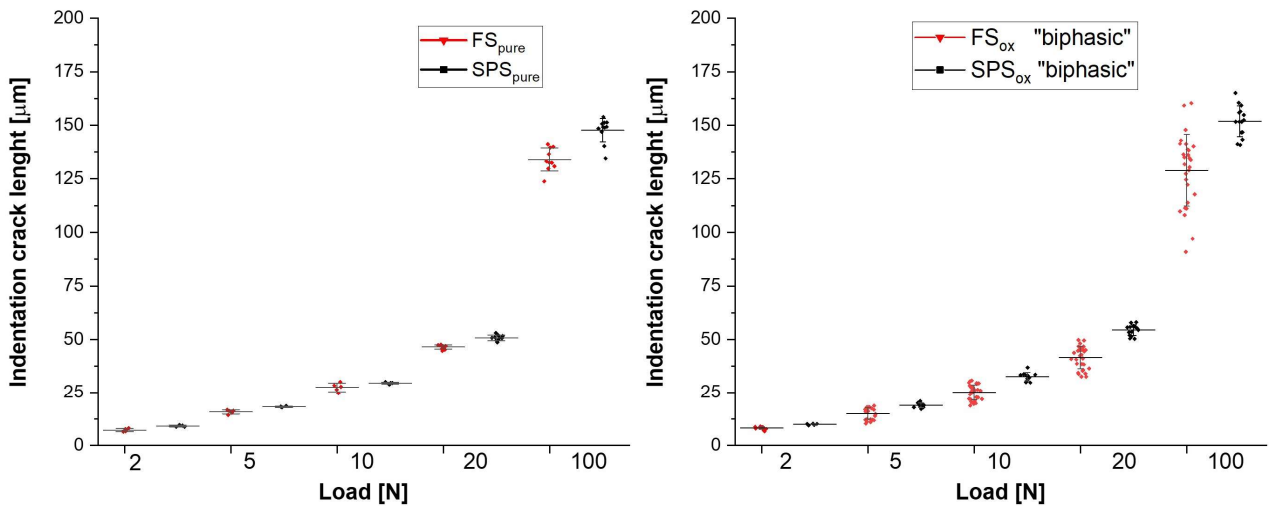
Figure 108 Comparison of the indentation crack lengths between FS and SPS samples.

It is worth noting that the Anstis method (Eq. 43) for fracture toughness evaluation using Vickers indentation can be inaccurate for real cracks. Quinn and Bradt [252] highlight various reasons for this. Real cracks possess bluntness and roughness, deviating from the assumption of a perfectly sharp crack. Incomplete closure of cracks during indentation leads to errors in measured crack length. Microstructural features like grain boundaries and residual stresses are not accounted for, affecting fracture toughness calculations. The method assumes plane strain conditions, but deformation may extend beyond the confined region, compromising accuracy. To summarize, the Anstis method overlooks real crack characteristics, incomplete closure, microstructural influences, and deviations from plane strain conditions, possibly leading to uncertainty in the toughness data presented in Figure 104. Considering the large discrepancy presented by Quinn and Bradt on the K_{IC} measured by various indentation fracture toughness equations with respect to the real K_{IC} of standardized test specimen, the results from indentation toughness are here presented as a way to compare the "*complex crack arrest phenomenon*" of WC samples sintered by the two said techniques (SPS and FS).

Indentation size effect (ISE) & fracture toughness

There are two possible origins for the indentation size effect (ISE), depending on the material's plasticity. For soft and deformable materials, the ISE has been successfully modeled by Nix and Gao, considering the interaction between the geometrically necessary dislocations (GNDs) and the statistically stored (SSD) ones (Figure 109, b) [253]. According to this theory the ISE is directly related to the increased density of GNDs with the inverse of the indentation depth. Hardness tends to increase by decreasing the indentation load, hence the size of the imprint, because of an increase in the strain gradient associate with the reduction of the deformed volume [253,254].

Conversely, as introduced before, for very hard material the plastic deformation occurs at a characteristic spacing (δ in Figure 109(a)) and the elastic displacement generated during the indentation may be comparable with the size of the measured final diagonal [250,255]. Smaller is the indent size and larger is the elastic displacement compared with the measured diagonal, effectively introducing an indentation size effect on the measured hardness (Figure 109(a)).

For materials with sufficient plasticity at room temperature the ISE effect can be used to analyze the effects of strain gradients on plasticity [256]. Tungsten carbide is a super hard refractory ceramic that is known to have some active slip systems at room temperature [233].

The proportional specimen resistance (PSR) model is used to separate the elastic and the plastic component affecting the ISE behaviour [255]. The following equation correlates the indentation load, P, to the diagonal length, d, by:

$$P = ad + bd^2 \tag{44}$$

where the total energy consumed during the indentation can be approximated to:

$$E_{ind} = \frac{1}{2} P_{max} \delta_{max} \tag{45}$$

If one considers the proportionality between the diagonal length (d) and the depth, the work for deformation can be represented by $W \cong \alpha_1^* P^* d$; $(\alpha_1 = \frac{1}{2} \frac{\delta_{max}}{d})$.

Multiplying the Eq. 44 by the diagonal length, d, one obtains:

$$Pd = ad^2 + bd^3 \tag{46}$$

According to this representation, the first term on the right is related to the indentation surface area and the second one to the deformed volume. The first coefficient of Eq. 46, "a" is then proportional to the surface work: the combination of friction energy and elastic resistance energy (elastic contribute), while "b" is proportinal to work done for plastically deform the material under the indenter (plastic contribute) [257]. The two adimensional parameters a and b, can be determined by plotting P/d versus d as shown in Figure 110. While the elastic coefficients, a, differs slightly among the tested samples of Figure 104, one

can notice a significative difference in b, between the flash sintered and the SPS samples. The significant

drop of b means that less work is necessary to permanently deform the FS materials under the indenter

tip (Figure 110).
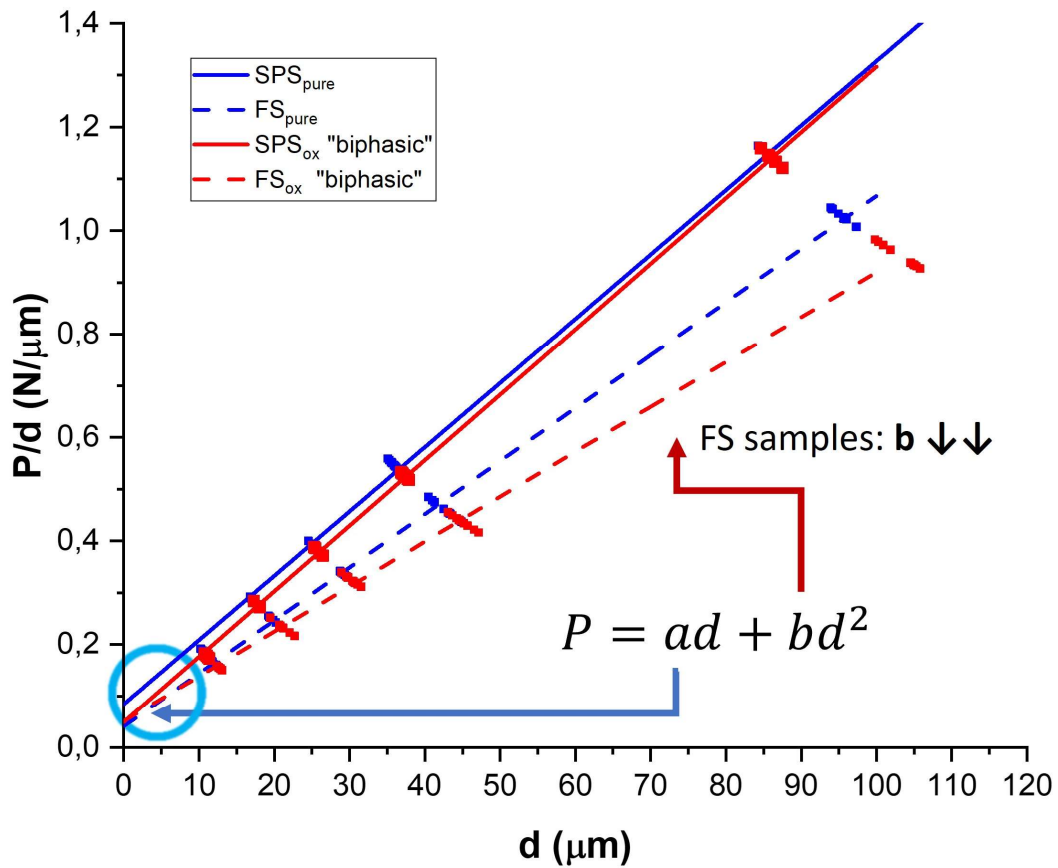
Figure 110 Proportional specimen resistance (PSR) model: plot of P/d over d (diagonal length of

indentation) for the evaluation of elastic (a) and the plastic (b) coefficients.

The two FS samples showing increased toughness are also softer concerning the SPS ones. They are

characterized by a lower elastic modulus, hardness, yield strength (Figure 88Figure 89), and plastic

contribution to the ISE effect. Since this plastic contribution is connected to the strain gradient in the

plastic zone, the decrease of b, as determined in Figure 109, equals a lower effect of the strain gradient over the indentation size effect (ISE).

A relatively high volume, equal to the submerged indenter volume, must be relocated somehow during indentation. This occurs easily for ductile material with a high dislocation activity like metals, but the situation is much more complex in ceramics, like WC. In this case, the material can be relocated by: (i) extensive microcracking, when they become interlinked, the material is allowed to dislodge, (ii) dislocation movement activated by high-stress levels and (iii) grain sliding in some particular cases. Usually, to accommodate plastic deformation below the indenter tip grains need to rotate according to the necessity in generating the geometrical necessary dislocations (Figure 109, b). The lower the load, the higher the strain gradient making the movement and the change in the direction of these dislocations much more difficult, experiencing a higher material's hardness. According to these concepts, the lower effect of strain gradient to the ISE can be associate with (i) weaker GB, grains can be relocated at lower stresses by extensive microcracking without the necessity to activate deformative mechanisms or (ii) flash sintered WC grains are "softer" and more easily deformable concerning the SPS ones.

It is difficult to discriminate which of the two effect is really affecting the indented material. However, if both are present, they can give origin to an indentation size effect also for K_{Ic} as follow. When the indentation size is small, plastic mechanisms are favored because the limited interaction volume limits the strain energy available for crack propagation. On the others side, with the increase in the interaction volume, hence at higher indentation loads, the material is more prone to accommodate the permanent deformation by microcracking, hence is more fragile causing the drop in K_{IC} observed in Figure 104 for the FS samples.

4.2.4 Conclusions

BTC ceramics produced by SPS are harder (30+ GPa), stiffer ($\cong$600-700 GPa) and denser (98-99%+) concerning the material consolidated by ERFS. From one side, SPS can densify pure WC powder with great control over the grain size and the phase composition, possibly retaining 100% of α-WC in spite of W_2C or WC_{1-x} secondary phases. On the other side, SPS ceramics are intrinsically more fragile, with a fracture toughness K_{Ic} limited to 4-5 MPa·m$^{0.5}$ because of the lack of any macroscopic toughening mechanisms. The ultra-fast sintering of pure WC leaves some residual porosity (3-4 vol%), which negatively affects the hardness (20-25 GPa) and modulus ($\cong$550 GPa) of the bulk, although it introduces some unique microstructural and mechanical features. It can produce biphasic WC/W_2C ceramics with toughness values almost twice higher ($K_{Ic} \cong$ 7-8 MPa·m$^{0.5}$) than any SPS sample. Abnormal WC grains, 5-7 μm in size, with an elongated shape and surrounded by softer W_2C grains create the conditions for crack deflection and bridging toughening mechanisms. In addition, flash-sintered BTC ceramics present a "softer" character with respect to the SPS ones. They show an indentation size effect (ISE) on the fracture toughness; i.e. K_{Ic} increases by decreasing the indentation size. The separation of the elastic from the plastic contribution over the ISE behaviour points out that FS ceramics require less plastic work to plastically deform the material.

Chapter 5

Conclusions & future perspectives

As outlined in this thesis, when a high-output AC current interacts with pure WC nanopowders, it triggers a rapid evolution of the material's resistivity and temperature, leading to an almost instantaneous densification of the material. The possibility of applying the flash sintering (FS) technology to tungsten carbide (WC), an electrically conductive "metallic ceramic", offers new and unexplored manufacturing routes. For highly conductive materials, this process is a combination between electrical resistance sintering (ERS) and flash sintering (FS), which gives names to the electrical resistance flash sintering (ERFS), as defined in this work. The ERFS process allows the ultrafast consolidation of binderless tungsten carbide (BTC) ceramics in a time scale of seconds because of the significant acceleration in the sintering rates experienced during the flash event. This event consists of an electro-thermal reaction, a thermal runaway of Joule heating, which creates the condition for a power surge of electric energy in the material. The rapidity of such phenomenon, hence the time required to bring the powder compact at the maximum sintering temperatures, is the key to understand how the densification phenomena occur at this time scale. Accelerating the solid-state sintering mechanisms during ERFS permits consolidating these highly refractory BTC ceramics at a fraction of the electrical energy concerning other processes. Figure 111 compares the specific electrical energy necessary to sinter a certain volume of WC powder. The ERFS process, which only lasts between 10 and 60 s [117], consumes almost 100 times less energy than a fast-sintering technology (SPS) and about a factor of 1000 if compared to conventional sintering in a high-T graphitic furnace.
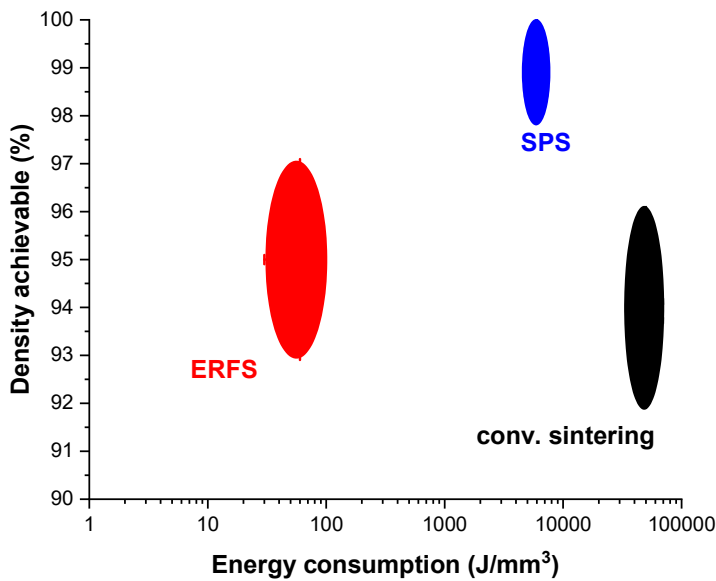
Figure 111 Specific electric energy consumption (J/mm³), and relative density, during the consolidation of binderless tungsten carbide (BTC) ceramics. Data regarding the ERFS process are taken from Table 2 and Table 3 [117]*; for the SPS we considered only the electrical energy consumed for heating the graphite die element and the WC powders at 2100 °C for 5min (200°C/min), SPS furnace Dr. Sinter 1050 (Sumitomo®). Conventional sintering is the pressureless sintering in a vacuum graphitic furnace (GERO® Carbolite model LHTG 100-200/22-1-G) at 2150°C for 2 h; nominal power consumption 22 kW. (Original figure by Mazo).*

However, at the current stage of development, ERFS is still inferior to SPS concerning the maximum density achievable (Figure 111). In section 2.3, we studied and reported the reasons behind this limitation, highlighting how the contact between the Mo electrodes and the powder to be sintered caused high thermal losses [258]. It is clear from Figure 49 and Figure 54 that the electrical contacts caused the WC pellet to be less dense at the top and bottom surfaces comparing to its centre. These thermal losses will certainly increase with the size of the sintering apparatus, hence with the dimension of the object to consolidate. In the hypothesis of scaling up the system, one must figure out new solutions to supply the

high current densities required for sustaining the flash in highly conductive ceramics while limiting at the same time the heat losses through the electrodes [258]. A possible solution facing this problem can be found in the contactless flash sintering concept, where the current is supplied to the sample without a physical contact. WC, and many other metallic ceramics, are electronic conductors. Besides, the electromagnetic induction effect can reasonably induce a parasitic (eddy) current in the conductive WC pellet (Figure 112(b)). It is reasonable to assume that an adequately intense eddy current will have the same Joule heating effect on a WC powder compact as the one described in this work, activating the same thermal runaway event. As summarized in Figure 112(c) and (d), the two currents, the parasitic and the one supported directly by the Mo electrodes, will only differ in the direction of the electric field. A possible induction-assisted flash sintering setup (Figure 112(b)) will allow to thermally insulate the WC powder by simply placing two ceramic inserts between the Mo electrodes of Figure 112(a).
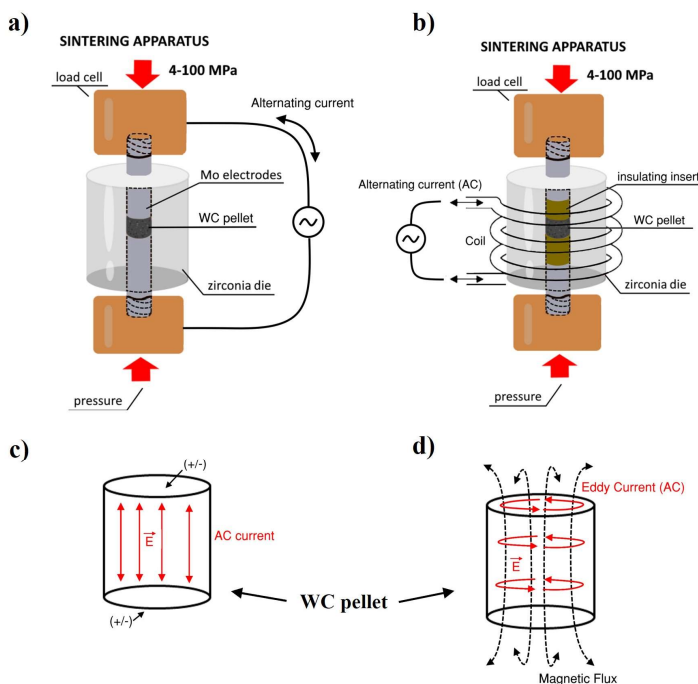
Figure 112 Schematics of a possible alternative to the ERFS apparatus used in this work (a), applying the current by an external induction coil (b). The corresponding electric field directions are represented in (c) and (d). (Original figure by Mazo).

As a future perspective and to prove how the ERFS process can be effectively implemented on other metallic ceramics, we presented some preliminary results on pure ZrB_2 powders (ZrB_2 grade B, Höganäs®), using the same ERFS sintering apparatus of Figure 15.

ZrB_2 is an ultra-high temperature ceramic (UHTC) with a melting point of 3246ºC, considerably more difficult to sinter than pure WC. Indeed, Figure 113(b) shows that the SPS at the maximum sintering temperature of 2300ºC fails to achieve full density, resulting in the presence of intragranular porosity and in a conspicuous microstructure coarsening.
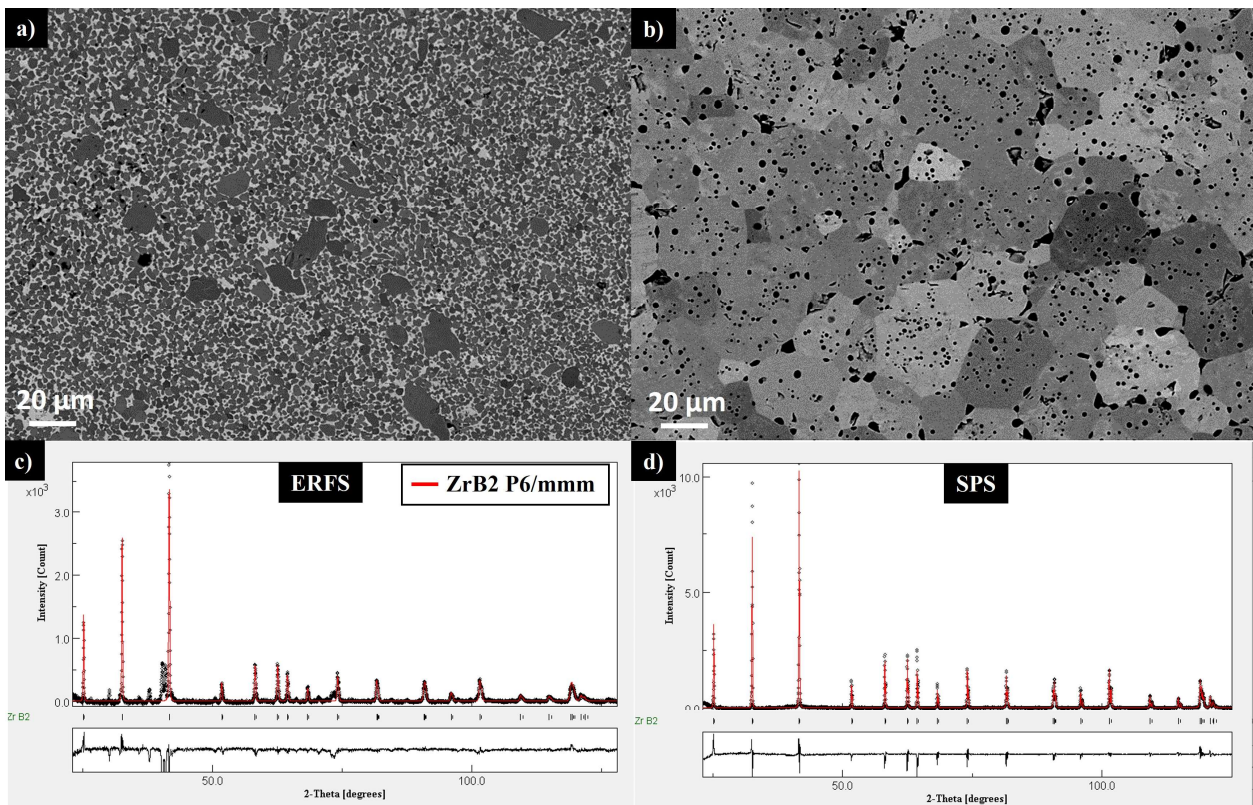
Figure 113 Microstructures (FESEM-BSE) of ZrB₂ ceramics sintered by ERFS (a) and by SPS (b) and corresponding XRD spectrograms (c) and (d). SPS sample was sintered at a maximum temperature of 2300 ºC for 7 min under 60 MPa of pressure (Dr Sinter 1050 furnace). ERFS pellets, 7 mm in height, were sintered at 4.5 V and 10 MPa for ≅15 s. (Original figure by Mazo).

Nevertheless, Figure 113(a)) proves that an ultrafast consolidation is achievable also for this material during ERFS experiments. The nature and the properties of the flash-sintered ZrB_2 microstructure are still under research, as evidenced by the presence of unknown phases in the XRD analysis of Figure 113(c), although Figure 114 reports how a very similar electric power surge event is occurring in ZrB_2 and WC ceramics. It is interesting to highlight how the flash sintering of ZrB_2 requires twice the amount of electrical power than WC to sinter the material (Figure 114) successfully.
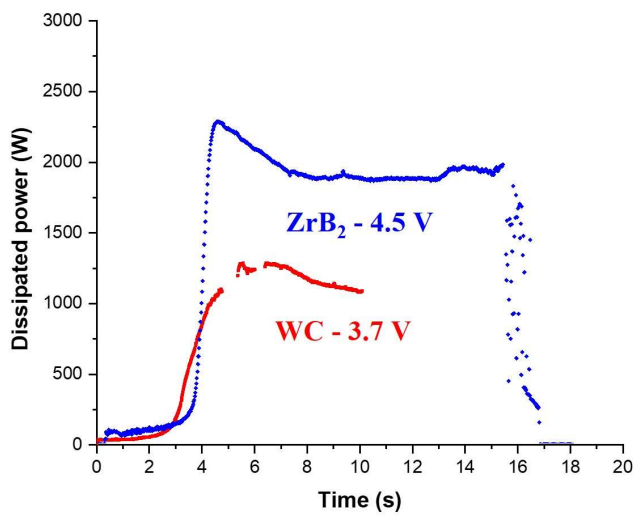
Figure 114 Characteristic power surges generated during the ERFS process of two metallic ceramics. Comparison in the electrical power required for the flash sintering of WC (T_m=2785 °C) and ZrB_2 (T_m=3246°C). (Original figure by Mazo).

In conclusion, the results reported and discussed in this work extend the applicability of the flash sintering process to tungsten carbide, a new class of conductive ceramics characterized by a positive coefficient of resistivity with temperature (PTC). This thesis also reported some peculiar "out of equilibrium" modifications of BTC ceramics prompted by the flash event. The metastable phase of the W-C system (WC_{1-x}), thermodynamically stable only above 2500°C, was retained and stabilized in the flash-sintered product after cooling to room temperature (3.2). Flash sintering was also demonstrated to alter the high-

temperature deformation for WC-ceramics, affecting the grain sliding mechanism during micropillar compression tests at 700ºC (4.1). The possibility to tailor new microstructures and/or mechanical properties by manipulating the consolidation conditions offer a great tool in the design of new and/or improved UHTC ceramics for the most important applications of the next future, like in the aerospace and high heat flux applications [73,74].

Supplementary materials
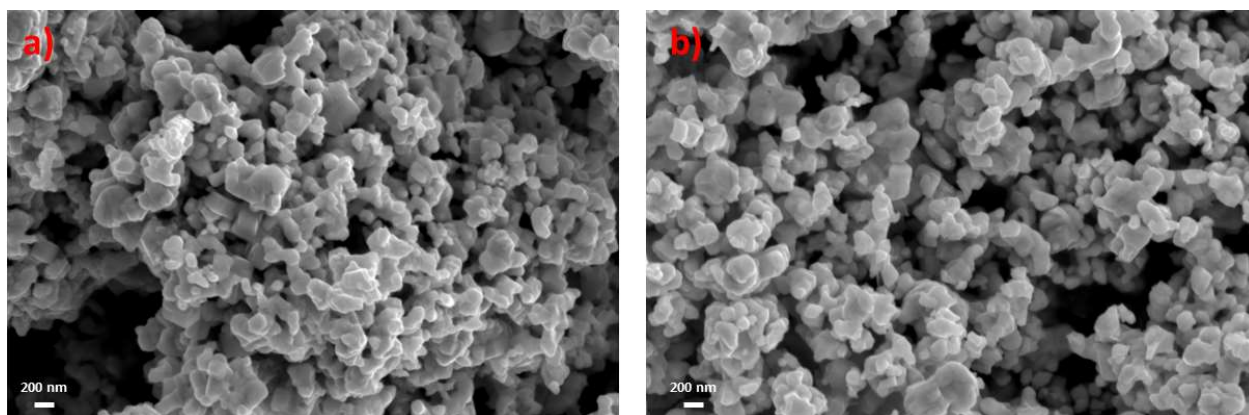
Figure S. 1. FESEM micrographs of ox-WC (a) and pure-WC (b) powders.
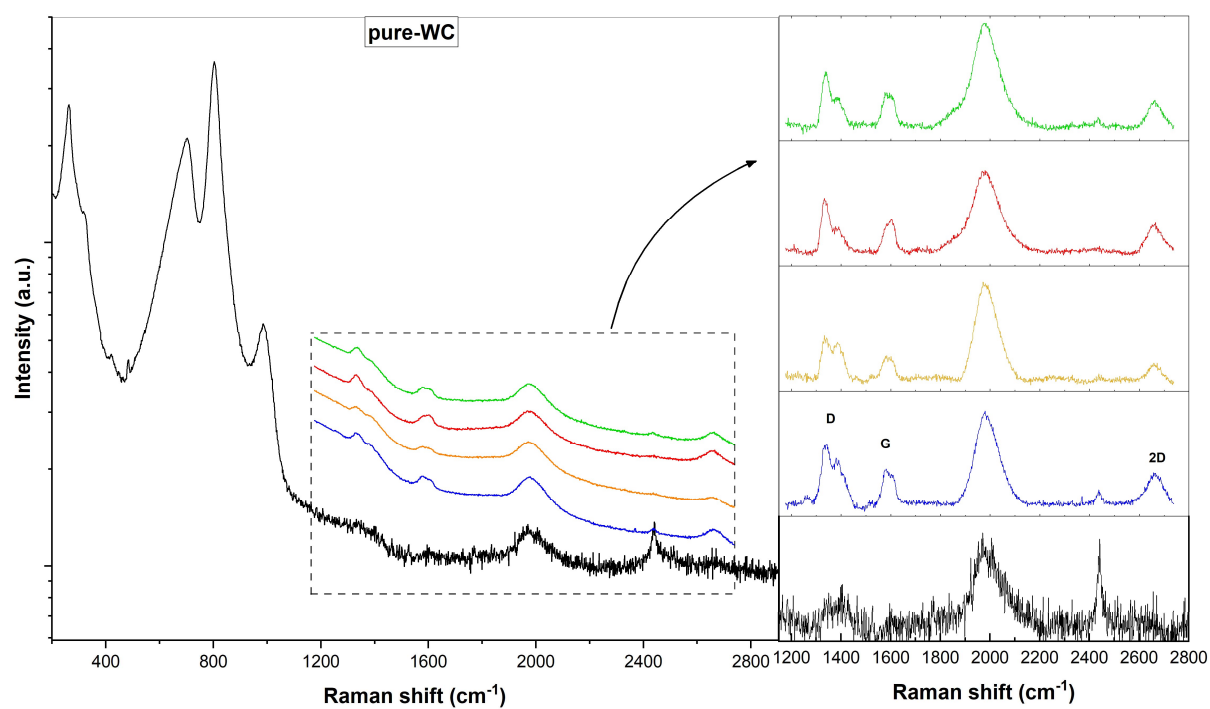
Figure S. 2. Complete Raman analysis of pure-WC powder. The bracket reports analyses acquired on different spots on the powder.
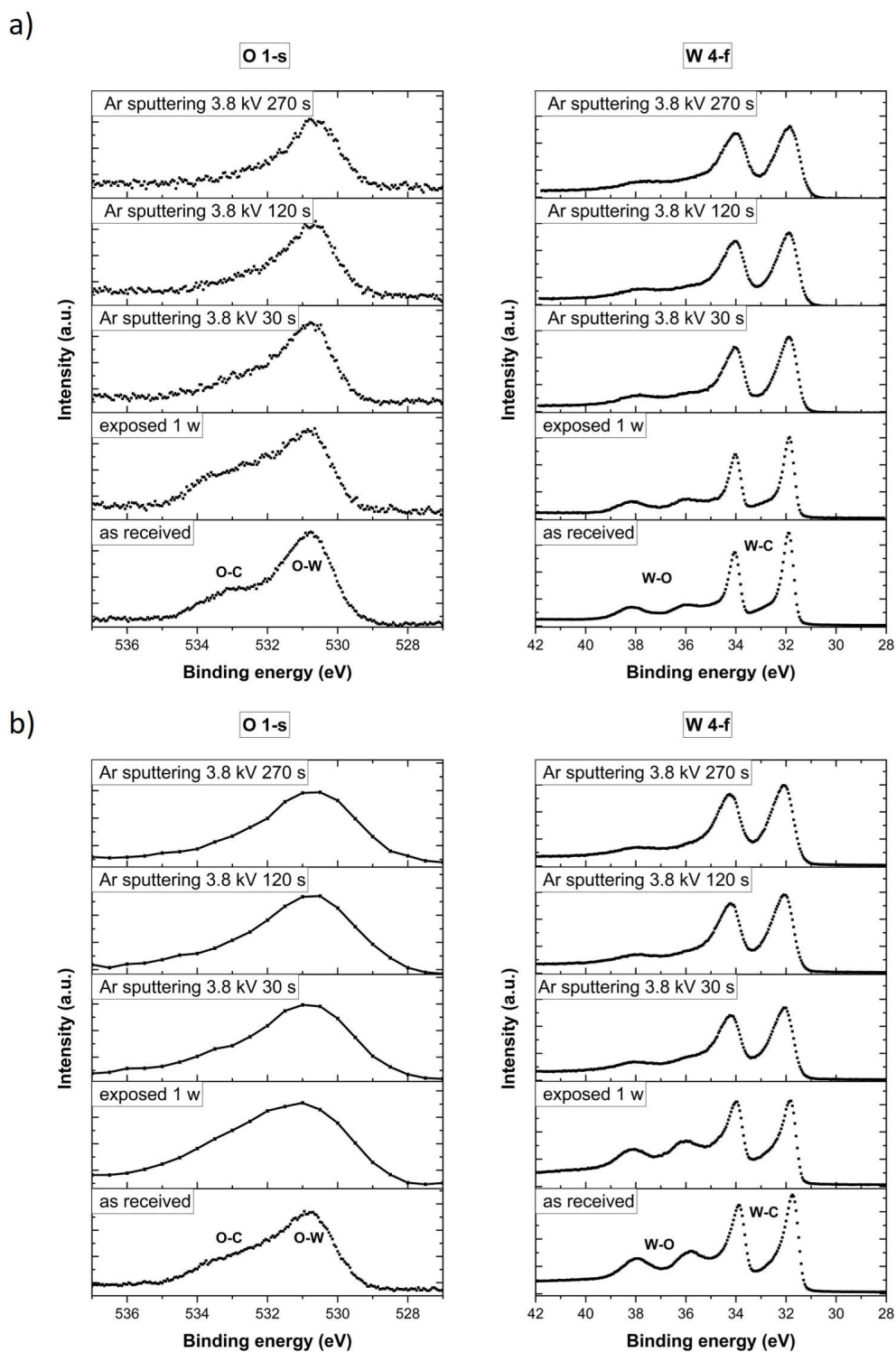
Figure S. 3. XPS spectra for ox-WC (a) and pure-WC (b) powders: O 1s and W 4f core levels are acquired at different sputtering conditions and after 1 week of exposure to the atmosphere.

236
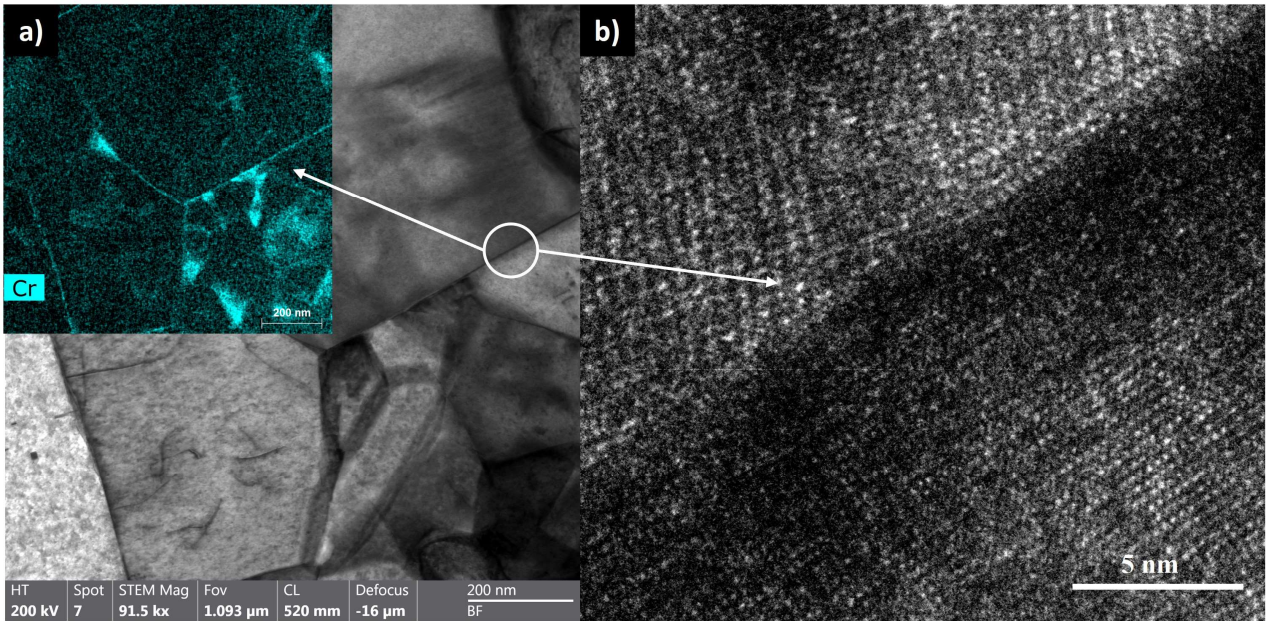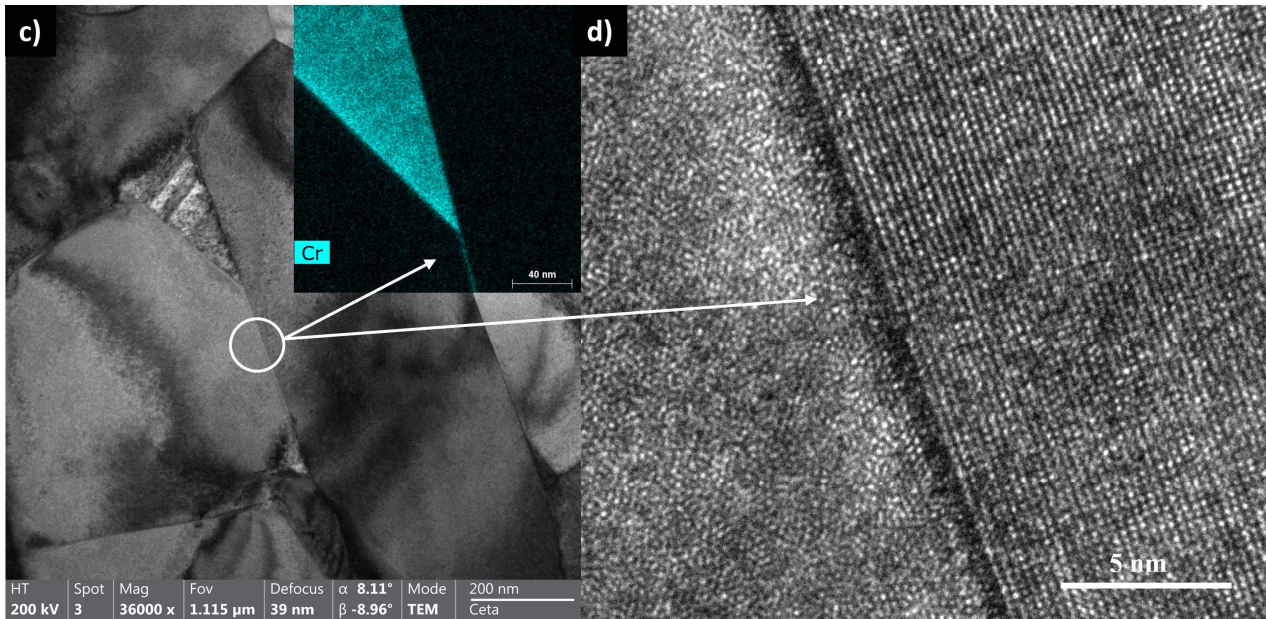
SPS_{pure}

FS_{pure}

Figure S. 4. HRTEM and EDXS analysis of some grains contained in SPS$_{pure}$ (a, b) and FS$_{pure}$ (c, d) pillars. The segregation of Cr is present in both materials at GB but is not related to a secondary phase at GB. Grain boundaries of materials (b) and (d) appear clean and in the absence of any glass phase.

237
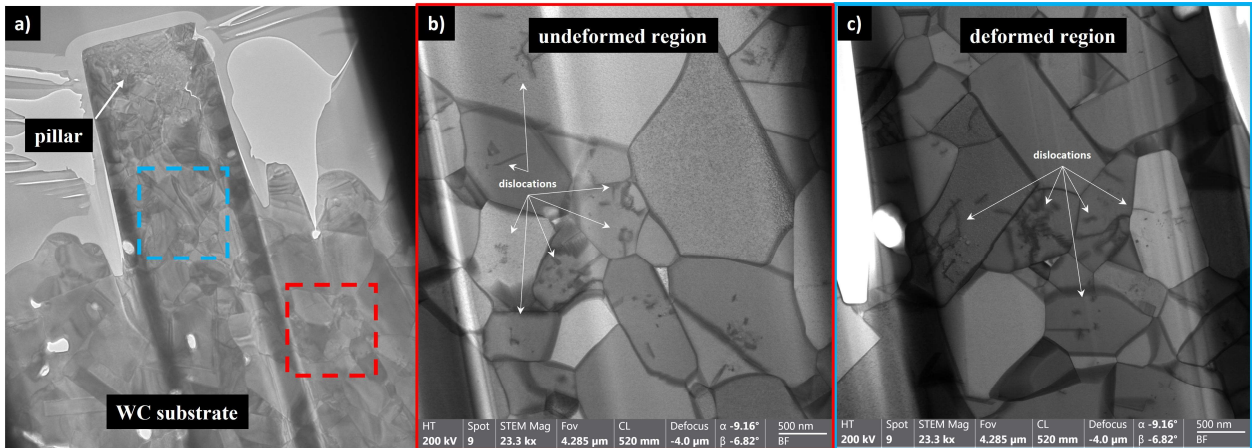
Figure S. 5. TEM micrograph of the lamella containing a FS$_{pure}$ pillars (a). Undissociated dislocations are present in the deformed material, compressed pillar (b), as well as in the undeformed region, WC substrate (c). Undissociated dislocations are introduced in the FS$_{pure}$ material during the flash sintering process.

Bibliography

[1]   P.A. Burr, S.X. Oliver, Formation and migration of point defects in tungsten carbide: Unveiling the sluggish bulk self-diffusivity of WC, J Eur Ceram Soc. 39 (2019) 165–172. https://doi.org/10.1016/j.jeurceramsoc.2018.10.001.

[2]   K. Kornaus, M. Rączka, A. Gubernat, D. Zientara, Pressureless sintering of binderless tungsten carbide, J Eur Ceram Soc. 37 (2017) 4567–4576. https://doi.org/10.1016/j.jeurceramsoc.2017.06.008.

[3]   J.H. P. Schwarzkopf, Production of hard metal alloys, especially for tools, 1.925.910., 1939. https://doi.org/10.1145/178951.178972.

[4]   Karl Schroeler, Sintered hardmetal alloy and procedure for its fabrication, DRP 420.689:, 1923.

[5]   G.S. Upadhyaya, Materials science of cemented carbides — an overview, Mater Des. 22 (2001) 483–489. https://doi.org/10.1016/S0261-3069(01)00007-3.

[6]   H.M. Ortner, P. Ettmayer, H. Kolaska, The history of the technological progress of hardmetals, Int J Refract Metals Hard Mater. 44 (2014) 148–159. https://doi.org/10.1016/j.ijrmhm.2013.07.014.

[7]   J. García, V. Collado Ciprés, A. Blomqvist, B. Kaplan, Cemented carbide microstructures: a review, Int J Refract Metals Hard Mater. 80 (2019) 40–68. https://doi.org/10.1016/j.ijrmhm.2018.12.004.

[8]   A.S. Kurlov, A.I. Gusev, Tungsten Carbides: Structure, Properties and Application in Hardmetals, Springer International Publishing, Cham, 2013. https://doi.org/10.1007/978-3-319-00524-9.

[9]   W.S. Williams, The thermal conductivity of metallics ceramics, Thermal Management. (1998) 62–66.

[10]   K.M. Tsai, C.Y. Hsieh, H.H. Lu, Sintering of binderless tungsten carbide, Ceram Int. 36 (2010) 689–692. https://doi.org/10.1016/j.ceramint.2009.10.017.

[11]   J. Sun, Y. Chen, J. Zhao, Nano-ceramic replacing cobalt in cemented carbide as binder phase: Is it feasible?, J Alloys Compd. 896 (2022) 162968. https://doi.org/10.1016/j.jallcom.2021.162968.

[12]   J. Sun, J. Zhao, Z. Huang, K. Yan, X. Shen, J. Xing, Y. Gao, Y. Jian, H. Yang, B. Li, A Review on Binderless Tungsten Carbide: Development and Application, Nanomicro Lett. 12 (2020) 13. https://doi.org/10.1007/s40820-019-0346-1.

[13]   H. Tripathy, C. Sudha, V.T. Paul, R. Thirumurugesan, T.N. Prasanthi, R. Sundar, N. Vijayashanthi, P. Parameswaran, S. Raju, High temperature thermophysical properties of spark plasma sintered tungsten carbide, Int J Refract Metals Hard Mater. 104 (2022) 105804. https://doi.org/10.1016/j.ijrmhm.2022.105804.

[14]   T. Dash, B.B. Nayak, M. Abhangi, R. Makwana, S. Vala, S. Jakhar, C.V.S. Rao, T.K. Basu, Preparation and neutronic studies of tungsten carbide composite, Fusion Science and Technology. 65 (2014) 241–247. https://doi.org/10.13182/FST13-663.

[15]   S.X. Oliver, M.L. Jackson, P.A. Burr, Radiation-Induced Evolution of Tungsten Carbide in Fusion Reactors: Accommodation of Defect Clusters and Transmutation Elements, ACS Appl Energy Mater. 3 (2020) 868–878. https://doi.org/10.1021/acsaem.9b01990.

[16]   S.A. Humphry-Baker, G.D.W. Smith, Shielding materials in the compact spherical tokamak, Philosophical Transactions of the Royal Society A: Mathematical, Physical and Engineering Sciences. 377 (2019) 20170443. https://doi.org/10.1098/rsta.2017.0443.

[17]   A. Kundu, J. Ma, J. Carrete, G.K.H. Madsen, W. Li, Anomalously large lattice thermal conductivity in metallic tungsten carbide and its origin in the electronic structure, Materials Today Physics. 13 (2020) 100214. https://doi.org/10.1016/j.mtphys.2020.100214.

[18]   S.A. Humphry-Baker, G.D.W. Smith, G. Pintsuk, Thermal shock of tungsten carbide in plasma-facing conditions, Journal of Nuclear Materials. 524 (2019) 239–246. https://doi.org/10.1016/j.jnucmat.2019.06.041.

[19]   A. Gubernat, P. Rutkowski, G. Grabowski, D. Zientara, Hot pressing of tungsten carbide with and without sintering additives, Int J Refract Metals Hard Mater. 43 (2014) 193–199. https://doi.org/10.1016/j.ijrmhm.2013.12.002.

[20]   J. Poetschke, V. Richter, R. Holke, Influence and effectivity of VC and Cr 3C 2 grain growth inhibitors on sintering of binderless tungsten carbide, Int J Refract Metals Hard Mater. 31 (2012) 218–223. https://doi.org/10.1016/j.ijrmhm.2011.11.006.

[21]   S. Lay, A. Antoni-Zdziobek, J. Pötschke, M. Herrmann, Microstructural investigations in binderless tungsten carbide with grain growth inhibitors, Int J Refract Metals Hard Mater. 93 (2020) 105340. https://doi.org/10.1016/j.ijrmhm.2020.105340.

[22]   A.S. Kurlov, A.I. Gusev, Tungsten carbides and W-C phase diagram, Inorganic Materials. 42 (2006) 121–127. https://doi.org/10.1134/S0020168506020051.

[23]   D. Mukhopadhyay, Identifying the causes of residual stress in polycrystalline diamond compact (PDC) cutters by X-Ray diffraction technique, Results in Materials. 11 (2021) 100216. https://doi.org/10.1016/j.rinma.2021.100216.

[24]   D. Ma, Z. Kou, Y. Liu, Y. Wang, S. Gao, X. Luo, W. Li, Y. Wang, Y. Du, L. Lei, Sub-micron binderless tungsten carbide sintering behavior under high pressure and high temperature, Int J Refract Metals Hard Mater. 54 (2016) 427–432. https://doi.org/10.1016/j.ijrmhm.2015.10.001.

[25]   Y. Zhang, Z. Kou, Z. Wang, M. Yang, J. Lu, H. Liang, S. Guan, Q. Hu, H. Gong, D. He, Magic high-pressure strengthening in tungsten carbide system, Ceram Int. 45 (2019) 8721–8726. https://doi.org/10.1016/j.ceramint.2019.01.195.

[26]   G.R. Anstis, P. Chantikul, B.R. Lawn, D.B. Marshall, A Critical Evaluation of Indentation Techniques for Measuring Fracture Toughness: I, Direct Crack Measurements, Journal of the American Ceramic Society. 64 (1981) 533–538. https://doi.org/10.1111/j.1151-2916.1981.tb10320.x.

[27]   R.O. Ritchie, The conflicts between strength and toughness, Nat Mater. 10 (2011) 817–822. https://doi.org/10.1038/nmat3115.

[28]   X. Liu, T. Lin, Z. Guo, F. Cui, J. Luo, Consolidation of Ultrafine Binderless Cemented Carbide by Spark Plasma Sintering, Journal of Iron and Steel Research, International. 14 (2007) 82–84. https://doi.org/10.1016/S1006-706X(08)60056-4.

[29]   B. Huang, L.D. Chen, S.Q. Bai, Bulk ultrafine binderless WC prepared by spark plasma sintering, Scr Mater. 54 (2006) 441–445. https://doi.org/10.1016/j.scriptamat.2005.10.014.

[30]   X. Li, Z. Xiao, C. Yang, S. Qu, Research on binderless tungsten carbide prepared by spark plasma sintering, Applied Mechanics and Materials. 37–38 (2010) 980–984. https://doi.org/10.4028/www.scientific.net/AMM.37-38.980.

[31]   H.T. Kim, J.S. Kim, Y.S. Kwon, Mechanical properties of binderless tungsten carbide by spark plasma sintering, Proceedings - 9th Russian-Korean International Symposium on Science and Technology, KORUS-2005. 1 (2005) 458–461. https://doi.org/10.1109/KORUS.2005.1507757.

[32]   A. Chang, B. Zhang, Y. Wu, Q. Zhao, H. Zhang, J. Yao, J. Xu, P. Zhao, Spark Plasma Sintering of Negative Temperature Coefficient Thermistor Ceramics, Sintering Techniques of Materials. (2015). https://doi.org/10.5772/59030.

[33]   J. Zhao, T. Holland, C. Unuvar, Z.A. Munir, Sparking plasma sintering of nanometric tungsten carbide, Int J Refract Metals Hard Mater. 27 (2009) 130–139. https://doi.org/10.1016/j.ijrmhm.2008.06.004.

[34]   S.I. Cha, S.H. Hong, Microstructures of binderless tungsten carbides sintered by spark plasma sintering process, Materials Science and Engineering A. 356 (2003) 381–389. https://doi.org/10.1016/S0921-5093(03)00151-5.

[35]   E.A. Lantsev, N. V. Malekhonova, V.N. Chuvil'Deev, A. V. Nokhrin, Y. V. Blagoveshchenskii, N. V. Isaeva, M.S. Boldin, P. V. Andreev, K.E. Smetanina, Binderless tungsten carbides with an increased oxygen content obtained by spark plasma sintering, J Phys Conf Ser. 1758 (2021). https://doi.org/10.1088/1742-6596/1758/1/012023.

[36]   V.N. Chuvil'deev, Y. V. Blagoveshchenskiy, A. V. Nokhrin, M.S. Boldin, N. V. Sakharov, N. V. Isaeva, S. V. Shotin, O.A. Belkin, A.A. Popov, E.S. Smirnova, E.A. Lantsev, Spark plasma sintering of tungsten carbide nanopowders obtained through DC arc plasma synthesis, J Alloys Compd. 708 (2017) 547–561. https://doi.org/10.1016/j.jallcom.2017.03.035.

[37]   E.A. Lantsev, N. V. Malekhonova, V.N. Chuvil'Deev, A. V. Nokhrin, M.S. Boldin, P. V. Andreev, K.E. Smetanina, Effect of initial particle size and various composition on the spark plasma sintering of binderless tungsten carbide, J Phys Conf Ser. 1758 (2021). https://doi.org/10.1088/1742-6596/1758/1/012022.

[38]   H.C. Kim, I.J. Shon, J.E. Garay, Z.A. Munir, Consolidation and properties of binderless sub-micron tungsten carbide by field-activated sintering, Int J Refract Metals Hard Mater. 22 (2004) 257–264. https://doi.org/10.1016/j.ijrmhm.2004.08.003.

[39]   J. Zhang, G. Zhang, S. Zhao, X. Song, Binder-free WC bulk synthesized by spark plasma sintering, J Alloys Compd. 479 (2009) 427–431. https://doi.org/10.1016/j.jallcom.2008.12.151.

[40]   D.M. Hulbert, A. Anders, D. v. Dudina, J. Andersson, D. Jiang, C. Unuvar, U. Anselmi-Tamburini, E.J. Lavernia, A.K. Mukherjee, The absence of plasma in "spark plasma sintering," J Appl Phys. 104 (2008). https://doi.org/10.1063/1.2963701.

[41]   M.N. Rahaman, Sintering of ceramics, CRC Press, 2007. https://doi.org/10.1201/b15869-2.

[42]   C.S. Bonifacio, T.B. Holland, K. van Benthem, Evidence of surface cleaning during electric field assisted sintering, Scr Mater. 69 (2013) 769–772. https://doi.org/10.1016/j.scriptamat.2013.08.018.

[43]   S. Deng, R. Li, T. Yuan, S. Xie, M. Zhang, K. Zhou, P. Cao, Direct current-enhanced densification kinetics during spark plasma sintering of tungsten powder, Scr Mater. 143 (2018) 25–29. https://doi.org/10.1016/j.scriptamat.2017.09.009.

[44]   Z. Trzaska, J.P. Monchoux, Electromigration experiments by spark plasma sintering in the silver-zinc system, J Alloys Compd. 635 (2015) 142–149. https://doi.org/10.1016/j.jallcom.2015.02.122.

[45]   O. Guillon, J. Gonzalez-Julian, B. Dargatz, T. Kessel, G. Schierning, J. Räthel, M. Herrmann, Field-assisted sintering technology/spark plasma sintering: Mechanisms, materials, and technology developments, Adv Eng Mater. 16 (2014) 830–849. https://doi.org/10.1002/adem.201300409.

[46]   S. Deng, R. Li, T. Yuan, P. Cao, S. Xie, Electromigration-Enhanced Densification Kinetics During Spark Plasma Sintering of Tungsten Powder, Metall Mater Trans A Phys Metall Mater Sci. (2019). https://doi.org/10.1007/s11661-019-05201-4.

[47]   M. Cologna, B. Rashkova, R. Raj, Flash sintering of nanograin zirconia in <5 s at 850°C, Journal of the American Ceramic Society. 93 (2010) 3556–3559. https://doi.org/10.1111/j.1551-2916.2010.04089.x.

[48]   M. Yu, S. Grasso, R. Mckinnon, T. Saunders, M.J. Reece, Review of flash sintering: materials, mechanisms and modelling, Advances in Applied Ceramics. 116 (2017) 24–60. https://doi.org/10.1080/17436753.2016.1251051.

[49]   M. Biesuz, V.M. Sglavo, Flash sintering of ceramics, J Eur Ceram Soc. 39 (2019) 115–143. https://doi.org/10.1016/j.jeurceramsoc.2018.08.048.

[50]   C.E.J. Dancer, Flash sintering of ceramic materials, Mater Res Express. 3 (2016). https://doi.org/10.1088/2053-1591/3/10/102001.

[51]   W. Ji, B. Parker, S. Falco, J.Y. Zhang, Z.Y. Fu, R.I. Todd, Ultra-fast firing: Effect of heating rate on sintering of 3YSZ, with and without an electric field, J Eur Ceram Soc. 37 (2017) 2547–2551. https://doi.org/10.1016/j.jeurceramsoc.2017.01.033.

[52]   K. v. Kuskov, M. Abedi, D.O. Moskovskikh, I. Serhiienko, A.S. Mukasyan, Comparison of conventional and flash spark plasma sintering of cu–cr pseudo-alloys: Kinetics, structure, properties, Metals (Basel). 11 (2021) 1–16. https://doi.org/10.3390/met11010141.

[53]   Y. Zhang, J. Nie, J.M. Chan, J. Luo, Probing the densification mechanisms during flash sintering of ZnO, Acta Mater. 125 (2017) 465–475. https://doi.org/10.1016/j.actamat.2016.12.015.

[54] W. Ji, J. Zhang, W. Wang, Z. Fu, R. Todd, The microstructural origin of rapid densification in 3YSZ during ultra-fast firing with or without an electric field, J Eur Ceram Soc. 40 (2020) 5829–5836. https://doi.org/10.1016/j.jeurceramsoc.2020.07.027.

[55] H. Charalambous, S.K. Jha, K.S.N. Vikrant, R.E. García, X.L. Phuah, H. Wang, H. Wang, A. Mukherjee, T. Tsakalakos, Electric field-induced grain boundary degradation mechanism in yttria stabilized zirconia, Scr Mater. 204 (2021) 114130. https://doi.org/10.1016/j.scriptamat.2021.114130.

[56] J. Narayan, Grain growth model for electric field-assisted processing and flash sintering of materials, Scr Mater. 68 (2013) 785–788. https://doi.org/10.1016/j.scriptamat.2013.01.008.

[57] J.M. Lebrun, C.S. Hellberg, S.K. Jha, W.M. Kriven, A. Steveson, K.C. Seymour, N. Bernstein, S.C. Erwin, R. Raj, In-situ measurements of lattice expansion related to defect generation during flash sintering, Journal of the American Ceramic Society. 100 (2017) 4965–4970. https://doi.org/10.1111/jace.15071.

[58] H. Charalambous, S.K. Jha, J.S. Okasinski, T. Tsakalakos, Generation of electric-field stabilized zirconium monoxide secondary phase within cubic zirconia, Scr Mater. 190 (2021) 22–26. https://doi.org/10.1016/j.scriptamat.2020.08.026.

[59] J. Cintas, R. Astacio, F.G. Cuevas, J.M. Montes, T. Weissgaerber, M.Á. Lagos, Y. Torres, J.M. Gallardo, Production of ultrafine grained hardmetals by electrical resistance sintering, Metals (Basel). 9 (2019). https://doi.org/10.3390/met9020159.

[60] J.M. Montes, F.G. Cuevas, J. Cintas, P. Urban, A One-Dimensional Model of the Electrical Resistance Sintering Process, Metall Mater Trans A Phys Metall Mater Sci. 46 (2015) 963–980. https://doi.org/10.1007/s11661-014-2643-0.

[61] J.M. Montes, F.G. Cuevas, F.J.V. Reina, F. Ternero, R. Astacio, E.S. Caballero, J. Cintas, Modelling and Simulation of the Electrical Resistance Sintering Process of Iron Powders, Metals and Materials International. 26 (2020) 1045–1059. https://doi.org/10.1007/s12540-019-00366-4.

[62] M.A. Lagos, I. Agote, T. Schubert, T. Weissgaerber, J.M. Gallardo, J.M. Montes, L. Prakash, C. Andreouli, V. Oikonomou, D. Lopez, J.A. Calero, Development of electric resistance sintering process for the fabrication of hard metals: Processing, microstructure and mechanical properties, Int J Refract Metals Hard Mater. 66 (2017) 88–94. https://doi.org/10.1016/j.ijrmhm.2017.03.005.

[63] J.M. Montes, F.G. Cuevas, F. Ternero, R. Astacio, E.S. Caballero, J. Cintas, Medium-frequency electrical resistance sintering of oxidized C.P. iron powder, Metals (Basel). 8 (2018) 1–14. https://doi.org/10.3390/met8060426.

[64] M.A. Lagos, I. Agote, T. Schubert, T. Weissgaerber, J.M. Gallardo, J.M. Montes, L. Prakash, C. Andreouli, V. Oikonomou, D. Lopez, J.A. Calero, Development of electric resistance sintering process for the fabrication of hard metals: Processing, microstructure and mechanical properties, Int J Refract Metals Hard Mater. 66 (2017) 88–94. https://doi.org/10.1016/j.ijrmhm.2017.03.005.

[65] M.A. Lagos, I. Agote, I. Leizaola, D. Lopez, J.A. Calero, Fabrication of chromium carbide cermets by electric resistance sintering process: Processing, microstructure and mechanical properties, Int J Refract Metals Hard Mater. 95 (2021) 105417. https://doi.org/10.1016/j.ijrmhm.2020.105417.

[66] R.M. Raihanuzzaman, Z. Xie, S.J. Hong, R. Ghomashchi, Powder refinement, consolidation and mechanical properties of cemented carbides - An overview, Powder Technol. 261 (2014) 1–13. https://doi.org/10.1016/j.powtec.2014.04.024.

[67] X. Wu, J. Shen, F. Jiang, H. Wu, L. Li, Study on the oxidation of WC-Co cemented carbide under different conditions, Int J Refract Metals Hard Mater. 94 (2021) 105381. https://doi.org/10.1016/j.ijrmhm.2020.105381.

[68] L. Silvestroni, N. Gilli, A. Migliori, D. Sciti, J. Watts, G.E. Hilmas, W.G. Fahrenholtz, Binderless WC with high strength and toughness up to 1500 °C, J Eur Ceram Soc. 40 (2020) 2287–2294. https://doi.org/10.1016/j.jeurceramsoc.2020.01.055.

[69] A. Nino, Y. Izu, T. Sekine, S. Sugiyama, H. Taimatsu, Effects of TaC and TiC addition on the microstructures and mechanical properties of Binderless WC, Int J Refract Metals Hard Mater. 82 (2019) 167–173. https://doi.org/10.1016/j.ijrmhm.2019.04.012.

[70] E. Lantsev, N. Malekhonova, A. Nokhrin, V. Chuvil'deev, M. Boldin, Y. Blagoveshchenskiy, P. Andreev, K. Smetanina, N. Isaeva, S. Shotin, Influence of oxygen on densification kinetics of WC nanopowders during SPS, Ceram Int. 47 (2021) 4294–4309. https://doi.org/10.1016/j.ceramint.2020.09.272.

[71] X. Liu, J. Zhang, C. Hou, H. Wang, X. Song, Z. Nie, Mechanisms of WC plastic deformation in cemented carbide, Mater Des. 150 (2018) 154–164. https://doi.org/10.1016/j.matdes.2018.04.025.

[72] D. Garbiec, P. Siwak, Microstructural evolution and development of mechanical properties of spark plasma sintered WC–Co cemented carbides for machine parts and engineering tools, Archives of Civil and Mechanical Engineering. 19 (2019) 215–223. https://doi.org/10.1016/j.acme.2018.10.004.

[73] M. Biesuz, S. Grasso, V.M. Sglavo, What's new in ceramics sintering? A short report on the latest trends and future prospects, Curr Opin Solid State Mater Sci. 24 (2020) 100868. https://doi.org/10.1016/j.cossms.2020.100868.

[74] M. Biesuz, V.M. Sglavo, Beyond flash sintering: How the flash event could change ceramics and glass processing, Scr Mater. 187 (2020) 49–56. https://doi.org/10.1016/j.scriptamat.2020.05.065.

[75] X.L. Phuah, J. Cho, T. Tsakalakos, A.K. Mukherjee, H. Wang, X. Zhang, Defects in flash-sintered ceramics and their effects on mechanical properties, MRS Bull. 46 (2021) 44–51. https://doi.org/10.1557/s43577-020-00014-y.

[76] R. Raj, A. Kulkarni, J.M. Lebrun, S. Jha, Flash sintering: A new frontier in defect physics and materials science, MRS Bull. 46 (2021) 36–43. https://doi.org/10.1557/s43577-020-00011-1.

[77] J. Li, J. Cho, J. Ding, H. Charalambous, S. Xue, H. Wang, X.L. Phuah, J. Jian, X. Wang, C. Ophus, T. Tsakalakos, R. Edwin García, A.K. Mukherjee, N. Bernstein, C. Stephen Hellberg, H. Wang, X. Zhang, Nanoscale stacking fault–assisted room temperature plasticity in flash-sintered TiO2, Sci Adv. 5 (2019) 1–10. https://doi.org/10.1126/sciadv.aaw5519.

[78] J. Cho, Q. Li, H. Wang, Z. Fan, J. Li, S. Xue, K.S.N. Vikrant, H. Wang, T.B. Holland, A.K. Mukherjee, R.E. García, X. Zhang, High temperature deformability of ductile flash-sintered ceramics via in-situ compression, Nat Commun. 9 (2018) 1–9. https://doi.org/10.1038/s41467-018-04333-2.

[79]   A. Börger, J. Mertens, H. Wenzl, Thermal runaway and thermal runaway propagation in batteries: What do we talk about?, J Energy Storage. 24 (2019) 100649. https://doi.org/10.1016/j.est.2019.01.012.

[80]   A. Eqbal, K.S. Arya, T. Chakrabarti, In-depth study of the evolving thermal runaway and thermal gradient in the dog bone sample during flash sintering using finite element analysis, Ceram Int. 46 (2020) 10370–10378. https://doi.org/10.1016/j.ceramint.2020.01.034.

[81]   Y. Zhang, J. Il Jung, J. Luo, Thermal runaway, flash sintering and asymmetrical microstructural development of ZnO and ZnO-Bi2O3 under direct currents, Acta Mater. 94 (2015) 87–100. https://doi.org/10.1016/j.actamat.2015.04.018.

[82]   R.I. Todd, E. Zapata-Solvas, R.S. Bonilla, T. Sneddon, P.R. Wilshaw, Electrical characteristics of flash sintering: Thermal runaway of Joule heating, J Eur Ceram Soc. 35 (2015) 1865–1877. https://doi.org/10.1016/j.jeurceramsoc.2014.12.022.

[83]   W. Ji, B. Parker, S. Falco, J.Y. Zhang, Z.Y. Fu, R.I. Todd, Ultra-fast firing: Effect of heating rate on sintering of 3YSZ, with and without an electric field, J Eur Ceram Soc. 37 (2017) 2547–2551. https://doi.org/10.1016/j.jeurceramsoc.2017.01.033.

[84]   K. Ren, J. Liu, Y. Wang, Flash sintering of yttria-stabilized zirconia: Fundamental understanding and applications, Scr Mater. 187 (2020) 371–378. https://doi.org/10.1016/j.scriptamat.2020.06.040.

[85]   S. Grasso, T. Saunders, H. Porwal, O. Cedillos-Barraza, D.D. Jayaseelan, W.E. Lee, M.J. Reece, Flash spark plasma sintering (FSPS) of pure ZrB2, Journal of the American Ceramic Society. 97 (2014) 2405–2408. https://doi.org/10.1111/jace.13109.

[86]   R. McKinnon, S. Grasso, A. Tudball, M.J. Reece, Flash spark plasma sintering of cold-Pressed TiB2-hBN, J Eur Ceram Soc. 37 (2017) 2787–2794. https://doi.org/10.1016/j.jeurceramsoc.2017.01.029.

[87]   B. McWilliams, J. Yu, F. Kellogg, S. Kilczewski, Enhanced Sintering Kinetics in Aluminum Alloy Powder Consolidated Using DC Electric Fields, Metall Mater Trans A Phys Metall Mater Sci. 48 (2017) 919–929. https://doi.org/10.1007/s11661-016-3861-4.

[88]   B. McWilliams, J. Yu, F. Kellogg, Sintering aluminum alloy powder using direct current electric fields at room temperature in seconds, J Mater Sci. 53 (2018) 9297–9304. https://doi.org/10.1007/s10853-018-2207-6.

[89]   M. Jongmanns, R. Raj, D.E. Wolf, Generation of Frenkel defects above the Debye temperature by proliferation of phonons near the Brillouin zone edge, New J Phys. 20 (2018) 093013. https://doi.org/10.1088/1367-2630/aadd5a.

[90]   C. Gorynski, U. Anselmi-Tamburini, M. Winterer, Controlling current flow in sintering: A facile method coupling flash with spark plasma sintering, Review of Scientific Instruments. 91 (2020). https://doi.org/10.1063/1.5119059.

[91]   Y. Liang, S. Xiang, T. Li, C. Yu, K. Leng, X. Zhang, Pressure-assisted flash sintering of ZnO ceramics, Journal of the American Ceramic Society. 104 (2021) 6131–6143. https://doi.org/10.1111/jace.18029.

[92] Z.Y. Hu, Z.H. Zhang, X.W. Cheng, F.C. Wang, Y.F. Zhang, S.L. Li, A review of multi-physical fields induced phenomena and effects in spark plasma sintering: Fundamentals and applications, Mater Des. 191 (2020) 108662. https://doi.org/10.1016/j.matdes.2020.108662.

[93] M. Biesuz, J. Dong, S. Fu, Y. Liu, H. Zhang, D. Zhu, C. Hu, S. Grasso, Thermally-insulated flash sintering, Scr Mater. 162 (2019) 99–102. https://doi.org/10.1016/j.scriptamat.2018.10.042.

[94] J.M. Montes, F.G. Cuevas, F. Ternero, R. Astacio, E.S. Caballero, J. Cintas, A method to determine the electrical resistance of a metallic powder mass under compression, Metals (Basel). 7 (2017) 1–9. https://doi.org/10.3390/met7110479.

[95] R. Raj, Joule heating during flash-sintering, J Eur Ceram Soc. 32 (2012) 2293–2301. https://doi.org/10.1016/j.jeurceramsoc.2012.02.030.

[96] E.A. Olevsky, S.M. Rolfing, A.L. Maximenko, Flash (Ultra-Rapid) Spark-Plasma Sintering of Silicon Carbide, Sci Rep. 6 (2016) 33408. https://doi.org/10.1038/srep33408.

[97] S. Deng, R. Li, T. Yuan, P. Cao, S. Xie, Electromigration-Enhanced Densification Kinetics During Spark Plasma Sintering of Tungsten Powder, Metallurgical and Materials Transactions A. 50 (2019) 2886–2897. https://doi.org/10.1007/s11661-019-05201-4.

[98] C. Wang, W. Ping, Q. Bai, H. Cui, R. Hensleigh, R. Wang, A.H. Brozena, Z. Xu, J. Dai, Y. Pei, C. Zheng, G. Pastel, J. Gao, X. Wang, H. Wang, J.-C. Zhao, B. Yang, X. (Rayne) Zheng, J. Luo, Y. Mo, B. Dunn, L. Hu, A general method to synthesize and sinter bulk ceramics in seconds, Science (1979). 368 (2020) 521–526. https://doi.org/10.1126/science.aaz7681.

[99] R.F. Guo, H.R. Mao, Z.T. Zhao, P. Shen, Ultrafast high-temperature sintering of bulk oxides, Scr Mater. 193 (2021) 103–107. https://doi.org/10.1016/j.scriptamat.2020.10.045.

[100] M. Yoshida, S. Falco, R.I. Todd, Measurement and modelling of electrical resistivity by four-terminal method during flash sintering of 3YSZ, Journal of the Ceramic Society of Japan. 126 (2018) 579–590. https://doi.org/10.2109/jcersj2.17256.

[101] M.Z. ev Becker, N. Shomrat, Y. Tsur, Recent Advances in Mechanism Research and Methods for Electric-Field-Assisted Sintering of Ceramics, Advanced Materials. 30 (2018) 1–8. https://doi.org/10.1002/adma.201706369.

[102] W.S. Williams, Electrical properties of hard materials, Int J Refract Metals Hard Mater. 17 (1999) 21–26. https://doi.org/10.1016/S0263-4368(99)00005-0.

[103] M. Biesuz, P. Luchi, A. Quaranta, V.M. Sglavo, Theoretical and phenomenological analogies between flash sintering and dielectric breakdown in α-alumina, J Appl Phys. 120 (2016). https://doi.org/10.1063/1.4964811.

[104] A. Mikrajuddin, F.G. Shi, H.K. Kim, K. Okuyama, Size-dependent electrical constriction resistance for contacts of arbitrary size: From Sharvin to Holm limits, Mater Sci Semicond Process. 2 (1999) 321–327. https://doi.org/10.1016/S1369-8001(99)00036-0.

[105] E. Zapata-Solvas, S. Bonilla, P.R. Wilshaw, R.I. Todd, Preliminary investigation of flash sintering of SiC, J Eur Ceram Soc. 33 (2013) 2811–2816. https://doi.org/10.1016/j.jeurceramsoc.2013.04.023.

[106] H. Lin, N. Liu, Z. Shi, Y. Guo, Y. Tang, Q. Gao, Cobalt-Doping in Molybdenum-Carbide Nanowires Toward Efficient Electrocatalytic Hydrogen Evolution, Adv Funct Mater. 26 (2016) 5590–5598. https://doi.org/10.1002/adfm.201600915.

[107] Y. Yan, B. Xia, X. Qi, H. Wang, R. Xu, J.Y. Wang, H. Zhang, X. Wang, Nano-tungsten carbide decorated graphene as co-catalysts for enhanced hydrogen evolution on molybdenum disulfide, Chemical Communications. 49 (2013) 4884–4886. https://doi.org/10.1039/c3cc41031e.

[108] C. Liu, J. Zhou, Y. Xiao, L. Yang, D. Yang, D. Zhou, Structural and electrochemical studies of tungsten carbide/carbon composites for hydrogen evolution, Int J Hydrogen Energy. 42 (2017) 29781–29790. https://doi.org/10.1016/j.ijhydene.2017.10.109.

[109] B.J. Han, Z.J. Huang, G. Wu, C.Y. Zhou, Y.S. Li, Q.H. Wang, Y.L. Zhang, Y.H. Yin, Z.P. Wu, Growth of carbon nanoshells on tungsten carbide for loading Pt with enhanced electrocatalytic activity and stable anti-poisoning performance, RSC Adv. 6 (2016) 75178–75185. https://doi.org/10.1039/c6ra12475e.

[110] Y.C. Kimmel, D. v. Esposito, R.W. Birkmire, J.G. Chen, Effect of surface carbon on the hydrogen evolution reactivity of tungsten carbide (WC) and Pt-modified WC electrocatalysts, Int J Hydrogen Energy. 37 (2012) 3019–3024. https://doi.org/10.1016/j.ijhydene.2011.11.079.

[111] A. Warren, A. Nylund, I. Olefjord, Oxidation of tungsten and tungsten carbide in dry and humid atmospheres, Int J Refract Metals Hard Mater. 14 (1996) 345–353. https://doi.org/10.1016/s0263-4368(96)00027-3.

[112] J. Lepage, A. Mézin, On the morphology of tungsten oxide layers, Vacuum. 43 (1992) 1185–1190. https://doi.org/10.1016/0042-207X(92)90020-W.

[113] K.M. Andersson, L. Bergström, Oxidation and dissolution of tungsten carbide powder in water, Int J Refract Metals Hard Mater. 18 (2000) 121–129. https://doi.org/10.1016/S0263-4368(00)00010-X.

[114] P. V. Krasovskii, O.S. Malinovskaya, A. V. Samokhin, Y. V. Blagoveshchenskiy, V.A. Kazakov, A.A. Ashmarin, XPS study of surface chemistry of tungsten carbides nanopowdersproduced through DC thermal plasma/hydrogen annealing process, Appl Surf Sci. 339 (2015) 46–54. https://doi.org/10.1016/j.apsusc.2015.02.152.

[115] M. Göthelid, E. Janin, Surface structures on sputtered/annealed WC(0001), Journal of Physics Condensed Matter. 12 (2000) 773–782. https://doi.org/10.1088/0953-8984/12/6/302.

[116] D.X. Luong, K. v. Bets, W.A. Algozeeb, M.G. Stanford, C. Kittrell, W. Chen, R. v. Salvatierra, M. Ren, E.A. McHugh, P.A. Advincula, Z. Wang, M. Bhatt, H. Guo, V. Mancevski, R. Shahsavari, B.I. Yakobson, J.M. Tour, Gram-scale bottom-up flash graphene synthesis, Nature. 577 (2020) 647–651. https://doi.org/10.1038/s41586-020-1938-0.

[117] I. Mazo, A. Molinari, V.M. Sglavo, Electrical resistance flash sintering of tungsten carbide, Mater Des. 213 (2022) 110330. https://doi.org/10.1016/j.matdes.2021.110330.

[118] I. Mazo, A. Molinari, V.M. Sglavo, Effect of pressure on the electrical resistance flash sintering of tungsten carbide, J Eur Ceram Soc. 42 (2022) 2028–2038. https://doi.org/10.1016/j.jeurceramsoc.2022.01.017.

[119] Inframat Advanced Materials, Tungsten Carbide nano powder, (1996). http://www.advancedmaterials.us/74N-0601.htm (accessed December 13, 2021).

[120] R. Chaim, Numerical model for particle size effects on flash sintering temperature of ionic nanoparticles, J Mater Sci. 53 (2018) 13853–13864. https://doi.org/10.1007/s10853-018-2604-x.

[121] M. Braunovic, V. v. Konchits, N.K. Myshkin, Electrical contacts: Fundamentals, applications and technology, CRC Press, 2017. https://doi.org/10.1201/9780849391088.

[122] D. Gall, Electron mean free path in elemental metals, J Appl Phys. 119 (2016). https://doi.org/10.1063/1.4942216.

[123] E.H. Sondheimer, The mean free path of electrons in metals, Adv Phys. 50 (2001) 499–537. https://doi.org/10.1080/00018730110102187.

[124] D. Gall, Electron mean free path in elemental metals, J Appl Phys. 119 (2016) 1–5. https://doi.org/10.1063/1.4942216.

[125] L.G. Radosevich, W.S. Williams, Phonon scattering by conduction electrons and by lattice vacancies in carbides of the transition metals, Physical Review. 181 (1969) 1110–1117. https://doi.org/10.1103/PhysRev.181.1110.

[126] D. Coster, H. De Lang, On the bands of conduction electrons in the tungsten crystal, Physica. 13 (1947) 385–391. https://doi.org/10.1016/0031-8914(47)90012-8.

[127] E.S. Alekseev, R.G. Arkhipov, S. V. Popova, Band Structure of Hexagonal Tungsten Carbide, Physica Status Solidi (B). 110 (1982) K151–K154. https://doi.org/10.1002/pssb.2221100256.

[128] J. Poetschke, V. Richter, T. Gestrich, A. Michaelis, Grain growth during sintering of tungsten carbide ceramics, Int J Refract Metals Hard Mater. 43 (2014) 309–316. https://doi.org/10.1016/j.ijrmhm.2014.01.001.

[129] A.S. Kurlov, A.I. Gusev, Peculiarities of vacuum annealing of nanocrystalline WC powders, Int J Refract Metals Hard Mater. 32 (2012) 51–60. https://doi.org/10.1016/j.ijrmhm.2012.01.009.

[130] G. Speranza, R. Canteri, RxpsG a new open project for Photoelectron and Electron Spectroscopy data processing, SoftwareX. 10 (2019) 100282. https://doi.org/10.1016/j.softx.2019.100282.

[131] M.P. Seah, W.A. Dench, Quantitative electron spectroscopy of surfaces: A standard data base for electron inelastic mean free paths in solids, Surface and Interface Analysis. 1 (1979) 2–11. https://doi.org/10.1002/sia.740010103.

[132] J. Díaz, G. Paolicelli, S. Ferrer, F. Comin, Separation of the and components in the C1s photoemission spectra of amorphous carbon films, Phys Rev B Condens Matter Mater Phys. 54 (1996) 8064–8069. https://doi.org/10.1103/PhysRevB.54.8064.

[133] B. Lesiak, L. Kövér, J. Tóth, J. Zemek, P. Jiricek, A. Kromka, N. Rangam, C sp 2 /sp 3 hybridisations in carbon nanomaterials – XPS and (X)AES study, Appl Surf Sci. 452 (2018) 223–231. https://doi.org/10.1016/j.apsusc.2018.04.269.

[134]   Adventitious Carbon Contamination in XPS analyses, (n.d.).
        https://www.jp.xpssimplified.com/elements/carbon.php (accessed January 11, 2022).

[135]   S.N. Basu, V.K. Sarin, Oxidation behavior of WC-Co, Materials Science and Engineering A. 209 (1996)
        206–212. https://doi.org/10.1016/0921-5093(95)10145-4.

[136]   D. Fang, F. He, J. Xie, L. Xue, Calibration of Binding Energy Positions with C1s for XPS Results, Journal
        Wuhan University of Technology, Materials Science Edition. 35 (2020) 711–718.
        https://doi.org/10.1007/s11595-020-2312-7.

[137]   A. Mezzi, S. Kaciulis, Surface investigation of carbon films: From diamond to graphite, Surface and
        Interface Analysis. 42 (2010) 1082–1084. https://doi.org/10.1002/sia.3348.

[138]   A. Nylund, I. Olefjord, Surface analysis of oxidized aluminium. 1. Hydration of Al2O3 and decomposition
        of Al(OH)3 in a vacuum as studied by ESCA, Surface and Interface Analysis. 21 (1994) 283–289.
        https://doi.org/10.1002/sia.740210504.

[139]   A. C. Ferrari and J. Robertson, Interpretation of Raman spectra of disordered and amorphous carbon A.,
        Phys Rev B. 61 (2000) 14095–14107. https://doi.org/10.1007/BF02543692.

[140]   A.C. Ferrari, J. Robertson, Raman spectroscopy of amorphous, nanostructured, diamond-like carbon,
        and nanodiamond, Philosophical Transactions of the Royal Society A: Mathematical, Physical and
        Engineering Sciences. 362 (2004) 2477–2512. https://doi.org/10.1098/rsta.2004.1452.

[141]   A. Milani, M. Tommasini, V. Russo, A.L. Bassi, A. Lucotti, F. Cataldo, C.S. Casari, Raman spectroscopy as a
        tool to investigate the structure and electronic properties of carbon-atom wires, Beilstein Journal of
        Nanotechnology. 6 (2015) 480–491. https://doi.org/10.3762/bjnano.6.49.

[142]   Y. Cheong, J. Calvo-castro, L. Ciric, M. Edirisinghe, E. Cloutman-green, U.E. Illangakoon, Q. Kang,
        Characterisation of the Chemical Composition and Structural Features of Novel Antimicrobial
        Nanoparticles, (2017) 1–16. https://doi.org/10.3390/nano7070152.

[143]   J. Poetschke, V. Richter, A. Michaelis, Fundamentals of sintering nanoscaled binderless hardmetals, Int J
        Refract Metals Hard Mater. 49 (2015) 124–132. https://doi.org/10.1016/j.ijrmhm.2014.04.022.

[144]   S. Jiang, T.J. Horn, V.K. Dhir, Numerical analysis of a radiant heat flux calibration system, Int J
        Thermophys. 21 (2000) 941–963. https://doi.org/10.1023/A:1006622526578.

[145]   R.I. Todd, E. Zapata-Solvas, R.S. Bonilla, T. Sneddon, P.R. Wilshaw, Electrical characteristics of flash
        sintering: Thermal runaway of Joule heating, J Eur Ceram Soc. 35 (2015) 1865–1877.
        https://doi.org/10.1016/j.jeurceramsoc.2014.12.022.

[146]   M.A. Lagos, I. Agote, T. Schubert, T. Weissgaerber, J.M. Gallardo, J.M. Montes, L. Prakash, C. Andreouli,
        V. Oikonomou, D. Lopez, J.A. Calero, Development of electric resistance sintering process for the
        fabrication of hard metals: Processing, microstructure and mechanical properties, Int J Refract Metals
        Hard Mater. 66 (2017) 88–94. https://doi.org/10.1016/j.ijrmhm.2017.03.005.

[147]   J.M. Montes, F.G. Cuevas, F. Ternero, R. Astacio, E.S. Caballero, J. Cintas, Medium-frequency electrical
        resistance sintering of oxidized C.P. iron powder, Metals (Basel). 8 (2018) 1–14.
        https://doi.org/10.3390/met8060426.

[148] Y. Mei, L. Li, X. Li, W. Li, H. Yan, Y. Xie, Electric-current-assisted sintering of nanosilver paste for copper bonding, Journal of Materials Science: Materials in Electronics. 28 (2017) 9155–9166. https://doi.org/10.1007/s10854-017-6649-4.

[149] B. McWilliams, J. Yu, F. Kellogg, Sintering aluminum alloy powder using direct current electric fields at room temperature in seconds, J Mater Sci. 53 (2018) 9297–9304. https://doi.org/10.1007/s10853-018-2207-6.

[150] L.B. Caliman, E. Bichaud, P. Soudant, D. Gouvea, M.C. Steil, A simple flash sintering setup under applied mechanical stress and controlled atmosphere, MethodsX. 2 (2015) 392–398. https://doi.org/10.1016/j.mex.2015.10.004.

[151] K.S.N. Vikrant, X.L. Phuah, J. Lund, H. Wang, C.S. Hellberg, N. Bernstein, W. Rheinheimer, C.M. Bishop, H. Wang, R.E. García, Modeling of flash sintering of ionic ceramics, MRS Bull. 46 (2021) 67–75. https://doi.org/10.1557/s43577-020-00012-0.

[152] W. Frei, Control Current and Voltage Sources with the AC / DC Module The Terminal boundary Condition, (2016). https://www.comsol.com/blogs/control-current-and-voltage-sources-with-the-acdc-module/.

[153] Ansori, Sensor Technology Handbook, Elsevier, 2005. https://doi.org/10.1016/B978-0-7506-7729-5.X5040-X.

[154] Engineering ToolBox, Resistivity and Conductivity - Temperature Coefficients Common Materials, (2003). https://www.engineeringtoolbox.com/resistivity-conductivity-d_418.html (accessed September 22, 2022).

[155] K. Raznjevic, Handbook of Thermodynamic Tables, Begell house, 1995.

[156] A. Alekseev, E. Andreenko, I. Orlovskiy, A. Gorshkov, S. Akhtyrsky, A. Kozlov, V. Smekalin, V. Ulyanitskiy, R. Khmelnitsky, S. Evlashin, S. Eberle, A study of methods to enhance infrared emissivity of Molybdenum surfaces, Fusion Engineering and Design. 146 (2019) 144–148. https://doi.org/10.1016/j.fusengdes.2018.12.002.

[157] J. Schreiber, Tungsten Carbides: Structure, Properties and Application in Hardmetals, Springer Series in Materials Science, 1990. https://doi.org/10.1524/zkri.1990.190.3-4.315.

[158] H.O. :Pierson, HANDBOOK OF REFRACTORY CARBIDES AND NITRIDES: Properties, Characteristics, Processing and Applications, Handbook of Refractory Carbides and Nitrides. (1996) 100–117. https://doi.org/10.1016/b978-081551392-6.50007-6.

[159] B. Palmieri, F. Cilento, C. Siviello, F. Bertocchi, M. Giordano, A. Martone, Mitigation of Heat Propagation in a Battery Pack by Interstitial Graphite Nanoplatelet Layer: Coupled Electrochemical-Heat Transfer Model, Journal of Composites Science. 6 (2022). https://doi.org/10.3390/jcs6100296.

[160] K. Ren, Q. Wang, Y. Lian, Y. Wang, Densification kinetics of flash sintered 3mol% Y2O3 stabilized zirconia, J Alloys Compd. 747 (2018) 1073–1077. https://doi.org/10.1016/j.jallcom.2018.02.308.

[161] M. Bram, A.M. Laptev, T.P. Mishra, K. Nur, M. Kindelmann, M. Ihrig, J.G. Pereira da Silva, R. Steinert, H.P. Buchkremer, A. Litnovsky, F. Klein, J. Gonzalez-Julian, O. Guillon, Application of Electric Current-Assisted

Sintering Techniques for the Processing of Advanced Materials, Adv Eng Mater. 22 (2020). https://doi.org/10.1002/adem.202000051.

[162] A.S. Semenov, J. Trapp, M. Nöthe, O. Eberhardt, T. Wallmersperger, B. Kieback, Thermo-electro-mechanical modeling, simulation and experiments of field-assisted sintering, J Mater Sci. 54 (2019) 10764–10783. https://doi.org/10.1007/s10853-019-03653-y.

[163] R. Chaim, Numerical model for particle size effects on flash sintering temperature of ionic nanoparticles, J Mater Sci. 53 (2018) 13853–13864. https://doi.org/10.1007/s10853-018-2604-x.

[164] I. Mazo, L.E. Vanzetti, J.M. Molina-Aldareguia, A. Molinari, V.M. Sglavo, Role of surface carbon nanolayer on the activation of flash sintering in tungsten carbide, Int J Refract Metals Hard Mater. (2022) 106090. https://doi.org/10.1016/j.ijrmhm.2022.106090.

[165] M. Jonson, G.D. Mahan, Mott's formula for the thermopower and the Wiedemann-Franz law, Phys Rev B. 21 (1980) 4223–4229. https://doi.org/10.1103/PhysRevB.21.4223.

[166] A. Yadav, P.C. Deshmukh, K. Roberts, N.M. Jisrawi, S.R. Valluri, An analytic study of the Wiedemann–Franz law and the thermoelectric figure of merit, J Phys Commun. 3 (2019). https://doi.org/10.1088/2399-6528/ab444a.

[167] S. Lee, K. Hippalgaonkar, F. Yang, J. Hong, C. Ko, J. Suh, K. Liu, K. Wang, J.J. Urban, X. Zhang, C. Dames, S.A. Hartnoll, O. Delaire, J. Wu, Anomalously low electronic thermal conductivity in metallic vanadium dioxide, Science (1979). 355 (2021) 371–374. https://doi.org/10.1126/science.aag0410.

[168] J.R. Groza, A. Zavaliangos, Sintering activation by external electrical field, Materials Science and Engineering A. 287 (2000) 171–177. https://doi.org/10.1016/s0921-5093(00)00771-1.

[169] E. Zapata-Solvas, D. Gómez-García, A. Domínguez-Rodríguez, R.I. Todd, Ultra-fast and energy-efficient sintering of ceramics by electric current concentration, Sci Rep. 5 (2015) 1–7. https://doi.org/10.1038/srep08513.

[170] J.S.C. Francis, R. Raj, Flash-sinterforging of nanograin zirconia: Field assisted sintering and superplasticity, Journal of the American Ceramic Society. 95 (2012) 138–146. https://doi.org/10.1111/j.1551-2916.2011.04855.x.

[171] A.K. Pannikkat, R. Raj, Measurement of an electrical potential induced by normal stress applied to the interface of an ionic material at elevated temperatures, Acta Mater. 47 (1999) 3423–3431. https://doi.org/10.1016/S1359-6454(99)00206-2.

[172] E.A. Olevsky, S.M. Rolfing, A.L. Maximenko, Flash (Ultra-Rapid) Spark-Plasma Sintering of Silicon Carbide, Sci Rep. 6 (2016) 1–9. https://doi.org/10.1038/srep33408.

[173] Y. Ye, X. Li, K. Hu, Y. Lai, Y. Li, The influence of premolding load on the electrical behavior in the initial stage of electric current activated sintering of carbonyl iron powders, J Appl Phys. 113 (2013). https://doi.org/10.1063/1.4808339.

[174] Y. Ye, X. Li, D. Zheng, S.G. Qu, Y. Li, Examination of electrical conduction of carbonyl iron powder compacts, Mater Trans. 56 (2015) 696–702. https://doi.org/10.2320/matertrans.M2014311.

[175] F. V. Lenel, Resistance Sintering Under Pressure, Jom. 7 (1955) 158–167. https://doi.org/10.1007/bf03377473.

[176] A. Nino, K. Takahashi, S. Sugiyama, H. Taimatsu, Effects of carbon addition on microstructures and mechanical properties of binderless tungsten carbide, Mater Trans. 53 (2012) 1475–1480. https://doi.org/10.2320/matertrans.M2012148.

[177] U. Anselmi-Tamburini, J.E. Garay, Z.A. Munir, Fundamental investigations on the spark plasma sintering/synthesis process, Materials Science and Engineering A. 407 (2005) 24–30. https://doi.org/10.1016/j.msea.2005.06.066.

[178] P. V. Andreev, K.E. Smetanina, E.A. Lantsev, X-ray powder diffraction analysis of a tungsten carbide-based ceramic, IOP Conf Ser Mater Sci Eng. 558 (2019). https://doi.org/10.1088/1757-899X/558/1/012003.

[179] L. Girardini, M. Zadra, F. Casari, A. Molinari, SPS, binderless WC powders, and the problem of sub carbide, Metal Powder Report. 63 (2008) 18–22. https://doi.org/10.1016/S0026-0657(09)70039-6.

[180] H. Taimatsu, S. Sugiyama, Y. Kodaira, Synthesis of W2C by reactive hot pressing and its mechanical properties, Mater Trans. 49 (2008) 1256–1261. https://doi.org/10.2320/matertrans.MRA2007304.

[181] E. Lantsev, N. Malekhonova, A. Nokhrin, V. Chuvil'deev, M. Boldin, Y. Blagoveshchenskiy, P. Andreev, K. Smetanina, N. Isaeva, S. Shotin, Influence of oxygen on densification kinetics of WC nanopowders during SPS, Ceram Int. 47 (2021) 4294–4309. https://doi.org/10.1016/j.ceramint.2020.09.272.

[182] T. Dash, B.B. Nayak, Preparation of WC-W2C composites by arc plasma melting and their characterisations, Ceram Int. 39 (2013) 3279–3292. https://doi.org/10.1016/j.ceramint.2012.10.016.

[183] T. Dash, B.B. Nayak, Preparation of multi-phase composite of tungsten carbide, tungsten boride and carbon by arc plasma melting: characterization of melt-cast product, Ceram Int. 42 (2016) 445–459. https://doi.org/10.1016/j.ceramint.2015.08.129.

[184] B.B. Nayak, Enhancement in the microhardness of arc plasma melted tungsten carbide, J Mater Sci. 38 (2003) 2717–2721. https://doi.org/10.1023/A:1024455207083.

[185] T. Dash, B.B. Nayak, Tungsten carbide – Titanium carbide composite preparation by arc plasma melting and its characterization, Ceram Int. 45 (2019) 4771–4780. https://doi.org/10.1016/j.ceramint.2018.11.170.

[186] J. Sun, J. Zhao, Z. Huang, K. Yan, X. Shen, J. Xing, Y. Gao, Y. Jian, H. Yang, B. Li, A Review on Binderless Tungsten Carbide: Development and Application, 2020. https://doi.org/10.1007/s40820-019-0346-1.

[187] S.I. Cha, S.H. Hong, Microstructures of binderless tungsten carbides sintered by spark plasma sintering process, Materials Science and Engineering A. 356 (2003) 381–389. https://doi.org/10.1016/S0921-5093(03)00151-5.

[188] F.G. Zhang, X.P. Zhu, M.K. Lei, Microstructural evolution and its correlation with hardening of WC-Ni cemented carbides irradiated by high-intensity pulsed ion beam, Surf Coat Technol. 206 (2012) 4146–4155. https://doi.org/10.1016/j.surfcoat.2012.04.011.

[189] A. Pak, A. Sivkov, I. Shanenkov, I. Rahmatullin, K. Shatrova, Synthesis of ultrafine cubic tungsten carbide in a discharge plasma jet, Int J Refract Metals Hard Mater. 48 (2015) 51–55. https://doi.org/10.1016/j.ijrmhm.2014.07.025.

[190] S. Tanaka, I. Bataev, H. Oda, K. Hokamoto, Synthesis of metastable cubic tungsten carbides by electrical explosion of tungsten wire in liquid paraffin, Advanced Powder Technology. 29 (2018) 2447–2455. https://doi.org/10.1016/j.apt.2018.06.025.

[191] F.G. Zhang, Friction and wear behavior of WC/Ni cemented carbide tool material irradiated by high-intensity pulsed electron beam, Ceram Int. 45 (2019) 15327–15333. https://doi.org/10.1016/j.ceramint.2019.05.025.

[192] Y. Lian, B. Han, D. Liu, Y. Wang, H. Zhao, P. Xu, X. Han, Y. Du, Solvent-Free Synthesis of Ultrafine Tungsten Carbide Nanoparticles-Decorated Carbon Nanosheets for Microwave Absorption, Nanomicro Lett. 12 (2020) 1–13. https://doi.org/10.1007/s40820-020-00491-5.

[193] M.D. Abad, M.A. Muñoz-Márquez, S. El Mrabet, A. Justo, J.C. Sánchez-López, Tailored synthesis of nanostructured WC/a-C coatings by dual magnetron sputtering, Surf Coat Technol. 204 (2010) 3490–3500. https://doi.org/10.1016/j.surfcoat.2010.04.019.

[194] M. Biesuz, S. Grasso, V.M. Sglavo, What's new in ceramics sintering? A short report on the latest trends and future prospects, Curr Opin Solid State Mater Sci. 24 (2020) 100868. https://doi.org/10.1016/j.cossms.2020.100868.

[195] S. Suzuki, Features of transmission EBSD and its application, Jom. 65 (2013) 1254–1263. https://doi.org/10.1007/s11837-013-0700-6.

[196] J. Sun, J. Zhao, Z. Huang, K. Yan, X. Shen, J. Xing, Y. Gao, Y. Jian, H. Yang, B. Li, A Review on Binderless Tungsten Carbide: Development and Application, 2020. https://doi.org/10.1007/s40820-019-0346-1.

[197] I. Shanenkov, D. Nikitin, A. Ivashutenko, Y. Shanenkova, Y. Vympina, D. Butenko, W. Han, A. Sivkov, Studies on the thermal stability of nanosized powder of WC1-x-based product prepared by plasma dynamic method, compaction feasibility of the powder and preparation of composite with aluminium, Ceram Int. 47 (2021) 6884–6895. https://doi.org/10.1016/j.ceramint.2020.11.035.

[198] N. Al-Aqeeli, Characterization of nano-cemented carbides Co-doped with vanadium and chromium carbides, Powder Technol. 273 (2015) 47–53. https://doi.org/10.1016/j.powtec.2014.12.032.

[199] I. Sugiyama, Y. Mizumukai, T. Taniuchi, K. Okada, F. Shirase, T. Tanase, Y. Ikuhara, T. Yamamoto, Formation of (W,V)Cx layers at the WC/Co interfaces in the VC-doped WC-Co cemented carbide, Int J Refract Metals Hard Mater. 30 (2012) 185–187. https://doi.org/10.1016/j.ijrmhm.2011.08.006.

[200] M.A. Yousfi, S. Norgren, H.O. Andrén, L.K.L. Falk, Chromium segregation at phase boundaries in Cr-doped WC-Co cemented carbides, Mater Charact. 144 (2018) 48–56. https://doi.org/10.1016/j.matchar.2018.06.034.

[201] S. Lay, S. Hamar-Thibault, A. Lackner, Location of VC in VC, Cr3C2 codoped WC-Co cermets by HREM and EELS, Int J Refract Metals Hard Mater. 20 (2002) 61–69. https://doi.org/10.1016/S0263-4368(01)00071-3.

[202] Y. Gao, X. Song, X. Liu, C. Wei, H. Wang, G. Guo, On the formation of WC 1-x in nanocrystalline cemented carbides, Scr Mater. 68 (2013) 108–110. https://doi.org/10.1016/j.scriptamat.2012.09.016.

[203] W. Li, L. Chen, D. Liu, J. Liu, L. An, Ultra-low temperature reactive flash sintering synthesis of high-enthalpy and high-entropy Ca0.2Co0.2Ni0.2Cu0.2Zn0.2O oxide ceramics, Mater Lett. 304 (2021) 130679. https://doi.org/10.1016/j.matlet.2021.130679.

[204] A. Rempel, R. Würschum, Atomic defects in hexagonal tungsten carbide studied by positron annihilation, Phys Rev B Condens Matter Mater Phys. 61 (2000) 5945–5948. https://doi.org/10.1103/PhysRevB.61.5945.

[205] A.R. Denton, N.W. Ashcroft, Vegards law, Phys Rev A (Coll Park). 43 (1991) 3161–3164. https://doi.org/10.1103/PhysRevA.43.3161.

[206] G. Dehm, B.N. Jaya, R. Raghavan, C. Kirchlechner, Overview on micro- and nanomechanical testing: New insights in interface plasticity and fracture at small length scales, Acta Mater. 142 (2018) 248–282. https://doi.org/10.1016/j.actamat.2017.06.019.

[207] J. Xiao, N. Wu, O. Ojo, C. Deng, Stacking fault and transformation-induced plasticity in nanocrystalline high-entropy alloys, J Mater Res. 36 (2021) 2705–2714. https://doi.org/10.1557/s43578-021-00140-6.

[208] S. Kiani, J.M. Yang, S. Kodambaka, Nanomechanics of Refractory Transition-Metal Carbides: A Path to Discovering Plasticity in Hard Ceramics, Journal of the American Ceramic Society. 98 (2015) 2313–2323. https://doi.org/10.1111/jace.13686.

[209] D.L. Kohlstedt, The temperature dependence of microhardness of the transition-metal carbides, J Mater Sci. 8 (1973) 777–786. https://doi.org/10.1007/BF02397907.

[210] Slip system determination in cubic carbides by hardness anisotropy, Proceedings of the Royal Society of London. A. Mathematical and Physical Sciences. 326 (1972) 409–420. https://doi.org/10.1098/rspa.1972.0017.

[211] H. Yu, M. Bahadori, G.B. Thompson, C.R. Weinberger, Understanding dislocation slip in stoichiometric rocksalt transition metal carbides and nitrides, J Mater Sci. 52 (2017) 6235–6248. https://doi.org/10.1007/s10853-017-0857-4.

[212] I. Shanenkov, D. Nikitin, A. Ivashutenko, I. Rahmatullin, Y. Shanenkova, A. Nassyrbayev, W. Han, A. Sivkov, Hardening the surface of metals with WC1-x coatings deposited by high-speed plasma spraying, Surf Coat Technol. 389 (2020) 125639. https://doi.org/10.1016/j.surfcoat.2020.125639.

[213] J. García, V. Collado Ciprés, A. Blomqvist, B. Kaplan, Cemented carbide microstructures: a review, Int J Refract Metals Hard Mater. 80 (2019) 40–68. https://doi.org/10.1016/j.ijrmhm.2018.12.004.

[214] Z. Roulon, J.M. Missiaen, S. Lay, Carbide grain growth in cemented carbides sintered with alternative binders, Int J Refract Metals Hard Mater. 86 (2020) 105088. https://doi.org/10.1016/j.ijrmhm.2019.105088.

[215] E.M. Garcia-Ayala, S. Tarancon, B. Ferrari, J.Y. Pastor, A.J. Sanchez-Herencia, Thermomechanical behaviour of WC-W2C composites at first wall in fusion conditions, Int J Refract Metals Hard Mater. 98 (2021) 105565. https://doi.org/10.1016/j.ijrmhm.2021.105565.

[216] K. Kornaus, M. Rączka, A. Gubernat, D. Zientara, Pressureless sintering of binderless tungsten carbide, J Eur Ceram Soc. 37 (2017) 4567–4576. https://doi.org/10.1016/j.jeurceramsoc.2017.06.008.

[217] Y. Cheng, T. Zhu, J. Zhang, Y. Li, S. Sang, Z. Xie, Oscillatory pressure sintering of binderless tungsten carbide, Ceram Int. 46 (2020) 25603–25607. https://doi.org/10.1016/j.ceramint.2020.07.033.

[218] J. Poetschke, V. Richter, A. Michaelis, Fundamentals of sintering nanoscaled binderless hardmetals, Int J Refract Metals Hard Mater. 49 (2015) 124–132. https://doi.org/10.1016/j.ijrmhm.2014.04.022.

[219] B. Yaman, H. Mandal, Spark plasma sintering of Co-WC cubic boron nitride composites, Mater Lett. 63 (2009) 1041–1043. https://doi.org/10.1016/j.matlet.2009.01.086.

[220] L.T. da Silva Soffner, A.A.A. dos Santos, R. da Silva Guimaraes, C.S. de Carvalho, M.E. Soffner, M.G. de Azevedo, M. Filgueira, Novel binder for NbC-based cemented carbides prepared by spark plasma sintering, Int J Refract Metals Hard Mater. 106 (2022). https://doi.org/10.1016/j.ijrmhm.2022.105864.

[221] H. Motomura, D. Tamao, K. Nambu, H. Masuda, H. Yoshida, Athermal effect of flash event on high-temperature plastic deformation in Y2O3-stabilized tetragonal ZrO2 polycrystal, J Eur Ceram Soc. 42 (2022) 5045–5052. https://doi.org/10.1016/j.jeurceramsoc.2022.04.055.

[222] M.S. Tarasova, B.A. Tarasov, I.I. Konovalov, The Role of Plastic Flow in Processes of High-speed Sintering of Ceramic Materials under Pressure, KnE Materials Science. 4 (2018) 498. https://doi.org/10.18502/kms.v4i1.2203.

[223] B. Yang, Z. Shang, J. Li, X.L. Phuah, J. Cho, H. Wang, X. Zhang, Effects of electric field on microstructure evolution and defect formation in flash-sintered TiO2, J Eur Ceram Soc. 42 (2022) 6040–6047. https://doi.org/10.1016/j.jeurceramsoc.2022.06.009.

[224] D.M. Evans, D.R. Småbråten, T.S. Holstad, P.E. Vullum, A.B. Mosberg, Z. Yan, E. Bourret, A.T.J. Van Helvoort, S.M. Selbach, D. Meier, Observation of Electric-Field-Induced Structural Dislocations in a Ferroelectric Oxide, Nano Lett. 21 (2021) 3386–3392. https://doi.org/10.1021/acs.nanolett.0c04816.

[225] J. Cho, J. Li, H. Wang, Q. Li, Z. Fan, A.K. Mukherjee, W. Rheinheimer, H. Wang, X. Zhang, Study of deformation mechanisms in flash-sintered yttria-stabilized zirconia by in-situ micromechanical testing at elevated temperatures, Mater Res Lett. 7 (2019) 194–202. https://doi.org/10.1080/21663831.2019.1575924.

[226] W. Rheinheimer, X.L. Phuah, H. Wang, F. Lemke, M.J. Hoffmann, H. Wang, The role of point defects and defect gradients in flash sintering of perovskite oxides, Acta Mater. 165 (2019) 398–408. https://doi.org/10.1016/j.actamat.2018.12.007.

[227] B. Qu, D. Eiteneer, L.A. Hughes, J. Preusker, J. Wood, W. Rheinheimer, M.J. Hoffmann, K. van Benthem, Defect redistribution along grain boundaries in SrTiO3 by externally applied electric fields, J Eur Ceram Soc. (2022). https://doi.org/10.1016/j.jeurceramsoc.2022.11.028.

[228] X. Fang, K. Ding, S. Janocha, C. Minnert, W. Rheinheimer, T. Frömling, K. Durst, A. Nakamura, J. Rödel, Nanoscale to microscale reversal in room-temperature plasticity in SrTiO3 by tuning defect concentration, Scr Mater. 188 (2020) 228–232. https://doi.org/10.1016/j.scriptamat.2020.07.033.

[229] S. Stich, K. Ding, Q.K. Muhammad, L. Porz, C. Minnert, W. Rheinheimer, K. Durst, J. Rödel, T. Frömling, X. Fang, Room-temperature dislocation plasticity in SrTiO 3 tuned by defect chemistry, Journal of the American Ceramic Society. 105 (2022) 1318–1329. https://doi.org/10.1111/jace.18118.

[230] B.D. Cullity., S.R. Stock, Elements of X-Ray Diffraction, Third Edit, PEARSON, 2014.

[231] H. Jelitto, G.A. Schneider, A geometric model for the fracture toughness of porous materials, Acta Mater. 151 (2018) 443–453. https://doi.org/10.1016/j.actamat.2018.03.018.

[232] H. Jones, V. Tong, R. Ramachandramoorthy, K. Mingard, J. Michler, M. Gee, Micropillar compression of single crystal tungsten carbide, Part 1: Temperature and orientation dependence of deformation behaviour, Int J Refract Metals Hard Mater. 102 (2022) 105729. https://doi.org/10.1016/j.ijrmhm.2021.105729.

[233] X. Liu, J. Zhang, C. Hou, H. Wang, X. Song, Z. Nie, Mechanisms of WC plastic deformation in cemented carbide, Mater Des. 150 (2018) 154–164. https://doi.org/10.1016/j.matdes.2018.04.025.

[234] V. Tong, H. Jones, K. Mingard, Micropillar compression of single crystal tungsten carbide, part 2: Lattice rotation axis to identify deformation slip mechanisms, Int J Refract Metals Hard Mater. 103 (2022). https://doi.org/10.1016/j.ijrmhm.2021.105734.

[235] F.R.N. Nabarro, S.B. Luyckx, U. V. Waghmare, Slip in tungsten monocarbide. I. Some experimental observations, Materials Science and Engineering A. 483–484 (2008) 139–142. https://doi.org/10.1016/j.msea.2006.09.153.

[236] F.R.N. Nabarro, S.B. Luyckx, U. V. Waghmare, Slip in tungsten monocarbide. II. A first-principles study, Materials Science and Engineering A. 483–484 (2008) 9–12. https://doi.org/10.1016/j.msea.2006.09.174.

[237] F. De Luca, H. Zhang, K. Mingard, M. Stewart, B.M. Jablon, C. Trager-Cowan, M.G. Gee, Nanomechanical Behaviour of Individual Phases in WC-Co Cemented Carbides, from Ambient to High Temperature., Materialia (Oxf). 12 (2020). https://doi.org/10.1016/j.mtla.2020.100713.

[238] X. Liu, J. Zhang, C. Hou, H. Wang, X. Song, Z. Nie, Mechanisms of WC plastic deformation in cemented carbide, Mater Des. 150 (2018) 154–164. https://doi.org/10.1016/j.matdes.2018.04.025.

[239] M. Lee, High temperature hardness of tungsten carbide, Metallurgical Transactions A. 14 (1983) 1625–1629. https://doi.org/10.1007/BF02654390.

[240] F. Wakai, N. Kondo, Y. Shinoda, Ceramics superplasticity, Curr Opin Solid State Mater Sci. 4 (1999) 461–465. https://doi.org/10.1016/S1359-0286(99)00053-4.

[241] B.-N. Kim, K. Hiraga, K. Morita, Y. Sakka, A high-strain-rate superplastic ceramic, Nature. 413 (2001) 288–291. https://doi.org/10.1038/35095025.

[242] I. Utke, J. Michler, R. Winkler, H. Plank, Mechanical properties of 3d nanostructures obtained by focused electron/ion beam-induced deposition: A review, Micromachines (Basel). 11 (2020). https://doi.org/10.3390/MI11040397.

[243] J.J. Roa, P. Sudharshan Phani, W.C. Oliver, L. Llanes, Mapping of mechanical properties at microstructural length scale in WC-Co cemented carbides: Assessment of hardness and elastic modulus by means of high speed massive nanoindentation and statistical analysis, Int J Refract Metals Hard Mater. 75 (2018) 211–217. https://doi.org/10.1016/j.ijrmhm.2018.04.019.

[244] S.J. Oh, B.S. Kim, I.J. Shon, Mechanical properties and rapid consolidation of nanostructured WC and WC-Al2O3 composites by high-frequency induction-heated sintering, Int J Refract Metals Hard Mater. 58 (2016) 189–195. https://doi.org/10.1016/j.ijrmhm.2016.04.016.

[245] T. Csanádi, M. Bľanda, A. Duszová, N.Q. Chinh, P. Szommer, J. Dusza, Deformation characteristics of WC micropillars, J Eur Ceram Soc. 34 (2014) 4099–4103. https://doi.org/10.1016/j.jeurceramsoc.2014.05.045.

[246] H. Jelitto, G.A. Schneider, Fracture toughness of porous materials e Experimental methods and data, Data Brief. 23 (2019) 103709. https://doi.org/10.1016/j.dib.2019.103709.

[247] C. Relias, D. Ngai, Indentation fracture toughness: A review and application, American Ceramic Society Bulletin. 97 (2018).

[248] D.K. Shetty, I.G. Wright, P.N. Mincer, A.H. Clauer, Indentation fracture of WC-Co cermets, J Mater Sci. 20 (1985) 1873–1882. https://doi.org/10.1007/BF00555296.

[249] A. Moradkhani, H. Baharvandi, M. Tajdari, H. Latifi, J. Martikainen, Determination of fracture toughness using the area of micro-crack tracks left in brittle materials by Vickers indentation test, Journal of Advanced Ceramics. 2 (2013) 87–102. https://doi.org/10.1007/s40145-013-0047-z.

[250] S.J. Bull, T.F. Page, E.H. Yoffe, An explanation of the indentation size effect in ceramics, Philos Mag Lett. 59 (1989) 281–288. https://doi.org/10.1080/09500838908206356.

[251] L. Ortiz-Membrado, N. Cuadrado, D. Casellas, J.J. Roa, L. Llanes, E. Jiménez-Piqué, Measuring the fracture toughness of single WC grains of cemented carbides by means of microcantilever bending and micropillar splitting, Int J Refract Metals Hard Mater. 98 (2021). https://doi.org/10.1016/j.ijrmhm.2021.105529.

[252] G.D. Quinn, R.C. Bradt, On the Vickers Indentation Fracture Toughness Test, Journal of the American Ceramic Society. 90 (2007) 673–680. https://doi.org/10.1111/j.1551-2916.2006.01482.x.

[253] W.D. Nix, H. Gao, Indentation size effects in crystalline materials: A law for strain gradient plasticity, J Mech Phys Solids. 46 (1998) 411–425. https://doi.org/10.1016/S0022-5096(97)00086-0.

[254] K. Durst, B. Backes, O. Franke, M. Göken, Indentation size effect in metallic materials: Modeling strength from pop-in to macroscopic hardness using geometrically necessary dislocations, Acta Mater. 54 (2006) 2547–2555. https://doi.org/10.1016/j.actamat.2006.01.036.

[255] A. Nino, A. Tanaka, S. Sugiyama, H. Taimatsu, Indentation size effect for the hardness of refractory carbides, Mater Trans. 51 (2010) 1621–1626. https://doi.org/10.2320/matertrans.M2010110.

[256] K. Sangwal, Review: Indentation size effect, indentation cracks and microhardness measurement of brittle crystalline solids - some basic concepts and trends, Crystal Research and Technology. 44 (2009) 1019–1037. https://doi.org/10.1002/crat.200900385.

[257] B.J. Wachtman, W.R. Cannon, M.J. Matthewson, MECHANICAL PROPERTIES OF CERAMICS, 2009. https://doi.org/10.1002/9780470451519.

[258] I. Mazo, B. Palmieri, A. Martone, M. Giordano, V.M. Sglavo, Flash sintering in metallic ceramics: finite element analysis of thermal runaway in tungsten carbide green bodies, Journal of Materials Research and Technology. (2023). https://doi.org/10.1016/j.jmrt.2023.02.213.

Scientific Production

Mazo, I.; Molinari, A.; Sglavo, M. V. Electrical resistance flash sintering of tungsten carbide. Materials & Design. **2022**.
https://doi.org/10.1016/j.matdes.2021.110330.

Mazo, I.; Molinari, A.; Sglavo, M. V. Effect of pressure on the electrical resistance flash sintering of tungsten carbide. Journal of the European Ceramic Society. **2022**.
https://doi.org/10.1016/j.jeurceramsoc.2022.01.017.

Mazo, I.; Vanzetti, E. L.; Molina-Aldareguia M. J.; Molinari, A.; Sglavo, M. V. Role of surface carbon nanolayer on the activation of flash sintering in tungsten carbide. International Journal of Refractory Metals and Hard Materials. **2023**.
https://doi.org/10.1016/j.ijrmhm.2022.106090.

Mazo, I.; Molina-Aldareguia M. J.; Molinari, A.; Sglavo, M. V. Room temperature stability, structure and mechanical properties of cubic tungsten carbide in flash sintered products. Journal of Materials Science. **2023**.
https://doi.org/10.1007/s10853-022-08109-4.

Mazo, I.; Palmieri B.; Martone, A.; Giordano M.; Sglavo, M. V. Flash sintering in metallic ceramics: finite element analysis of thermal runaway in tungsten carbide green bodies. Journal of Materials Research and Technology Science. **2023**.
https://doi.org/10.1016/j.jmrt.2023.02.213.

Internships

1 year as visiting PhD student at the IMdea Materials research center in Madrid, Spain. The scientific collaboration was coordinated by the principal investigator (PI) Prof. Jon Molina-Aldareguia and in part by Prof. Miguel Monclus. The exchange period was focused on the study of the effect of different consolidation techniques on the plasticity of tungsten carbide sintered ceramics.

Participation to congresses and schools

Poster presentation.
Online Summer School on Electric and Magnetic Field-assisted Processing of Inorganic Materials, Forschungszentrum Jülich (Germany). **2020**.

Oral presentation.
European Congress and Exhibition on Advanced Materials and Processes (EUROMAT). Leoben (Austria) **2021**.

Invited talk (co-author).
45th International Conference and Exposition on Advanced Ceramics and Composites (ICACC). Daytona Beach, Florida (USA). **2021.**

Oral presentation.
46th International Conference and Exposition on Advanced Ceramics and Composites (ICACC). Daytona Beach, Florida (USA). **2022.**

Poster presentation.
32nd International Conference on Diamond and Carbon Materials (ICDCM). Lisbon (Portugal). **2022**.

Oral presentation.
Ceramics in Europe, XVII European Ceramic Society Conference (ECerS). Krakow (Poland). **2022**.

Oral presentation.
47th International Conference and Exposition on Advanced Ceramics and Composites (ICACC). Daytona Beach, Florida (USA). **2023.**

Permissions

Room temperature stability, structure and mechanical properties of cubic tungsten carbide in flash sintered products

Author: Isacco Mazo et al
Publication: Journal of Materials Science
Publisher: Springer Nature
Date: Jan 4, 2023

Order Completed

Your confirmation email will contain your order number for future reference.

License Number	5503090753345	🖨 Printable Details
License date	Mar 06, 2023	
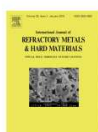
Cemented carbide microstructures: a review

Author: José García,Verónica Collado Ciprés,Andreas Blomqvist,Bartek Kaplan
Publication: International Journal of Refractory Metals and Hard Materials
Publisher: Elsevier
Date: April 2019

Creative Commons Attribution-NonCommercial-No Derivatives License (CC BY NC ND)

BACK
CLOSE WINDOW

Anomalously large lattice thermal conductivity in metallic tungsten carbide and its origin in the electronic structure

Author: A. Kundu,J. Ma,J. Carrete,G.K.H. Madsen,W. Li
Publication: Materials Today Physics
Publisher: Elsevier
Date: June 2020

Order Completed

Your confirmation email will contain your order number for future reference.

License Number	5503080193396	🖨 Printable Details
License date	Mar 06, 2023	

Thermal shock of tungsten carbide in plasma-facing conditions

Author: S.A. Humphry-Baker,G.D.W. Smith,G. Pintsuk

Publication: Journal of Nuclear Materials

Publisher: Elsevier

Date: October 2019

Order Completed

Thank you for your order.

This Agreement between Mr. isacco mazo ("You") and Elsevier ("Elsevier") consists of your license details and the terms and conditions provided by Elsevier and Copyright Clearance Center.

Your confirmation email will contain your order number for future reference.

License Number	5503080756713	🖨 Printable Details
License date	Mar 06, 2023	

Hot pressing of tungsten carbide with and without sintering additives

Author: Agnieszka Gubernat,Paweł Rutkowski,Grzegorz Grabowski,Dariusz Zientara

Publication: International Journal of Refractory Metals and Hard Materials

Publisher: Elsevier

Date: March 2014

Order Completed

Thank you for your order.

This Agreement between Mr. isacco mazo ("You") and Elsevier ("Elsevier") consists of your license details and the terms and conditions provided by Elsevier and Copyright Clearance Center.

Your confirmation email will contain your order number for future reference.

License Number	5503080987388	🖨 Printable Details
License date	Mar 06, 2023	

Sub-micron binderless tungsten carbide sintering behavior under high pressure and high temperature

Author: Dejiang Ma,Zili Kou,Yinjuan Liu,Yongkun Wang,Shangpan Gao,Xi Luo,Wentao Li,Yonghua Wang,Yanchun Du,Li Lei

Publication: International Journal of Refractory Metals and Hard Materials

Publisher: Elsevier

Date: January 2016

Order Completed

Thank you for your order.

This Agreement between Mr. isacco mazo ("You") and Elsevier ("Elsevier") consists of your license details and the terms and conditions provided by Elsevier and Copyright Clearance Center.

Your confirmation email will contain your order number for future reference.

License Number	5503081190539	🖨 Printable Details
License date	Mar 06, 2023	

Evidence of surface cleaning during electric field assisted sintering

Author: Cecile S. Bonifacio,Troy B. Holland,Klaus van Benthem

Publication: Scripta Materialia

Publisher: Elsevier

Date: December 2013

Order Completed

Thank you for your order.

This Agreement between Mr. isacco mazo ("You") and Elsevier ("Elsevier") consists of your license details and the terms and conditions provided by Elsevier and Copyright Clearance Center.

Your confirmation email will contain your order number for future reference.

License Number	5503081373516	🖶 Printable Details
License date	Mar 06, 2023	

Development of electric resistance sintering process for the fabrication of hard metals: Processing, microstructure and mechanical properties

Author: M.A. Lagos,I. Agote,T. Schubert,T. Weissgaerber,J.M. Gallardo,J.M. Montes,L. Prakash,C. Andreouli,V. Oikonomou,D. Lopez,J.A. Calero

Publication: International Journal of Refractory Metals and Hard Materials

Publisher: Elsevier

Date: August 2017

Order Completed

Thank you for your order.

This Agreement between Mr. isacco mazo ("You") and Elsevier ("Elsevier") consists of your license details and the terms and conditions provided by Elsevier and Copyright Clearance Center.

Your confirmation email will contain your order number for future reference.

License Number	5503090003321	🖶 Printable Details
License date	Mar 06, 2023	

An explanation of the indentation size effect in ceramics

Author: S. J. Bull, , T. F. Page, et al

Publication: Philosophical Magazine: Letters

Publisher: Taylor & Francis

Date: Jun 1, 1989

Thesis/Dissertation Reuse Request

Taylor & Francis is pleased to offer reuses of its content for a thesis or dissertation free of charge contingent on resubmission of permission request if work is published.

BACK   CLOSE